

Tao Zhao

---

# Coupled DEM-CFD Analyses of Landslide-Induced Debris Flows



Science Press  
Beijing



Springer

# Coupled DEM-CFD Analyses of Landslide-Induced Debris Flows

Tao Zhao

# Coupled DEM-CFD Analyses of Landslide-Induced Debris Flows

Tao Zhao  
State Key Laboratory of Hydraulics  
and Mountain River Engineering  
College of Water Resource  
and Hydropower, Sichuan University  
Chengdu, Sichuan  
China

ISBN 978-981-10-4626-1      ISBN 978-981-10-4627-8 (eBook)  
DOI 10.1007/978-981-10-4627-8

Jointly published with Science Press, Beijing, China  
ISBN: 978-7-03-052630-4 Science Press, Beijing, China

The printed edition is not for sale in China Mainland. Customers from China Mainland please order the print book from Science Press

Library of Congress Control Number: 2017937737

© Springer Nature Singapore Pte Ltd. & Science Press 2017

This work is subject to copyright. All rights are reserved by the Publishers, whether the whole or part of the material is concerned, specifically the rights of translation, reprinting, reuse of illustrations, recitation, broadcasting, reproduction on microfilms or in any other physical way, and transmission or information storage and retrieval, electronic adaptation, computer software, or by similar or dissimilar methodology now known or hereafter developed.

The use of general descriptive names, registered names, trademarks, service marks, etc. in this publication does not imply, even in the absence of a specific statement, that such names are exempt from the relevant protective laws and regulations and therefore free for general use.

The publishers, the authors and the editors are safe to assume that the advice and information in this book are believed to be true and accurate at the date of publication. Neither the publishers nor the authors or the editors give a warranty, express or implied, with respect to the material contained herein or for any errors or omissions that may have been made. The publishers remains neutral with regard to jurisdictional claims in published maps and institutional affiliations.

Printed on acid-free paper

This Springer imprint is published by Springer Nature  
The registered company is Springer Nature Singapore Pte Ltd.  
The registered company address is: 152 Beach Road, #21-01/04 Gateway East, Singapore 189721, Singapore

# Preface

In recent years, the increasing impacts of landslide hazards on human lives and life-line facilities worldwide has advanced the necessity to find out both economically acceptable and useful techniques to predict the occurrence and destructive power of landslides. Though many projects exist to attain this goal, the current investigation set out to establish an understanding of the initiation and propagation mechanisms of landslides via numerical simulations, so that mitigation strategies to reduce the long-term losses from landslide hazards can be made.

This book summarizes some of the recent researches on landslides via the Discrete Element Method (DEM) and Computational Fluid Dynamics (CFD). These two methods have been used to investigate the mechanical and hydraulic behaviour of granular materials involved in landslides. The main challenge is to provide rational analyses of large-scale landslides via small-scale numerical simulations. To solve this problem, dimensional analyses have been performed on a simple granular column collapse model. The influence of governing dimensionless groups on the debris runout distance and deposit height has been studied for the terrestrial and submerged granular flows.

3D DEM simulations of granular flows in plane strain conditions have been performed in this research. The input parameters of the DEM model have been calibrated by the numerical triaxial tests, based on which, the relationships between the microscopic variables and the macroscopic soil strength properties were analysed. Using the simple granular column collapse model, the influences of column aspect ratio, characteristic strain, model size ratio and material internal friction angle on the runout distance and deposit height of granular materials have been examined. Additionally, the deformation and energy evolution of dry granular materials are also discussed. The DEM–CFD coupling model has been employed to study the mechanical and hydraulic behaviour of highly mobilized terrestrial/submarine landslides. This model has been validated via numerical simulations of fluid flow through a porous soil sample and grain batch sedimentations. The simulations of granular flows in the submerged environment have led to some meaningful insights into the flow mechanisms, such as the mobilization of

sediments, the generation and dissipation of excess pore water pressures and the evolution of effective stresses.

Overall, this study shows that the proposed numerical tools are capable of modelling the mechanical and hydraulic behaviour of terrestrial and submarine landslides.

Chengdu, China

Tao Zhao

# Acknowledgements

First, and above all, I would like to thank my wife Xiaoxiu Shen for her total support of my work. Without her effortless yet dedicated love and encouragement, this book would have never been possible.

My heartfelt appreciation devotes to my Ph.D. supervisors, Prof. Guy Housby and Dr. Stefano Utili, for their invaluable professional guidance. I owe a particular debt of gratitude to Guy for inspiring me to carry out research on the most intricate problems. I am indebted to Stefano for his encouragement and enthusiasm, which led me to persevere with my research. Their support has also greatly contributed to further develop my critical thinking and analytical skills. I would like to acknowledge the DEM research group at the University of Oxford: Dr. Chiara Modenese, Dr. Chia Weng Boon, Kovthaman Murugaratnam and Giulia Macaro for their patient discussions with me on my project. I am very grateful for the help from Dr. Feng Chen on the DEM–CFD coupling program. I would also like to thank all the users and developers of the open-source codes ESyS-Particle and OpenFOAM, whose invaluable guidance and advice have largely contributed to the success of this research project. In particular, I would like to acknowledge Prof. Jidong Zhao from Hong Kong University of Science and Technology for discussions on the modelling of granular materials and multiphase flows. I also would like to thank the Geotechnical Engineering research group at Sichuan University for their support of my work.

Finally, I am particularly grateful to the financial support by the National Natural Science Foundation of China (Grant No. 41602289), the State Key Program of National Natural Science of China (Grant No. 51639007), and the National Program on Key Basic Research Project (Grant No. 2015CB057903).

# Contents

<b>1</b>	<b>Introduction to Landslides</b>	1
1.1	Background	1
1.2	Terrestrial Landslides	3
1.2.1	Classification and Characteristics	3
1.2.2	Major Research on Terrestrial Landslides	6
1.3	Submerged Landslides	9
1.3.1	Classification and Characteristics	10
1.3.2	Major Research on Submerged Landslides	13
1.4	Model Testing—Granular Column Collapse	14
1.5	Numerical Investigations	16
1.5.1	The Finite Element Method	17
1.5.2	The Smoothed Particle Hydrodynamics	18
1.5.3	The Discrete Element Method	19
1.5.4	The DEM-CFD Coupling Method	21
<b>2</b>	<b>Introduction to Discrete Element Method</b>	25
2.1	The Discrete Element Method	25
2.1.1	Particle Motion	26
2.1.2	The Particle—Particle Contact Model	27
2.1.3	The Calculation of Stress in the DEM	30
2.1.4	Coordination Number	30
2.2	Model Validation	31
2.2.1	Input Parameters of the DEM Model	31
2.2.2	Determination of Numerical Time Step	31
2.2.3	Numerical Simulation of Triaxial Tests	34
2.2.4	Material Angle of Repose	42
2.3	Conclusions	45

<b>3 Investigation of Dry Granular Flows . . . . .</b>	47
3.1 The Granular Column Collapse Model . . . . .	47
3.2 Dimensional Analysis . . . . .	49
3.3 Numerical Simulations . . . . .	51
3.3.1 Deformation of the Granular Assembly . . . . .	52
3.3.2 Influence of Initial Column Aspect Ratio . . . . .	58
3.3.3 Influence of Model Size Ratio . . . . .	62
3.3.4 Influence of Column Characteristic Strain . . . . .	63
3.3.5 Influence of Material Internal Friction Angle . . . . .	65
3.4 Mechanical Analyses . . . . .	65
3.4.1 Evolution of Granular Velocity . . . . .	67
3.4.2 Granular Energy . . . . .	70
3.4.3 Linear Momentum . . . . .	73
3.4.4 Flux of Kinetic Energy . . . . .	74
3.4.5 Distribution of Kinetic Energy and Linear Momentum . . . . .	79
3.4.6 Evolution of Force Chains . . . . .	81
3.4.7 Distribution of Stress . . . . .	82
3.4.8 Distribution of Coordination Number . . . . .	84
3.4.9 Destination of Surface Grains . . . . .	85
3.4.10 Influence of Air Viscous Force . . . . .	87
3.5 Conclusions . . . . .	89
<b>4 Introduction to the DEM-CFD Coupling Model . . . . .</b>	91
4.1 Fluid–Solid Interaction . . . . .	91
4.2 Governing Equations of Fluid Flow . . . . .	94
4.2.1 Fluid Mass Conservation Law . . . . .	95
4.2.2 Fluid Momentum Conservation Law . . . . .	96
4.3 The Viscous Shear Stress . . . . .	99
4.3.1 Laminar Flow Regime . . . . .	99
4.3.2 Turbulent Flow Regime . . . . .	100
4.3.3 Near-Wall Treatment . . . . .	102
4.3.4 Initial Conditions . . . . .	105
4.4 The MPI Implementation and Data Exchange . . . . .	105
4.5 Fluid Flow Through a Porous Soil Sample . . . . .	108
4.5.1 Analytical Solution of Soil Permeability . . . . .	110
4.5.2 Numerical Model Configuration . . . . .	112
4.5.3 Laminar Flow . . . . .	113
4.5.4 Turbulent Flow . . . . .	114
4.6 Numerical Investigation of Granular Sedimentation . . . . .	115
4.6.1 The Settling of a Single Particle . . . . .	119
4.6.2 Batch Granular Sedimentation . . . . .	121
4.7 Conclusions . . . . .	132

<b>5 Investigation of Submerged Debris Flows . . . . .</b>	135
5.1 Model Configuration. . . . .	135
5.2 Physical Properties of Sediments . . . . .	136
5.3 Dimensional Analysis. . . . .	138
5.3.1 Discussion of the Dimensionless Groups. . . . .	140
5.3.2 Summary of the Dimensionless Groups. . . . .	142
5.4 Modelling of Small-Scale Submerged Debris Flows. . . . .	143
5.4.1 Deformation of the Granular Assembly. . . . .	144
5.4.2 Influence of Initial Column Aspect Ratio . . . . .	146
5.4.3 Influence of Model Size Ratio. . . . .	148
5.4.4 Influence of Characteristic Strain and Reynolds Number. . . . .	150
5.4.5 Influence of Material Internal Friction Angle . . . . .	153
5.5 Mechanical and Hydrodynamic Analyses . . . . .	153
5.5.1 Evolution of Particle Velocity Field . . . . .	153
5.5.2 Fluid Velocity Field . . . . .	155
5.5.3 Relative Velocity Between Particle and Water . . . . .	156
5.5.4 Distribution of Excess Pore Water Pressure. . . . .	158
5.5.5 Evolution of Force Chains. . . . .	159
5.5.6 Distribution of Effective Stress . . . . .	159
5.5.7 Distribution of Bulk Coordination Number . . . . .	162
5.5.8 Evolution of the Run-out Distance and Deposit Height . . . . .	162
5.6 Modelling of Large-Scale Landslides . . . . .	163
5.6.1 Determination of Numerical Time Step . . . . .	166
5.6.2 The Mobility of Large-Scale Submerged Landslides . . . . .	169
5.6.3 Mechanical and Hydraulic Behaviour of Loose Sample . . . . .	170
5.6.4 Mechanical and Hydraulic Behaviour of Dense Sample . . . . .	176
5.7 Conclusions . . . . .	183
<b>6 Conclusions and Recommendations for Future Work . . . . .</b>	185
6.1 Summary and Conclusions . . . . .	185
6.2 Recommendations for Future Work . . . . .	188
<b>Appendix A: Summary of the Selected Landslides . . . . .</b>	189
<b>Appendix B: Calculation of Porosity . . . . .</b>	195
<b>Appendix C: Input Parameters for Simulations . . . . .</b>	203
<b>References . . . . .</b>	205

# Nomenclature

## Variables of the DEM Model

$\beta, \eta$	Coefficients of rolling stiffness and plastic moment
$\varepsilon_1, \varepsilon_2, \varepsilon_3$	Components of the principal strains of a soil sample
$\varepsilon_v$	Volumetric strain of a soil sample
$\theta$	Inter-particle friction angle
$\varphi$	Material internal friction angle
$\varphi_{peak}, \varphi_{cv}$	Peak and constant volume material internal friction angle
$\rho_s$	Density of solid particle
$\omega_i$	Angular velocity of particle $i$
$\sigma_{ij}$	Stress tensor of a granular assembly
$\sigma_1, \sigma_2, \sigma_3$	Components of the principal stress of a soil sample
$C_i$	Coordination number of particle $i$
$\bar{C}$	Bulk coordination number of a granular assembly
$D$	Particle diameter
$f_{nc}, f_{tc}$	Normal, shear contact force
$g$	Gravitational acceleration
$I_i$	Moment of inertia about the grain centroid for particle $i$
$K_n$	Normal contact stiffness
$K_r$	Rolling stiffness
$K_s$	Shear contact stiffness
$m_i$	Mass of particle $i$
$M_r$	Rolling resistant moment
$n$	Porosity of a soil sample
$p, q$	Mean and deviatoric stresses of soil sample
$r_c$	Vector from the particle mass centre to the contact point
$r$	Radius of the particle
$\Delta t$	DEM time step
$U_n$	Normal overlap distance between two spheres
$dU_s$	Incremental tangential displacement between two particles

$v_{pi}$	Volume of particle $i$
$\mathbf{V}$	Particle velocity
$x_i$	Position of the centroid of particle $i$

## Variables of the DEM–CFD Coupling Model

$\beta$	Fluid–solid momentum transfer coefficient
$C_d$	Drag force coefficient
$\chi$	Coefficient of porosity correction term in drag force
$\mathbf{F}_d$	Fluid viscous drag force
$f_{fluid}$	Interaction forces between fluid and particles
$f_{hs}$	Hydrostatic force
$\mathbf{U}_r$	Relative velocity between fluid and a solid particle

## Variables of CFD Model

$\tau$	Fluid viscous stress tensor
$\tau_T$	Reynolds stress tensor
$k, \varepsilon$	Turbulent kinetic energy and its dissipation rate in the $k$ - $\varepsilon$ model
$\kappa$	Von Karman constant
$C_1, C_2, C_\mu, \sigma_k, \sigma_\varepsilon$	Constants of the $k$ - $\varepsilon$ model
$\delta$	Identity tensor
$\rho_f$	Density of fluid
$C$	Courant number of fluid flow
$F_b$	Body force acting on a fluid mesh element
$f_g$	Gravity force of a fluid mesh element
$I$	Intensity of fluid turbulence
$l$	Turbulent length scale
$Re_p$	Reynolds number defined at particle scale
$\mathbf{U}, \mathbf{U}'$	Mean and fluctuating fluid velocity in turbulent flow
$p, p'$	Mean and fluctuating fluid pressure in turbulent flow
$u, v, w$	Components of fluid velocity in a 3D Cartesian coordinate system
$x, y, z$	3D Cartesian coordinate system
$\mu$	Dynamic viscosity of fluid
$\nu$	Kinematic viscosity of fluid
$u^*$	Friction velocity in the wall function of turbulent modelling
$y^+, u^+$	Normalized distance and fluid velocity in the wall function
$\Delta x$	Minimum size of the fluid mesh cell

## Variables of Granular Flow Simulations

$\alpha$	Scaling factor of fluid viscous drag force
$\theta_f$	Inclination angle of the slope failure plane
$a$	Column aspect ratio
$c_v$	Coefficient of consolidation
$M$	Total mass of the granular assembly
$E_0$	Total energy of the initial granular column
$E_{diss}$	Dissipative energy of the granular assembly
$E_k$	Kinetic energy of the granular assembly
$E_p$	Potential energy of the granular assembly
$p$	Momentum of the granular material
$F_{x,y,z}$	Components of the flux of granular momentum
$\mathbf{F}_c$	Particle contact force
$h$	Height of the granular assembly during the debris flow
$H_i, H_f$	Initial, final granular deposit height
$L_i, L_f$	Initial, final granular deposit length
$L_{max}, H_{max}$	Maximum granular runout distance and deposit height
$m_v$	Coefficient of volume compressibility
$t$	Duration time of granular flow
[F]	Normalized particle contact force
[L]	Normalized particle runout distance
[H]	Normalized deposit height
[S]	Model size ratio
[T]	Normalized duration time of the granular flow
[ $T_s$ ], [ $T_v$ ]	Characteristic settling and consolidation time of a soil sample
[V]	Normalized debris sliding velocity
[ $\epsilon$ ]	Characteristic strain of the initial granular column
[ $\sigma$ ]	Normalized stress of the granular assembly

## Variables of Fluid Flow Through Porous Soil Sample

$a, b$	Coefficients of linear and nonlinear pressure head loss
$\Delta L$	Length of the flow passage
$\Delta h$	Fluid pressure head loss
$i$	Fluid hydraulic gradient
$k$	Coefficient of soil permeability
$v_o$	Constant settling velocity of a single spherical particle
$u$	Excess pore water pressure
$\rho_b$	Bulk density of a fluid–solid suspension

# Chapter 1

## Introduction to Landslides

### 1.1 Background

In recent years, the growing world population and the expansion of settlements and developments over landslide-prone areas are increasing the impacts of landslide disasters on human lives and life-line facilities worldwide (Glade 1998). In addition, human activities offshore, especially in the Exclusive Economic Zones, also increase the potential risk of submarine landslide hazards. The term “landslide” describes a variety of events that lead to the downward and outward movement of slope-forming materials such as rock, soil and some artificial fills *en masse* under gravity (Highland and Bobrowsky 2008), in either terrestrial (USGS 2004) or submarine (Lee et al. 1991) environments. Long runout landslides normally present very high mobility with “fluid-like” motions (Andrade et al. 2012), such that they can travel distances several times larger than the initial size of the source topography along flat or almost flat ground surfaces, sweeping away populated areas located far away from the landslide source (Dade and Huppert 1998; Carrara et al. 2008; Crosta et al. 2009), threatening to sweep away populated areas even if located far away from the mountainsides (Crosta et al. 2005). These natural disasters have been studied intensively due to their significant destructive power.

The related field investigations, laboratory experiments and numerical simulations has focused on exploring the initiation and propagation mechanisms of landslides (Cannon and Michael 2011). In field investigations, researchers always have to study landslides after the event has taken place, because direct measurements during the time of occurrence are difficult or even impossible as the work is too dangerous (Zenit 2005). In addition, the stochastic nature of their occurrence and magnitude hampers the collection of detailed data on landslides. Furthermore, the topography plays an important role in controlling the post-failure motion of granular materials, which is believed to be essential to understanding the dynamic motion and destructive power of landslides (Lube et al. 2005; Zenit 2005; Thompson and Huppert 2007). The problem has been a topic of intensive research

by experimental and numerical investigations, with special focus on the mechanical behaviour of dense flowing granular materials (e.g. landslides, rock and debris avalanches).

The loss of human lives due to landslides is larger in developing countries, whereas economic losses are more severe in developed countries (Schuster and Fleming 1986). However, few effective measures used to predict and control landslides have been implemented. Developing countries usually have difficulties in meeting the high costs of related engineering works and land-use planning, while developed countries are increasingly reluctant to invest money in landslide mitigation due to the economic recession (Guzzetti et al. 1999). Economic and social considerations suggest that we need to develop both economically acceptable and useful techniques to predict the initiation and propagation of landslides (USGS 1982; Mitchell 1988). Consequently, landslide warning systems and land utilization regulations can be implemented, so that the loss of lives and properties can be minimized without investing in long-term, costly projects of ground stabilization (Schuster and Fleming 1986; Guzzetti et al. 1999). Based on these considerations, the current study presents a suitable numerical investigation of landslides using the Discrete Element Method (DEM) (Cundall and Strack 1979) and Computational Fluid Dynamics (CFD) (Anderson 1995), with special focus on revealing the mechanical and hydraulic behaviour of solid and fluid materials involved in landslides. The numerical technique allows the modelling of solid materials (e.g. soil and rock) as a collection of individual spherical grains which interact with each other through well-defined microscopic contact laws (Mindlin and Deresiewicz 1953; Itasca 2003), while the influence of fluid (e.g. water and air) on debris motion is simulated using empirical solid–fluid interaction models (Ergun 1952; Wen and Yu 1966; Di Felice 1994). The behaviour of fluid flow is resolved by solving the modified Navier–Stokes equations in the CFD. Furthermore, the implementation of the DEM and CFD in open source codes makes this technique accessible and affordable by the majority of researchers worldwide.

The laboratory and numerical experiments on landslides have provided useful insights into hazard assessments (Cleary and Sawley 2002; Zenit 2005), when a potential source of landslide can be identified (McDougall and Hungr 2004). Whilst it is well known that both solid and fluid phases can affect the behaviour of landslides significantly, the governing equations for the motion of each phase and the interactions between materials involved are still not well established. The real soil mass consists of a mixture of solid particles, water and air, which produces the complex mechanical behaviour of landslides. Thus, a rational model describing the behaviour of landslides should consider both grain collisions, friction and the interactions between solid and fluid (Tsuji et al. 1993; Zeghal and El Shamy 2004; Shafipour and Soroush 2008; Shimizu 2011).

The main purpose of this research is to investigate the initiation and propagation mechanisms of landslides using numerical tools. The DEM is used to investigate the mechanical behaviour of dry granular flows, while a coupled DEM-CFD model is used to study debris motions in the submerged environment. A well-developed discrete-continuum coupling algorithm (Anderson and Jackson 1967; Brennen

2005) has been implemented in the DEM and CFD programs to simulate the fluid–solid interactions. The main challenge is to provide complete analyses of large scale landslides based on small scale numerical models. This problem has been addressed in studying slope failures using small scale models (Sharma and Bolton 1996; Gui 1999), from which the behaviour of real slopes can be obtained via well-defined scaling laws. This method has been employed in the current research, in which the model size is constrained by the total number of grains generated in the DEM. Based on the DEM model, a set of scaling relationships of the governing dimensionless groups have been derived from detailed dimensional analyses. By studying the mechanical behaviour of the solid and fluid materials using the scaling relationships, it is hoped that a preliminary understanding of the mechanical and hydraulic behaviour of landslides can be obtained.

## 1.2 Terrestrial Landslides

Terrestrial landslides commonly occur together with other natural hazards such as earthquakes, volcanoes and floods, displacing solid materials in a process that can be in abrupt soil or rock collapsing, creeping, falling, toppling, sliding, spreading and flowing (Hung et al. 2001). As illustrated in USGS (2004), the fundamental features of terrestrial landslides are a series of rupture surfaces and a large amount of displaced solid mass. During sliding, the solid materials such as soil and rock can fail along one or several rupture surfaces, as the shear strength of soil is unable to maintain equilibrium with the downslope driving stresses. The displaced solid mass might remain intact, be slightly or highly deformed or disintegrate into distinct solid blocks, generating pore water pressure and producing debris flows (Wang and Sassa 2001). For instance, large rockslides-avalanches can have volumes of  $10^7$ – $10^{11}$  m<sup>3</sup>, and areal spreading of up to 1000 km<sup>2</sup> (Hayashi and Self 1992; Bowman et al. 2012). For large rock masses (e.g. with volume larger than 10<sup>5</sup> m<sup>3</sup>), the disintegration can lead to intense interactions between rock fragments, involving punching, shearing and stripping processes (Locat et al. 2006). Some notable landslides with significant socioeconomic impacts, occurring in the last century are summarized in Table 1.1.

### 1.2.1 Classification and Characteristics

The classification of landslides is complex due to different types of triggering mechanisms, movement and depositional morphology. As a consequence, landslide classifications are generally based on different discriminating factors, sometimes very subjective (Hutchinson 1988; Cruden and Varnes 1996; Hung et al. 2001; Locat and Lee 2002). Based on the kinematic motion and material properties, a

**Table 1.1** Catastrophic landslides in the last century [after Highland (2010)]

Date	Place	Name	Trigger	Casualties
19/05/1919	Indonesia	Kelut lahars	Volcano	5110
16/12/1920	China	Haiyuan landslide	Earthquake	>100,000
25/08/1933	China	1933 Diexi landslide	Earthquake	3100
13/12/1941	Peru	Huaraz debris flow	Earth-dam break	4000–6000
1953	Japan	Arida river landslide	Typhoon	1046
1958	Japan	Kanogawa landslides	Rainfall	1094
10/01/1962	Peru	1962 Nevado Huascarán debris avalanche	Collapse of glacier	4000–5000
31/05/1970	Peru	1970 Nevado Huascarán debris avalanche	Earthquake	>22,000
13/11/1985	Colombia	Armero tragedy	Volcano	23,000
14/12/1999	Venezuela	Vargas tragedy	Heavy storm	30,000
09/08/2009	China	Taiwan, Xiaolin	Typhoon	600
08/08/2010	China	Zhouqu county mudslide	Rainfall	1287

classification of terrestrial landslides made by Hungr et al. (2001) is given in Table 1.2.

The major triggering mechanisms of terrestrial landslides consist of three categories: geological processes, morphological events and human activities. Among these categories, the influence of water, seismic events and volcanic activities are dominant.

- Rapid water infiltration due to intense rainfall, snowmelt, changes of ground-water level along earth dams, the banks of lakes or reservoirs lead to increase of slope saturation, and the pore water pressure, and thus trigger slope failure.
- The influence of seismic activity on slope failure can be very significant because the ground shaking can loosen the soil and rock mass triggering landslides.
- The landslides triggered by volcanoes are normally very devastating events, as the volcanic lava can melt soil or rock at a rapid rate, accelerating the motion of solid materials and destroying anything along its path.

Once failed, the debris materials tend to be disintegrative, which means that the slope mass would break into small blocks during the downslope motion. Because of this feature, the solid mass can develop large strains, lose its internal structure, and consequently, break up into debris or rubble, forming fast moving debris flows. As defined by USGS (2004), a debris flow is an event of rapid mass movement, which consists of loose soil, rock, air and water. It is commonly triggered by intense surface flow resulting from heavy rainfall or rapid ocean current, such that the loose soil or rock on steep slopes can be mobilized.

Field investigations have revealed that rainfall induced debris flows have very high occurrence frequency and can be mobilized from various types of terrains,

**Table 1.2** Classification of terrestrial landslides [after Hungr et al. (2001)]

Material	Water content	Special condition	Velocity	Name
Silt, sand, gravel, debris	Dry, moist or saturated	<ul style="list-style-type: none"> <li>– No excess pore-pressure</li> <li>– Limited volume</li> </ul>	Various	Non-liquefied landslides
Silt, sand, weak rock	Saturated at rupture surface content	<ul style="list-style-type: none"> <li>– Liquefiable material</li> <li>– Constant water</li> </ul>	Extremely (Ex.) rapid	Sand (silt, rock) flow slide
Sensitive clay	At or above liquid limit	<ul style="list-style-type: none"> <li>– Liquefaction in situ</li> <li>– Constant water content</li> </ul>	Ex. rapid	Clay flow slide
Peat	Saturated at rupture surface content	<ul style="list-style-type: none"> <li>– Excess pore-pressure</li> </ul>	Slow to very rapid	Peat flow
Clay or earth	Near plastic limit	<ul style="list-style-type: none"> <li>– Slow movements</li> <li>– Plug flow (sliding)</li> </ul>	<Rapid	Earth flow
Debris	Free water present	<ul style="list-style-type: none"> <li>– Flood</li> </ul>	Ex. rapid	Debris flood
Debris	Partly or fully	<ul style="list-style-type: none"> <li>– No established channel</li> <li>– Relatively shallow</li> <li>– Steep slope</li> </ul>	Ex. rapid	Debris avalanche
Fragmented rock	Various, mainly dry	<ul style="list-style-type: none"> <li>– Intact rock at source</li> <li>– Large volume</li> </ul>	Ex. rapid	Rock avalanche

travelling very long distances. Small debris flows generally occur on hillsides or embankments where slopes with nearly the angle of repose become saturated with water (Rodine 1974). Some large debris flows may result from the coalescence of numerous, small slope failures (Fairchild 1987), or from flow enlargement due to the incorporation of bed and bank debris materials (Bovis and Dagg 1992), or from large, individual landslides that mobilize partially or completely (Vallance and Scott 1997). They can occur with little warning information as a consequence of slope failure in mountainsides and continental margins, exerting significant impulsive loads on any objects encountered along the sliding paths. Two conditions may contribute to the mobilization of debris flows: (a) sufficient water to saturate the slope, and (b) induced excess pore water pressure to initiate slope failure. This process could cause significant slope deformation and increase of pore water pressure. Although the increase of bulk soil weight due to rainfall infiltration can possibly trigger slope failure (Brand 1981), the mainstream assumption is that the

induced positive excess pore water pressure in a saturated soil mobilizes debris flows. This condition is satisfied when the infiltrating water encounters soil with low permeability (Reid et al. 1988).

### ***1.2.2 Major Research on Terrestrial Landslides***

It has long been researchers' interests to explore the terrestrial landslides, especially debris flows, due to their significant destructive power and unexplained mechanisms of long travelling distances (Iverson 1997). Once the debris flow is initiated, the solid and fluid materials would play vital roles, influencing the dynamic motion and depositional morphology of solid materials, which distinguishes the debris flow from other related natural hazardous events, such as rock avalanches, turbidity currents and water laden flood (Cruden and Varnes 1996). Many hypotheses have been proposed to explain the apparent high mobility of debris flows, including the air cushion trapped at the failure plane (Shreve 1968), basal rock melting (De Blasio and Elverhøi 2008), sand fluidization (Hung and Evans 2004), destabilization of loose granular materials at the failure plane (Iverson et al. 2011), acoustic fluidization (Collins and Melosh 2003) or grain segregation-induced friction decrease (Phillips et al. 2006). These models have provided some scientific insights into the initiation and propagation mechanisms of landslides based on the geological and physical properties of slopes (Iverson 1997). Though some of these mechanisms invoked may be important in some specific landslide events, none of them has been widely recognized as a universal explanation of landslide mobility, and the debate continues (Legros 2002). In general, the related research can be categorized as field investigations, laboratory experiments and numerical simulations.

Field investigations of terrestrial landslides mainly focus on the occurrence of landslides within a specific region and a given time period, including landslide frequency, locations and triggering mechanisms. These information can be summarized as landslide inventories or landslide maps, which are used by engineers or policy-makers to plan land resources and mitigate landslide hazards (Guzzetti et al. 1999). However, these maps are empirical and site-dependent, so that they may not be applicable to different regions. To have a model of general applicability, the mechanisms of landslide initiation and propagation have to be considered. According to the field investigations, landslides are frequently triggered by rainfall, and this is especially true for the majority of landslides occurred in mountainous regions. The rainfall-induced landslides can be triggered by either the increase of pore water pressure due to soil shear contraction or the infiltration of water after intensive rainfall (Casagrande 1936; Harp et al. 1990; Li 1997). Some well-documented examples include the landslides occurred at Huascarán (Plafker and Erickson 1978), Mount St. Helens (Voight et al. 1983), Mount Rainier (Vallance and Scott 1997) and Cotopaxi (Mothes et al. 1998). Prediction of rainfall-induced landslides has traditionally been based on the recognition of

landslide-prone terrain (Soeters and van Westen 1996) and record of rainfall duration and intensity that cause slope failures (Wieczorek 1987).

Based on the field observations, laboratory experiments have been conducted to investigate slope stability with various fluid and solid materials. Iverson et al. (2000) demonstrated that the shearing of a loose loamy sand can trigger rapid increase of pore water pressure because, as the soil begins to collapse, the weight of solid materials is shifted onto the pore fluid. As a result, positive excess pore water pressure would occur within the mixture. The pore water pressure generated in the fluid can reduce the effective normal stress of soil acting on the sliding surface to essentially zero, such that the solid materials are liquefied. At the liquefaction state, the whole weight of solid materials is supported by the fluid, and hence increasing the flow mobility (Bagnold 1954; Iverson et al. 1997). However, the transient excess pore pressure cannot be maintained during the deceleration stage, and as a consequence, the solid grains would gradually deposit along the landslide flowing path (Spence and Guymer 1997). In this process, the liquefaction of solid materials has been observed subsequent to the failure and the excess pore water pressure is mainly generated within the shearing layers (Eckersley 1990). Iverson et al. (1997) has concluded that two processes may contribute to the mobilization of landslides: (1) widespread failure within soil, rock or sediment mass, and (2) partial or complete liquefaction of solid materials with consequent generation of pore water pressures.

Poorly sorted, water-saturated debris flows can move as one or more unsteady surges along the sliding path. The relationship between the flow thickness, basal normal stress and pore fluid pressure varies remarkably as the surge passes (Iverson et al. 1997). Iverson et al. (1997) have stated that coarse gravels or sands accumulate at the front of the surge, while the fine grains suspend or deposit at the tail region. Therefore, grains locating at the front region of the flow may generate high resistant forces due to friction and collision, which would hinder the motion of grains behind. The measurement of pore water pressure at the base shows that the front surge has little or no excess pore water pressure, while regions behind has high excess pore water pressures. This high excess pore water pressure can persist due to the compressibility and low permeability of debris mass. Wang and Sassa (2001) have noticed that the initial dry density and thickness of debris materials can affect the generation of pore water pressure and debris motion after failure. Additionally, the portion of fine grains in the slope mass can affect the dissipation of pore water pressure in the shear zone and consequently influence the debris motion.

To develop robust theories for describing the mobilization and deposition of debris flows, analytical and numerical models are needed (Iverson 1997). Yano and Daido (1965) and Johnson (1965) first independently recognized that debris flows have physical properties similar to both viscous fluids and plastic solids. These properties have been the basis of the development of Bingham, or visco-plastic model (Johnson 1984) for the equivalent continuum representation of the debris flows. In the Bingham model, the mechanical behaviour of solid materials is characterized by an elastic perfectly plastic stress and strain relationship. Under small shear loading, the debris materials can flow as a rigid mass and deform

elastically until the yield strength is reached, while in the plastic deformation, the fluid–solid mixture flows like a viscous fluid. The yield strength is equivalent to the material shear strength, which also denotes the transition limit between the “solid-like” and “liquid-like” behaviour of granular materials (Doraiswamy et al. 1991). The viscosity of the flow is determined by running elementary tests for various shear strain rates (Johnson 1984; Coussot and Piau 1994).

Although the Bingham model can describe the failure and motion of debris flows, it has significant limitations (Iverson 1985; Iverson and Major 1986). In this model, it is assumed that the momentum transport and energy dissipation during debris flows are caused only by viscous shearing. However, the rate-dependent energy dissipation can also happen within debris materials, where solid grains can interact with each other through inter-particle friction, inelastic collision and basal friction (Adams and Briscoe 1994). Consequently, the Bingham model turns out to be inappropriate since it oversimplifies the behaviour of real granular materials (Gabet and Mudd 2006). To overcome the limitation of the Bingham model, an alternative method of hydraulic approximations (e.g. depth-averaged theory) is adopted to study debris flows. An analytical model describing the motion of granular materials released from rest on a rough inclined plane has been developed by Savage and Hutter (1989). In this model, the granular mass is treated as an incompressible frictional continuum with a Coulomb-like basal friction law. The evolution equations of the deposit profiles are derived from the mass and momentum conservation laws using the depth-averaged method. Based on this one-phase granular flow model, a three-dimensional solid–fluid mixture model (i.e. two phase model) has been developed by Denlinger and Iverson (2001) to study the behaviour of debris mass in the initiation, propagation and deposition processes. The average parameters (e.g. velocity, pressure) and the solid and fluid volume fractions are used in the governing equations, from which the forces acting on solid and fluid phases and the solid–fluid interactions are derived explicitly.

Although the continuous hydraulic models have provided some useful insights into the mechanical and hydraulic behaviour of debris flows, they have significant limitations on the models’ predictive capability, resulting from the assumption that the granular flows can maintain constant masses throughout the simulation (Denlinger and Iverson 2001). As a consequence, these models would predict relatively longer runout distances of debris flows than the real cases. However, field investigations reveal that the hydrology of some natural slopes is strongly influenced by discontinuities, such as fractures and joints (Pierson 1983; McDonnell 1990). In addition, the basal erosion during debris flow can change the slope mass, when the original moving debris mass interacts with the entrained basal topsoil, by shearing along their non-slip contact surface (Voight and Sousa 1994; Chen et al. 2006; Crosta et al. 2009). Thus, numerical investigations considering these features of landslides are needed, as will be discussed in Sect. 1.5.

### 1.3 Submerged Landslides

Approximately 71% of the earth's surface, or  $362 \times 10^6 \text{ km}^2$ , is covered by oceans, of which,  $28.7 \times 10^6 \text{ km}^2$  comprise the continental slope (Burk and Drake 1974). This huge area forms the geographic settings of potential submerged landslides. In general, submerged landslides differ from their terrestrial counterparts for their far greater sizes. For instance, the solid volume displaced in terrestrial landslides can range from  $10^5$  to  $10^{11} \text{ m}^3$ , while it can be up to  $10^{13} \text{ m}^3$  in the submerged topography (Legros 2002). The largest submerged landslide recorded in history is the Storegga slide which involves approximate  $3000 \text{ km}^3$  of sediments, affecting  $95,000 \text{ km}^2$  of the Norwegian basin (Haflidason et al. 2004). The submerged landslides frequently happen on very gentle slopes which are generally believed to be stable according to the conventional slope stability analyses (Andresen and Bjerrum 1967). The displaced sediments can travel very long distances, representing significant hazards to the offshore and seabed infrastructures, such as telecommunication cables, pipelines, wind and tidal turbines. Thus, it is important to understand the mechanisms of debris motion and the potential destructive power of submerged landslides.

However, our awareness of the importance and extent of submerged landslide hazards has evolved. Before the late 1970s, the major observations of submerged landslides were mainly qualitative, because a complete slope stability analysis requires knowledge of slope topographic profile, geometry of failure planes and the physical properties of sediments—information that was seldom available at that time. In recent years, the development of remote-sensing instruments, such as acoustic-reflection profilers, swath-bathymetry systems or side scanner sonar imagers (e.g. GLORIA<sup>1</sup>) (Lee et al. 1991) has increased our understanding of submarine landslides (Hampton et al. 1996). Sometimes, direct field investigations by submersibles or seabed photography can also be used as a complement of remote-sensing investigations (Greene et al. 1991). It has long been thought that the submerged landslides are rare in ocean basins, except on steep continental slopes with soft sediments, or in seismically active areas. However, recent investigations reveal that landslides are common in coastal areas, such as fjords, river deltas, continental margins, submarine canyons and oceanic volcanic islands, where weak geologic materials are subject to very strong environmental loads, such as earthquake shaking, large storm waves and high excess pore water pressures (Hampton et al. 1996). In these events, large volumes of solid materials are involved in the submarine slope failures, and they occur on slopes of various steepness (Moore et al. 1970; Carlson and Molnia 1977).

---

<sup>1</sup>GLORIA: Geologic Long-Range Inclined Asdic.

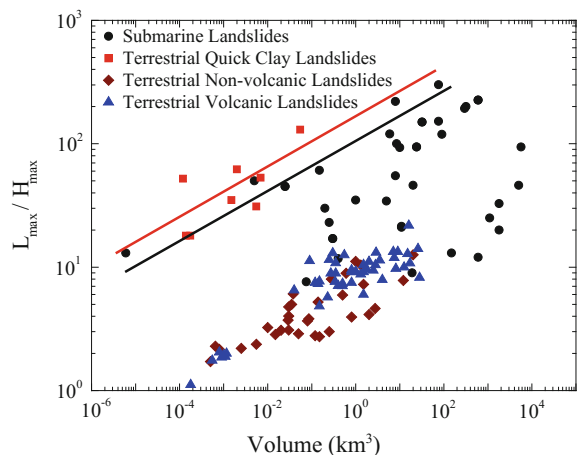
### 1.3.1 Classification and Characteristics

It has been observed from site investigations that submerged landslides have distinct mechanisms of slope failure and dynamic motion from their terrestrial counterparts, that they can be initiated from very gentle slopes and involve a huge amount of solids (Edgers and Karlsrud 1982; Hampton et al. 1996; Legros 2002). In the analyses, the evaluation of landslide sizes and depositional geometries are of the first priority, as they can be measured directly and provide unique information of a specific landslide event. In the current research, the estimation of solid volume involved in landslides has been made as the best as could be summarized from the cited reference (see Appendix A). However, the author found it is still almost impossible, for most of these recorded slides, to distinguish clearly between the slide pit (source area), path, and materials transported by the slide. A brief summary of these events, reinterpreted as the relationship between the landslide volume and mobility coefficient [i.e. the ratio of the final runout distance ( $L_{\max}$ ) to the deposit height ( $H_{\max}$ )], for the terrestrial and submarine landslides is illustrated in Fig. 1.1.

According to Fig. 1.1, several observations can be made:

- (i) In general, the coefficient of landslide mobility increases with the volume of sliding mass. The solid mass involved in the terrestrial landslides are far less than that of the majority of submarine landslides. In the submerged environment, landslides normally involve solid materials with volumes larger than  $1 \text{ km}^3$  and it can be up to  $10^4 \text{ km}^3$ , while for the terrestrial landslides, the volume of solid materials displaced can hardly exceed  $10 \text{ km}^3$ .
- (ii) The results of terrestrial and submerged landslides are very scattered due to the approximation of site investigation. The upper envelopes of these scattered data are represented by red and black lines, respectively. It is very

**Fig. 1.1** Relationship between the landslide volume and mobility coefficient (the source data is listed in Appendix A)



interesting to observe that the terrestrial quick clay landslides have relatively larger mobility coefficient than the submerged landslides.

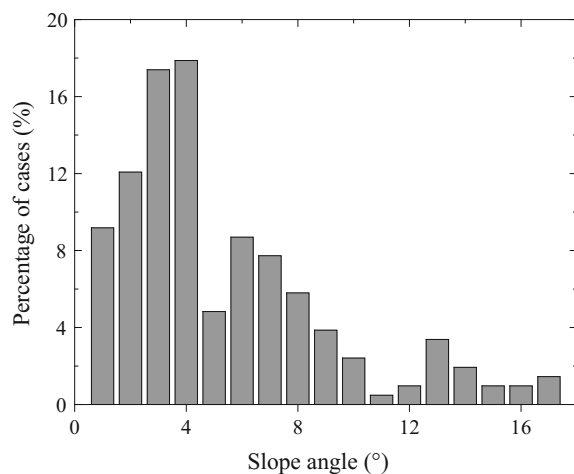
- (iii) Apart from the extreme conditions of terrestrial quick clay slides, the results of terrestrial volcanic and non-volcanic landslides are distributed in a very narrow range and can be fitted by a straight line.

According to Edgers and Karlsrud (1982), for the same solid volume, the runout distance of a terrestrial quick clay landslide can be potentially larger than that of a submarine slide. This conclusion is logical in view of the following two considerations:

- (i) The downslope gravitational force acting on solid materials of a terrestrial landslide is nearly twice as large as those in the submerged environment due to the fluid buoyancy;
- (ii) During the submerged landsliding, the velocity of solid mass is partly controlled by the fluid viscous drag force which is proportional to the square of the relative velocity between fluid and solid materials. Thus, any high kinetic energy initially acquired from the potential energy in submerged environment would be quickly dissipated, and thus shorten the runout distance.

Figure 1.2 summarizes the frequency of submarine landslides occurred on slopes of various inclination angles from 207 individually mapped cases, after the data from Booth et al. (1991) and Hampton et al. (1996). According to Fig. 1.2, it can be concluded that the majority of submarine landslides occur on slopes of 4° or less. There is a dramatic drop in landslide frequency at slope angles greater than 8°, and landslides on slope angles of 11° and 12° are rare. In addition, although the submarine landslides can occur on slopes of angles greater than 16°, it is apparent that steep angle is not a necessary condition for the initiation of numerous submarine slope failures.

**Fig. 1.2** Occurrence frequency of submerged landslide at various slope angles (from 207 cases)



A detailed study of the morphologic settings and occurrence frequency of submarine slope failures occurred on the U.S. Atlantic Continental Margins has been carried out by Booth et al. (1988). They have categorized these settings and occurrence percentage as the open slope (47%), canyons (37%), ridges (14%) and other settings (2%). This information indicates that submarine landslides have occurred with significant frequency on either very steep continental margin (canyon) or smooth, gentle slopes (open slope). Figure 1.3 shows that the average-sized open slope landslides ( $\approx 100 \text{ km}^2$ ) generally occur at very low slope angles, while the canyon landslides ( $\approx 6 \text{ km}^2$ ) tend to occur at slopes with angles range from  $3^\circ$  to  $15^\circ$ . Large-scale landslides ( $>100 \text{ km}^2$ ) tend to be associated with gentle slopes ( $\approx 3^\circ\text{--}4^\circ$ ), while small-scale landslides ( $<6 \text{ km}^2$ ) generally occur on steep slopes ( $\geq 10^\circ$ ). This feature indicates that the area of submarine landslides decreases with the slope angle, which can be explained by the fact that the sediment deposits can be easily accumulated on gentle slopes. However, no unique theory has been established to validate this explanation.

The majority of submarine slopes have been reported to be inherently stable (Masson et al. 2006), while some factors can undermine the slope stability. According to Figs. 1.2 and 1.3, large submarine landslides generally occur on very gentle slopes (e.g. less than  $10^\circ$ ) which is well below those normally required to initiate landslides (Booth et al. 1991). Legros (2002) stated that the submerged landslide must be initially saturated and there must be some mechanisms to initiate the sliding. Table 1.3 lists some significant submarine landslides and their triggering mechanisms. The major triggering mechanisms can vary from sudden impacts (e.g. earthquakes, volcanoes) operating on time scale of minutes to long geological processes lasting tens to hundreds thousands of years [(e.g. climate change (Weaver and Kuijpers 1983))]. Generally, they can be classified into two types: those related to geological characteristics of solid materials [e.g. overpressure of slope, high sediment rate (Coleman and Garrison 1977)] and those driven by transient events (e.g. hurricanes and earthquakes).

**Fig. 1.3** Relationship between the size and slope angle of open slope and canyon landslides (areas shown within  $3^\circ$  interval are average values) [data cited from Booth et al. (1991)]

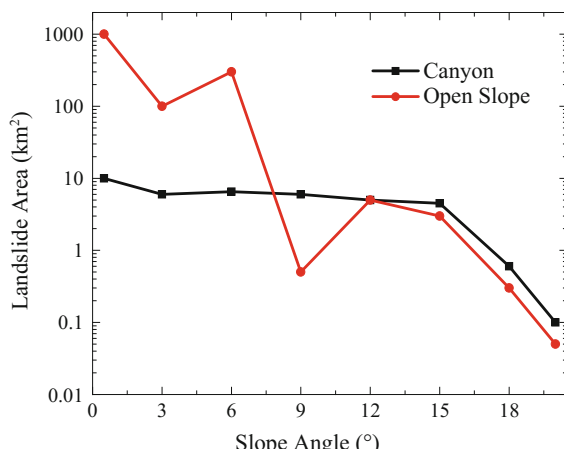


**Table 1.3** Factors contributing to the failure of submarine landslides [after Masson et al. (2006)]

Triggering mechanism	Examples	References
Earthquakes	Grand Banks	Fine et al. (2005)
Hurricanes or cyclic loading	Mississippi delta	Prior and Coleman (1982)
Loading or over-steepening of slopes	Nice, Canary islands	Assier-Rzadkiewicz et al. (2000)
Under-consolidation (overpressure)	Mississippi delta	Prior and Coleman (1982)
Rainfall (where landslides have a subaerial extension)	Norway, Hawaii	Longva et al. (2003)
Slope parallel weak layers in bedded sequences	East coast US, Storegga, west Africa	O'Leary (1991); Hafliðason et al. (2003); Bryn et al. (2005)
<i>(Suggested but less well documented)</i>		
Gas hydrate dissociation	East coast US, Storegga	Sultan et al. (2003)
Sea-level change	Madeira Abyssal Plain	Weaver and Kuijpers (1983)
Volcanic activity	Hawaii, Canaries	Masson et al. (2002)

### 1.3.2 Major Research on Submerged Landslides

Laboratory researches on submerged landslides mainly focus on small scale modelling at 1 g (Mohrig et al. 1998; Vendeville and Gaullier 2003; Ilistad et al. 2004) and centrifuge modelling (Phillips and Byrne 1994; Zhou et al. 2002). Mohrig et al. (1998) investigated the flowing patterns of debris materials composed of silt and sand at 1 g. They observed a thin layer of fluid entrapped between the moving solid mass and the underlying slope surface, which could increase the mobility of debris flows. The sudden increase of excess pore water pressure at the flow front would lead the fluid beneath the debris to penetrate into the slope mass and trigger hydroplaning. It has been recognized that fluid flow with low viscosity can be sheared easily, leading to a dramatic reduction of basal friction and thus increase the flow mobility (Mohrig et al. 1999; Ilistad et al. 2004). For a clay–sand mixture, it has been observed that the velocity of clay-rich flows decreases gradually due to the hydroplaning phenomenon, while for a sand-rich flow, a constant propagating velocity can be maintained, resulting in a turbulent flow front (Ilistad et al. 2004).

Centrifuge experiments can reproduce the correct stress and strain states of submarine landslides due to the high acceleration fields used. In a high acceleration field, the slope mass can be liquefied due to static loading (Phillips and Byrne 1994), which would trigger slope instability. The investigation of the physical properties of sliding materials using the centrifuge modelling could provide useful information related to the previous history of seabed mass motion (Boylan and Gaudin 2010). In the presence of other external transient loadings, such as earthquake shaking, the excess pore pressure and subsequent liquefaction can occur

more readily. In these events, the value of excess pore pressure increases with the magnitude of earthquake loading (Coulter 2005).

As noted by Gue (2012), the 1 g laboratory experiments of submarine landslides are generally easier and cheaper to conduct than the centrifuge modelling. However, it is still questionable to justify the mechanical and hydraulic behaviour of debris materials based on the experimental results, because the stresses in small-scale models are normally very small when compared with those of real submarine landslides. As for the centrifuge modelling, it has many limitations in terms of model configurations and proper scaling laws used for the input and output parameters. The major restriction of the centrifuge modelling is the variation of acceleration in the radial direction of the model. As the centrifugal acceleration is scaled by  $r\omega^2$ , with  $r$  being the radius of the centrifugal rig and  $\omega$  being the angular velocity, the centrifugal forces acting on individual grains would increase with the distance. In addition, the acceleration field always orients towards the rotational centroid on the centrifugal rig, such that the centrifugal acceleration field cannot match the distribution pattern of earth's gravity field. This problem becomes very much worse for centrifuge rigs with short radii. Therefore, the soil stresses reproduced by the centrifuge modelling can hardly match those of real slopes. For the time being, a precise prediction of submerged landslides is far beyond our ability. Though areas at risk are relatively easy to identify, we are still unable to forecast the occurrence and magnitude of each individual event.

To overcome these problems and get repeatable testing methods, numerical simulation seems to be the most obvious way forward, for the understanding and predicting the mechanisms of submerged landslides. The related model tests and numerical methods will be discussed in the following sections.

## 1.4 Model Testing—Granular Column Collapse

In small-scale laboratory experiments, direct investigation of water-laden debris flows remains a major challenge, because the appropriate water content and deformation of reconstructed soil samples are not well defined (Phillips and Davies 1991; Major and Pierson 1992). It has been recognized that the solid materials in debris flows and dry granular flows may behave similarly: for instance, they can sustain shear stresses in a static state with very slow deformation due to the enduring, frictional grain contacts, and they can flow rapidly as characterized by inelastic grain collisions (Iverson 1997). Thus, researchers in this field mainly focus on the mechanical behaviour of dry, granular flows under simple and well controlled model configurations. From these researches, it is hoped that the initiation and propagation mechanisms of real debris flows can be highlighted (Lajeunesse et al. 2005; Lube et al. 2005; Lacaze et al. 2008). Although these studies make significant simplifications of the problem, they are still useful in elucidating the mechanical behaviour of granular flows under simple, well controlled conditions (Crosta et al. 2009).

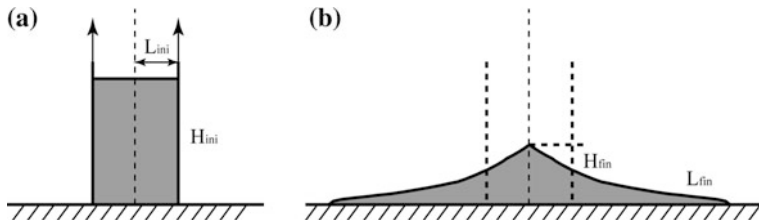


**Fig. 1.4** Setup of granular column collapse model (cited and modified from Lube et al. (2005), page 2) **a** Left initial state; **b** Right final deposit state

A simple model of granular column collapse in plane strain condition (see Fig. 1.4) has been widely used in experimental and numerical research because of its simplicity, the richness of observed dynamics and obviously geophysical applications (Lajeunesse et al. 2006; Phillips et al. 2006; Lucas and Mangeney 2007). In this model, an assembly of dense granular materials is initially generated within a rectangular prism. After quickly removing the confining wall, all the solid grains would fall downwards and spread horizontally along a channel (*N.B.* the width of the channel is the same as the granular column). Finally, a static granular deposit is formed on the horizontal floor. During this process, dense granular assemblies would dilate, while loose samples would contract to reach the mobilization state (Hung 1995; Walton et al. 2007; Mangeney et al., 2010).

This granular column collapse model is very similar to the classical dam-break problem studied in the fluid mechanics, in which the confined materials are released immediately and flow under gravity (Hogg 2007; Ancey et al. 2008). However, the current model involves various granular materials, such as grit, glass beads, salt, sand, rice and sugar. Using this model, a series of well documented experiments have been reported in the literature (Balmforth and Kerswell 2005; Lajeunesse et al. 2005; Lube et al. 2005; Siavoshi and Kudrolli 2005; Lacaze et al. 2008; Crosta et al. 2009). According to Fig. 1.4, a two-dimensional model with an initial height of  $H_{\text{ini}}$  and half-length of  $L_{\text{ini}}$ , is used to simulate the symmetric and unidirectional spreading of solid grains. The final deposit height and length are  $H_{\text{fin}}$  and  $L_{\text{fin}}$ , respectively.

Staron and Hinch (2007) indicated that this model is useful to obtain insights into the complicated landslide phenomena, with special emphasis on the influence of slope topography, geometric and physical properties of granular materials. Lube et al. (2004) and Lajeunesse et al. (2004) concurrently observed that the duration time and velocity, the final deposit morphology and the cumulative energy dissipation of granular flows can be scaled quantitatively and with no dependence on particle properties (e.g. size, shape and roundness), substrate properties and released solid mass. The scaling laws are formulated to quantify the relationship between the initial model geometry [i.e. initial column aspect ratio,  $\alpha$ , defined as the ratio of the initial height ( $H_{\text{ini}}$ ) to the initial length ( $L_{\text{ini}}$ )] and final debris runout distance and deposit height (Lube et al. 2005; Mangeney et al. 2005; Staron and Hinch 2007;

Lacaze et al. 2008). Empirical equations have been proposed by Lube et al. (2005) as:

$$\frac{L_{\text{fin}} - L_{\text{ini}}}{L_{\text{ini}}} \cong \begin{cases} 1.2a & a \leq 1.8 \\ 1.9a^{2/3} & a > 2.8 \end{cases} \quad (1.1)$$

$$\frac{H_{\text{fin}}}{L_{\text{ini}}} \cong \begin{cases} a & a \leq 1.15 \\ a^{2/5} & a > 1.15 \end{cases} \quad (1.2)$$

and by Lajeunesse et al. (2005) as:

$$\frac{L_{\text{fin}} - L_{\text{ini}}}{L_{\text{ini}}} \cong \begin{cases} a & a \leq 3 \\ a^{2/3} & a > 3 \end{cases} \quad (1.3)$$

$$\frac{H_{\text{fin}}}{L_{\text{ini}}} \cong \begin{cases} a & a \leq 0.7 \\ a^{1/3} & a > 0.7 \end{cases} \quad (1.4)$$

Balmforth and Kerswell (2005) proposed the scaling laws for plane strain channelled tests with different size of gaps (i.e. narrow: 1 cm, and large: 20 cm) between lateral confining walls, as:

$$\frac{L_{\text{fin}} - L_{\text{ini}}}{L_{\text{ini}}} \cong \begin{cases} \lambda a^{0.65 \pm 0.05} & \text{narrow gap} \\ \lambda a^{0.9 \pm 0.1} & \text{large gap} \end{cases} \quad (1.5)$$

$$\frac{H_{\text{fin}}}{L_{\text{ini}}} \cong \begin{cases} a^{0.4} & \text{narrow gap} \\ a^{0.5} & \text{large gap} \end{cases} \quad (1.6)$$

where the coefficient  $\lambda$  is a function of material properties (e.g. basal and internal friction).

These empirical relationships suggest that the depositional morphology of granular materials depends only on the column aspect ratio. Nevertheless, as stated by Staron and Hinch (2005), the physics of the exponent of these equations is still under discussion and no model offers a comprehensive explanation of the debris collapse dynamics.

## 1.5 Numerical Investigations

As discussed before, numerical investigation is a promising way to study the mechanical and hydraulic behaviour of landslides (Hung 1995; Denlinger and Iverson 2001; Crosta et al. 2005; Mangeney et al. 2005; Chen et al. 2006; Ancey 2007; Bui et al. 2008). The most commonly adopted numerical methods include the Finite Element Method (FEM) (Chen et al. 2006), Smoothed Particle Hydrodynamics (SPH) (Bui et al. 2008; Vacondio et al. 2013) and the Discrete

Element Method (DEM) (Cundall and Strack 1979). This study uses the DEM and its coupling with the Computational Fluid Dynamics (CFD) to investigate the initiation, propagation and deposition of landslides in the terrestrial and submerged environments. A brief introduction of the DEM and DEM-CFD coupling methods is given in this section, while more detailed theoretical background will be provided in Chap. 2.

### 1.5.1 *The Finite Element Method*

The Finite Element Method (FEM) has long been employed to investigate the slope stability (Rahman 1997; Potts and Zdravkovic 2001; Chen et al. 2007; Xu et al. 2011). However, the traditional Lagrangian-based FEM is not appropriate for studying landslides with large displacements, because the finite element mesh would rapidly become highly distorted, leading to inaccurate results (Crosta et al. 2009). To overcome this problem, a combined Eulerian–Lagrangian (CEL) method has been developed (Crosta et al. 2003; Crosta et al. 2004; Chen et al. 2006), which does not distort the FE mesh and guarantees accurate calculation results.

The CEL has been employed by Crosta et al. (2009) in investigating the collapse of a granular column on erodible and non-erodible ground surface, in which the slope failure is triggered by instantaneously deleting a retaining wall. The numerical results can match the well-documented experimental data, in terms of flow development, duration, slope profile, velocity distribution, erosion and deposition. They stated that the numerical results fit the experimental observations better than those obtained by the Discrete Element Method and depth averaged model, because the latter two methods always predict a much longer runout distance. The mechanism of solid mass changes due to basal erosion or surficial material entrainment during debris transportation is also elucidated by numerical simulations using the CEL (Chen et al. 2006).

The advantage of the CEL is that only the well-known material parameters from laboratory tests, such as the modulus of elasticity, material internal friction angle and cohesion, are used in the numerical simulations. In addition, it has shown the capability of investigating slope failure with large displacement (Chen et al. 2006; Crosta et al. 2009). However, the CEL cannot fully simulate the extreme tapering of the flow front during the propagation of granular flows, as observed in experimental tests with cohesionless materials. This can be explained by the fact that the continuum model is unable to reproduce the same discontinuous properties as the real granular materials (Crosta et al. 2009). Furthermore, as the FEM is a grid-based technique, it suffers from grid distortion at large deformation, which could lead to inaccurate solutions or even computation failure (Bui et al. 2008). This problem becomes more evident in studying the complex free-surface behaviour of geo-physical flows, such as wave motion, fragmentation and splashing (Cleary and Prakash 2004). Though the CEL can handle the moving boundary problems, it comes with very high computational costs (Crosta et al. 2009).

### 1.5.2 *The Smoothed Particle Hydrodynamics*

Smoothed Particle Hydrodynamics (SPH) is one type of Lagrangian meshless methods, commonly used to simulate the large deformation of continuum or dispersed materials (Bui et al. 2008). In the SPH, the fluid (or solid) domain is discretized as a series of elements and the material properties are attributed to the element centres, which are then interpreted as material particles. These material particles carry field variables such as mass, density and stress tensor, and move with the material velocity. The governing differential equations for the continuum are converted into equations of motion of these particles and then solved by a Lagrangian numerical scheme.

SPH can be used in studying geophysical flows (Gutfraind and Savage 1998; Cleary and Prakash 2004). When compared with other grid-based numerical methods, SPH has several advantages, as:

- (i) As SPH is a fully transient method, it is suitable for simulating environmental flows that are not in steady state, in which the large deformation and post-failure response of granular flows are handled very well, due to its Lagrangian and adaptive nature. The free surfaces of flow are modelled easily and naturally. As the SPH particles move to new locations, the shape of the free surface is simply the boundary particles wherever they happen to be.
- (ii) SPH can easily include complex geometries and complicated physics (e.g. solidification and freezing). This ability arises partially from the flexibility of the continuum modelling; partially from the fact that the SPH material particles can evolve over space and time; and also from the ability to impose specific rule bases on the particles, such that the governing equations can be adapted easily.

As the SPH particles are used to mimic the behaviour of granular solids, they would repel each other when the soil mass is compressed, while they can attract each other if the soil mass expands. However, when the solid material is stretched, the attraction would result in the formation of SPH particle clumps (Swegle et al. 1995). This is commonly called the “tensile instability” problem for SPH in modelling the mechanical behaviour of solids. This problem is negligible for non-cohesive soil with small friction angle, but become troublesome for high friction angles. For cohesive soil, the tensile instability is very serious, so that special treatments are needed during the simulations (Dyka and Ingel 1995; Johnson and Beissel 1996). Bui et al. (2008) pointed out that this problem would result in unrealistic fracture at the soil surface at large deformation. To resolve this problem, different approaches have been proposed (Dyka and Ingel 1995; Johnson and Beissel 1996). Monaghan (2000) and Gray et al. (2001) have proposed an effective method by introducing a small repulsive force between neighbouring particles, which prevents SPH particles from getting closer at tensile state in the original SPH formulation.

Furthermore, the SPH simulations may encounter the problem of “particle deficiency” near or on the boundary (Bui et al. 2008). For particles near or on the boundary, only the neighbouring particles inside the boundary contribute to the calculation of gradients, and no contribution comes from the outside since there are no particles beyond the boundary. This one-sided contribution leads to inaccurate solutions. To overcome this problem, the virtual particle method can be employed in SPH (Takeda et al. 1994; Morris et al. 1997).

### **1.5.3 *The Discrete Element Method***

The application of DEM in the simulation of granular flows, as firstly proposed by Cleary and Campbell (1993), appears to be useful for understanding the behaviour of dry granular flows and is likely to yield many insights into this problem, if it can closely mimic the experimental setup (Lacaze et al. 2008). Within the last two decades, it has become a complementary research method to the laboratory experiments, revealing the fundamental mechanical characteristics of landslides (Staron and Hinch 2007; Tang et al. 2009). As Zenit (2005) pointed out, the use of DEM in landslide simulations is very powerful, because all the numerical data are accessible at any stage of the test, including quantities which are very difficult, or even impossible, to be obtained directly from laboratory experiments, such as the individual particle trajectories and transient interaction forces. This information is essential for understanding the underlying physics of dry granular flows. The flexibility of the DEM can also be extended to the loading configurations, particle size distribution and physical properties of solid particles.

Recent numerical research has revealed that the initial model dimension, especially the model aspect ratio, controls the mechanisms of granular flows and determines the geometry of final deposits (Staron and Hinch 2005; Zenit 2005). This conclusion is validated by experimental observations in the model tests in Sect. 1.4. Zenit (2005) used a two dimensional (2D) discrete element code to simulate the mechanical behaviour of granular column collapse with different initial aspect ratios. The numerical model has the same configuration as that shown in Fig. 1.4. In this 2D model, the debris mass is simulated as a collection of circular disks which interact with each other at discrete contact points. Based on this simplified model, qualitatively good results were obtained when compared to the experimental observations in axisymmetric conditions. A critical granular column aspect ratio, that determines whether or not the final granular deposit has a flat top profile, has been systematically discussed.

Although Zenit (2005) has observed different depositional morphology of granular materials in numerical simulations, he did not analyse this phenomenon further to explore the mechanisms governing the long runout distance of debris materials. It seems that a positive correlation between the column height and the maximum deposit runout distance exists, which indicates that landslide deposits can have a common shape, such that the maximum debris runout distance can be

determined solely by the initial model geometry. Based on this idea, Staron and Hinch (2005) used a 2D discrete element model to study the collapse of a granular assembly onto a horizontal floor. They found that the collapse is mainly driven by the free fall of granular materials at large aspect ratios, while there is no free fall process when the aspect ratio is small. This result suggests that the initial column aspect ratio determines the final depositional morphology of granular materials.

While the 2D DEM simulations have revealed the fundamental influence of initial model geometry on the mechanisms of granular flow, the numerical results obtained cannot quantitatively match the experimental ones very well, because the 2D model cannot take the particle shape effect into consideration. Cleary and Frank (2006) used 3D DEM analyses to investigate the axisymmetric collapse of an assembly of spherical particles. In their work, a set of governing parameters of granular column collapse model were identified, based on which, a series of numerical simulations were performed in order to analyse the influence of grain properties on the depositional morphology of granular materials. They pointed out that the particle shape has a significant influence on the dynamic motion and deposition of granular flows. To analyse the particle shape effect, they have employed the microscopic particle rolling resistant moment in the DEM model. The results obtained can qualitatively match those observed in the laboratory model tests.

In general, the motions of granular materials are resisted by the sliding friction and geometrical interference (Rowe 1962; Terzaghi et al. 1996), when grains slide along the adjacent particle surfaces. This frictional effect is characterized by the internal friction angle of granular materials which depends mainly on the particle surface roughness and interlocking, while it is independent of the confining stress and density (Barrett 1980). From a microscopic point of view, both the particle rotation and grain length scale structure can influence the mechanical behaviour of soil (Muhlhaus and Vardoulakis 1987; Jiang et al. 2005), which can be investigated numerically by the Discrete Element Method (DEM) (Cundall and Strack 1979). In the standard DEM, the particle rotation is assumed to be either free or strictly prevented (Bardet and Proubet 1991). The simulations using free particle rotations may lead to a reduced granular internal friction and develop a soil structure different from that of natural soils (Ting et al. 1989; Rothenburg and Bathurst 1992; Thornton 2000). As the inter-particle rotation can be an important mechanism governing the peak shear strength and dilatancy of granular materials (Oda et al. 1982; Oda and Kazama 1998), many researchers have devoted to implementing particle rolling resistance (Jiang et al. 2005; Belheine et al. 2009) and angular shaped particles models (Houlsby 2009; Boon et al. 2013; Williams et al. 2014) in the DEM to increase the soil strength and thus to reproduce realistic soil behaviour.

Although Cleary and Frank (2006) have discussed the influence of several factors on granular flows, relatively little knowledge has been provided to explain the mechanisms governing the long runout distances of debris materials. Staron and Lajeunesse (2009) used a 3D DEM model to study the intertwined role of volume and topography in landslides. The runout distance of granular materials under gravity can be decomposed into two contributions: sliding along the topography

and spreading of the unconsolidated materials. The sliding property is independent of the granular volume and closely related to the mobility of landslide avalanche (i.e. the ratio of the deposit runout distance to the height). On the other hand, the spreading of solid mass is strongly dependent on the granular volume. Based on these relationships, a clear understanding of the mechanical behaviour of dry granular flows can be obtained via 3D DEM simulations.

The modelling of granular column collapse using the classical DEM is a possible way to study the complicated behaviour of landslides. However, the model discussed above is not satisfactory, since it fails to consider the presence of water in granular flows. As a consequence, the spreading of a fluid-absent, dry granular flow is not able to explain the high mobility of natural landslides (Legros 2002). To analyse the influence of fluid on the motion of granular flows, the DEM-CFD coupling method needs to be employed, as discussed below.

#### 1.5.4 The DEM-CFD Coupling Method

Researches on the rapid failures of large scale landslides using the DEM is challenging because a huge number of particles need to be employed to model the realistic mechanical behaviour of granular flows, which would lead to unrealistically long computational time (Siavoshi and Kudrolli 2005). In addition, a typical landslide involves the motion of solid particles and fluid, which presents complicated interactions in a solid–fluid mixture. Figure 1.5 illustrates the constituents of real soil and its numerical representations. The soil mass in nature is a three-phase mixture consisting of solid particles, water and air. The solid particles of various sizes interconnect with each other and have void space among them, which in turn, serve as the flow passage for both water and air (N.B. the influence of air on landslide is negligible, and will not be discussed in this book.). The void space within the soil mass is generally continuous, which allows water to flow from one point to another under hydraulic gradients (Craig 1997).

According to Fig. 1.5, it can be observed that a rational numerical model of a fluid–solid mixture need to describe a discrete skeleton structure of solid particles, continuous pore fluid flow and coupled discrete–continuum interactions between the two phases (Tsuji et al. 1993; Zeghal and El Shamy 2004; Shafipour and

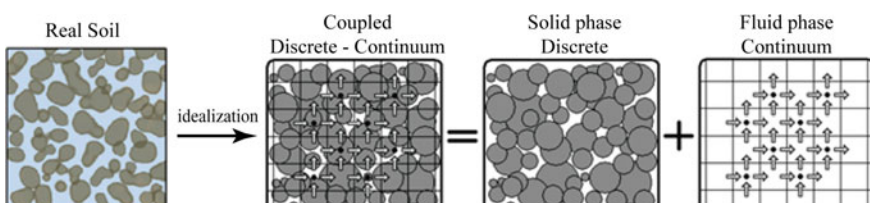


**Fig. 1.5** Numerical representation of soil (cited from Shafipour and Soroush (2008), page 675)

**Table 1.4** Flow regimes of fluid flow through porous media

	$Re_p \approx 1$	$Re_p \approx 100$	$Re_p \approx 800$	Turbulent regime
Darcy regime	Forchheimer regime	Transition regime		
Creeping flow (no inertial influence)	Laminar flow (increasing inertial influence)	Inertial flow with increasing random, irregular flow	Flow entirely random and irregular	
$\Delta h/\Delta L = \frac{1}{k} V$	$\Delta h/\Delta L = \gamma_f V + \beta_f V^2$		$\Delta h/\Delta L = \gamma_f V + \beta_f V^2$	

Note  $Re_p$  is the Reynolds number defined at the particle size scale;  $\Delta h$  is the pressure head loss;  $\Delta L$  is length of the flow passage;  $V$  is the superficial fluid velocity

Soroush 2008; Chen 2009; Shimizu 2011). The mechanical behaviour of the solid and fluid phases can be studied by the DEM and CFD, respectively, while their interactions are analysed using the well-developed discrete–continuum theories (Anderson and Jackson 1967; Ding and Gidaspow 1990; Brennen 2005). Based on the flow properties, the fluid motion can be categorized into four distinct regimes, as shown in Table 1.4 (Trussell and Chang 1999).

According to Table 1.4, it can be observed that the Darcy Regime is limited to a fluid condition that the Reynolds number is smaller than 1.0. Fluid flow in this regime is not only laminar but also “creeping”, which means that there is no significant inertial contribution to the fluid motion. The second regime is named the Forchheimer Regime. Fluid flow in this regime is also steady laminar flow, but as the Reynolds number increases, inertial effect becomes increasingly important. At the lower end of this regime, the fluid head loss is proportional to  $V$  with a small  $V^2$  dependence, while at the upper end, the head loss is  $V^2$  related, with a small dependence on  $V$ . Furthermore, stationary vortices are formed in fluid cells between solid grains at the upper end of this flow regime. The transition regime represents the transition of fluid motion from more or less full inertial to fully developed turbulence. The equation used to describe the relationship between fluid pressure head loss and flow velocity in this regime makes a transition from the Forchheimer form with one set of constants,  $\alpha_F$  and  $\beta_F$ , to the turbulent regime with another set of constants,  $\alpha_T$  and  $\beta_T$ . At the lower end of this regime, turbulence just begins to appear in some part of fluid domain, while at the upper end, turbulence appears in the whole fluid domain. When the Reynolds number is larger than 800, the turbulent regime occurs, in which, all parts of the flow are turbulent and the fluid velocity is randomly fluctuating about the mean value.

Based on the category of fluid regimes, extensive research using the fluid–solid coupling methods have been carried out to investigate the intricate behaviour of a fluid–solid mixture system. Tsuji et al. (1993) firstly proposed a DEM-CFD coupling approach to study the mechanical behaviour of a fluidized bed, and thereafter, this method has been widely applied to study multiphase flows (e.g. fluidized bed (Duursma et al. 2009), material transport). In these numerical studies, the behaviour of individual solid particles is modelled by the DEM, while the fluid motion is simulated by solving equations of the fluid mass and momentum conservations using the locally averaged quantities, such as fluid velocity and pressure, in a standard CFD solver (Anderson and Jackson 1967). In addition, the space and time variation of porosity is identified as a major factor affecting the coupling response of fluid-solid mixture (Di Felice 1994; Zeghal and El Shamy 2004).

Whilst the existing coupling work has shown its potential to simulate the liquefaction and transportation of saturated granular materials, a detailed study of the mechanical and hydraulic behaviour of large scale landslides is still rare in the literature. The fact that a multiphase landslide always starts from a very small Reynolds number and develops into a very large Reynolds number, corresponding to the transition from the Darcy to Turbulent flow regimes, is still a problem that remains to be addressed. The current research will contribute to knowledge in this field using the DEM-CFD coupling method.

# **Chapter 2**

## **Introduction to Discrete Element Method**

This chapter provides a review of the theories and methodologies of the Discrete Element Method (DEM), and its validation via numerical triaxial tests on sands. Based on the triaxial tests and granular column collapse model, the fundamental strength properties of material internal friction angle and stress–strain behaviour have been studied. The goal of this study is to calibrate these parameters, so that they can be used in the investigation of the mechanical behaviour of granular flows will be presented in the following chapters.

### **2.1 The Discrete Element Method**

The Discrete Element Method (DEM) is a numerical method for modelling the dynamics of solid particles which interact with each other at discrete contact points. Since it was firstly proposed by Cundall and Strack (1979) to study the mechanical behaviour of rock at the microscopic level, the DEM has been developed rapidly, with applications in rock/soil mechanics, chemical engineering and pharmacy (Thornton 2000; Cleary and Sawley 2002; Cui and O’Sullivan 2006; Wu and Cocks 2006; Jing and Stephansson 2007; Lu and McDowell 2007; Ng 2009; Plassiard et al. 2009; Yu et al. 2013).

In DEM simulations, the properties of a stressed assembly of rigid spherical particles (e.g. position, velocity and contact forces) are updated at every numerical iteration time step. The translational and rotational displacements of each particle are obtained by explicitly integrating the governing differential equations based on the Newton’s second law of motion, while the contact forces between particles are calculated using well-defined force–displacement contact models (Hertz 1882; Mindlin and Deresiewicz 1953; Cundall and Strack 1979; Itasca 2003). In this process, the interactions between particles are monitored at all contacts and the movement of each individual particle is traced. It is assumed that the velocity of

each particle is constant within each iteration step. Since the explicit integration technique is used in the DEM calculation, the time step is required to be very small so that stable numerical solutions can be achieved.

Figure 2.1 illustrates the mechanical loop of the DEM calculations. The simulation starts by detecting the contact points between particles. The contact point and the particle overlapping distance are then used to calculate the interaction forces via the force-displacement relationships. The resulting contact forces are applied at the centre of each particle, causing particles to move. According to the Newton's second law of motion, the particle acceleration, velocity and displacement are updated at the end of each numerical iteration step. This mechanical loop continues until the prescribed total iteration steps are reached.

### 2.1.1 Particle Motion

According to the Newton's second law of motion, the equation governing the translational motion of a single particle is expressed as

$$m_i \frac{d^2}{dt^2} \vec{x}_i = m_i \vec{g} + \sum_{N_c} (\vec{f}_{nc} + \vec{f}_{tc}) + \vec{f}_{fluid} \quad (2.1)$$

where  $m_i$  is the mass of a particle  $i$ ;  $\vec{x}_i$  is the position of its centroid;  $\vec{g}$  is the gravitational acceleration;  $\vec{f}_{nc}$  and  $\vec{f}_{tc}$  are the normal and tangential inter-particle contact forces exerted by the neighbouring particles; the summation of the contact forces are over all the contacts ( $N_c$ );  $\vec{f}_{fluid}$  is the interaction forces between fluid and particles, as will be discussed in Sect. 4.1.

The rotational motion of a single particle is given as below

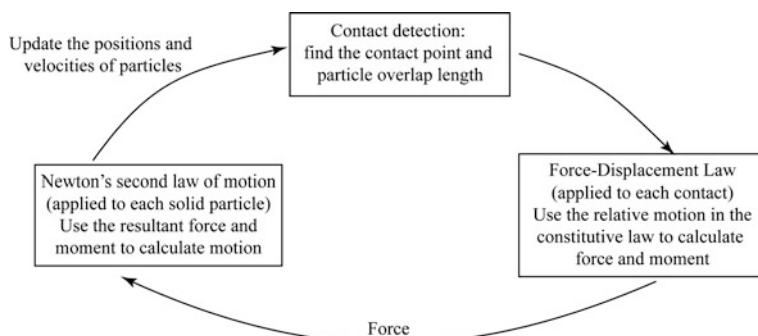


**Fig. 2.1** Calculation cycle in the DEM

$$I_i \frac{d}{dt} \vec{\omega}_i = \sum_{Nc} \vec{r}_c \times \vec{f}_{tc} + \vec{M}_r, \quad (2.2)$$

where  $I_i$  is the moment of inertia about the grain centroid;  $\vec{\omega}_i$  is the angular velocity;  $\vec{r}_c$  is the vector from the particle mass centre to the contact point;  $\vec{M}_r$  is the rolling resistant moment, which inhibits particle rotation over other particles.

### 2.1.2 The Particle—Particle Contact Model

The accuracy of DEM modelling depends highly on the contact models used to calculate the particle–particle interactions. This topic has long been discussed by geotechnical researchers, such as Iwashita (1998), Jiang et al. (2005) and Belheine et al. (2009). The fundamental problem is how to reproduce the correct interactions between two solid grains in the DEM. The classical DEM model treats all solid grains as either disks (i.e. two-dimensional (2D) model) or spheres (i.e. three-dimensional (3D) model), as this would greatly simplify the calculation of the overlap distance between particles. Though this model has shed some lights on the mechanical behaviour of granular materials, it is inaccurate due to the oversimplified assumptions that all solid particles are spherical and free to rotate. However, real particles and their contacts are much more complicated, for example, the particle is normally not spherical and have a rough surface texture, possibly can be covered by a thin film of weathered materials. For non-spherical particles, the line of action of the normal contact force no longer passes through the centre of mass of the particles and hence generating rotational moments (Belheine et al. 2009).

To account for the particle shape effects, three ways of DEM modelling can be used. The first of the three is to use a clump of spherical particles based on the bonded-particle method (Potyondy and Cundall 2004). In this method, the real shape of soil/rock mass is approximated by a clump of bonded spherical grains, which behaves as a rigid body. The second approach is to model the soil/rock blocks as polygons (Cundall 1988; Boon et al. 2012). The third method is to include the rolling resistant moment at the particle contacts (Jiang et al. 2005). This research uses the last method in simulating the mechanical behaviour of granular materials due to its simplicity.

As shown in Fig. 2.2, the real solid grains have irregular shapes, while the DEM model approximates the irregular shape with circles (or spheres). Because of this simplification, the contact point detected in the numerical model can be dramatically different from the real one. The distance between the real and numerical contact points is defined as  $\eta r$ , with  $r$  being the average radius between the two particles in contact;  $\eta$  being a coefficient quantifying the offset of the contact point. In addition, the position of the contact point might change during the simulation as individual grains can rotate due to the unbalanced moment acting on the geometrical centre. Assuming particle B rotates in the anticlockwise direction, the resultant

rolling resistant moment from the normal contact force would act in the clockwise direction, resisting the particle rotation. For simplicity, the rolling resistant moment is defined to act in a direction opposite to the relative rotation.

The open source DEM code ESyS-Particle (Weatherley et al. 2011) was employed to run simulations presented herein. Using this code, a series of preliminary runs of granular column collapse tests (see Chap. 3) employing the non-linear, elastic Hertz–Mindlin contact model (Hertz 1882; Mindlin and Deresiewicz 1953) and linear elastic contact model (Zhang and Whiten 1996) have been conducted. No significant difference was found. Hence, since the linear elastic contact requires less computational time, it is used in the current research. The detailed description of the model can be found in Jiang et al. (2005) and Belheine et al. (2009). As shown in Fig. 2.3, the classical DEM model may be modified by introducing an additional rolling moment component at each contact point whereby rolling resistance can be accounted for. Thus, three distinct particle contact models can be identified, namely, (a) the normal contact model; (b) the tangential contact model; and (c) the rolling contact model. The mechanical responses of these three different contact models are closely related to the relative displacement between the two particles, as shown in Fig. 2.4. The interaction forces between two spheres include the normal ( $F_n$ ) and tangential ( $F_t$ ) forces, and rolling moment ( $M_r$ ), respectively.

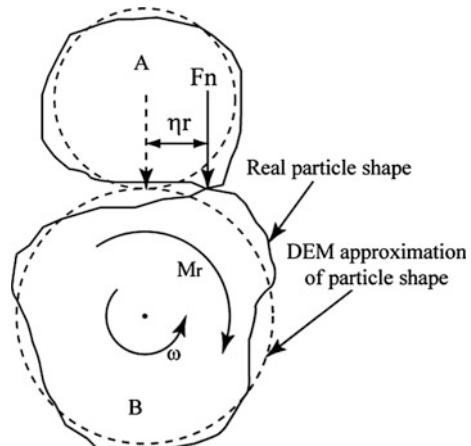
In Fig. 2.4a, the normal contact force ( $F_n$ ) acting on a single particle is linearly proportional to the overlap distance between two particles, which is expressed as

$$F_n = K_n \cdot U_n \quad (2.3)$$

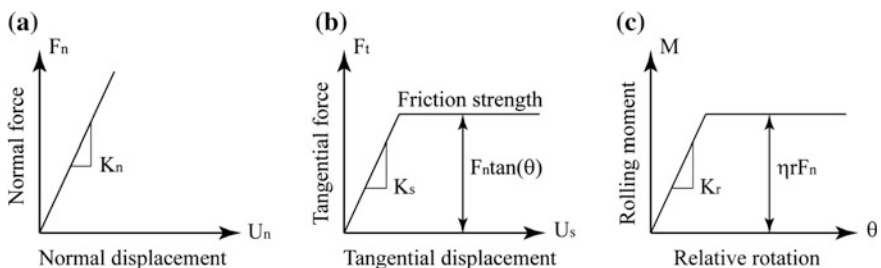
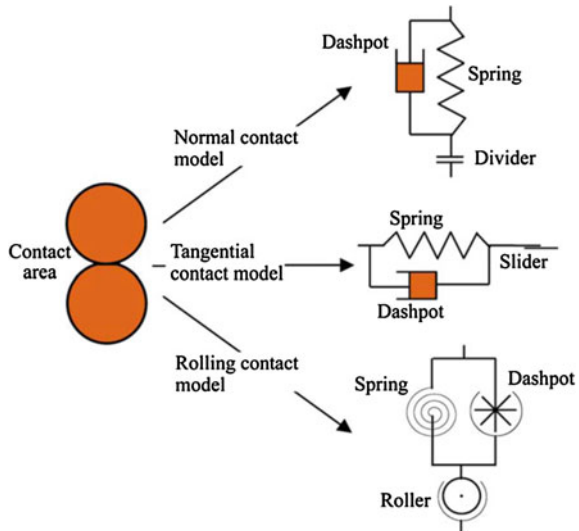
in which  $K_n$  is the normal contact stiffness,  $U_n$  is the normal overlap distance.

Figure 2.4b shows that a maximum tangential force ( $F_n \tan(\theta)$ ) exists, before which, the tangential force ( $F_t$ ) can be calculated incrementally, as

**Fig. 2.2** The approximation of real grain contact using the DEM model



**Fig. 2.3** The contact model between two spheres (cited from Jiang et al. (2005), p. 348)



**Fig. 2.4** Particle contact model (cited from Belheine et al. (2009), p. 324)

$$F_t^n = F_t^{n-1} + K_s \cdot dU_s, \quad (2.4)$$

where  $F_t^n$  and  $F_t^{n-1}$  are tangential forces calculated at current and previous iteration steps.  $K_s$  is the shear stiffness, and  $dU_s$  is the incremental tangential sliding displacement.

Figure 2.4c shows that the rolling resistant moment increases gradually from zero to the maximum value when two particles come into contact and rotate over each other. The magnitude of elastic rolling moment ( $M_r$ ) is proportional to the relative rotational angle, as calculated incrementally by Eq. (2.5).

$$M_r^n = M_r^{n-1} + K_r \cdot \Delta\theta_r, \quad (2.5)$$

where  $M_r^n$  and  $M_r^{n-1}$  are the rolling moment calculated at the current and previous iteration steps;  $K_r = \beta K_s r^2$  is the rolling stiffness, with  $\beta$  being the coefficient of

rolling stiffness,  $r$  being the average particle radius at contact (i.e.  $r = (R_1 + R_2)/2$ );  $\Delta\theta_r$  is the relative rotational angle between the two particles within one iteration time step. The magnitude of the maximum rolling moment is defined as

$$M_p = \eta \cdot r \cdot |F_n| \quad (2.6)$$

in which,  $\eta$  is the coefficient of plastic moment.

### 2.1.3 The Calculation of Stress in the DEM

As the DEM is applicable only for modelling the mechanical behaviour of discrete materials (e.g. sand and rock), it is not straightforward to obtain the stress distribution within the granular assembly based on the definition of stress in continuum mechanics. Instead, in the DEM, the homogenization or micro–macro averaging technique is used to calculate the stress tensor (Thornton and Antony 2000). For an assembly of granular materials within a measurement volume ( $V$ ), the stress tensor ( $\bar{\sigma}_{ij}$ ) is defined as

$$\bar{\sigma}_{ij} = - \left( \frac{1-n}{\sum_{N_p} V^{(p)}} \right) \sum_{N_p} \sum_{N_c} \left| x_i^{(c)} - x_i^{(p)} \right| n_i^{(c,p)} F_j^{(c)} \quad (2.7)$$

where the summation is taken over  $N_p$  particles with their centroids locating within the measurement volume;  $n$  is the porosity of the measurement volume;  $V^{(p)}$  is the volume of a single particle;  $N_c$  is the number of contacts around a single particle;  $x_i^{(p)}$  is the location of the particle centroid, and  $n_i^{(c,p)}$  is the unit normal directed from the particle centre to the contact location ( $x_i^{(c)}$ );  $F_j^{(c)}$  is the force acting at the contact.

### 2.1.4 Coordination Number

The concept of coordination number comes from chemistry and crystallography, where it is defined as the number of atoms around a central atom in a molecule or crystal (De 2007; Hermann et al. 2007). In the DEM, this variable is used to quantify the packing state of granular materials. The coordination number of a particle is the number of neighbouring particles it contacts with. As studied in the numerical biaxial tests (Thornton 2000; Jiang et al. 2010), the coordination number has been identified as an important variable to study soil failure. According to Jiang et al. (2010), the coordination number is small in the shear band of soil sample. By tracking the distribution of coordination number, it is possible to identify the

potential weak zone of soil sample. During the simulation, the bulk coordination number of a granular assembly in a volume ( $V$ ) is calculated via the coordination number of individual particles ( $C_i$ ), as

$$\bar{C} = \frac{1}{N_p} \sum_{i=1}^{N_p} C_i, \quad (2.8)$$

where  $N_p$  is the total number of particles within the volume.

## 2.2 Model Validation

The previously discussed DEM model was validated by performing numerical triaxial tests on sands. The properties of the sand sample are selected by trial and error, close to those reported in the literature, and will be used in the analyses of the next chapters.

### 2.2.1 *Input Parameters of the DEM Model*

The particle-size distribution (PSD) is one of the most important material properties controlling soil strength, deformation and permeability. The PSD of debris flows vary hugely at different locations (see for instance Casagli et al. 2003). In addition, the grain-size distribution may vary significantly within the same landslide mass at different depths (Crosta et al. 2007). Figure 2.5 shows examples of particle-size distributions from seven landslide sites in the Northern Apennines (Casagli et al. 2003) and six cases of rock avalanches in Val Pola in the Alps (Crosta et al. 2007). It can be observed that the grain size ranges from 0.001 to 1000 mm, with a large percentage of fine- and medium-sized grains and a small amount of coarse grains. Large discrepancies can be observed between the various site investigations.

According to Fig. 2.5, the solid grains with diameters ranging from 0.1 to 10 mm were widely observed in different locations. However, in DEM simulations, due to computational limitations, a much narrower particle-size distribution with the ratio of maximum to minimum particle sizes of 2 is used, as shown by the red curve in Fig. 2.5. The input parameters are listed in Table 2.1.

### 2.2.2 *Determination of Numerical Time Step*

The choice of the numerical time step used in the DEM simulation is very important because if it is too large, inaccurate results and violation of thermodynamic laws

**Fig. 2.5** Particle size distribution of landslides in the Northern Apennines (Italy) (after Casagli et al. 2003) and rock avalanches in the Alps (Italy) (after Crosta et al. 2007). The particle size distribution adopted in the numerical simulations is plotted as the dashed red curve

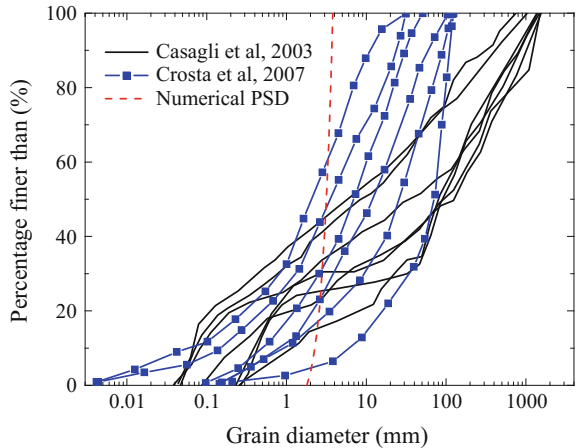


**Table 2.1** Input parameters of DEM simulations

DEM parameters	Value	DEM parameters	Value
Particle diameter, $D$ (mm)	See Fig. 2.5	Damping coefficient	0.0
Sample packing porosity, $n$	(Loose) 0.45 (Dense) 0.37	Coefficient of rolling stiffness, $\beta$	1.0
Particle density, $\rho_s$ (kg/m <sup>3</sup> )	2650	Coefficient of plastic moment, $\eta$	0.1
Normal stiffness, $K_n$ (N/m)	$3 \times 10^7$	<i>Simulation parameters</i>	<i>Value</i>
Shear stiffness, $K_s$ (N/m)	$2.7 \times 10^7$	Gravity, $g$ (m/s <sup>2</sup> )	-9.81
Particle friction angle, $\theta$ (°)	30	DEM Time step, $\Delta t$ (s)	$10^{-7}$

(i.e. violation of conservation of energy) may result (Tsuji et al. 1993). Since the linear elasticity contact model is adopted in the current simulations, the time step is assumed to have a simple expression (Bathe and Wilson 1976; Tsuji et al. 1992) of

$$\Delta t = \lambda \sqrt{m/K_n}, \quad (2.9)$$

where  $\lambda$  is a reduction factor;  $m$  is the particle mass;  $K_n$  is the normal contact stiffness.

Theoretically, a system consisting of a large number of particles should conserve energy if no energy dissipation mechanism is active. However, the explicit numerical integration techniques (e.g. forward, backward or central difference) used in the DEM, would inevitably lead to slight numerical errors in the calculations of grain velocity and position during each iteration step. These numerical errors result from the assumption adopted in the DEM that the velocities of solid grains can keep constant within one iteration time step. However, it is not true for the real granular system, because the forces acting on solid grains might vary over time. In general, the larger the numerical time step employed in the simulations, the larger the resulting errors introduced in the analyses. Thus, to conserve energy in numerical

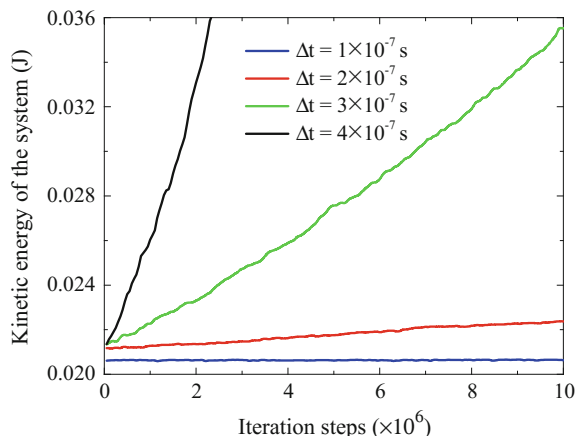
simulations, a proper reduction factor ( $\lambda$ ), should be used in Eq. (2.9) to obtain a smaller numerical time step, such that the integration errors can be neglected.

Hence, in this work, to determine the time step, simulations of elastic particle collision using various values of time step have been performed, in which 1250 particles were randomly generated within a prismatic box. The initial velocities of these particles were randomly set with each component in a range of  $[-1.0, 1.0]$  m/s employing the Mersenne Twister algorithm (Matsumoto and Nishimura 1998). All particle collisions, either particle–particle or particle–wall collision, are purely elastic (i.e. the coefficient of restitution is equal to 1.0). In addition, the gravity, friction coefficient, rolling and damping parameters were all set to zero, so that no mechanism of energy dissipation exists. Other DEM parameters have the same values as those listed in Table 2.1.

In Fig. 2.6, the results are plotted in terms of kinetic energy of the granular system against time. It emerges that for time step larger than  $1.0 \times 10^{-7}$  s, the total kinetic energy of the granular system is not conserved even though no mechanism of energy dissipation is introduced in the tests. The lack of energy conservation can be entirely ascribed to the numerical algorithm of the DEM code. Further decrease of time step would significantly increase the computational cost. Thus, the value  $1.0 \times 10^{-7}$  s is chosen as the proper time step used in this research. This issue with DEM simulations has been discussed by Tsuji et al. (1992). Unfortunately there are several publications where no parametric analysis on the choice of the time step is carried out, so that the simulations may be affected by errors due to the unphysical artificial energy introduced by the numerical algorithms employed.

According to the discussion above, the elastic grain collision model has effectively determined the time step of an un-damped granular system. As the un-damped particles can move faster than grains in a damped condition (e.g. models with granular friction, fluid viscous drag forces and plastic contacts) under the same initial and boundary conditions, the time step determined by the current model would be smaller than the theoretical time step used in the granular flow model.

**Fig. 2.6** The kinetic energy of the granular system



Thus, the time step determined in this section can be used in the subsequent simulations of granular flows and submerged debris flows.

In the DEM–CFD model, the DEM time step is determined by the elastic grain collision model, while the maximum time step used in the CFD is determined by the Courant–Friedrichs–Lowy condition (CFL condition) (Courant 1928; Guo 2010) that the Courant number of the system should be smaller than 1.0.

$$C = \frac{nU_r \cdot \Delta t}{\Delta x} \leq 1.0, \quad (2.10)$$

where  $C$  is the Courant number;  $U_r$  is the relative velocity between fluid and solid particle;  $\Delta x$  is the minimum size of a CFD mesh cell;  $\Delta t$  is the time step used in the CFD.

According to Eq. (2.10), the time step used in the CFD should satisfy the condition as

$$\Delta t \leq \frac{\Delta x}{nU_r} \quad (2.11)$$

According to Eqs. (2.9) and (2.11), the critical time step used in the CFD model is generally larger than that used in the DEM simulation (Kafui et al. 2002). Therefore, in numerical simulations using the DEM–CFD coupling method, the total numerical simulation time is mainly determined by the critical time step of the DEM model.

In this research, no numerical damping was employed. There are two reasons to be considered. First, although several damping models exist in the literature, few of them have physical bases. The use of damping can dissipate kinetic energy in a granular system and bring the whole system to the steady state very quickly. As a result, it is often used in quasi-static simulations as only the static state is of interest (Jiang et al. 2005; Modenese et al. 2012). However, in the simulations of landslides, the granular materials would go through dynamic motion, such that any damping would alter the mechanical behaviour of the system significantly. Even though the viscous damping forces have been used to model energy dissipation due to plastic particle contacts (Brilliantov et al. 2007), the magnitude of energy dissipation is very difficult to be evaluated correctly. Thus, this research assumes that the energy dissipation in landslides only comes from frictions between particles.

### 2.2.3 Numerical Simulation of Triaxial Tests

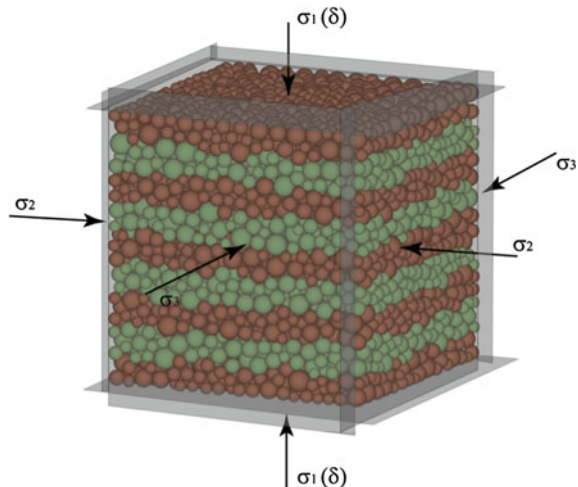
Both the strength and stiffness of soil can influence the mechanical behaviour of landslides at different stages of granular motion. For instance, the elastic deformation under loading is mainly determined by the stiffness properties (e.g. Young's Modulus), while for slope failure with large deformations, the strength parameters,

such as the peak and residual soil strengths, are dominant (Fang 1991). In this study, the primary purpose is to investigate the large deformation of soil. Thus, the strength parameters are calibrated in this section, so that they can be used to simulate soil behaviour during granular flows. In general, the motion of granular materials is resisted by the sliding friction and geometrical interference (Rowe 1962; Terzaghi et al. 1996), when grains slide along the adjacent particle surfaces. This frictional effect is characterized by the internal friction angle of granular materials ( $\varphi$ ) which depends mainly on the particle surface roughness and interlocking, while it is independent of the confining stress and density (Barrett 1980). As the drained strength of sand is widely used in experimental and numerical studies, the current research will mainly focus on the calibration of soil strength properties using the numerical drained triaxial tests. Particular emphasis is given to the soil behaviour at the critical state, i.e. the state that soil mass can be sheared continuously without further changes in stresses and volume (Schofield and Wroth 1968; Wood 1990).

### 2.2.3.1 Model Configuration

The DEM triaxial testing model for drained condition of sands is shown in Fig. 2.7. An assembly of polydispersed solid grains is packed within a parallelepiped prism bounded by six smooth and rigid walls. These walls can move freely so that the prescribed confining stress and strain can be achieved. The particle properties, such as particle-size distribution, contact stiffness are listed in Table 2.1. Since the quasi-static (QS) conditions are desired during the triaxial tests, the particle density is scaled up to be  $2.65 \times 10^{12} \text{ kg/m}^3$ . In such a case, the inertial forces of grains are

**Fig. 2.7** The DEM model configuration of the triaxial test



negligible when compared with the inter-particle contact forces (Thornton and Antony 1998; Modenese 2013).

The triaxial test consists of two stages: isotropic compression and deviatoric shear. In the isotropic compression stage, the same confining pressures are applied on the boundary walls in the  $x$ -,  $y$ - and  $z$ -directions. The magnitude of the confining pressure increases gradually from zero to the projected confining pressure ( $p_0$ ). After reaching  $p_0$ , the confining pressures will remain constant until the deviatoric shear stage starts. In the deviatoric shear stage, the confining pressures in the lateral directions are maintained constant (i.e.  $\sigma_2 = \sigma_3 = p_0$ ), while the sample is compressed in the vertical direction at a constant strain rate (e.g.  $10^{-4} \text{ s}^{-1}$ ). The deviatoric shear of the soil sample continues until the prescribed axial strain is reached (e.g. 30%).

Loose and dense granular samples are obtained using different inter-particle friction and rolling parameters. For loose samples, the friction and rolling coefficients are set as the same values as those listed in Table 2.1, and the isotropic compression can produce a relatively loose granular sample. Dense samples are prepared as the following steps:

- (i) Isotropic compression of the sample with zero friction and rolling coefficients until the aimed confining pressure and QS conditions are reached;
- (ii) Set the inter-particle friction and rolling coefficients to those listed in Table 2.1 and a sufficient number of iteration steps are used to stabilize the sample;
- (iii) Isotropic compression of the sample until the desired confining pressure and QS conditions are reached.

The total number of particles in the model is 10,000, which can satisfy the definition of Representative Elementary Volume (REV) of triaxial tests (Modenese 2013). By using the REV, the number of particles in the model is believed to be large enough, such that the size of the DEM sample has no impact on the numerical results. After sample generation, the dense and loose samples have porosities of 0.37 and 0.45, respectively.

### 2.2.3.2 Results

In the analyses, the compressive components of stress are defined as positive. The mean and deviatoric stresses are defined as

$$p = (\sigma_1 + \sigma_2 + \sigma_3)/3 \quad (2.12)$$

$$q = (\sigma_1 - \sigma_3) \quad (2.13)$$

These two stress invariants are defined such that, for isotropic, homogeneous materials,  $p$  corresponds to the hydrostatic stress, responsible for the isotropic volumetric changes, and  $q$  incorporates all the shear stresses which cause the

material distortion. The strain is defined as  $\varepsilon_i = -(l_i - L_i)/L_i$ , where  $l_i$  is the current length of the sample in the  $i$ -th direction (e.g.  $i = 1$  is for the vertical direction; 2 and 3 are for lateral directions.).  $L_i$  is the length of sample prior to deformation. In this definition, the compressive strains are positive, as in classical soil mechanics. The volumetric strain is defined as  $\varepsilon_v = -\Delta V/V_0$  with  $V_0$  being the volume prior to the deformation and  $\Delta V$  being the change of volume.

Figure 2.8 compares the stress–strain and porosity–strain behaviour of the dense and loose sand samples under confining pressures of 50 and 100 kPa, respectively. For the dense sand sample, there is a considerable degree of particle interlocking which, together with the material friction and rolling resistance at contacts, leads to very high shear strength. Thus, the shear stress increases to its peak value at a relatively low strain, and then decreases with the increasing strain as the particle interlocking is progressively overcome. Eventually, the shear stress reaches an ultimate value (i.e. the critical state shear strength at failure). For the loose sand sample, the shear stress increases gradually with the axial strain, until the final peak strength is reached. With the same initial model configurations (e.g. confining pressure, microscopic particle friction and rolling properties), the dense and loose samples will arrive at the same value of critical shear strength.

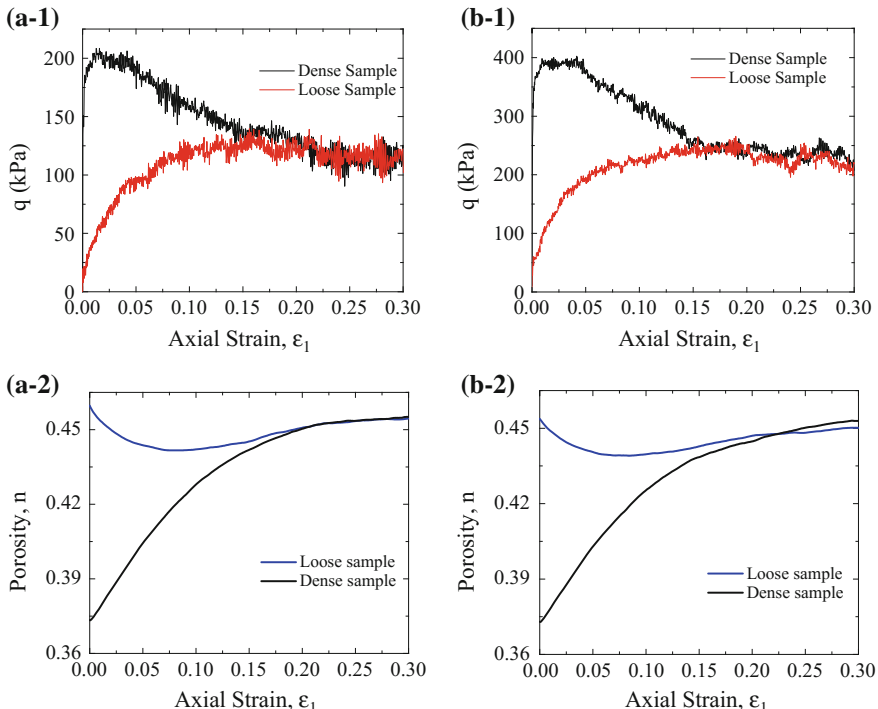
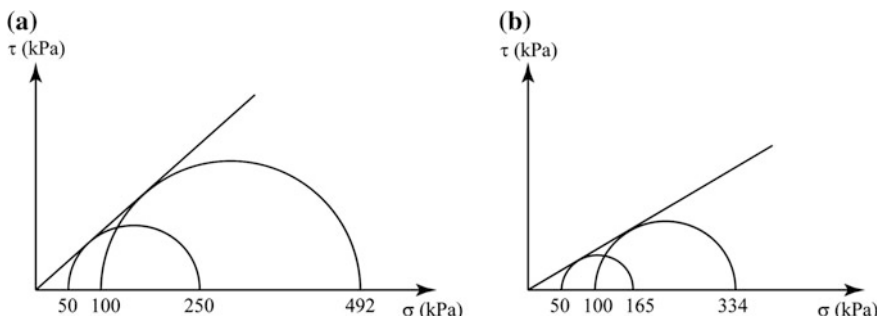


**Fig. 2.8** Stress–strain and porosity–strain behaviour: **a** left the lateral confining pressure is 50 kPa and **b** right the lateral confining pressure is 100 kPa

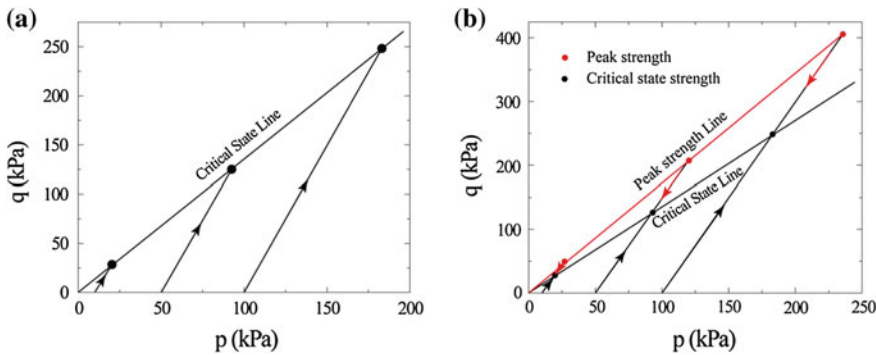
During the deviatoric shear stage, it can be observed that the evolution of porosity of the granular samples at different confining pressures behaves similarly. The loose samples contract, while the dense samples dilate to reach a constant porosity (i.e. 0.454). The axial strain at constant porosity is around 0.20, which corresponds to the axial strain at the critical state. Therefore, the critical state is also called the constant volume state. For simulations at a confining pressure of 100 kPa, the porosity of dense sample is slightly larger than that of loose sample at the critical state. The reason for the observed deviation is due to the large constraints on the rearrangement of solid grains at relatively high confining stresses. The Mohr circles representing stress states at failure are shown in Fig. 2.9a, b, from which the peak and critical (constant volume) material internal friction angle is measured as  $41.8^\circ$  and  $32.6^\circ$ , respectively.

Figure 2.10 illustrates the stress path of loose and dense sand samples during the deviatoric shear stage. In this analysis, triaxial tests using confining pressures of 10, 50 and 100 kPa have been investigated. According to Fig. 2.10a, the deviatoric stress of loose sample increases gradually from zero to the critical shear stress at the failure state. The envelope or the critical state line of the shear strength of sand at failure is a straight line. For the dense sand sample (Fig. 2.10b), the shear stress initially increases to the peak strength in a short period of time. Then, it decreases gradually to reach the critical shear strength at failure.

Based on the discussion above, it can be concluded that the microscopic inter-particle friction angle and rolling parameters can influence the mechanical and deformational behaviour of granular assembly significantly. In order to obtain a comprehensive understanding of how the material internal friction angle is determined by the combination of  $\theta$  and  $\eta$ , a series of triaxial tests have been conducted. The numerical results obtained are plotted as contour curves in Fig. 2.11. According to Fig. 2.11a, b, it can be observed that the peak material internal friction angle ( $\varphi_{\text{peak}}$ ) is within a range of  $[32^\circ, 51^\circ]$ , while the constant volume material internal friction angle ( $\varphi_{\text{cv}}$ ) is within a range of  $[26^\circ, 40^\circ]$ . The typical value of  $\varphi_{\text{cv}}$  for real quartz sand is found to range from  $32^\circ$  to  $34^\circ$ . For the combination of large values of  $\eta$  and  $\theta$ , the gradient of internal friction angle contour curves is relatively



**Fig. 2.9** Mohr–Coulomb representation of stress conditions at failure using the maximum and minimum principal stresses: **a** left the peak strength and **b** right the critical strength



**Fig. 2.10** Stress paths for **a** loose sand sample, and **b** dense sand sample

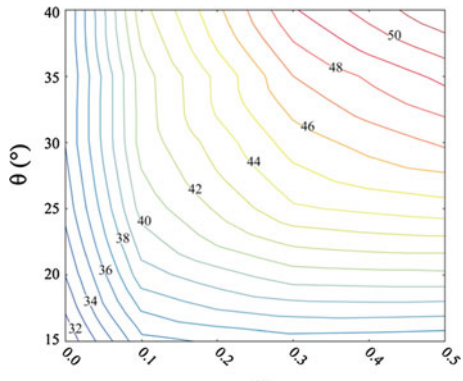
small, indicating that the material internal friction angle is not very sensitive to the change of microscopic particle friction and rolling parameters. From Fig. 2.11c, it can be observed that the higher the inter-particle friction is, the larger the difference between the peak and constant volume material internal friction angles ( $\varphi_{\text{peak}} - \varphi_{\text{cv}}$ ) will be. For typical dense sand materials, the value of ( $\varphi_{\text{peak}} - \varphi_{\text{cv}}$ ) is between  $9^\circ$  and  $10^\circ$ , while for typical loose sand materials, this value is less than  $5^\circ$ .

Based on these graphs, the selection of microscopic particle friction and rolling parameters in the DEM model can be made rationally, so that the projected values of peak and constant volume material internal friction angles can be reproduced. To highlight the influence of  $\theta$  and  $\eta$ , two series of numerical results of stress-strain and volumetric strain behaviour of the dense DEM samples are illustrated in Fig. 2.12a, b. According to Fig. 2.12a, it can be concluded that on average the inter-particle friction angle can influence the peak strength of soil sample significantly, while little impact is found on the critical state strength. As the inter-particle friction angle ranges from  $15^\circ$  to  $40^\circ$ , the peak shear strength of granular sample increases progressively. However, the critical state strength of soil remains almost unchanged, except for the simulation using an inter-particle friction angle of  $15^\circ$ . High fluctuations of the stress-strain curves is found in simulations using large inter-particle friction angles (i.e.  $\theta = 40^\circ$ ), particularly towards the critical state where particle rearrangement becomes dominant.

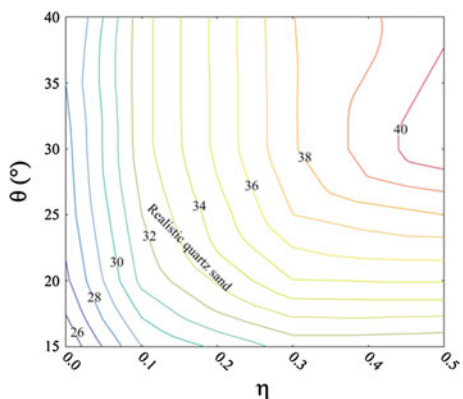
Figure 2.12b shows that on average the volumetric strain of the granular sample increases with the axial strain, which suggests that the dense granular sample would dilate during the triaxial tests. The volumetric strain tends to remain constant at the critical state. At any specific value of axial strain, the magnitude of volumetric strain increases with the inter-particle friction angle. For samples with different  $\theta$ , the peak and constant volume material internal friction angles are given in Table 2.2.

To investigate the influence of grain rolling resistance on the soil strength properties, a series of triaxial tests using different values of rolling plastic moment have been conducted in this research. As shown in Fig. 2.13a, the rolling plastic

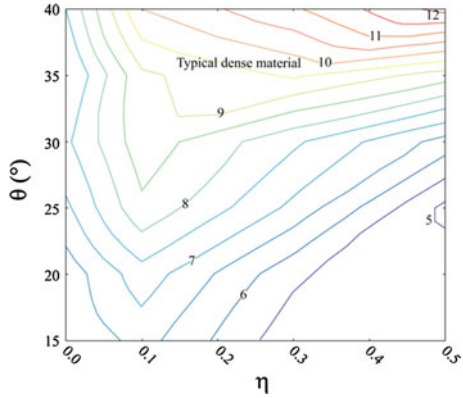
**Fig. 2.11** Contours of material internal friction angles for different combinations of  $\theta$  and  $\eta$



(a) peak material internal friction angle ( $\phi_{peak}$  (°))



(b) constant volume material internal friction angle ( $\phi_{cv}$  (°))



(c)  $\phi_{peak} - \phi_{cv}$

**Fig. 2.12** Results of triaxial test using different friction angles ( $\beta = 1.0, \eta = 0.1$ )

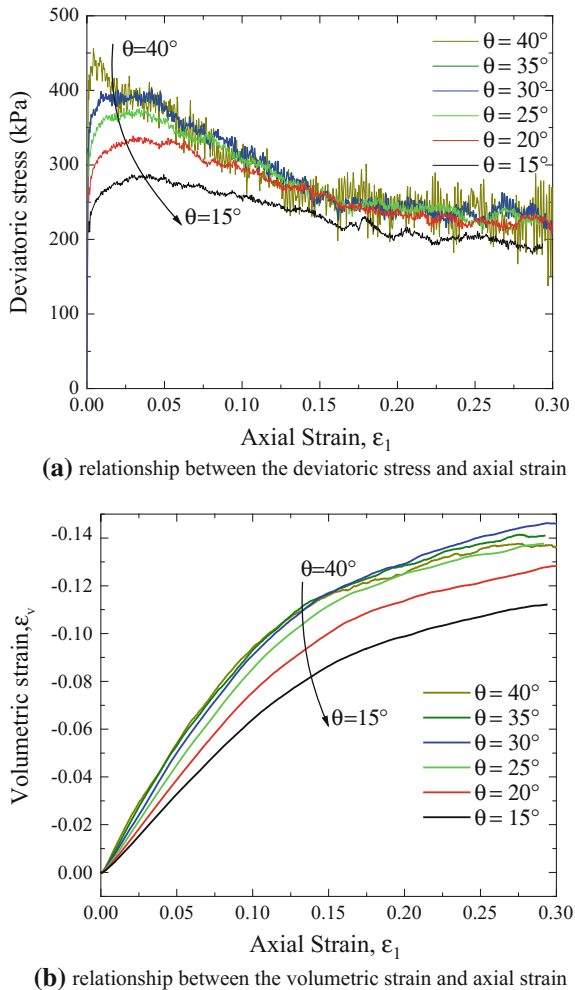


**Table 2.2** The peak and constant volume material internal friction angles ( $\beta = 1.0, \eta = 0.1$ )

$\theta$ (°)	15	20	25	30	35	40
$\varphi_{\text{peak}}$ (°)	35.7	38.6	40.4	41.4	41.5	42.6
$\varphi_{\text{cv}}$ (°)	29	31.3	32	32.6	32.6	32.6

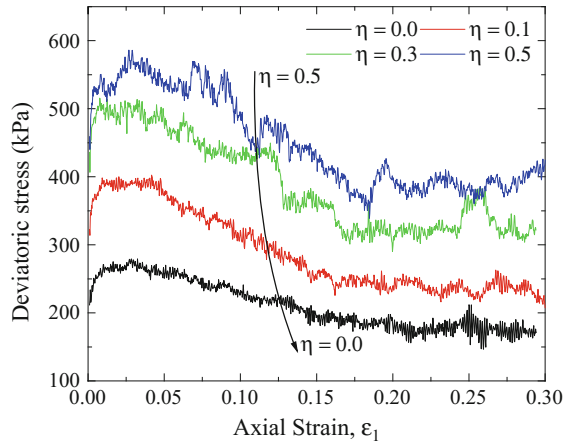
moment can influence both the peak and critical state strengths of soil significantly. On average, the magnitudes of peak and critical state strengths increase with  $\eta$ . Figure 2.13b shows that the volumetric strain of sand sample varies little as  $\eta$  increases from 0.1 to 0.5. However, for the simulation with  $\eta$  of 0.0 (i.e. free rolling particles), the volumetric strain is smaller than those of other simulations, indicating that the dilation of granular sample during shearing is not significant for free rolling

particles. This phenomenon is similar to the results obtained by Modenese (2013). For samples using different coefficients of rolling plastic moment, the peak and constant volume material internal friction angles are summarized in Table 2.3.

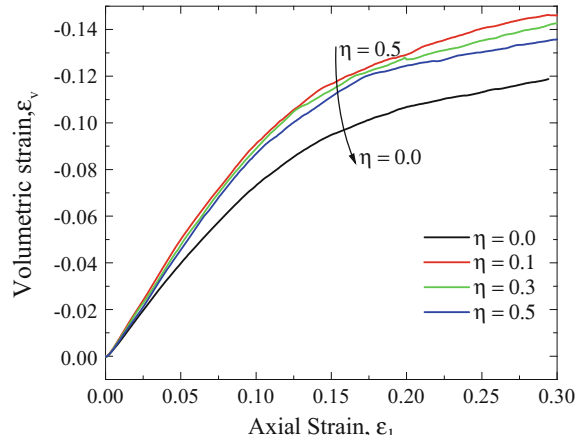
### 2.2.4 Material Angle of Repose

To study the depositional behaviour non-cohesive granular materials, it is useful to measure the angle of repose. This variable is defined as the steepest angle of the descent of slope relative to the horizontal plane, when grains on the slope surface are on the verge of sliding (Lowe 1976). The granular materials start to move if the

**Fig. 2.13** Results of triaxial tests using different coefficients of plastic moment ( $\theta = 30^\circ$ ,  $\beta = 1.0$ )



(a) relationship between the deviatoric stress and axial strain



(b) relationship between the volumetric strain and axial strain

**Table 2.3** The peak and residual friction angles ( $\theta = 30$ ,  $\beta = 1.0$ )

$\eta$	0	0.1	0.3	0.5
$\varphi_{\text{peak}}$ (°)	35.0	41.4	45.5	47.2
$\varphi_{\text{cv}}$ (°)	27.6	32.6	37.9	40.9

slope inclination angle is above the angle of repose, while it is stable if the slope angle is below the angle of repose. The typical values of angle of repose can range from  $25^\circ$  (for smooth spherical particles) to  $40^\circ$  (for rough angular particles) (Carrigy 1970; Pohlman et al. 2006). Once in motion, the grains would flow below the angle of repose, while at the end of the flow, the granular materials would deposit at the angle of repose (Hungr 1995; Walton et al. 2007; Mangeney et al. 2010). Theoretically, the angle of repose is approximately close to the macroscopic material internal friction angle ( $\varphi$ ). This section will calibrate the angle of repose, as a verification of the material internal friction angle discussion in Sect. 2.2.3.

A simple granular column collapse model is used to study the angle of repose. As shown in Fig. 2.14a, the solid grains (i.e. dry sand used in this research) are poured into a vertically placed container to form a static sand pile. The width and height of the pile are 0.05 m and 0.05 m, respectively. After consolidation, the frontal boundary (B) is removed quickly, so that the granular materials can fall downwards under gravity and spread horizontal along the ground floor. The horizontal ground floor is covered with solid grains of the same properties as grains in the pile, so that the roughness of the ground floor can be modelled. When all the grains stop moving, the angle of repose is measured as the steepest angle of the deposit profile (Fig. 2.14b). In addition, it is also possible to observe a failure plane of the slope, which is defined as the sliding surface of the granular flow.

In order to simulate the mechanical behaviour of debris materials, the numerical model should produce the same angle of repose as that observed in laboratory experiments. As suggested by Lube et al. (2005), the angle of repose for different granular materials used in small-scale laboratory experiments ranges from  $29^\circ$  to  $35^\circ$ , as listed in Table 2.4. The grain properties of the DEM sample used in this research can approximately match that of coarse quartz sands, in which the angle of repose is close to  $31^\circ$ . Thus, in the numerical model, the microscopic friction angle

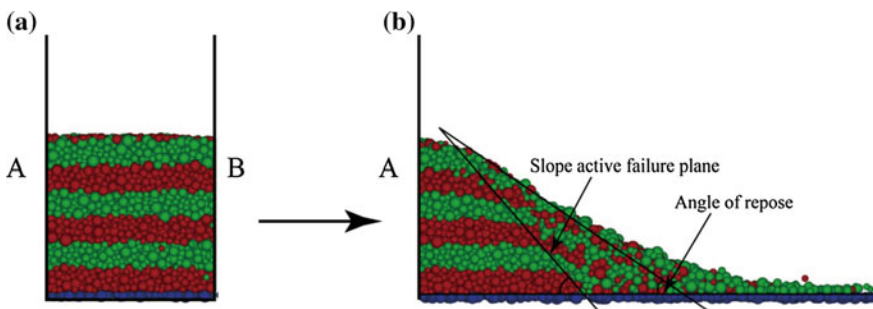


**Fig. 2.14** Model configuration for testing the granular angle of repose

**Table 2.4** Grain properties used in experiments (data cited from Lube et al. 2005)

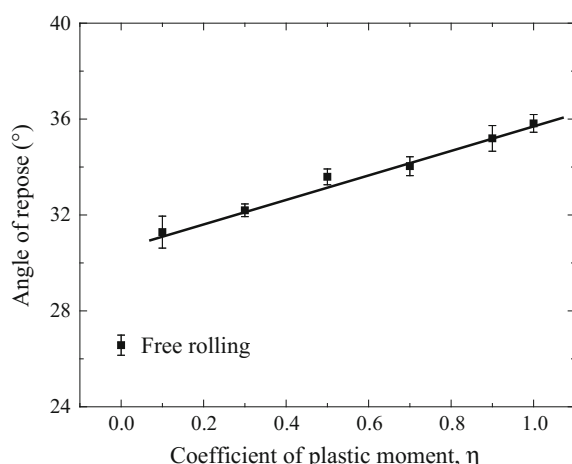
Particle	Mean density ( $\text{g}/\text{cm}^3$ )	Mean grain size (mm)	Angle of repose ( $^\circ$ )
Fine quartz sand	2.6	0.15	29.5
Coarse quartz sand	2.6	1.5	31
Sugar	1.58	1	35
Rice	1.46	4.5	32

between grains has initially been set as  $30^\circ$ , while the rolling resistance parameters (of particular importance is the coefficient of plastic moment (Modenese et al. 2012)) increase gradually from the minimum value of 0.0 to the maximum value of 1.0. During this process, the rolling stiffness is assumed to change very little, as is expected not to influence the debris motion significantly.

#### 2.2.4.1 Results

In a normal gravity field (1 g), the relationship between the macroscopic angle of repose and the coefficient of plastic moment in the microscopic rolling resistance model is shown in Fig. 2.15. It can be observed that the simulation with  $\eta$  being 0.0 can lead to a relatively small angle of repose, while simulations with  $\eta > 0.0$  can reproduce realistic angles of repose, when compared to that of materials used in laboratory experiments. When the rolling resistance model is active, there is a sudden increase of the angle of repose. This result is in accordance with the conclusions made by Rothenburg and Bathurst (1992); Pöschel and Buchholtz (1993) and Modenese (2013) that the free rolling spherical particles have a smaller angle of repose than the spherical particles with rolling resistance.

**Fig. 2.15** Angle of repose for granular materials with different rolling resistance (for each point, the error bar is achieved for two measurements at different locations on the slope surface)



According to Fig. 2.15, the numerical results obtained from the simulations using a combination of inter-particle friction angle of  $30^\circ$  and the coefficient of rolling plastic moment of 0.1 can lead to an angle of repose being equal to  $31.3^\circ$ , which is close to the value of coarse quartz grains given by Lube et al. (2005) and the constant volume material internal friction angle calibrated in Sect. 4.3.1.

## 2.3 Conclusions

This chapter has outlined the DEM model and the configurations of numerical model used in this research, based on which, a series of calibration tests were carried out with three main objectives: (i) to determine the time step for simulations of granular flows; (ii) to calibrate the angle of repose and material internal friction angle for the DEM model; and (iii) to give insights into the mechanical and deformational behaviour of sand under shearing. The main findings and remarks can be concluded as

- (i) A combination of microscopic friction angle of  $30^\circ$  and rolling plastic moment coefficient of 0.1 can produce an angle of repose of  $31.3^\circ$  and a material internal friction angle of  $32.6^\circ$ , respectively. These two parameters can qualitatively match the property of coarse quartz sands and will be used in the simulations in the following chapters.
- (ii) In the triaxial tests, different combinations of  $\theta$  and  $\eta$  can lead to distinct values of material internal friction angle, as represented by the contour curves in this chapter. These graphs can be used as guidelines for selecting appropriate microscopic particle friction and rolling resistance parameters in the DEM model.
- (iii) The un-damped particle collision model is used in this research to determine the numerical time step used in the DEM simulations. Based on the input parameters, a DEM time step of  $10^{-7}$  s is chosen for simulations of granular flows.

# **Chapter 3**

## **Investigation of Dry Granular Flows**

This chapter presents numerical investigations of dry granular flows generated by the collapse of prismatic columns via 3D discrete element method (DEM) simulations in plane strain conditions. First, by means of dimensional analysis, the governing parameters of the problem are identified, and variables are clustered into independent and dependent dimensionless groups. Through parametric studies, the influence of these dimensionless groups on the run-out distance and deposit height of the granular materials are analyzed. Detailed analyses of the mechanical behaviour of the granular assembly throughout the simulation are performed for a granular column with aspect ratio of 3.3. Qualitatively good results, in terms of the granular flowing velocity, energy evolution, stress variation, bulk coordination number, force chain and the mobility of solid grains, are presented.

### **3.1 The Granular Column Collapse Model**

The study of flowing dense granular material is very important for understanding the propagation of geophysical mass flows (e.g. landslides, pyroclastic flows, rock and debris avalanches). For instance, long run-out granular flows can travel distances several times larger than the size of the source topography along flat or almost flat surfaces, sweeping away populated areas located considerably far away from the mountainside (Crosta et al. 2005; Carrara et al. 2008). Research in this field mainly focus on small-scale laboratory experiments and numerical simulations of dry granular materials, aiming to study the mechanical behaviour of granular flows (Kerswell 2005; Lajeunesse et al. 2005; Lube et al. 2005; Saucedo et al. 2005; Staron and Hinch 2007; Mangeney et al. 2010; Roche et al. 2011). Among various issues raised, the prediction of their run-out distance is of the primary importance, mainly due to their high destructive power. The main objective is to establish scaling functions to relate the initial slope geometry and the final granular

depositional morphology, so that possible predictions of the landslide hazards can be made.

The current research employs a three-dimensional (3D) DEM model to investigate the initiation and propagation of granular flows, based on which, the general features of granular flows, such as slope deformation, grain propagation and deposition, and energy evolution will be analysed. The numerical model configuration used in this research is based on a simple granular column collapse model proposed by Lube et al. (2005). As shown in Fig. 3.1a, the back wall (*A*) is rigid and frictionless, while a removable gate (*B*) is placed in the front of the model to control the granular collapse. The horizontal floor (*D*) is made of particles of the same PSD as the granular column that were kept fixed at all times to simulate a non-erodible base of the same roughness as the flowing material.

In this DEM model, if a rigid wall boundary condition is used, a low sphere packing fraction would occur near the boundary wall due to wall friction and confinement. As a consequence, the numerical conditions of homogeneity cannot be satisfied (Radjaï and Dubois 2011). In addition, the rigid wall boundary cannot reproduce realistic grain friction and interlocking effects near the boundary. To eliminate the wall effects, the periodic boundary (Parrinello and Rahman 1980; Cundall 1987) is implemented in the lateral direction of the DEM model. In this framework, all the granular materials are packed within a unit periodic cell in the form of a parallelepiped, from which the plane strain condition is achieved. Any particle with its centroid moving out of the cell through one particular face is mapped back into the cell at a corresponding location on the opposite side of the cell. Particles with only one part of the volume laying outside the cell can interact with the particles near the boundary and an image particle is introduced into the opposite side at a corresponding location, so that it can interact with other particles near the opposite boundary face (Cundall 1987). The use of periodic boundary in

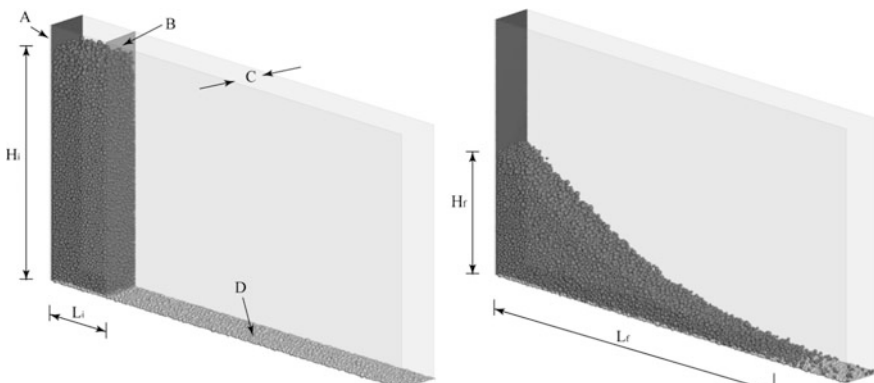


**Fig. 3.1** Model configurations: **a** Left initial sample; **b** Right final deposit (*A* fixed smooth back wall; *B* removable front gate; *C* the DEM periodic boundary; *D* fixed coarse floor;  $L_i$  initial column length;  $H_i$  initial column height;  $L_f$  final run-out length;  $H_f$  final deposit height)

the numerical model presents three main advantages: first, the number of particles is small, and as a consequence, the computational time is reduced (Allen and Tildesley 1989). Second, the numerical simulation can produce macroscopically homogeneous strain, because the boundary configuration can effectively eliminate the spurious surface effects resulting from the rigid wall boundaries (Radjaï and Dubois 2011). Thirdly, the plane strain condition can be easily employed in simulations, so that the granular flow can reproduce realistic depositional morphology.

In Fig. 3.1a, a loose granular column consisting of randomly placed polydispersed spheres is initially generated within a parallelepiped prism bounded by the planes A, B, C and D. After generation, gravity is applied to all particles, leading to granular deposition. The porosity of the loose sample is 0.45. At the end of the deposition, a dense sample with a height of  $H_i$  and porosity of 0.37 is obtained. Once a static granular pile is obtained, gate B is removed immediately to initiate the granular flow. The granular materials would fall downwards and spread horizontally along the coarse floor (D). When grains stop moving, the final run-out distance ( $L_f$ ) and height ( $H_f$ ) of the granular deposit is measured, as shown in Fig. 3.1b. The definition of  $L_f$  is not very clear, or even confusing in the literature. According to Zenit (2005), the outermost edge of the deposit is the location where the majority of the flowing materials remain in contact with each other, disregarding individual loose particles locating very far away from the debris mass centre. In this study, in order to track the position of the front in a way consistent among the various simulations (the number of particles moving ahead depends on the aspect ratio), an algorithm which identifies the front as the boundary between 99 and 1% of the flow mass, i.e., 1% of the mass is travelling ahead of the boundary is implemented. This approach guarantees that the front is not confused with the position of loose single particles jumping ahead the flow.

## 3.2 Dimensional Analysis

In simulating dry granular flows, a number of physical parameters are used to determine the response of granular materials, regarding their dynamic motion and depositional morphology. These parameters include microscopic soil properties, geometric properties and debris flow velocity and duration time, as listed in Table 3.1, where the units are expressed using fundamental dimensions of mass ( $M$ ), length ( $L$ ) and time ( $T$ ), respectively.

Based on how these parameters are related during the simulation, they can be categorized into independent and dependent ones. Since the objective of this research is to investigate the large deformation and destructive power of granular flows, the dependent parameters are selected as the final run-out distance ( $L_f$ ), deposit height ( $H_f$ ), particle velocity ( $V$ ) and flow duration time ( $t$ ). The other parameters, such as the microscopic soil properties and the initial model configurations, are termed as the independent parameters.

**Table 3.1** The governing parameters of the granular column collapse model

	Parameter	Symbol	Unit of measure
Independent parameters	Initial column length	$L_i$	[L]
	Initial column height	$H_i$	[L]
	Particle diameter	$D$	[L]
	Particle density	$\rho_s$	[ML <sup>-3</sup> ]
	Gravitational acceleration	$g$	[LT <sup>-2</sup> ]
	Sample porosity	$n$	[−]
	Normal stiffness	$K_n$	[MT <sup>-2</sup> ]
	Shear stiffness	$K_s$	[MT <sup>-2</sup> ]
	Particle friction angle	$\theta$	[−]
	Coefficient of rolling stiffness	$\beta$	[−]
Dependent parameters	Coefficient of plastic moment	$\eta$	[−]
	Final deposit length	$L_f$	[L]
	Final deposit height	$H_f$	[L]
	Particle velocity	$V$	[LT <sup>-1</sup> ]
	Debris flow duration time	$t$	[T]

In this study, the governing parameters of the microscopic particle contact model are the normal and shear particle contact stiffness (i.e.  $K_n$ ,  $K_s$ ), particle friction angle ( $\theta$ ) and the coefficients of rolling resistance model (i.e.  $\beta$ ,  $\eta$ ). The parameters  $\theta$ ,  $\beta$  and  $\eta$  characterize the roughness of solid grains, which are closely related to the macroscopic frictional property of granular materials and can be bundled together as the macroscopic material internal friction angle ( $\varphi$ ) (see also Sect. 2.2.3). In addition, the soil porosity has been identified to have a significant influence on the mechanical behaviour of granular flows. However, this influence varies widely from study to study, depending on the packing state and slope geometry. As the purpose of this study is to explore the applicability of the DEM in modelling dry granular flows, the porosity of the numerical samples are assumed to be the same as those of real landslides. Assuming a link exists between the independent and dependent quantities, a functional relationship can be written as:

$$(L_f, H_f, V, t) = f(L_i, H_i, D, \rho_s, g, K_n, K_s, n, \varphi) \quad (3.1)$$

Performing the dimensional analysis (Palmer 2008), and assuming that the sample porosity is the same for all the tests, Eq. (3.1) can be rewritten in a form as:

$$([L], [H], [V], [T]) = f(a, [\varepsilon], [S], \varphi), \quad (3.2)$$

where  $[L] = (L_f - L_i)/L_i$  is the normalized particle run-out distance;  $[H] = H_f/L_i$  is the normalized deposit height;  $[V] = V/\sqrt{gH_i}$  is the normalized sliding velocity of the granular materials;  $[T] = t/\sqrt{H_i/g}$  is the normalized duration time of the granular flow;  $a = H_i/L_i$  is the initial column aspect ratio;  $[\varepsilon] =$

**Table 3.2** Typical ranges of dimensionless groups

	$a$	$[\epsilon]$	$[S]$	$\varphi$
Real landslides	–	$[0.002, 0.06]$	$[1.1 \times 10^5, 9.33 \times 10^8]$	$[25, 40]$
Laboratory tests	$[0, 20]$	$[2.8, 10] \times 10^{-7}$	$[2000, 1000]$	$[25, 35]$
Numerical simulations	$[0, 12]$	$[0.0001, 0.1]$	$[25, 250]$	$[25, 40]$

$\rho_s g H_i (1 - n) / (K_n / D)$  is the characteristic strain of the initial granular column;  $[S] = H_i / D$  is the model size ratio.

In principle, the dimensionless groups of the granular column collapse model should be kept the same for both the numerical model and the prototype (e.g. laboratory tests, in situ landslides), so that unique behaviour of granular motion can be achieved. The ranges of the input dimensionless groups are shown in Table 3.2. It can be observed that the numerical model can reproduce correct values of characteristic strain and material internal friction angle, while it is impossible to get the model size ratio correct.

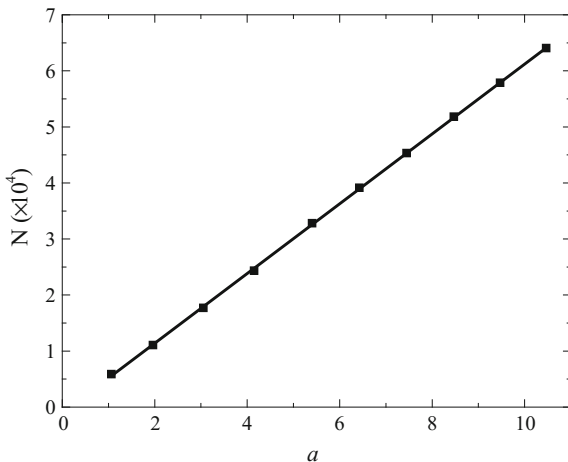
According to Table 3.2, the model size ratio of numerical simulations is far smaller than that of real landslides. This dimensionless group indicates that  $L_i$  and  $D$  should be scaled down by the same factor, so that the model size ratio can remain the same for both model and prototype. If so, a huge number of particles need to be generated in the DEM model, which would place an extremely heavy burden on the computational power and memory capacity of computers. In addition, the grain size can influence the soil properties (e.g. bulk density, hydraulic permeability) significantly. Therefore, it is essential to keep the grain size the same as that of real soil materials and use small model dimensions.

Actually, the model size ratio effectively represents the total number of grains in the model, as estimated by the relationship:  $N \approx (H_i / D)^3$ , with  $N$  being the total number of grains. As discussed by Modenese (2013), it is necessary to select a representative elementary volume (REV) for the DEM model, in which the number of grains in the model is sufficiently high, so that the size of granular sample only have little or no impact on the numerical results. To obtain the REV, a general approach is to study the influence of model size ratio on the simulations by using small-scale model dimensions and real grain sizes (Taylor 1995). Detailed discussions will be presented in the following sections.

### 3.3 Numerical Simulations

This study aims to simulate the mechanical behaviour of granular flows composed of non-cohesive sand grains. According to the discussion in Chap. 2, the physical properties of granular assembly depend highly on the microscopic grain properties, such as the inter-particle friction angle and rolling resistance parameters. By calibrating these parameters, the DEM model is found to be able to reproduce realistic

**Fig. 3.2** The number of grains in granular columns



material internal friction angle, as that of granular materials used in laboratory experiments. According to these microscopic parameters, a detailed analysis of granular flow will be given in this chapter.

In the current numerical simulations, the dimensions of granular sample are largely constrained by the computational power and memory capacity of computer. To speed up the calculations, the size of the periodic cell is set as 0.03 m and the width of the granular column is 0.05 m. The total number of grains in the model increases with column aspect ratio, as shown in Fig. 3.2. In the current analyses, the total number of grains employed in the DEM model is limited to be less than 70,000, so that the calculations are affordable on a standard desktop PC (i.e. Intel® Core™ i7 CPU (2.93 GHz), Memory 7.8 GiB).

### 3.3.1 Deformation of the Granular Assembly

The deformation of granular assemblies can be visualized by taking snapshots of the model successively from the lateral direction after removing the front confining gate. The input parameters of the DEM simulations are listed in “SD1” of Appendix C. Initially, the whole granular column is divided into 10 equal-sized layers with alternant colour red and green along the vertical direction. The coarse ground floor is coloured blue, as shown in Fig. 3.3. By doing so, the motion and deposition of granular materials can be visualized clearly.

Once released, the granular materials in the upper region of the sample fall downwards and spread horizontally. The deformation starts from the region near the confining wall and moves inwards into the static region gradually, leading to intensive shearing along the flowing thickness and the travelling directions. The deformed layers remain approximately parallel to each other at the initial stage of

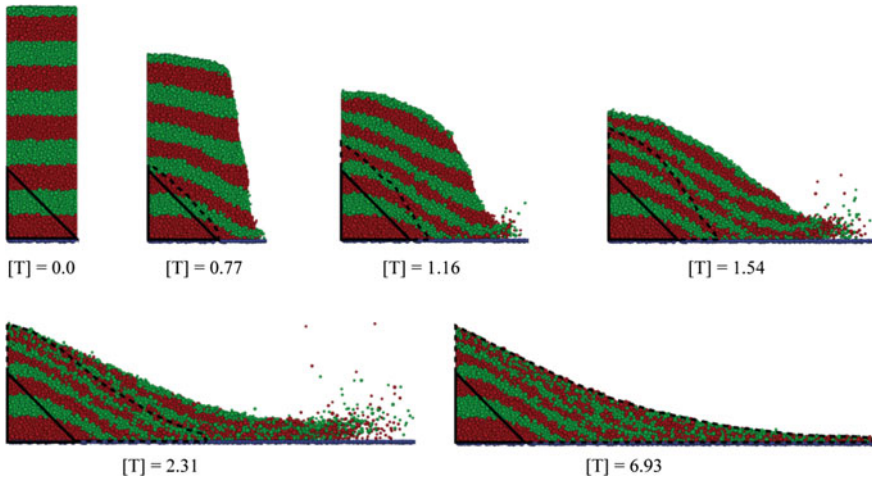
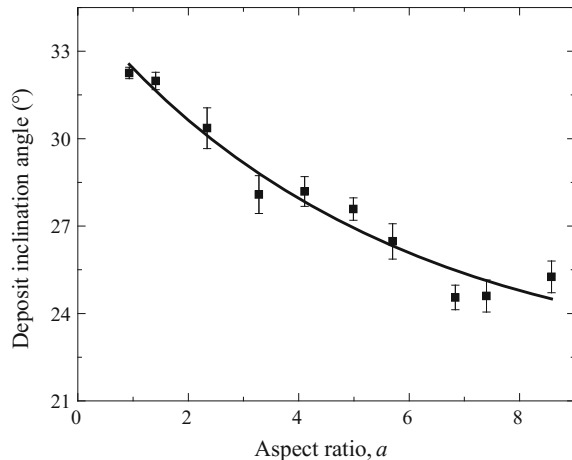


**Fig. 3.3** The deformation of granular assembly during the simulation (Evolution of the static granular pile is illustrated by region bounded by the *solid and dashed curves*)

the collapse, while they mingle together once the solid grains collide onto the ground floor. Throughout the simulation, there exists a static pile at the bottom left region of the column (i.e. the region enclosed by the black solid curves), over which, the upper debris materials continuously slide horizontally. As the granular velocity decreases, the volume of the static pile increases gradually, as shown by the evolution of the black dashed curves in Fig. 3.3. At the end of the simulation, the granular materials can form a static, loose deposit along the horizontal floor. The maximum inclination angle of the deposit is measured and plotted against the column aspect ratio in Fig. 3.4.

**Fig. 3.4** Inclination angle of the granular deposit for different granular columns (for each point, the error bar is achieved for two measurements at different locations on the slope surface)



Theoretically, the inclination angle of the granular deposit should be equal to the angle of repose, which has been calibrated as  $31.4^\circ$  using a small granular column collapse model in Sect. 2.2.4. In the calibration process, the motion of granular materials is mainly controlled by the inter-particle friction, so that the granular materials can deposit slowly, resulting in an inclination angle close to the angle of repose. In this study, small granular columns can effectively reproduce the same model configurations as those used in Sect. 2.2.3, such that the measured inclination angle of granular deposits can match the angle of repose. However, for large granular columns, the granular motion is mainly controlled by the inertial forces of the solid materials, in which the majority of solid grains are in dynamic motion, resulting in very flat deposits with much smaller inclination angles.

After removing the confining wall, the granular materials start to move under gravity. In Fig. 3.5a, grains with velocities smaller than 1% of the characteristic velocity ( $\sqrt{gH_i}$ ) are coloured grey, while grains moving at higher velocities are coloured red. The shearing failure of the sample occurs approximately along a plane as represented by the dashed line. As it takes time for solid grains to acquire velocities under gravity, the failure of granular assembly is assumed to occur at the normalized time of 0.07, at which, the majority of grains near the slope surface are involved in motion.

According to the Rankine (1857) theory of earth pressure, the failure of the granular column corresponds to the active failure state, in which, the inclination angle of the failure plane ( $\theta_f$ ) can be estimated by Eq. (3.3).

$$\theta_f = 45^\circ + \varphi/2, \quad (3.3)$$

where  $\varphi$  is the internal friction angle of grains (calibrated as  $31.3^\circ$  in Sect. 2.2.3).

Figure 3.5b shows that the inclination angle of the active failure plane is approximately equal to  $61^\circ$  for different granular columns, which is very close to the theoretical value obtained from Eq. (3.3) ( $\approx 60.7^\circ$ ).

During the granular flow, grains at the running front are in dynamic motion, such that it is very difficult to obtain correct profiles of the sample, if focus is placed only on the positions of individual solid particles. To overcome this limitation, the author has proposed a numerical method to track the grain contact points within the whole sample during the simulation. The profile of the granular assembly is obtained by connecting the contact points at the debris surface with straight lines, as shown in Fig. 3.6. The dispersed grains outside the profile are ignored, because there is no particle contact existing out there. At the front region, a “plug” shape profile can be observed. This is due to the implementation of a frictional boundary condition on the ground floor, so that the granular materials near the floor are decelerated by the basal friction, while the upper grains can move faster with fewer constraints.

Depending on the value of initial aspect ratio, different regimes of granular flows can be observed for columns, as illustrated by a sequence of deposit profiles in Fig. 3.7. For granular columns with small aspect ratios (e.g.  $a = 0.93$ ), only a small portion of grains are involved in motion. The upper surface of the sample inclines gradually until the angle of repose is reached. The final deposit has a shape of

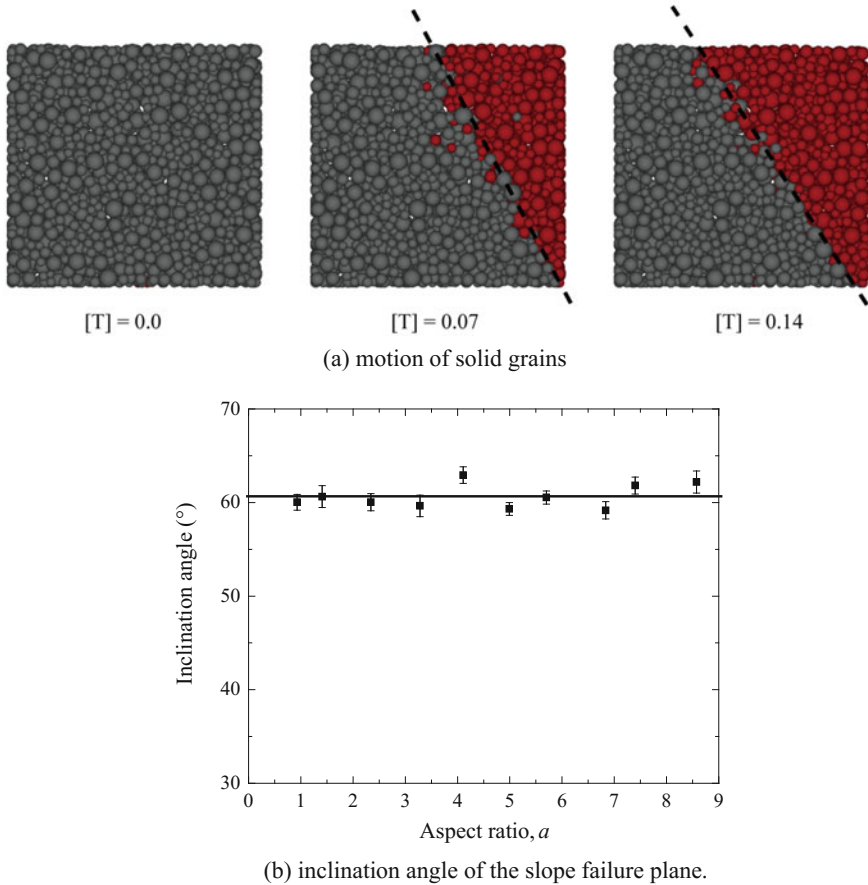


**Fig. 3.5** Active failure state of the granular sample (for each data point in (b), the error bar is achieved for two measurements at different locations on the slope surface)

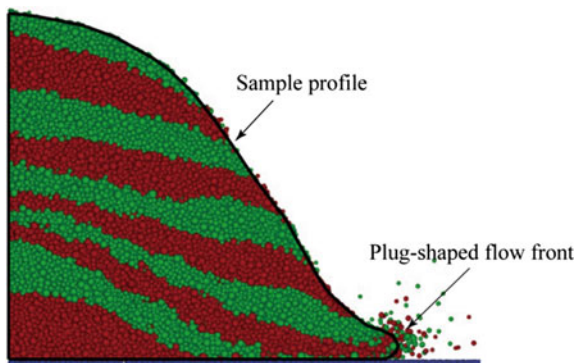


**Fig. 3.6** The measurement of the sample profile

curved trigonal prism with its height close to the initial column height. As the value of column aspect ratio increases gradually (e.g.  $a = 3.26, 5.91, 9.27$ ), the major portion of the debris mass would collapse downwards and spread horizontally along the ground floor. For these samples, solid grains at the upper front would go through a short period of free fall, and then collide with grains at the lower region, after removing the confining wall. As the simulation continues, the granular assembly stretches along the horizontal floor, forming an elongated and thin profile.

A comparison of the evolution of sample profiles between the current DEM analyses and the results from finite element modelling by Crosta et al. (2009) is given in Fig. 3.8. It can be observed that the shape of the slope profiles from the DEM and FEM simulations are very similar to each other, when the initial column aspect ratios are approximately the same. The final granular deposit of the DEM sample is steeper, and the run-out distance of granular materials is longer than that of the FEM model. Furthermore, the FEM model is unable to simulate the extreme tapering of the flow front. This can be explained by the fact that the discrete solid grains have a greater mobility than the continuous soil elements. In the DEM, all the solid grains can move independently, while in the FEM, the motion of soil elements are largely constrained by the constitutive models used in the simulation (e.g. the limitation of mesh grid distortion).

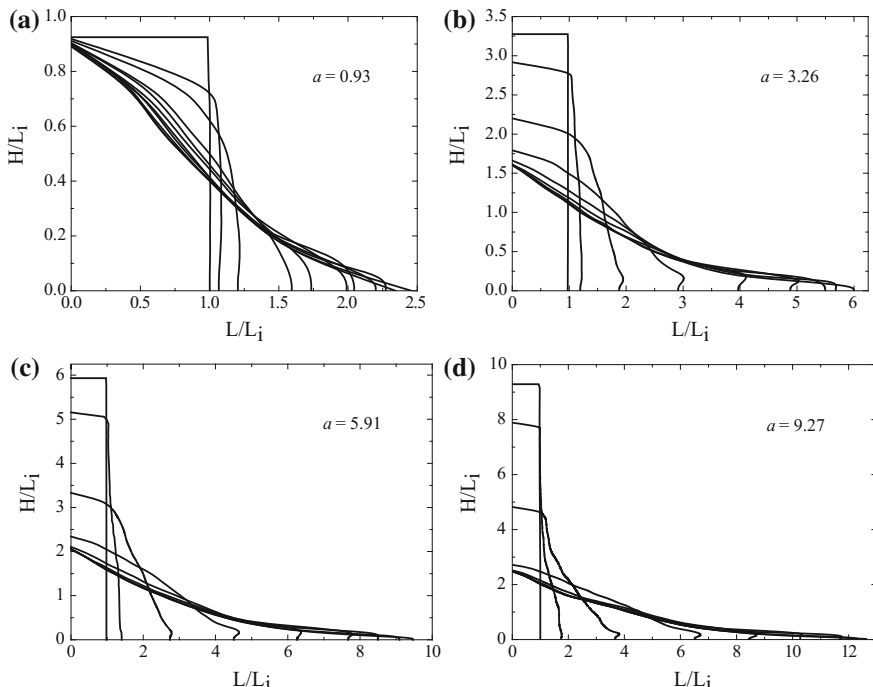
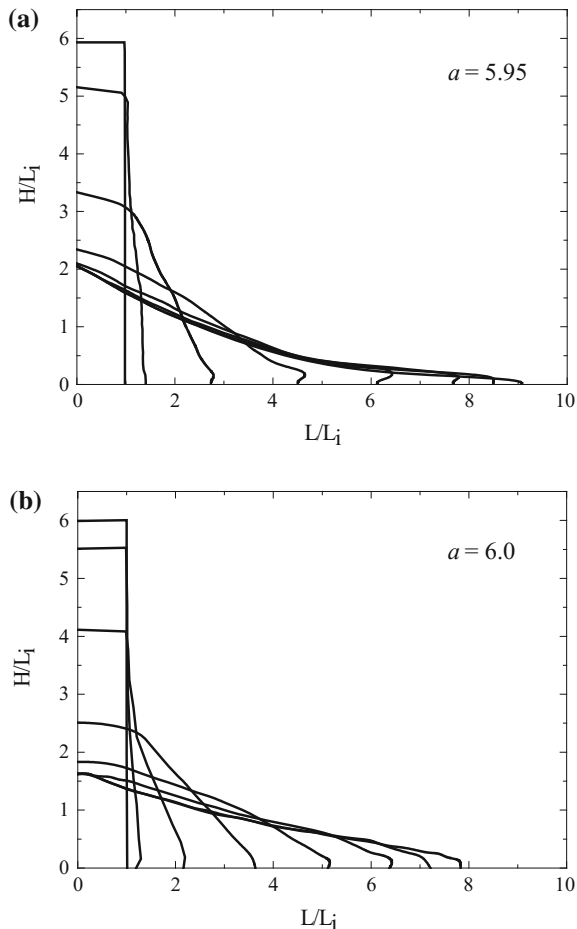


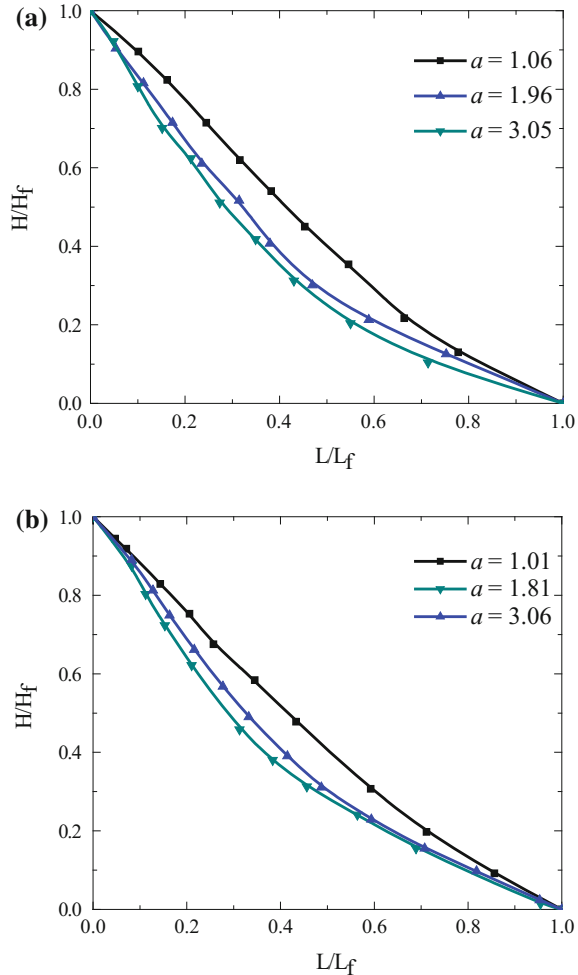
**Fig. 3.7** Evolution of deposit profiles for different granular columns [Profiles are traced at successive time ( $\Delta[T] = 0.5$ )]

**Fig. 3.8** Comparison of granular profile evolutions:  
**a** DEM simulation results;  
**b** FEM modelling results by Crosta et al. (2009) [Profiles are traced at successive time ( $\Delta[T] = 0.5$ )]



According to the discussion above, it is clear to identify that the profiles of the granular deposits depend highly on the value of the initial column aspect ratios, which suggests that the best way to present the numerical results is to make them dimensionless and plot in the same length scale (Lube et al. 2005). In Fig. 3.9, the final profiles of the granular assembly normalized by the final run-out distance and deposit height are plotted. It emerges that the normalized profiles of the DEM simulations and experiments have nearly the same distribution patterns, regardless of the initial aspect ratios. The numerical results from various granular columns can match the experimental results very well.

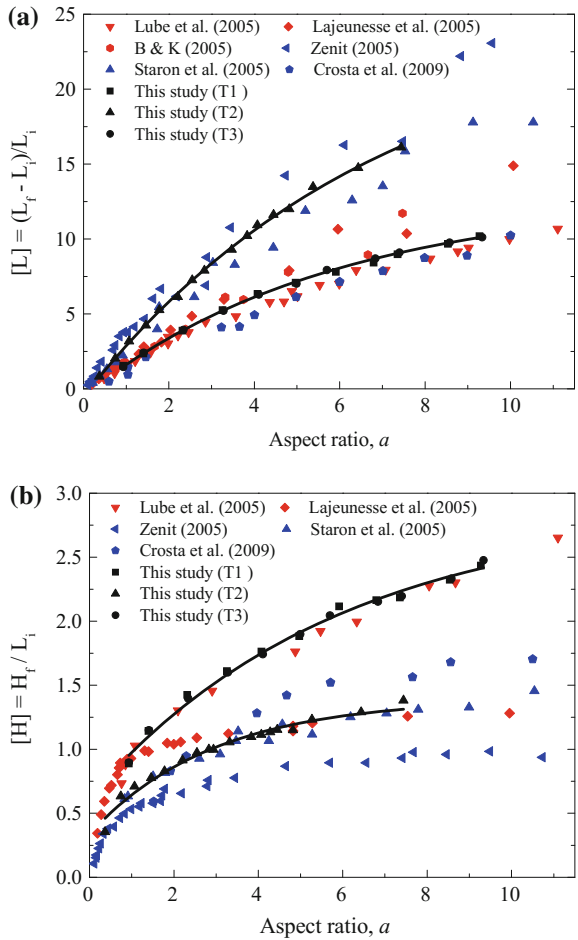
**Fig. 3.9** Normalized profiles of the granular deposit: **a** 3D DEM results; **b** experimental results by Lube et al. (2005)



### 3.3.2 Influence of Initial Column Aspect Ratio

In the case of rock avalanches and debris flows, the assessment of the final run-out distance is of primary importance, as it determines the extent of regions affected by the avalanche or landslide. In Fig. 3.10, the current numerical results have been compared with previous numerical simulations (Staron and Hinch 2005; Zenit 2005; Crosta et al. 2009) and experimental observations (Balmforth and Kerswell 2005; Lajeunesse et al. 2005; Lube et al. 2005) from the literature. The input parameters of DEM for this study are listed in “SD1” of Appendix C and the corresponding dimensionless groups are listed in Table 3.3.

**Fig. 3.10** The influence of aspect ratio on **a** normalized run-out distance, and **b** final deposit height. The symbols coloured red are experimental results; symbols coloured blue are numerical results; the symbols coloured black are the numerical results of this study



Three sets of simulations were performed: T1 and T2 refer to simulations run for the same values of  $\varepsilon$  (ranging from  $6.5 \times 10^{-7}$  to  $6.5 \times 10^{-6}$ ), but with  $\eta = 0.1$  and  $\eta = 0$ , respectively, whilst T3 refers to simulations run for  $\varepsilon$  ranging from  $6.5 \times 10^{-5}$  to  $6.5 \times 10^{-4}$  and  $\eta = 0.1$ . Some of the T1 and T2 simulations were run with a gravity scaled up of 100 times and  $K_n = 3 \times 10^7$  N/m, whereas some others with unscaled gravity but particles 100 times softer, i.e.  $K_n = 3 \times 10^5$  N/m. In fact, in light of dimensional analysis, scaling can be introduced by scaling either the value of gravitational acceleration or particle stiffness. The fact that the obtained results are aligned in consistent trends in Fig. 3.10 can be seen as a verification of the correctness of the performed dimensional analysis. Comparison between T1 and T2 simulations allows examining the influence of particle shape on the run-out, whereas comparison between T1 and T3 the influence of  $\varepsilon$ .

**Table 3.3** Parameters for the experimental and numerical simulations

	Material	$a$	$[\varepsilon]$	$[S]$	$\varphi(^{\circ})$
Lube et al. (2005)	Quartz sand	[0.5, 20]	$[4.7, 140] \times 10^{-9}$	[9, 1000]	[29.5, 32]
Lajeunesse et al. (2005)	Glass beads	[0.2, 12]	$[1.2, 8.7] \times 10^{-8}$	[100, 300]	[21.5, 22.5]
B & K (2005)	Glass beads	[0.5, 40]	$[5.2, 420] \times 10^{-9}$	[12, 1000]	[22.5, 26.5]
Zenit (2005)	–	[0.1, 10]	$[2.1, 13.1] \times 10^{-5}$	[28, 173]	30
Staron (2005)	–	[0.2, 17]	–	[14, 369]	20
This study (T1) <sup>a</sup>	–	[1, 10]	$[6.5, 65] \times 10^{-7}$	[25, 250]	31.7
This study (T2) <sup>b</sup>	–	[1, 10]	$[6.5, 65] \times 10^{-7}$	[25, 250]	26.1
This study (T3) <sup>a</sup>	–	[1, 10]	$[6.5, 65] \times 10^{-5}$	[25, 250]	31.7

<sup>a</sup>Numerical simulation using rolling resistance model

<sup>b</sup>Numerical simulation using free rolling model

According to Fig. 3.10a, it can be observed that the final normalized run-out distance obtained from the simulations matches well from a qualitative viewpoint both the experimental observations of Lube et al. (2005) obtained in plane strain conditions, and the 2D FEM numerical analyses of Crosta et al. (2009). Also it emerges that if rolling resistance is not employed (simulations T2), unrealistically large run-out distances are obtained since particle angularity tends to reduce the granular run-out. In other words, a flow of spherical particles is more prone to sliding than a flow of particles with non-spherical shape. Equally, if 2D DEM simulations are employed (Staron and Hinch 2005), unrealistically long run-outs are obtained. Presumably, this is due to the fact that the 2D kinematics of particle interaction is too different from the real 3D kinematics. Comparison between the simulation series T1 and T3 shows that the characteristic strain of a granular column,  $\varepsilon$ , has no influence on the observed flow behaviour, at least for the range of values here employed. In conclusion, simulations T1 and T3 show that if particle shape is accounted for, albeit by means of a very crude approximation (i.e. employing a moment—relative rotation law with spherical particles which avoids simulating the real non-spherical geometry of the particles), the obtained run-out and final heights of the simulated flows are in good agreement with experimental data.

The evolutions of granular spreading distances for different granular columns over time are plotted on Fig. 3.11. The granular flow duration time has been normalized by the characteristic free fall time of the granular column. The current numerical simulation series T1 and T3 are compared with the numerical (Crosta et al. 2009) and experimental (Lajeunesse et al. 2005; Lube et al. 2005) observations. The time evolution of the granular spreading distance in this study can match the evolution of debris run-out distance described by Crosta et al. (2009) and Lajeunesse et al. (2005) very well, in which four distinct regimes can be identified,

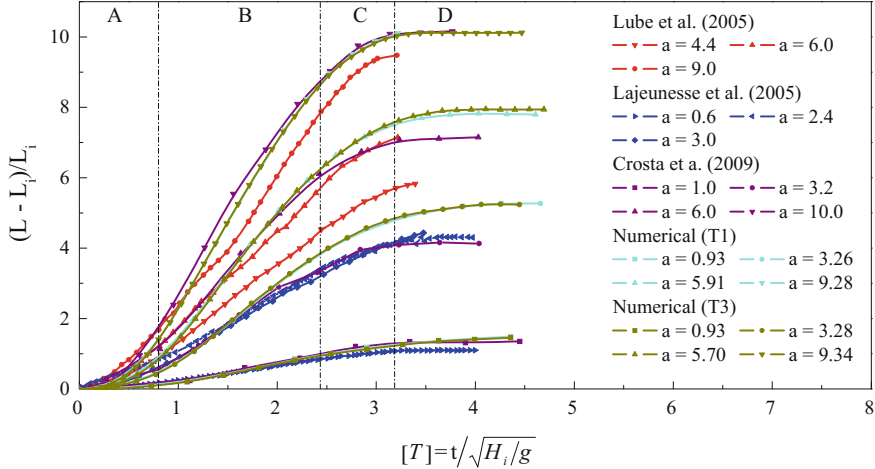


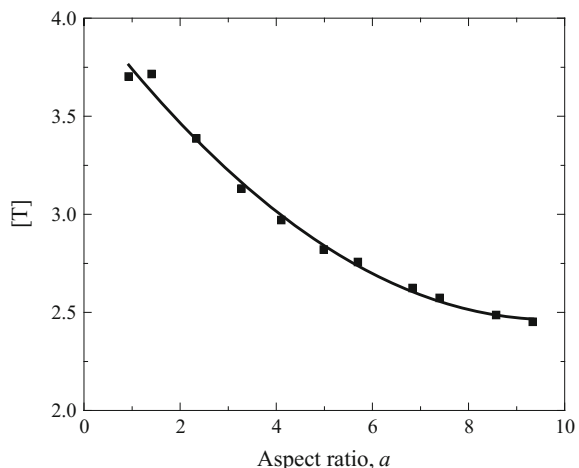
**Fig. 3.11** Normalized granular flow distance versus the normalized duration time

namely the initial transient acceleration (*A*), the constant velocity spreading (*B*), the gradual deceleration (*C*) and the final static deposition (*D*).

The duration time of the granular flow is obtained as the time instant when the run-out distance approaches a constant value. For granular columns of various initial aspect ratios, a comparison between the granular flow duration time is given in Fig. 3.12. It can be observed that the normalized duration time decreases with the aspect ratio and it will finally approach an asymptotic value of 2.5, which is in good agreement with that obtained by Lacaze et al. (2008).

As discussed in Sect. 3.3.1, a short period of free fall exists for the collapse of large granular columns. This phenomenon has been observed by Staron and Hinch

**Fig. 3.12** The duration time of different granular columns



(2007) and Lacaze et al. (2008) in 2D and plane strain conditions. Theoretically, the free fall of the granular materials should satisfy the following condition:

$$\frac{1}{2}gt^2 = H_i - h, \quad (3.4)$$

where  $h$  is the height of the granular column at time  $t$ .

Equation (3.4) can also be rewritten in a dimensionless form, as:

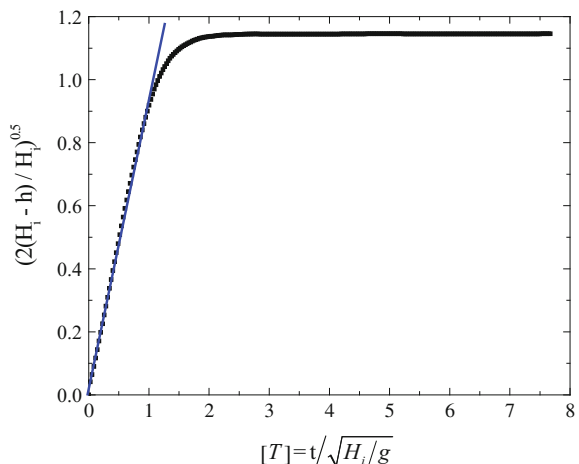
$$[T] = \sqrt{2(H_i - h)/H_i} \quad (3.5)$$

Figure 3.13 illustrates the relationship between  $\sqrt{2(H_i - h)/H_i}$  and  $[T]$ , with the free fall period represented by a blue straight line of gradient 1.0. It can be observed that the free fall of grains occurs within a short time period (i.e.  $[T] < 1.0$ ), after which, the upper grains would collide onto the lower ones, leading to a gradual decrease of vertical velocity. As a static granular pile would form near the slope source region during the simulation, the velocity of the topmost grains would finally approach zero, resulting in a constant deposit height after  $[T] = 2.0$ .

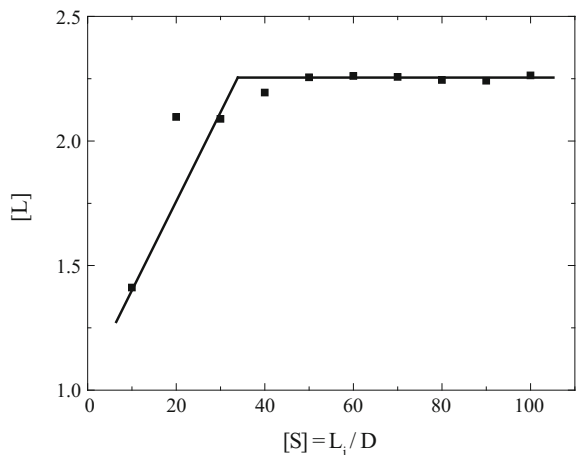
### 3.3.3 Influence of Model Size Ratio

The model size ratio effectively reflects the representativity of DEM models. In general, the size ratio  $[S] = H_i/D$  of real landslides can range from  $10^4$  to  $10^7$ , while it can hardly be larger than 1000 for numerical models due to the limitation of computational power and memory capacity. As a result, it is impossible to get this group correct in small-scale numerical models. This is especially true for DEM

**Fig. 3.13** Evidence of the free fall at the beginning of the granular collapse



**Fig. 3.14** Influence of model size ratio on the normalized run-out distance



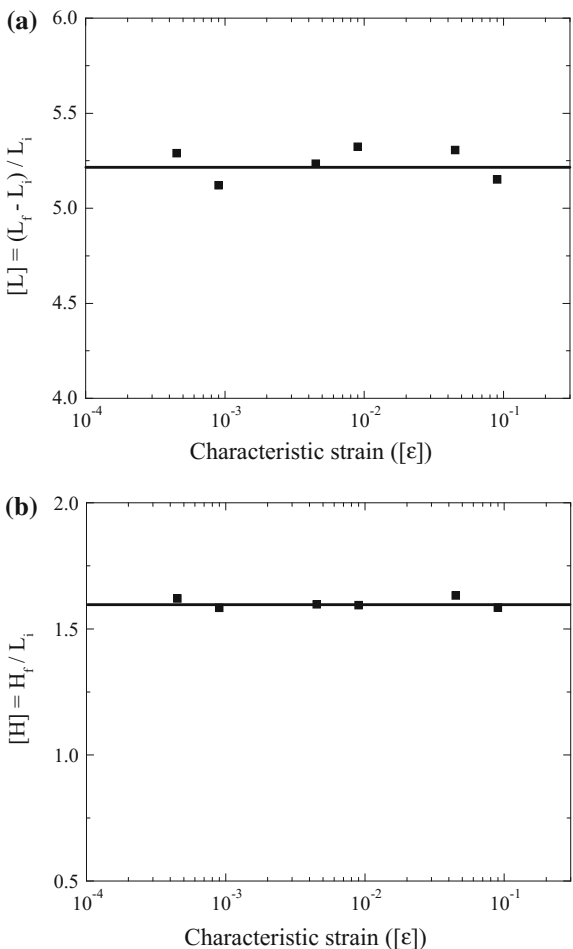
simulations, because only a limited number of particles can be employed using the current computational resources.

To investigate the influence of model size ratio on the depositional behaviour of granular materials, simulations of granular flows using granular columns with the initial aspect ratio of 2.0 were performed. As shown in Fig. 3.14,  $[S]$  can influence the run-out distance of granular flows significantly only if it is smaller than 40, while little influence can be observed for larger values of  $[S]$ . Thus, it can be postulated that further increase of  $[S]$  will not change the depositional morphology of dry granular flows. Therefore, a model size ratio of 40 can be regarded as the critical model size ratio of the granular column collapse model. In the current research using small-scale DEM models, the model size ratio is chosen as 50, while  $D_{10}$  is set the same as that obtained from field investigations.

### 3.3.4 Influence of Column Characteristic Strain

Field investigations reveal that the dimensions of landslides can range from 10 to 3000 m and the corresponding characteristic strains ranges from  $1.3 \times 10^{-4}$  to 0.04 (see Appendix A). The current numerical model has tried to reproduce this number by using a small-scale granular column model with an initial aspect ratio of 3.3. According to Fig. 3.15, it can be concluded that on average the normalized run-out distance and final deposit height remain constant for different characteristic strains, which indicates that the characteristic strain does not influence the depositional behaviour of granular flows. This phenomenon can be explained by the energy conservation of the granular system. As the normal contacts between particles are perfectly elastic, there is no energy dissipation through particle normal collisions.

**Fig. 3.15** Relationships between the normalized run-out distance, deposit height and  $[\varepsilon]$



As a consequence, the energy dissipation depends only on the inter-particle frictions, rolling resistance and air viscous drag forces.

The energy conservation of the granular system is expressed as:

$$\bar{m}g(H_0 - H_1) + \mu\bar{m}g(L_0 - L_1) + E_0 = 0, \quad (3.6)$$

where  $\bar{m}$  is the mass of granular materials;  $\mu$  is the coefficients of friction;  $E_0$  is the energy dissipation due to inter-particle friction and air viscous drag effect;  $H_0$ ,  $H_1$  and  $L_0$ ,  $L_1$  are the initial and final height and length of the granular mass centre, respectively.

Rearranging Eq. (3.6), one can get:

$$\frac{H_0 - H_1}{L_0} = \mu \frac{L_1 - L_0}{L_0} - \frac{E_0}{\bar{m}gL_0} \quad (3.7)$$

In Eq. (3.7), the second term on the right-hand side is assumed to be constant. Thus, the normalized height and length of the granular deposit are linearly related, and independent of the characteristic strain of the initial granular column. Therefore, granular materials would have the same final normalized deposit length and height, if the initial column aspect ratios are the same.

### 3.3.5 *Influence of Material Internal Friction Angle*

Investigation of the mechanical behaviour of granular materials using the DEM is challenging, because the numerical model generally includes some oversimplifications, for instance the shape of solid particles is normally assumed to be spherical. As a result, the particle interlocking, realistic friction can hardly be reproduced. To overcome this problem, the current research has implemented the rolling resistance contact model in the open source DEM code, such that the shape effect of solid grains can be included in the analyses (Iwashita 1998; Jiang et al. 2005; Belheine et al. 2009).

As discussed in Sect. 2.2.3, any combination of the microscopic inter-particle friction angle and rolling parameters can produce a unique value of material internal friction angle ( $\varphi$ ). According to the input parameters used in the DEM model, the value of  $\varphi$  is in the range of [27.5°, 42.5°]. Within this range, the relationship between the normalized run-out distance and  $\varphi$  for various granular columns is given in Fig. 3.16. It can be concluded that as the material internal friction angle increases from 27.5° to 42.5°, the normalized granular run-out distance decreases exponentially. The debris materials have very high mobility at small values of internal friction angle, which effectively reflect the depositional behaviour of either smoothed or rounded solid grains. However, at larger values of internal friction angle, the solid grains can only travel very short distances, representing the motion of angular solid blocks, such as rock and debris avalanches.

## 3.4 Mechanical Analyses

To analyse the mechanical behaviour of dry granular flows, the granular properties such as particle velocity, force chain, stress distribution and bulk coordination number can be plotted as contours on a two-dimensional plane, parallel to the flowing direction. Since the wall effects of the numerical model can be diminished effectively by the plane strain and periodic boundary conditions, these parameters

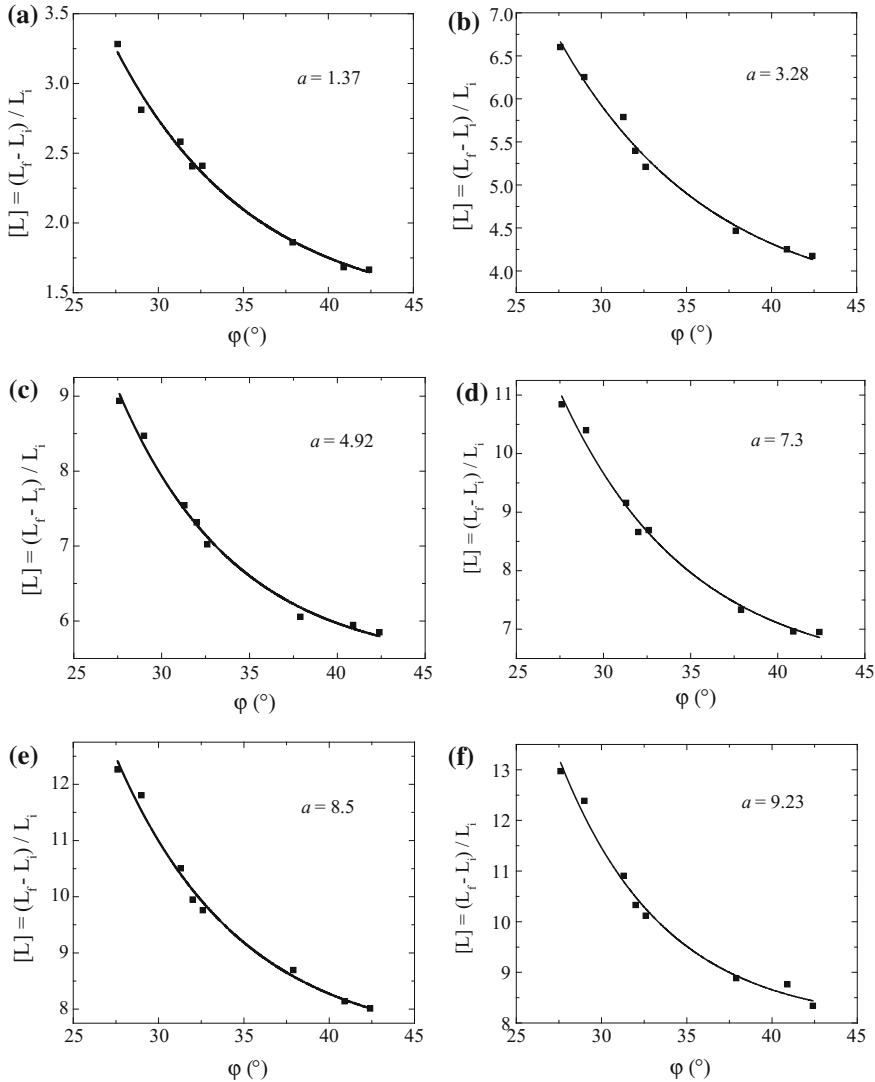


**Fig. 3.16** Influence of material internal friction angle on the normalized run-out distance

can be taken as the average values within each discrete measurement cell, as shown in Fig. 3.17.

The averaging process can be summarized as:

- (1) Discretize the model domain into a number of equal-sized measurement cells. The dimensions of a measurement cell are  $0.005 \text{ m} \times 0.03 \text{ m} \times 0.005 \text{ m}$ ;
- (2) Check if the measurement cell contains any grains. If so, get the average properties of solid grains (e.g. velocity, stress and bulk coordination number).

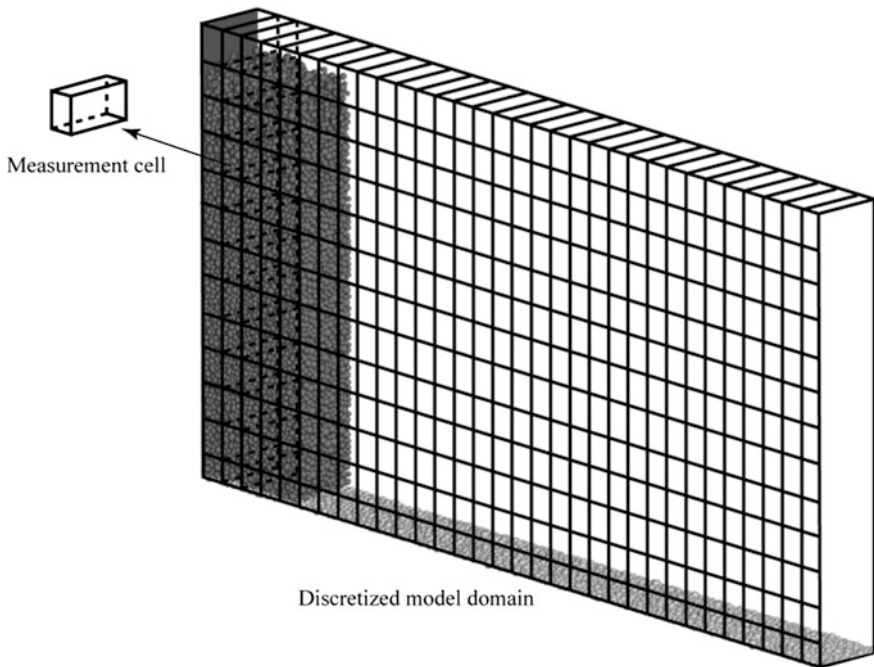


**Fig. 3.17** The discretized domain and measurement cells

The input parameters of the DEM simulations are listed in “SD2” of Appendix C.

### 3.4.1 Evolution of Granular Velocity

Once released, the granular materials fall downwards and spread horizontally along the ground floor. During this process, the motion of granular materials goes through three stages of dynamic motion: acceleration, constant velocity and deceleration. As shown in Fig. 3.18, particle velocity vectors are scaled by the magnitudes of velocities. On these graphs, particles with various velocities are distinguished by different sizes and colours. According to Fig. 3.18, it can be observed that the debris motion mainly involves the upper region of the granular column, while grains located in the bottom region of the sample remain static throughout the simulation. Initially, the solid materials accelerate to fall downwards under gravity forces. The grain velocity increases quickly to reach the maximum normalized value of 0.8 at  $[T] = 4.3$ . Meanwhile, due to the intensive inter-particle friction and rolling resistance, the acceleration of solid grains would decrease gradually.

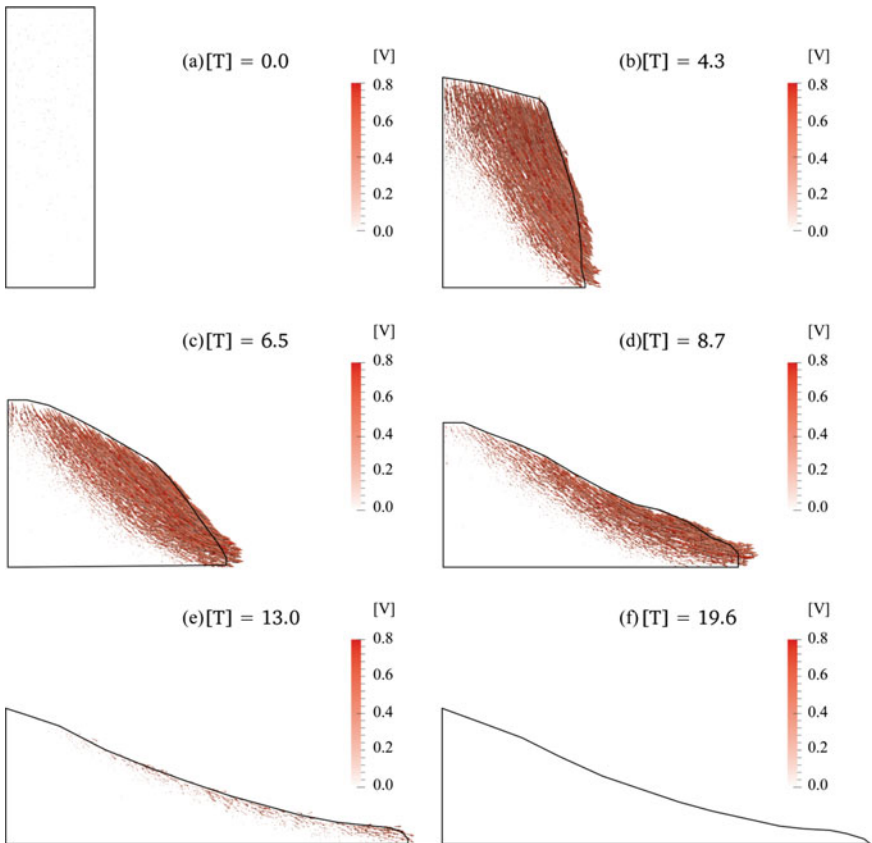
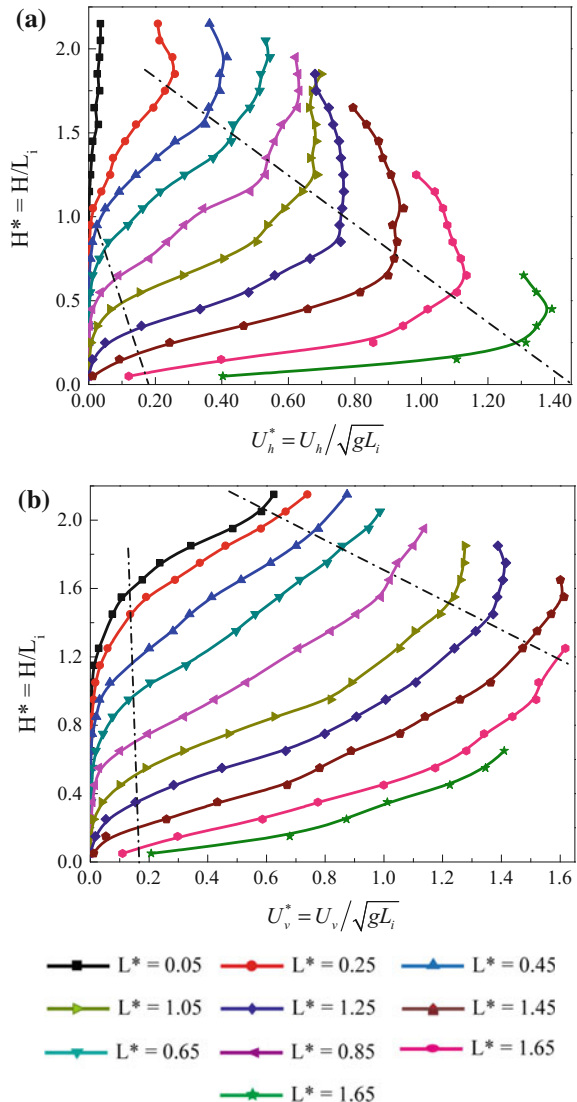


**Fig. 3.18** Evolution of particle velocity field during the simulation

When the gravity of a particle is balanced by the net contact forces, the solid grains would move at constant velocities. At the deceleration stage, the motion of grains mainly occurs at the surface of the granular assembly, as represented by the particle vector fields. Due to the influence of inter-particle friction and rolling resistance, the grain velocity would finally approach zero and a static granular deposit is formed on the ground floor. At the propagation stage of the granular flow, it is also possible to record the profiles of particle velocities within the granular assembly. At any measurement location, the length ( $L$ ) and height ( $H$ ) away from the bottom left origin of the model are normalized by the initial column width, while the grain velocity is normalized by the characteristic velocity ( $\sqrt{gL_i}$ ). Figure 3.19 shows the velocity profiles (i.e. horizontal ( $h$ ) and vertical ( $v$ ) components) of granular flows with an initial aspect ratio of 3.3 at the normalized time of  $[T] = 0.77$  (N.B. at this time instant, the upper grains have already fall downwards, thus, the normalized height shown on the graph is smaller than 3.3).

**Fig. 3.19** Distribution of particle velocity: **a** left horizontal velocity; **b** right vertical velocity



For particles located within the initial granular domain ( $L^* < 1.0$ ), the velocity profile starts from the original point and remains zero in the static granular pile region. In the upper region of the sample, the vertical ( $U_v$ ) and horizontal ( $U_h$ ) velocities increase gradually. For regions with  $L^*$  being larger than 1.0, the horizontal velocity increases approximately linearly with the height from zero to the maximum value at the middle upper part of the sample. Beyond this region, the horizontal velocity decreases gradually with the height, due to the dominant role of the vertical fall of grains in the upper region. For the vertical velocity of grains, it

increases gradually with the height and the maximum value occurs at the top of the sample where individual grains are in free fall. The reciprocal value of the slope of these curves represents the shear rate (Zhou and Ng 2010). As shown in Fig. 3.19, intensive shearing of the granular sample occurs within a region between the two dashed lines.

### 3.4.2 Granular Energy

The potential energy of the granular column at any time is calculated as:

$$E_p = \sum_{i=1}^N m_i g h_i, \quad (3.8)$$

where  $m_i$  and  $h_i$  are the mass and height of a single particle  $i$ , respectively, and  $N$  is the total number of particles of the column.

The kinetic energy of the system at any time is calculated as:

$$E_k = \frac{1}{2} \sum_{i=1}^N (m_i v_i^2 + I_i \omega_i^2), \quad (3.9)$$

where  $v_i$  and  $\omega_i$  are the translational and angular velocities respectively of a generic particle  $i$ , and  $I$  is its moment of inertia (for a spherical particle  $I = 0.4mR^2$ ).

A part of potential energy gets dissipated rather than being transformed into kinetic energy, due to plastic particle collisions (e.g. plastic particle rebounds and frictional sliding). In light of the principle of energy conservation, the energy dissipated in the flow at any given time can be calculated as:

$$E_{\text{diss}} = E_0 - E_p - E_k, \quad (3.10)$$

where  $E_0$  is the total energy of the system, which can be calculated from the initial potential energy of the column before particles start to move, as:

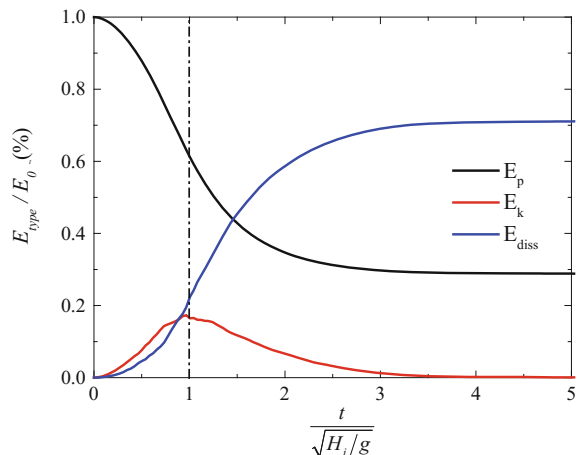
$$E_0 = MgH_i/2, \quad (3.11)$$

where  $M = \sum_{i=1}^N m_i$ .

At the particle level, energy is mainly dissipated via frictional sliding at particle contacts and viscous damping along both the normal and tangential directions of contacts when damping is present, but also by the relative rotation between particles once the plastic limit of the rolling moment is reached (see Fig. 2.4c).

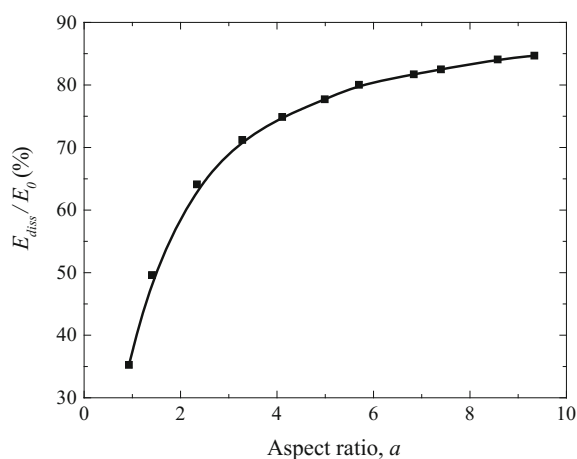
In Fig. 3.20, the temporal evolution of the energy components of the flows, from start of column collapse until end of motion, is plotted. After the instantaneous removal of the confining gate at  $T = 0$ , particles start to fall downwards, with

**Fig. 3.20** Variation of energy during granular flow ( $\alpha = 3.26$ ) ( $E_0$  initial total energy;  $E_p$  potential energy;  $E_k$  kinetic energy;  $E_{\text{diss}}$  cumulative energy dissipation)



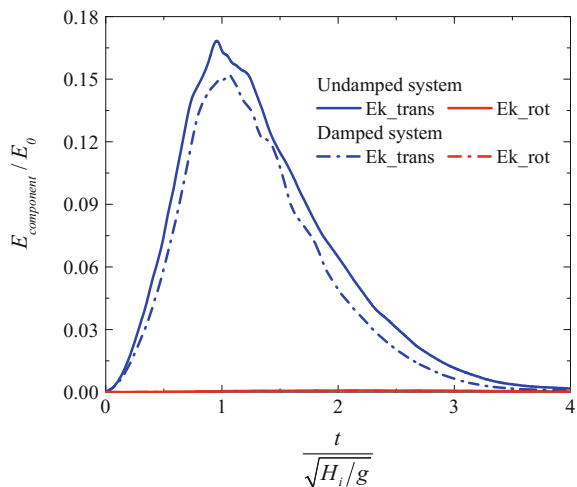
potential energy being progressively transformed into kinetic energy. The kinetic energy exhibits a peak at around  $T = 1.0$  (see the dashed line in the figure), when both the rate of potential energy loss and the rate of cumulative energy dissipation (see the slopes of the curves in the figure) reach their maximum values. After this time instance, both potential and kinetic energy decrease. The flow comes to a stop at about  $T = 4.0$ . Considering now columns of different aspect ratios, the dissipated energy in terms of percentage of the initial total energy of the columns, has been plotted against their aspect ratio in Fig. 3.21. From the simulations, it emerges that the higher the aspect ratio is, the larger the proportion of energy dissipated during the flow can be.

**Fig. 3.21** Total energy dissipated during the flow normalized by the initial potential energy versus column aspect ratio



Then, it is necessary to investigate how much of the kinetic energy of the flow is due to the translation of particles and how much is due to their rotations. In Fig. 3.22, the two sources of kinetic energy are plotted separately against time. Unfortunately, viscous damping coefficients strongly depend on the type of material making the granular flow. Furthermore, a reliable experimental determination of damping coefficients for granular flows is currently not yet available. Therefore, in this research, two cases of simulations were run: one without viscous damping and the other one with a viscous damping coefficient of 0.3, in order to obtain a rough indication of the potential influence of viscous damping on the variables of interest but without trying to model any specific natural debris flow. In the simulations with viscous damping, the damping coefficient of 0.3 was employed in both the normal and tangential directions of particle contacts. This value corresponds to a coefficient of restitution of around 0.5 (Tsuji et al. 1992). In Fig. 3.22, it can be noted that the kinetic energy stemming from particle rotations remains negligible at all times (i.e. less than 0.5% of the total kinetic energy) in both cases, with and without the presence of viscous damping. In light of this finding, in the next section, where the spatial distribution of the momentum inside the flow is investigated, special attention is concentrated on the linear momentum since the angular momentum is negligible. Also, from Fig. 3.22, it emerges that the curves obtained for flows with and without damping, are similar. This implies that the presence of damping decreases the magnitude of the kinetic energy of the system, of the same proportion, throughout the duration of the flow.

**Fig. 3.22** Evolution of kinetic energy over time ( $a = 3.26$ ) ( $E_{k\_trans}$  and  $E_{k\_rot}$  are the translational and rotational sources, respectively of the kinetic energy of the system)



### 3.4.3 Linear Momentum

The evolution over time of the linear momentum of the flow,  $\vec{p} = \sum_{i=1}^N m_i \vec{v}_i$ , is plotted in Fig. 3.23a, in the case of the presence of viscous dissipation and in its absence. Given, the imposition of the periodic boundary condition along the  $y$  axis, it is expected  $p_y$  to be negligible at all times, as it is shown in Fig. 3.23a. This confirms the effective presence of plane strain conditions in the  $x-z$  plane for the simulated flows. In the following analyses, the subscript ‘ $x$ ’ denotes the direction of flow propagation; ‘ $y$ ’ denotes the out of plane direction, while ‘ $z$ ’ denotes the vertical direction.

Analogously to the energy analysis of the flow, it is convenient to normalize  $\vec{p}$ , for the sake of generality in presenting results. To this end, a scalar quantity,  $p_0$  is introduced, with:

$$p_0 \equiv M \sqrt{g H_i}. \quad (3.12)$$

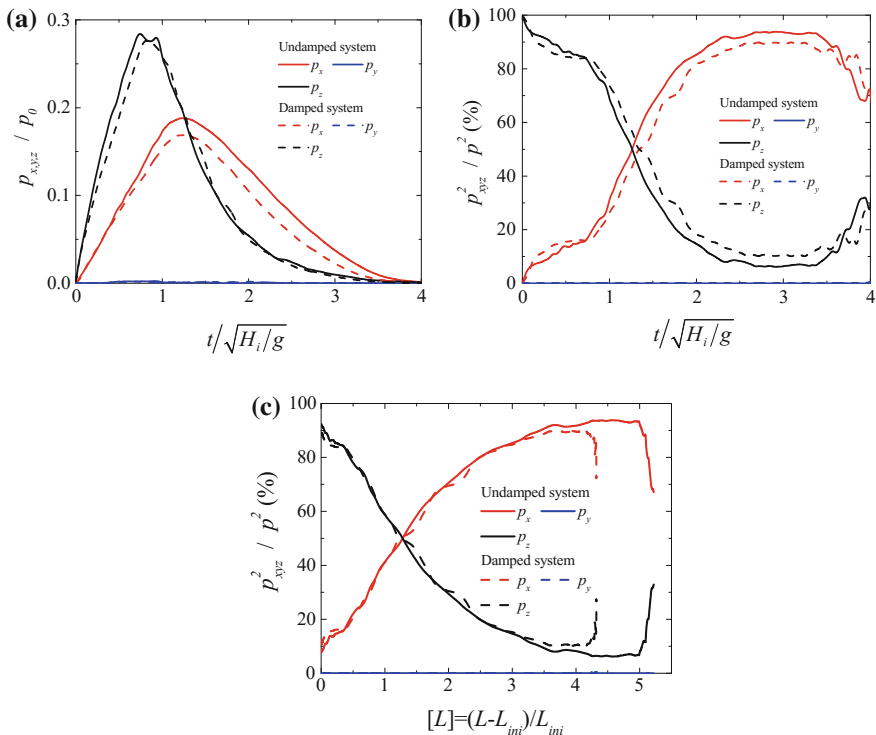


**Fig. 3.23** Evolution of linear momentum over normalized time for flow with and without damping: **a** momentum components normalized by  $p_0$ ; **b** components of momentum as a percentage of the total momentum against normalized time; **c** components of momentum as a percentage of the total momentum against normalized run-out

This quantity can be thought of as an approximate average of the momentum of the flow:  $p_0 \equiv M\sqrt{gH_i} \cong M \cdot H_i / \sqrt{gH_i}$  with  $H_i/\sqrt{gH_i}$  being the average velocity of the flow. In Fig. 3.23a, the components of the linear momentum along the  $x$ ,  $y$  and  $z$  axes, normalized by  $p_0$ , are plotted against dimensionless time. A small difference between the curves for the case with and without damping is noted with damping having the effect of reducing the amount of momentum as it is expected. From the figure, it emerges that the momentum in the vertical direction,  $p_z$ , exhibits a higher peak than the momentum in the direction of flow propagation,  $p_x$ . The two peaks occur at different times. To better investigate which one is dominant and when, it is convenient to make a relative comparison between the two components. To this end, the square of each component over the square of the magnitude of the vector ( $\vec{p}$ ) is plotted in Fig. 3.23b, c. The use of squares allows for plotting the components as percentage, since  $\frac{p_x^2}{p^2} + \frac{p_y^2}{p^2} + \frac{p_z^2}{p^2} = 100\%$ . From the figure, it can be noted that at the beginning of the flow, the vertical component,  $p_z$ , dominates due to the fact that the motion of the particles is mainly gravity-driven free fall. Then, during the propagation phase, the horizontal component,  $p_x$ , becomes dominant, stabilising itself at around 90%. Finally, when the flow is coming to rest, a surge of vertical component appears. This is due to the presence of decelerating particles exhibiting bouncing in the vertical direction, especially, near the flow forefront. In comparison with Fig. 3.23b, the start point of the chart in Fig. 3.23c looks shifted ahead in time, since it takes some time for the flow front to propagate since gate removal.

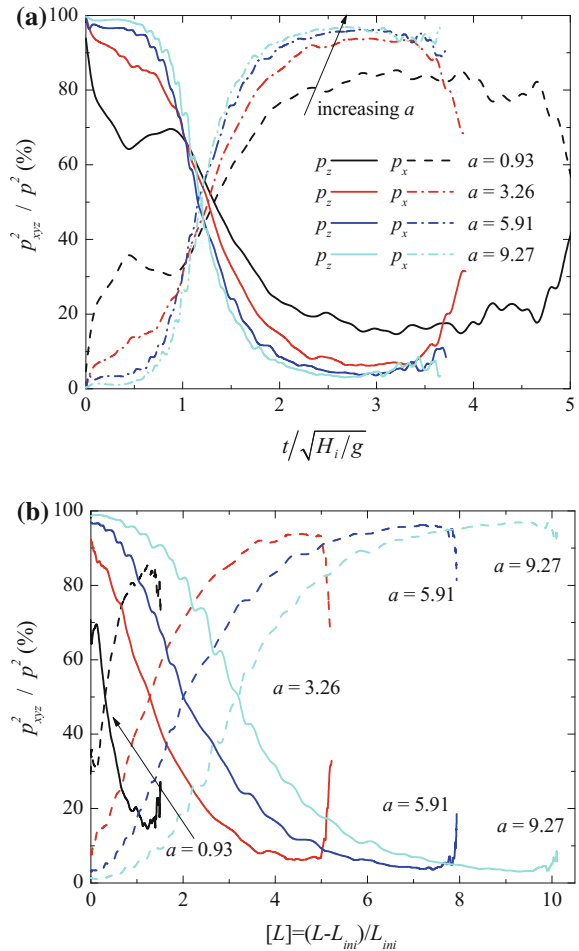
One other study is to analyse the influence of the column aspect ratio on linear momentum. This is an important aspect in order to ascertain how general the observed trends on the linear momentum of the flow are. In Fig. 3.24, the evolution of the vertical and horizontal components of the linear momentum are plotted (as percentage over the magnitude of the vectorial quantity  $\vec{p}$ ) against dimensionless time for columns of various aspect ratios. Similar trends among the curves can be noted. However, in the initial phase of the flow (for  $T < 1.1$ ), the vertical component of momentum increases with the aspect ratio and obviously the opposite are true for the horizontal one. Instead, after  $T = 1.1$ , the vertical component of momentum decreases with the aspect ratio. A possible explanation for the observed aspect ratio dependent trend could be that the gravity-driven free fall of particles, which gives rise to the particle vertical motion, increases with the height of the column whereas the friction between particles, which opposes the horizontal motion of the particles, is independent of the column aspect ratio. In Fig. 3.24b, the components of the momentum are plotted against run-out distance.

### 3.4.4 Flux of Kinetic Energy

To assess the vulnerability of existing structures hit by a debris flow/avalanche and to design engineering works for the protection of existing structures, two quantities

**Fig. 3.24** Evolution of linear momentum over time for various aspect ratios (with viscous damping):

**a** components of momentum as a percentage of the total momentum against normalized time;  
**b** components of momentum as a percentage of the total momentum against normalized run-out. ‘*x*’ is the direction of flow propagation (dashed curves), ‘*z*’ is the vertical direction (solid curves)



are of interest: energy and momentum. The kinetic energy of the particle flow can be seen as an upper bound on the destructive energy that could be unleashed on the structure impacted by the flow. The amount of kinetic energy transferred from the flow to the structure, depends on how flow and structure interact during the time the structure is impacted by the flow. Hence, the amount of energy released by the flow on the structure is a function of the characteristics of both, flow and structure (for instance the relative stiffness between the two). Also the flow—structure interaction is likely to change over time, for instance due to the development of irrecoverable (plastic) deformations in the structure. So, it is not possible to predict the transfer of energy (and equally of momentum), unless a specific flow and a structure of interest are modelled. Here, however, an analysis of the linear momentum and kinetic energy of the flow, measured at various distances from the initial position of the columns is provided, in order to identify an upper bound on the maximum energy

that may be imparted to structures knocked by debris flows, under the simplifying assumption of disregarding the effects of any structure—flow interactions (Utili et al. 2015).

Considering an imaginary vertical section perpendicular to the direction of horizontal propagation of the flow (see the vertical plane depicted in Fig. 3.25), the flow mass transiting through such a section is a function of time. This is nil until the front reaches the position, then it increases gradually, then decreases and eventually becomes nil again once the flow comes to a stop. In the following analyses, five locations along the flow path, shown in Fig. 3.26, are considered. Each location is identified by a letter.

A convenient measure of the maximum energy transferred from the flow to the impacted structure is the flux of kinetic energy. This is evaluated as follows: for a given location of interest, the kinetic energy of the particles passing through the vertical plane oriented in the direction perpendicular to the flow, is recorded during a specified time interval  $\Delta t$  and their total kinetic energy,  $\Delta E$ , is evaluated. The flux of kinetic energy through the plane is given by the ratio,  $\Delta E/\Delta t$  a quantity with dimension of power. It is convenient to normalise this quantity, so that a comparison of fluxes between columns of various sizes can be made. A simple way of doing so is to normalise both numerator ( $\Delta E$ ), and denominator ( $\Delta t$ ). Thus, the normalized flux of energy is defined as:

$$P \equiv \frac{\Delta E}{E_0} \left/ \frac{\Delta t}{\sqrt{H_i/g}} \right. \quad (3.13)$$

Substituting  $E_0$  from Eq. (3.11) into Eq. (3.13) and rearranging, Eq. (3.13) is rewritten as:

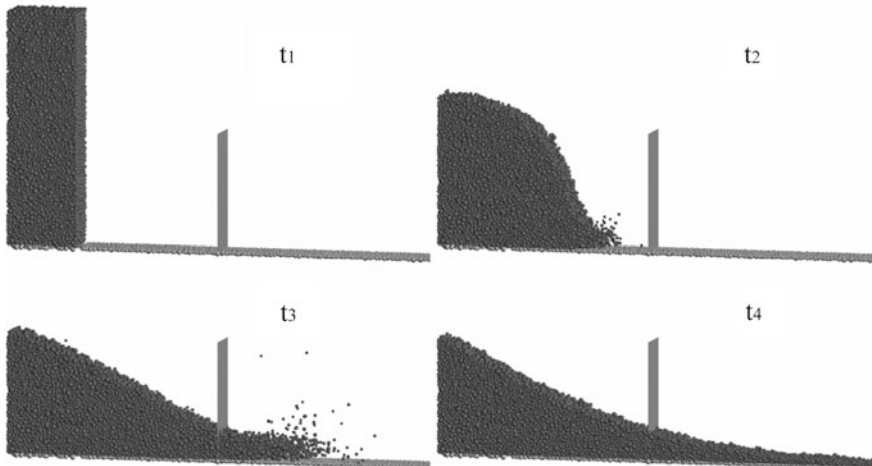


**Fig. 3.25** Schematic view of granular flows past a structure

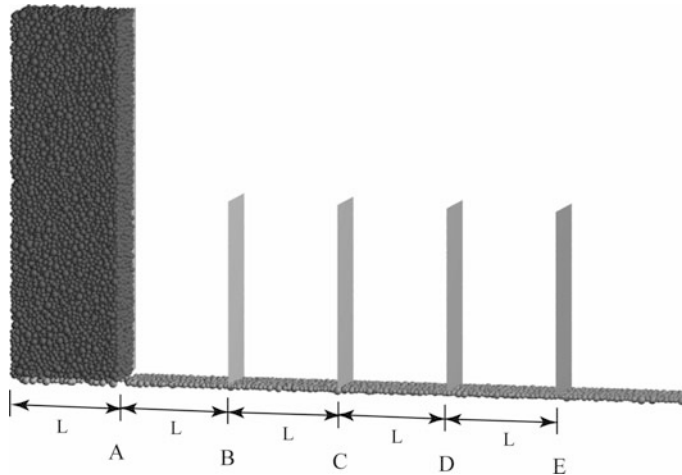
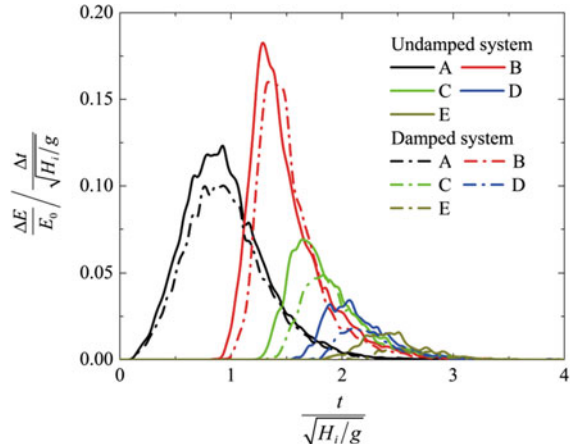


**Fig. 3.26** Location of the sections for the granular flow measurement along the flow path

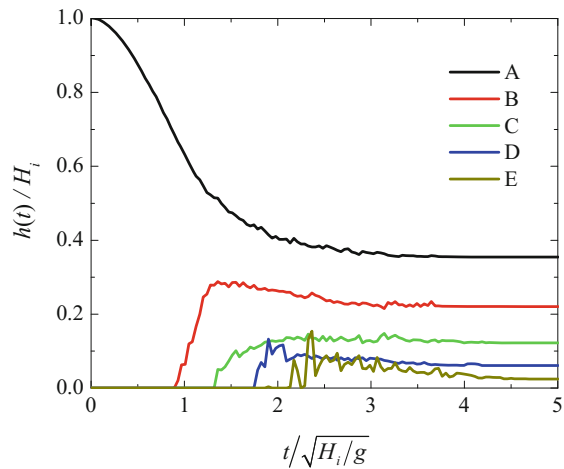
$$P = \frac{\Delta E}{\Delta t} \cdot \frac{2}{M \sqrt{g^3 H}}. \quad (3.14)$$

Equation (3.14) makes clear that  $\frac{2}{M \sqrt{g^3 H}}$  is the multiplying factor to normalize the flux  $\Delta E/\Delta t$ . The flux represents the maximum energy that can be transferred from the flow to the impacted structure. In fact, if all the energy were to be transferred away, the flow would be suddenly deprived of all its kinetic energy and therefore it would come to a stop, which is evidently an unrealistic scenario. In reality, only a portion of the energy is lost in the interaction with the structure that will cause the flow to slow down but not to stop. So,  $P$  can be thought of, as an upper bound on the maximum destructive power that the flow may impart on the impacted structure. In Fig. 3.27a, the flux of kinetic energy at the selected locations is plotted versus dimensionless time. It can be noted that the section with highest flux is *B*. Obviously, the fluxes in the case damping is present are smaller than the case of un-damped flow. An interesting finding is the fact that the peak takes place at a different time, with the time of peak for the damped system shifting progressively ahead of the peak time for the un-damped one. Also, the difference of value between the peaks for the damped and un-damped systems increases with the distance of the section investigated from the column initial position reaching up to 50% of the peak value for the un-damped system. Figure 3.27b illustrates the evolution of the height of the granular mass at different locations. From the figure, it

**Fig. 3.27** Evolution of the flux of destructive energy and height of debris mass



(a) Flux of kinetic energy at different locations ( $a = 3.26$ )



(b) Height of flow at different locations ( $a = 3.26$ )

can be concluded that the further the location is away from the slope source region, the lower the height of the final granular mass is.

Figure 3.28 illustrates the evolution of the flux of kinetic energy for different column aspect ratios. From the figure, it can be observed the position of the section where the flux is highest depends on the aspect ratio. For instance, in the case of small aspect ratios (e.g.  $a = 0.93$ ), the peak flux of destructive energy at location A is the largest, with only a small amount of particles travelling to locations further down section B. For intermediate aspect ratios (e.g.  $a = 3.26, 5.91$ ), the largest flux takes place at location B. For large aspect ratios (e.g.  $a = 9.27$ ), the largest flux occurs again at section A.

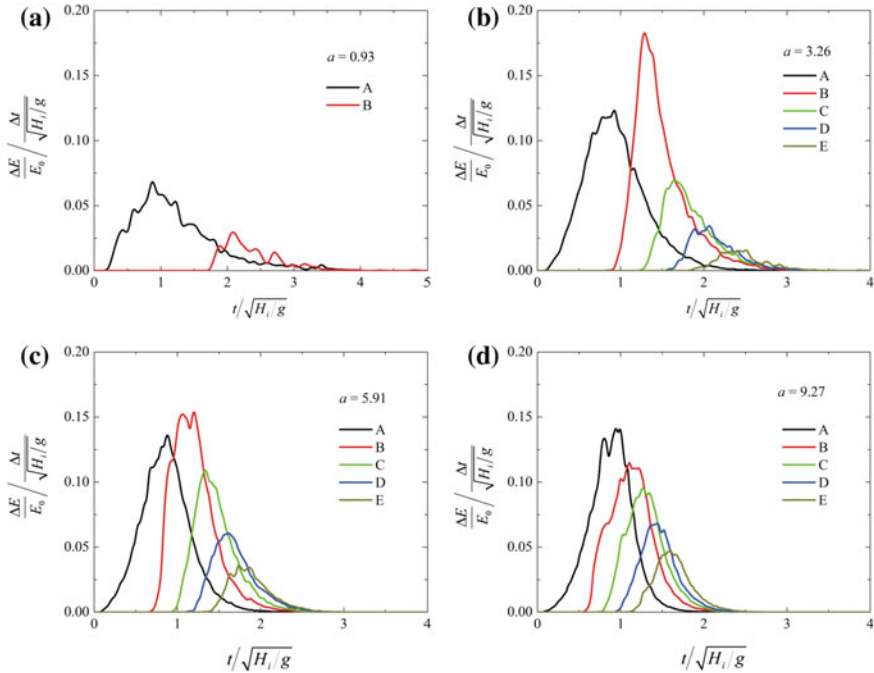


**Fig. 3.28** Evolution of the flux of destructive energy for different granular columns

### 3.4.5 Distribution of Kinetic Energy and Linear Momentum

To be able to design protective structures as effectively as possible, the spatial distribution of kinetic energy and momentum over the depth of the considered section are also needed. Considering section B, the depth of the flow,  $h(t)$ , has been split into five parts and the flux of kinetic energy through the section for each part is calculated so as to obtain a vertical profile of the flux of kinetic energy (see Fig. 3.29a). Looking at the figure, it emerges that the profile of the flux is initially bilinear, with the maximum flux at middle height of the column, then the flux evolves into a linear profile whose amplitude progressively reduces over time until becoming nil. The bilinear distribution points out to the presence of an uppermost layer of particles in an agitated loose state, which, after some time, consolidates so that a linear distribution is obtained. The presence of this layer of loose material is confirmed by the calculation of the profile of mass rate in the unit of time in the section (see Fig. 3.29c).

A convenient measure of the maximum momentum that could be transferred by the flow to the impacted structure is the flux of linear momentum over time. Analogously to the flux of kinetic energy, it is useful to evaluate the linear momentum of the particles passing through the vertical section of interest,  $\Delta p$ , during a specified time interval  $\Delta t$ . The flux of linear momentum through the whole

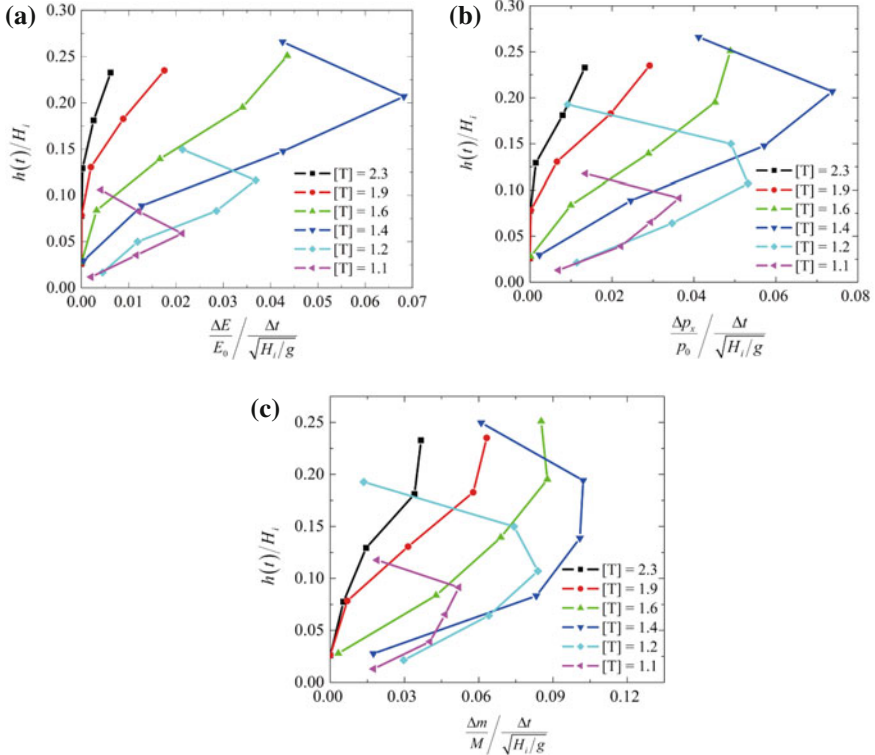


**Fig. 3.29** Profile of kinetic energy, momentum and mass at plane  $B$ . **a** Profile of kinetic energy flux at location  $B$  for different times ( $a = 3.26$ ). **b** Profile of normalised momentum along the plane  $B$  at different times ( $a = 3.26$ ). ( $\Delta p_x$  is the summation of momentum at a specific region;  $p_0 = M \cdot \sqrt{H_i g}$  is the average momentum of the granular system, with  $M = \sum_i^N m_i$  being the total mass of grains in the system,  $N$  being the total number of grains in the system). **c** Profile of granular mass moving through the plane  $B$  at different times ( $a = 3.26$ ) ( $\Delta m$  is the mass flowing through the plane  $B$ ;  $M$  is the total mass of grains in the system)

section or parts of it, is given by  $\Delta p/\Delta t$ , a quantity with the dimensions of force (so, it is called  $F$ ). It is convenient to normalize this quantity so that comparison of fluxes between columns of various sizes can be carried out. A simple way of doing this is by normalizing both numerator and denominator. So, the normalized linear momentum of the flow in the unit of time is defined as:

$$F_{x,y,z} \equiv \frac{\Delta p_{x,y,z}}{p_0} \left/ \frac{\Delta t}{\sqrt{H_i/g}} \right., \quad (3.15)$$

with  $p_0$  being an average linear momentum for the flow here defined in Eq. (3.12). Rearranging Eq. (3.15) can also be written as:

$$F_{x,y,z} = \frac{\Delta p_{x,y,z}}{\Delta t} \cdot \frac{1}{Mg}. \quad (3.16)$$

Equation (3.16) makes it clear that  $1/Mg$  is the multiplying factor to normalize the momentum going through the plane in the unit of time. In terms of the flux value of the momentum at various sections in time, similar figures as those obtained for the flux of kinetic energy are obtained (Figs. 3.27 and 3.28) which are not reported here. To locate critical sections and times of interest one of the two fluxes, either the flux of kinetic energy or of momentum, are enough. However, it is of interest to practitioners appointed with designing engineering works for the mitigation of the flow hazard, to know the value of the flux of linear momentum over depth in order to have an idea of the distribution of the pressure that can act on the structure. In Fig. 3.29b, the distribution of the horizontal component of the linear momentum along the direction of flow propagation,  $F_x$ , over depth and is plotted against time. As it can be expected, the same shape of the profile as the profile of the flux of kinetic energy is found.

### 3.4.6 Evolution of Force Chains

The force chains within a granular sample illustrate the distribution of contact forces and their magnitudes. Based on the plots of force chains, it is very convenient to study the distribution and evolution of contact forces within a granular assembly during the granular flow. In these graphs, straight lines are used to connect the centres of each pair of particles in contact. The thickness of these lines represent the magnitudes of the normal contact forces, while the tangential direction of these curves at a specific point corresponds to the orientation of the contact force vector, as shown in Fig. 3.30. In the current analyses, the contact forces ( $F_c$ ) are normalized by the characteristic force acting on a single particle, as:

$$[F] = \frac{F_c}{(1 - n)\rho_s g H_i D^2} \quad (3.17)$$

At  $[T] = 0.0$ , the sample is densely packed due to consolidation under self-weight. The normal contact forces increase linearly with the height and the orientations direct mainly vertically. When the confining wall is removed, the contact forces near the front surface are suddenly released, and their magnitudes decrease quickly to smaller than 0.25. The force chains in the inner part of the model incline towards the fixed back wall. As grains in the upper region fall downwards, the force chains previously existing there disappear, while new force chains would build up in the flowing front. Discrete lines exist near the granular surface, in which some particles bounce up in the air and collide with each other. At  $[T] = 4.24$ , the granular materials stop moving, forming a static deposit on the floor. The force chains have triangular prism shapes, with small contact forces near the surface and large contact forces in the inner part of the deposits.

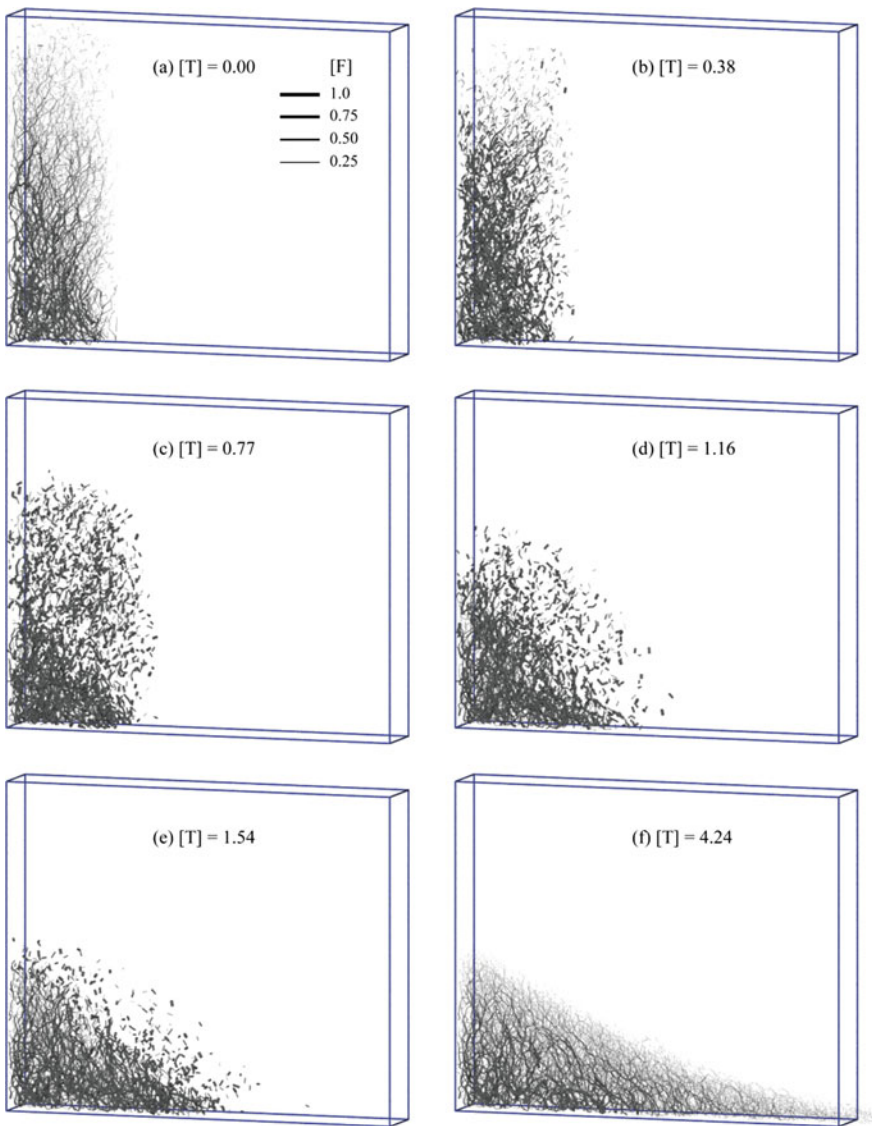


**Fig. 3.30** Force chains within the granular assembly during the flow

### 3.4.7 Distribution of Stress

In accordance with the analyses of the continuum mechanics, the distribution and evolution of the major principal stresses of the granular assembly is plotted in Fig. 3.31. The magnitude of the stress is normalized by the characteristic stress of the granular sample, as:

$$[\sigma] = \frac{\sigma}{(1-n)\rho_s g H_i} \quad (3.18)$$

At the beginning of the simulation, the stress distributes non-uniformly within the sample, such that it increases gradually along the depth of the granular column due to the self-weight of grains. After removing the frontal confining wall, the granular materials fall downwards quickly. The inertial forces exerted by the upper grains would place additional loads on the lower grains, which in turn increase the stresses in the bottom region. Near the slope surface, there are few contacts between grains, thus, the magnitudes of stresses are very small. The maximum stress occurs in the static granular pile region. After  $[T] = 4.29$ , a static granular deposit is formed on the horizontal floor, with the normalized stresses smaller than 0.25.

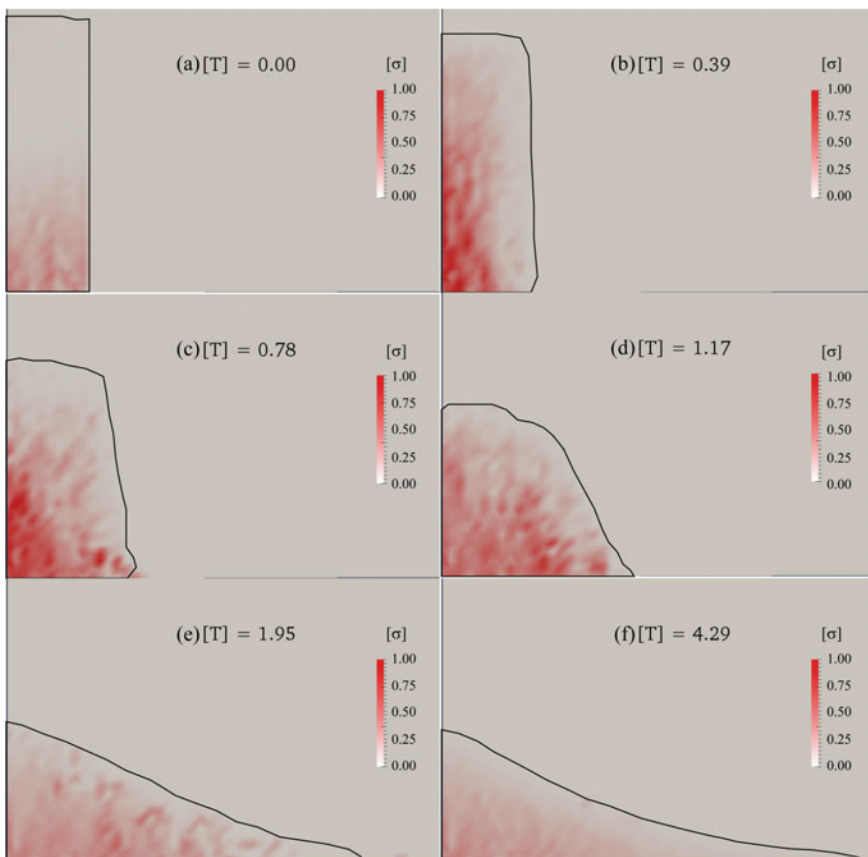


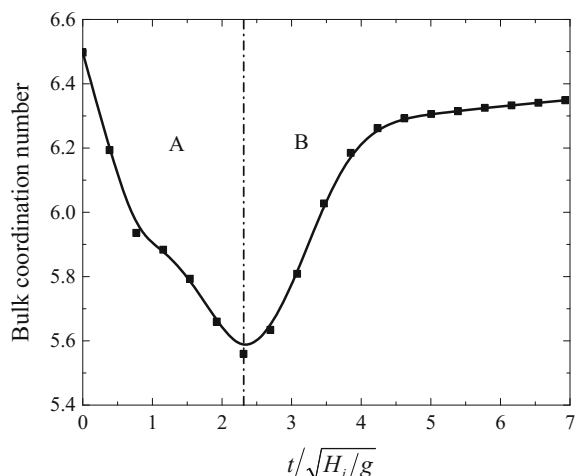
**Fig. 3.31** Evolution of stress within the sample (the *black curves* represent granular profiles)

### 3.4.8 Distribution of Coordination Number

As discussed in Chap. 2, the coordination number of a granular assembly can be used to quantify its packing state. A dense granular sample normally has a large bulk coordination number, while a loose sample has a very small bulk coordination number. In addition, the spatial distribution and variation over time of the bulk coordination number is a good indication of the bulk density of the granular assembly. Figure 3.32 illustrates the evolution of bulk coordination number of the granular assembly during the simulation. It can be observed that two distinct regions of the evolution of bulk coordination number can be identified. Once released, the initial densely packed granular mass falls downwards and spreads horizontally. In this process, the granular assembly would expand and the corresponding bulk coordination number decreases gradually from its maximum value of 6.50 to the minimum value of 5.6 in region A. At time  $[T] = 2.3$ , the minimum value of bulk coordination number occurs, and it corresponds to the time for the occurrence of maximum kinetic energy of the system in Fig. 3.20. After this point, the solid grains move slowly along the ground floor. In region B, the system gradually comes to a rest and a relatively dense granular deposit builds up on the ground floor. The corresponding coordination number increases gradually to the final stable value of 6.3.

Figure 3.33 shows the distribution and evolution of bulk coordination numbers over time within the sample. The vertical and horizontal boundaries delimit the dimensions of the model, while the coloured blocks represent the bulk coordination numbers of grains in that region. The initial densely packed sample is found at time  $[T] = 0.0$ , when the bulk coordination numbers are larger than 6.5 within the sample. After the initiation of granular flow, the middle and upper grains descend downwards and spread horizontally, leading to intensive shearing on an inclined

**Fig. 3.32** Evolution of bulk coordination number within the sample



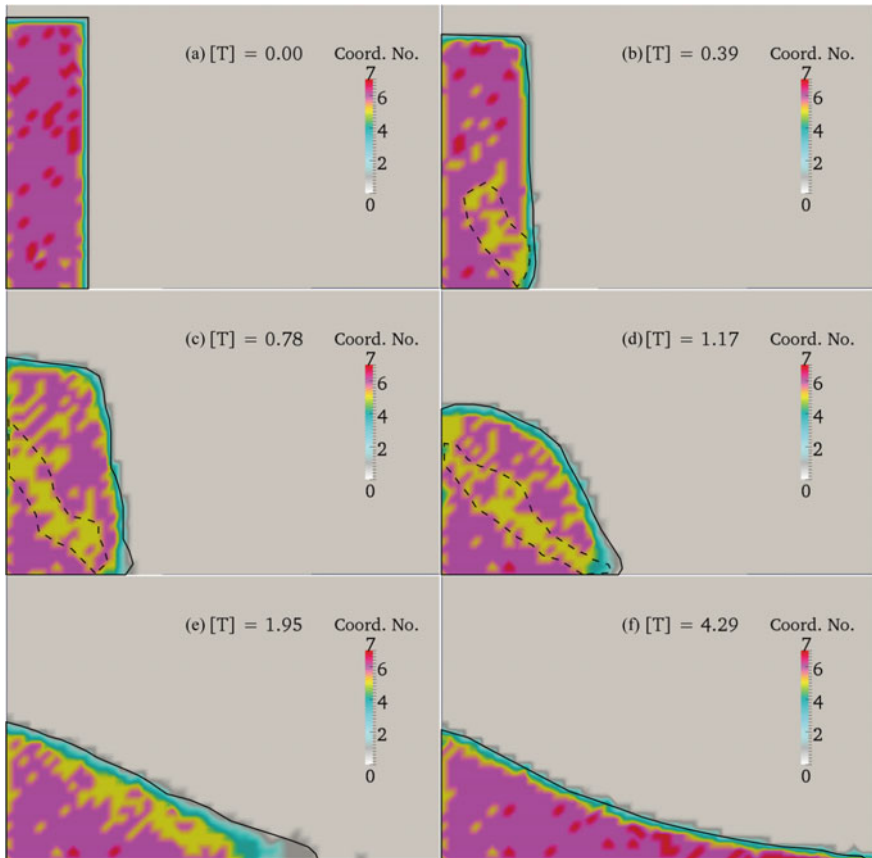


**Fig. 3.33** Distribution of bulk coordination numbers within the sample

surface between the static and moving grains. Within the shearing zone, the coordination number is relatively small, showing a dilation region of the granular assembly. During the simulation, the dilation zone locates approximately parallel to the inclined upper surface of the static granular pile region, as illustrated by regions enclosed by dashed curves. Near the surface of the granular mass, solid grains are in dynamic motion with the bulk coordination numbers smaller than 2.

### 3.4.9 Destination of Surface Grains

During the granular flow, solid grains with the highest mobility can run a long distance, stretching into very thin and wide layers at the outermost region on the floor. In the current analyses, the grains travelling to the outermost region are

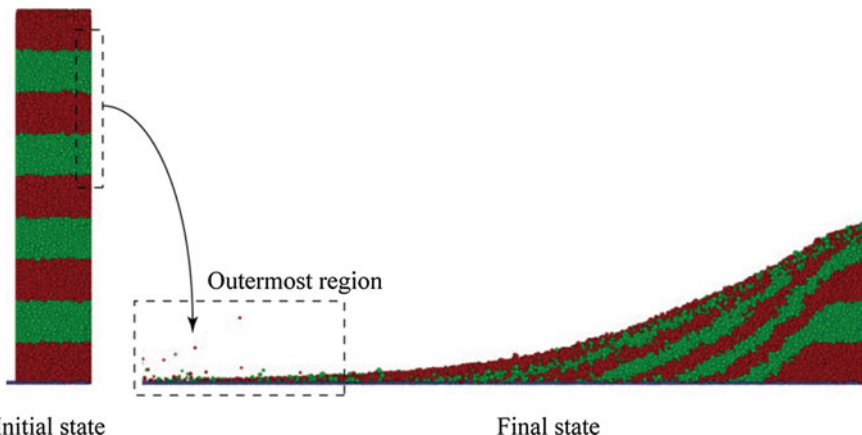


**Fig. 3.34** Destination of surface grains

identified as the most hazardous solid materials, as they have the highest mobility during the flow. By investigating the locations of these grains in the initial granular column, a general understanding of the major hazardous zones of the slope can be obtained (see Fig. 3.34). This is of special importance for identifying the hazardous regions of a potential unstable slope.

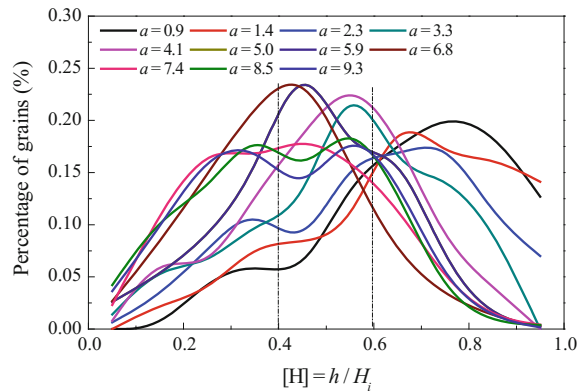
This problem has been studied in the axisymmetric and two-dimensional conditions by Thompson and Huppert (2007) who used a number of coloured grains as markers in different layers of the initial granular column and then traced the movement of these grains during granular flows. At the end of the experiment, they singled out these coloured grains at the outermost point of the deposit and mapped their positions back into the original column. By tracing the mobilized grains, the potential hazardous region of the initial granular assembly can be identified. In this research, instead of studying the outermost grains of the final deposit, focus has been placed on a region that contains a reasonable number of grains near the outermost point. As discussed in Sect. 3.1, this region contains solid mass amounting to 1% of the total mass of grains in the model. To quantify the grain locations, a normalized height of an individual particle has been defined as:

$$\bar{H} = \frac{h_i}{H}, \quad (3.19)$$

where  $h_i$  is the height of particle  $i$  in the initial column;  $H$  is the height of the initial column.

Figure 3.35 shows the distribution of hazardous grains in the initial granular column. It can be observed that for columns with aspect ratios smaller than 3.0, the majority of hazardous grains come from the top of the initial granular column, while for columns with aspect ratios larger than 3.0, the hazardous grains mainly come from a region of  $\bar{H} \in [0.40, 0.60]$ . When compared with the conclusion made by

**Fig. 3.35** The mapped initial height of grains in the outermost region of granular deposits



Thompson and Huppert (2007), the current numerical results of short granular columns can match the experimental ones very well, in which the hazardous grains come from a height in the range of  $0.67 \pm 0.07$ . However, for granular columns with large aspect ratios, the hazardous grains mainly come from the middle of the initial granular assembly.

### 3.4.10 Influence of Air Viscous Force

The DEM simulations discussed in the previous sections have ignored the influence of air viscous drag force, as it is expected to have a much smaller influence on granular flows than that of the inter-particle contact forces. However, quite few theoretical bases have been found to justify the ignorance of the air viscous drag forces. The current section will investigate into this problem and give out reasonable justifications.

An accurate evaluation of air viscous drag force requires the use of the DEM–CFD coupling algorithm (see also Chap. 4), in which the governing equations for the DEM and CFD can be resolved accurately. This process is computationally very expensive for simulations of granular column collapse consisting of a large number of particles. As a preliminary study, the current research only utilizes a modified version of air viscous drag force model, in which the air is assumed to be static throughout the simulation. Based on this assumption, the air viscous drag force ( $\mathbf{F}_d$ ) acting on a single particle is calculated as:

$$\mathbf{F}_d = \frac{1}{2} C_d \rho_f \frac{\pi d_p^2}{4} |\mathbf{V}| \mathbf{V} + \rho_f g \frac{\pi d_p^3}{6}, \quad (3.20)$$

where  $\rho_f = 1.204 \text{ kg/m}^3$  is the air density at 20 °C, 1.0 atm;  $d_p$  is the particle diameter;  $V$  is the particle velocity;  $C_d$  is the drag force coefficient as evaluated by Eq. (3.21).

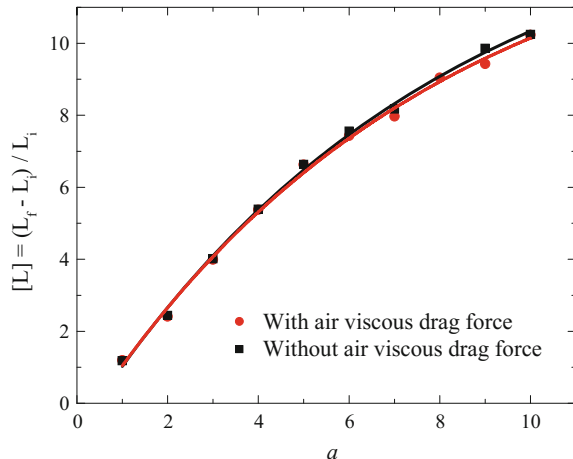
$$C_d = \frac{24}{\overline{\text{Re}}} \left( 1 + 0.150 \overline{\text{Re}}^{0.681} \right) + \frac{0.407}{1 + \frac{8710}{\overline{\text{Re}}}}, \quad (3.21)$$

where  $\overline{\text{Re}}$  is the “pseudo Reynolds number” defined as:  $\overline{\text{Re}} = \rho_f d_p |V| / \mu$ , with  $\mu = 1.702 \text{ Pa s}$ , being the viscosity of air at 20 °C, 1.0 atm.

Figure 3.36 compares the normalized run-out distance of granular columns from two series of simulations under conditions with and without considering the air viscous drag forces. It can be concluded that the air viscous drag force has very little influence on the motion of grains during granular flows. When the column aspect ratio is smaller than 7, numerical results obtained from the two sets of simulations are identically the same, while slight discrepancy is observed at larger aspect ratios in which the air viscous drag forces are considerably high due to relatively large velocities of solid particles.

In this study, the air has been assumed to be static during the simulation. However, this is not true for real solid–fluid systems, in which air can move together with particles due to the viscous drag forces. As a result, the relative velocity between particle and air in simulations of real landslides would be smaller than that used in the preliminary estimation discussed above. Thus, the air viscous drag forces used in this research can be regarded as the upper bound of air resistant forces acting on solid grains. According to Fig. 3.36, the air viscous drag force has a very small influence on grain motions for various granular columns. Thus, the numerical results discussed in the previous sections without using air viscous drag forces are validated to be acceptable for this research. In addition, the implementation of Eq. (3.20) in the DEM code can reduce the computational cost

**Fig. 3.36** Comparison between simulations with and without air viscous drag forces



significantly when compared with the simulations using the DEM–CFD coupling program (e.g. see Chap. 5), because there is no need to transfer data between different codes during the simulation. The proposed air viscous drag force model in this study is superior to the majority of air damping force models used in the literature with a clear physical meaning. As this model only considers the motion of solid phase, it is thus called the “semi-coupling” model.

### 3.5 Conclusions

This chapter presents a numerical investigation of dry granular flows generated by the collapse of prismatic columns via 3D DEM simulations under plane strain conditions. This type of analysis showcases the potential of the DEM to investigate the phenomenology of dry granular flows and to gather unique information currently unachievable by experimentation. By means of dimensional analysis, the governing parameters of the problem were identified. Then, the influence of key variables of the problem was analyzed. The main results are summarized as below:

- (i) Different regimes of granular motion have been observed, depending on the initial aspect ratios. The DEM results qualitatively match the FEM analyses by Crosta et al. (2009) and the experimental results by Lube et al. (2005). The granular material slides along a plane which approximately corresponds to the active failure plane of the column in agreement with Rankine’s theory.
- (ii) Quantitative relationships between the column aspect ratio and normalized run-out distance and deposit height were established. Using the rolling resistance model, i.e. assigning a moment—relative rotation contact law, the DEM simulations, give rise to run-out distances, deposit height which match well the available numerical and experimental results.
- (iii) A detailed analysis of how energy is dissipated by granular flows was performed from which emerges that most of the energy of the columns is dissipated by inter-particle friction, with frictional dissipation increasing with the column aspect ratio. Also, the translational and rotational components of the kinetic energy of the flows, associated to particle rotational and translational motions, respectively, were monitored during the simulations. It is found that the rotational component is negligible in comparison with the translational one; hence in order to calculate the destructive power of a debris flow slide, only the translational contribution of the kinetic energy is relevant.
- (iv) A methodology is presented to calculate the flux of kinetic energy over time carried by the granular flow through any vertical section of interest. This can be related to the energy released by landslide induced granular flows impacting against engineering structures under the simplifying assumption of neglecting all structure–flow interactions. This represents the first step towards achieving a computational tool quantitatively predicting the

destructive power of a given flow at any location of interest along its path. This could be useful for the design of engineering works for natural hazard mitigation. To this end, the distribution of the linear momentum of the flow over depth was calculated. It emerges that the distribution is initially bilinear, due to the presence of an uppermost layer of particles in an agitated loose state, but after some time it becomes linear. The grains running to the outermost region of the granular deposit mainly originate from a normalized height of  $\bar{H} \in [0.4, 0.6]$  in the initial column.

# Chapter 4

## Introduction to the DEM–CFD Coupling Model

This chapter introduces the DEM–CFD coupling model, and its validation via two well-established case studies: (a) fluid flow through a porous soil sample, and (b) modelling of grain batch sedimentation. The goal of the tests is to examine whether the numerical tool is capable of modelling the behaviour of fluid–solid interactions. The calibrated DEM–CFD coupling model will be used later on to investigate submerged debris flows.

### 4.1 Fluid–Solid Interaction

The interaction force between fluid and particles ( $\vec{f}_{\text{fluid}}$ ) consists of two parts: hydrostatic and hydrodynamic forces (Shafipour and Soroush 2008). The hydrostatic force accounts for the fluid pressure gradient around an individual particle (i.e. buoyancy) (Zeghal and El Shamy 2004; Chen et al. 2011; Kafui et al. 2011), and can be expressed as

$$\vec{f}_b^i = -v_{pi} \nabla p, \quad (4.1)$$

where  $\vec{f}_b^i$  is the hydrostatic buoyant force acting on particle  $i$ ,  $v_{pi}$  is the volume of particle  $i$ ;  $p$  is the fluid pressure.

The hydrodynamic forces acting on a particle are the drag, lift and virtual mass forces. The drag force is caused by the shearing effect of fluid onto the particle, in the direction of the relative velocity between fluid and particle; the lift force is caused by the high fluid velocity gradient-induced pressure difference on the surface of the particle and the virtual mass force is caused by relative acceleration between particle and fluid (Drew and Lahey 1990; Kafui et al. 2002; DEMSolutions 2010). The latter two forces are normally very small when compared to the drag force in simulating fluid flow at relatively low Reynolds numbers

(Kafui et al. 2002). Thus, the lift and virtual mass forces are neglected in the current CFD-DEM coupling model. In this process, the drag force is assumed to act at the particle centre in a direction opposite to the relative velocity between particle and fluid (Guo 2010). In order to quantify the drag force, experimental correlations (Stokes 1901; Ergun 1952; Wen and Yu 1966) and numerical simulations (Zhang et al. 1999; Choi and Joseph 2001; Beetstra et al. 2007) have been reported in the literature. The drag force is calculated as

$$\mathbf{F}_d = \beta(\mathbf{U} - \mathbf{V}) \quad (4.2)$$

where  $\beta$  is the fluid–solid momentum transfer coefficient,  $\mathbf{U}$  and  $\mathbf{V}$  are the velocities of fluid and solid particle, respectively.

The momentum transfer coefficient is derived from the experimental correlations by Ergun (1952) and Wen and Yu (1966), as

$$\beta = \frac{3}{4} \frac{C_d n(1-n)\rho_f}{D} |\mathbf{U} - \mathbf{V}|, \quad (4.3)$$

where  $C_d$  is the drag force coefficient;  $n$  is the porosity of soil sample;  $D$  is the particle diameter, and  $\rho_f$  is the fluid density.

The drag force coefficient is defined in Eq. (4.4), in which the Ergun's correlation is used if the sample porosity is smaller than 0.8, while the Wen and Yu's correlation is used for larger sample porosities.

$$C_d = \begin{cases} \frac{200(1-n)}{n\text{Re}_p} + \frac{1}{3n} & \text{if } n < 0.8 \\ \begin{cases} \frac{24}{\text{Re}_p} \left(1 + 0.15(\text{Re}_p)^{0.687}\right) n^{-2.65} & \text{if } \text{Re}_p < 1000 \\ 0.44 n^{-2.65} & \text{if } \text{Re}_p \geq 1000 \end{cases} & \text{if } n \geq 0.8 \end{cases} \quad (4.4)$$

where  $\text{Re}_p = \rho_f d |\mathbf{U} - \mathbf{V}| / \mu$  is the Reynolds number defined at the particle size level, with  $\mu$  being the fluid viscosity.

As Ergun's equation is obtained by experiments of fluidization on dense granular beds, it is not applicable to dilute granular sample (Jackson 2000). For loose granular samples with porosities larger than 0.8, the Wen and Yu's correlation should be used. As a result, the definition of drag force coefficient in Eq. (4.4) would cause discontinuity in calculating drag forces if the sample porosity varies from the intermediate to large values during the simulation (Syamlal 1987; Kafui et al. 2002). To get rid of this problem, the drag force model proposed by Di Felice (1994) is used in this research. The drag force is defined as

$$F_{di} = \frac{1}{2} C_d \rho_f \frac{\pi D^2}{4} |\mathbf{U} - \mathbf{V}| (\mathbf{U} - \mathbf{V}) n^{-\chi+1} \quad (4.5)$$

The porosity correction function  $n^{-(\chi+1)}$  represents the influence of the concentration of granular materials on the drag force. The term  $\chi$  is defined as

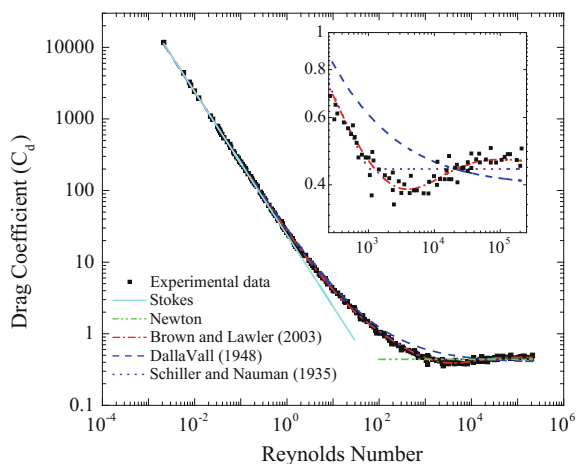
$$\chi = 3.7 - 0.65 \exp \left[ -\frac{(1.5 - \log_{10} \text{Re}_p)^2}{2} \right] \quad (4.6)$$

There are several definitions of drag force coefficient in the literature (DallaVall 1948; Brown and Lawler 2003; Beetstra et al. 2007). A comparison between these correlations and the experimental data is given in Table 4.1 and Fig. 4.1. According to Fig. 4.1, it can be observed that the Stokes' and Newton's correlations can predict accurate drag force coefficients for fluid flows at very small and large Reynolds numbers, respectively. The correlations by Schiller and Nauman (1935), DallaVall (1948) and Brown and Lawler (2003) can give out reasonable drag force coefficients for the Reynolds number in the range of  $[10^{-2}, 100]$  and  $[10^4, 10^5]$ . However, in the range of  $[100, 10^4]$ , only the correlation of Brown and Lawler (2003) can match the experimental data well. Thus, the drag force coefficient has been implemented in the current DEM–CFD coupling method as

**Table 4.1** Some well-defined correlations of drag force coefficient

Stokes (1880)	$\frac{24}{\text{Re}_p}$
Newton (Inertial)	0.44
Schiller and Nauman (1935)	$\begin{cases} \frac{24}{\text{Re}_p} (1.0 + 0.15\text{Re}_p^{0.687}) & \text{Re}_p \leq 1000 \\ 0.44 & \text{Re}_p > 1000 \end{cases}$
DallaVall (1948)	$\left[ 0.63 + \frac{4.8}{\sqrt{\text{Re}_p}} \right]^2$
Brown and Lawler (2003)	$\frac{24}{\text{Re}_p} \left( 1 + 0.150\text{Re}_p^{0.681} \right) + \frac{0.407}{1 + 8710/\text{Re}_p}$

**Fig. 4.1** Drag coefficients from various correlations and experimental results



$$C_d = \frac{24}{\text{Re}_p} \left( 1 + 0.150 \text{Re}_p^{0.681} \right) + \frac{0.407}{1 + \frac{8710}{\text{Re}_p}} \quad (4.7)$$

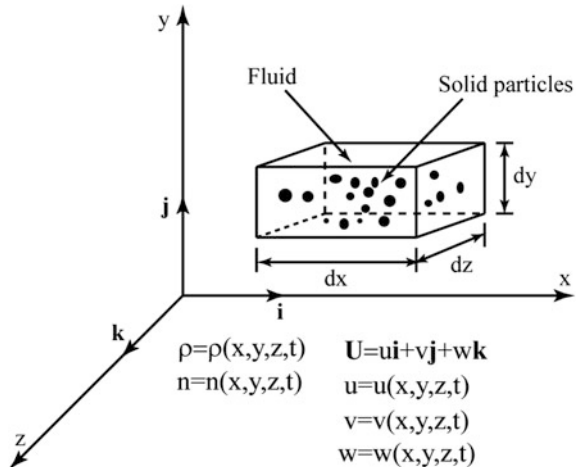
Therefore, the force exerted by fluid on a single solid particle is expressed as

$$\overrightarrow{f_{\text{fluid}}} = -v_{pi} \nabla p + \frac{1}{2} C_d \rho_f \frac{\pi d^2}{4} |\mathbf{U} - \mathbf{V}| (\mathbf{U} - \mathbf{V}) n^{-\chi+1} \quad (4.8)$$

## 4.2 Governing Equations of Fluid Flow

In the Computational Fluid Dynamics (CFD), the governing equations of fluid flow in a fluid–solid mixture system are derived from the theory of multiphase flow (Brennen 2005). The mixture system consists of fluid and solid particles and it is assumed that the solid materials are well mixed in the fluid so that the system can be regarded as homogeneous in all directions. As shown in Fig. 4.2, the fluid density ( $\rho$ ), the three components of fluid velocity ( $u, v, w$ ) and the fluid volume fraction ( $n$ ) are all functions of position and time. The discussion below will focus on the mass and momentum conservations of fluid flow in the mixture system, in which the fluid volume is taken as the product of  $n$  and the mesh element volume ( $dx dy dz$ ). The open source CFD code OpenFOAM (OpenCFD 2004) was modified and employed for the simulations presented herein.

**Fig. 4.2** The infinitesimally small element of the fluid–solid system



### 4.2.1 Fluid Mass Conservation Law

Figure 4.3 illustrates the fluid flow through faces of a mixture element. The fluid velocity has been averaged to make it homogenous within the control volume (Anderson and Jackson 1967). The average fluid velocity is defined as  $\bar{U} = n\mathbf{U} = nu \vec{i} + nv \vec{j} + nw \vec{k}$  over the control volume, which represents the superficial fluid velocity in the fluid mesh cell.

The equation of mass conservation for fluid in the  $x$  direction of this element is derived as

$$\left[ \rho n u + \frac{\partial(\rho n u)}{\partial x} dx \right] dy dz - (\rho n u) dy dz = \frac{\partial(\rho n u)}{\partial x} dx dy dz \quad (4.9)$$

Similarly, the net out flow in the  $y$  and  $z$  directions can be derived as  $\frac{\partial(\rho n v)}{\partial y} dx dy dz$  and  $\frac{\partial(\rho n w)}{\partial z} dx dy dz$ , respectively. Thus, the total net outflow of the fluid element is

$$\left[ \frac{\partial(\rho n u)}{\partial x} + \frac{\partial(\rho n v)}{\partial y} + \frac{\partial(\rho n w)}{\partial z} \right] dx dy dz = \nabla \cdot (\rho n \mathbf{U}) dx dy dz \quad (4.10)$$

On the other hand, the time rate change of fluid mass is expressed as

$$\frac{\partial(\rho n dx dy dz)}{\partial t} = \frac{\partial(\rho n)}{\partial t} (dx dy dz) \quad (4.11)$$

According to the mass conservation law, the net fluid mass outflow must be equal to the time rate decrease of fluid mass inside the element. If the decreasing rate of fluid mass is defined as negative, the mass conservation law can be expressed as

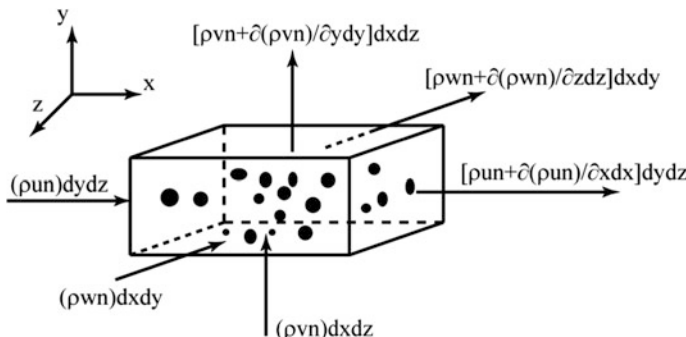


**Fig. 4.3** Fluid flow through faces of the mesh element

$$\frac{\partial(\rho n)}{\partial t} + \nabla \cdot (\rho n \mathbf{U}) = 0 \quad (4.12)$$

As a comparison, the continuity equation of pure fluid ( $n = 1$ ) (Anderson 1995) is given as

$$\frac{\partial(\rho)}{\partial t} + \nabla \cdot (\rho \mathbf{U}) = 0 \quad (4.13)$$

#### 4.2.2 Fluid Momentum Conservation Law

The forces acting on a fluid element (in the  $x$ -direction) is sketched in Fig. 4.4. According to the Newton's second law of motion, the net forces acting on the fluid element are equal to the product of fluid mass and acceleration. For simplicity, the derivation hereinafter presented only considers the momentum equation in the  $x$ -direction, as

$$F_x = m \times a_x \quad (4.14)$$

In general, there are two different types of forces acting on the fluid element: (a) body force, such as gravity, drag, electric and magnetic forces; (b) surface force, such as the pressure, viscous shear and normal forces acting on the element surface (Anderson 1995).

Without the electric and magnetic forces, the body force can be written as

$$\vec{F}_b = \vec{f}_g + \vec{f}_{\text{fluid}} \quad (4.15)$$

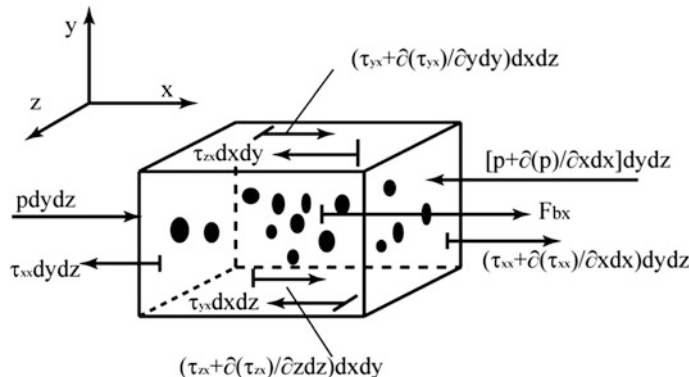


**Fig. 4.4** The forces acting on the surface of fluid element

in which  $\vec{f}_g$  is the gravity force defined as  $\vec{f}_g = n\rho\vec{g} \frac{dxdydz}{dxdydz}$ ; and  $\vec{f}_{\text{fluid}}$  is the interaction force between fluid and solid particles.

Thus, the body force per unit volume is expressed as

$$\begin{aligned}\vec{f} &= n\rho\vec{g} + \frac{\sum_{i=1}^N \left( v_{pi} \nabla p - v_{pi} \nabla \cdot \tau + \vec{F}_{di} \right)}{dxdydz} \\ &= n\rho\vec{g} + (1-n)\nabla p - (1-n)\nabla \cdot \tau + \frac{\sum_{i=1}^N \vec{F}_{di}}{dxdydz}\end{aligned}\quad (4.16)$$

where  $N$  is the total number of solid particles within the volume. Let  $\vec{f}_d = \sum_{i=1}^N \vec{F}_{di} / dxdydz$  be the drag force per unit volume, then  $\vec{f} = n\rho\vec{g} + (1-n)\nabla p - (1-n)\nabla \cdot \tau + \vec{f}_d$ .

The surface forces are forces directly acting on the surface of the fluid element. There are two sources of surface force: (a) the hydraulic pressure imposed by the outside fluid surrounding the fluid element, and (b) the shear and normal stresses acting on the surface (also imposed by the outside fluid by means of viscous friction). The unbalanced surface force acting on the fluid element in the  $x$ -direction is

$$\begin{aligned}F_s &= \left[ p - \left( p + \frac{\partial p}{\partial x} dx \right) \right] dydz + \left[ \left( \tau_{xx} + \frac{\partial \tau_{xx}}{\partial x} dx \right) - \tau_{xx} \right] dydz \\ &\quad + \left[ \left( \tau_{yx} + \frac{\partial \tau_{yx}}{\partial y} dy \right) - \tau_{yx} \right] dx dz + \left[ \left( \tau_{zx} + \frac{\partial \tau_{zx}}{\partial z} dz \right) - \tau_{zx} \right] dx dy \\ &= \left[ -\frac{\partial p}{\partial x} + \frac{\partial \tau_{xx}}{\partial x} + \frac{\partial \tau_{yx}}{\partial y} + \frac{\partial \tau_{zx}}{\partial z} \right] dx dy dz\end{aligned}\quad (4.17)$$

From Eqs. (4.16) and (4.17) the total force in the  $x$ -direction is summarized as

$$F_x = \left\{ -n\nabla p_x + n \left[ \frac{\partial \tau_{xx}}{\partial x} + \frac{\partial \tau_{yx}}{\partial y} + \frac{\partial \tau_{zx}}{\partial z} \right] + n\rho g_x + f_{dx} \right\} dx dy dz \quad (4.18)$$

The acceleration of fluid flow in the  $x$ -direction is calculated as the material derivative of flow velocity

$$a_x = \frac{Du}{Dt} = \frac{\partial u}{\partial t} + \mathbf{U} \cdot \nabla u \quad (4.19)$$

The term  $\frac{\partial u}{\partial t}$  is the time rate change of momentum, while  $\mathbf{U} \cdot \nabla u$  is the net flux of the momentum out of the mixture element in the  $x$  direction. Thus, Eq. (4.10) is rewritten as

$$\rho n \frac{\partial u}{\partial t} + \rho n \mathbf{U} \cdot \nabla u = -n \nabla p_x + n \left[ \frac{\partial \tau_{xx}}{\partial x} + \frac{\partial \tau_{yx}}{\partial y} + \frac{\partial \tau_{zx}}{\partial z} \right] + n \rho g_x + f_{dx} \quad (4.20)$$

The following transformations can be applied to the two terms on the left-hand side of Eq. (4.20) in the analysis, as

$$\rho n \frac{\partial u}{\partial t} = \frac{\partial(\rho n u)}{\partial t} - u \frac{\partial(\rho n)}{\partial t} \quad (4.21)$$

$$(\rho n \mathbf{U}) \cdot \nabla u = \nabla \cdot (\rho n u \mathbf{U}) - u \nabla \cdot (\rho n \mathbf{U}) \quad (4.22)$$

By substituting the above two terms into the left-hand side of Eq. (4.20), one can get

$$\rho n \frac{\partial u}{\partial t} + \rho n \mathbf{U} \cdot \nabla u = \frac{\partial(\rho n u)}{\partial t} + \nabla \cdot (\rho n u \mathbf{U}) - u \left[ \frac{\partial(\rho n)}{\partial t} + \nabla \cdot (\rho n \mathbf{U}) \right] \quad (4.23)$$

Recalling Eq. (4.12), that  $\frac{\partial(\rho n)}{\partial t} + \nabla \cdot (\rho n \mathbf{U}) = 0$ , Eq. (4.23) can be reduced to

$$\rho n \frac{\partial u}{\partial t} + \rho n \mathbf{U} \cdot \nabla u = \frac{\partial(\rho n u)}{\partial t} + \nabla \cdot (\rho n u \mathbf{U}) \quad (4.24)$$

Consequently, the momentum equation in the  $x$ -direction is written as

$$\frac{\partial(\rho n u)}{\partial t} + \nabla \cdot (\rho n u \mathbf{U}) = -n \nabla p_x + n \left[ \frac{\partial \tau_{xx}}{\partial x} + \frac{\partial \tau_{yx}}{\partial y} + \frac{\partial \tau_{zx}}{\partial z} \right] + n \rho g_x + f_{dx} \quad (4.25)$$

The momentum equations in the  $y$ - and  $z$ - directions can be derived accordingly. Thus, the momentum balance equation for the solid–fluid mixture system is summarized as

$$\frac{\partial(\rho n \mathbf{U})}{\partial t} + \nabla \cdot (\rho n \mathbf{U} \mathbf{U}) = -n \nabla p + n \nabla \cdot \boldsymbol{\tau} + n \rho \vec{g} + \vec{f}_d \quad (4.26)$$

The momentum equation for pure fluid ( $n = 1$ ) (Anderson 1995) is given here as

$$\frac{\partial(\rho \mathbf{U})}{\partial t} + \nabla \cdot (\rho \mathbf{U} \mathbf{U}) = -\nabla p + \nabla \cdot \boldsymbol{\tau} + \rho \vec{g} \quad (4.27)$$

## 4.3 The Viscous Shear Stress

In simulating large-scale landslides, the fluid flow can range from the laminar to turbulent regimes. In each flow regime, the calculation of the fluid viscous shear stress tensor ( $\tau$ ) is different. In the following sections, a detailed discussion of the derivation of the fluid shear stress tensor of viscous, incompressible and Newtonian fluid in the laminar and turbulent flow regimes is presented.

### 4.3.1 Laminar Flow Regime

In the laminar fluid flow regime, the shear stress is a product of fluid viscosity and velocity gradient. The corresponding equation was first proposed by Isaac Newton in the late seventeenth century as

$$\tau_{ij} = \mu \left( \frac{\partial U_i}{\partial x_j} + \frac{\partial U_j}{\partial x_i} \right) \quad (4.28)$$

For a fluid–solid mixture system, the bulk viscosity of a suspension can be larger than that of pure fluid (Yang et al. 2008; Schupp 2009) due to the presence of fine particles in the suspension (Iverson 1997). The bulk viscosity can be estimated by Einstein’s equation or its modifications, as can be found in the literature (Kunitz 1926). Most of these equations are only applicable to very dilute suspensions, while some others depend highly on the model configurations. For example, the empirical equation of suspension viscosity of glass beads (spherical particles of size in the order of micro-metres) proposed by Toda and Furuse (2006) is expressed as

$$\mu_s = \left( \frac{1 + 0.5\kappa(\frac{1-n}{n})}{(1 - \kappa + n\kappa)^2} \right) \mu \quad (4.29)$$

with

$$\kappa = 1.6 - 0.6 n, \quad (4.30)$$

where  $n$  is the porosity of suspension, which ranges from 0.55 to 1.0.

However, in this study, the difference between the pure water and bulk viscosity is not considered as important, because the solid grains are relatively coarse and the packing porosity is out of the suggested range. Based on Eq. (4.28), it can be observed that the fluid viscous stress tensor is a function of fluid velocity, which is independent of the influence of solid grains. Thus, the gradient of fluid shear stress in the  $x$  direction is written as

$$\begin{aligned}
& \frac{\partial \tau_{xx}}{\partial x} + \frac{\partial \tau_{yx}}{\partial y} + \frac{\partial \tau_{zx}}{\partial z} \\
&= \frac{\partial}{\partial x} \left( \mu \left( \frac{\partial(u)}{\partial x} + \frac{\partial(u)}{\partial x} \right) \right) + \frac{\partial}{\partial y} \left( \mu \left( \frac{\partial(u)}{\partial y} + \frac{\partial(v)}{\partial x} \right) \right) + \frac{\partial}{\partial z} \left( \mu \left( \frac{\partial(u)}{\partial z} + \frac{\partial(w)}{\partial x} \right) \right) \\
&= \mu \frac{\partial^2(u)}{\partial x^2} + \mu \frac{\partial^2(u)}{\partial y^2} + \mu \frac{\partial^2(u)}{\partial z^2} + \mu \frac{\partial^2(u)}{\partial x^2} + \mu \frac{\partial^2(v)}{\partial y \partial x} + \mu \frac{\partial^2(w)}{\partial z \partial x} \\
&= \mu \nabla^2(u) + \mu \frac{\partial}{\partial x} \left( \frac{\partial(u)}{\partial x} + \frac{\partial(v)}{\partial y} + \frac{\partial(w)}{\partial z} \right)
\end{aligned} \tag{4.31}$$

According to Eq. (4.13), the following expression holds true (*N.B.* the fluid density is a constant as it is incompressible.)

$$\left( \frac{\partial(u)}{\partial x} + \frac{\partial(v)}{\partial y} + \frac{\partial(w)}{\partial z} \right) = \nabla \cdot (\mathbf{U}) = 0 \tag{4.32}$$

Thus, Eq. (4.21) is reduced to

$$\frac{\partial(n\rho u)}{\partial t} + \nabla \cdot (n\rho u \mathbf{U}) = -n \frac{\partial p}{\partial x} + n\mu \nabla^2(u) + n\rho g_x + f_{dx} \tag{4.33}$$

Summarizing the momentum equation for  $x$ ,  $y$  and  $z$  components together, one can get

$$\frac{\partial(n\rho \mathbf{U})}{\partial t} + \nabla \cdot (n\rho \mathbf{U} \mathbf{U}) - n\mu \nabla^2(\mathbf{U}) = -n \nabla p + n\rho \vec{g} + \vec{f}_d \tag{4.34}$$

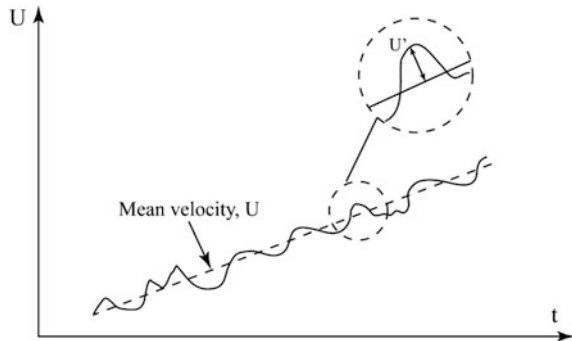
### 4.3.2 Turbulent Flow Regime

In the turbulent flow regime, the fluid flow is characterized by irregular velocity fluctuation, vortices, energy cascade, irreversibility and high dissipation rate, high diffusivity of momentum (Tennekes and Lumley 1972). Figure 4.5 illustrates the variation of fluid flow velocity over time. In general, the fluid velocity and pressure can be written in the following forms as

$$\mathbf{U} = \bar{\mathbf{U}} + \mathbf{U}' p = \bar{p} + p', \tag{4.35}$$

where  $\bar{\mathbf{U}}$  and  $\bar{p}$  are the mean fluid velocity and pressure, while  $\mathbf{U}'$  and  $p'$  are their fluctuating components. If the mean flow is steady, the following relationships are satisfied

**Fig. 4.5** Variation of fluid velocity over time in a turbulent flow



$$\bar{U} = \frac{1}{t} \int_0^t U dt \quad \bar{p} = \frac{1}{t} \int_0^t p dt \quad (4.36)$$

Substituting Eq. (4.35) into Eqs. (4.34), (4.12) and eliminating all terms containing the products of mean and fluctuating values (Pope 2000; Schlichting and Gersten 2000; Wilcox 2006), the following equation can be obtained:

$$\frac{\partial(\rho n)}{\partial t} + \nabla \cdot (\rho n \bar{U}) = 0 \quad (4.37)$$

$$\frac{\partial(n\rho \bar{U})}{\partial t} + \nabla \cdot (n\rho \bar{U} \bar{U}) - \nabla \cdot (n\mu \nabla(\bar{U}) + n\rho \bar{U}' \bar{U}') = -n\nabla \bar{p} + n\rho \vec{g} + \vec{f}_d \quad (4.38)$$

When compared with Eq. (4.34), there is a new term,  $\nabla \cdot (n\rho \bar{U}' \bar{U}')$ , in Eq. (4.38). The number of unknown variables is more than the number of governing equations. Thus, more equations are needed to relate the extra turbulence terms to the mean flow variables. It is necessary to introduce a “turbulence model” to solve the “turbulence closure problem”. Equations (4.37) and (4.38) are called the Reynolds-Averaged Navier–Stokes (RANS) model for a fluid–solid mixture system.

The Reynolds stress tensor is defined as

$$\tau_T = -\rho \bar{U}' \bar{U}' \quad (4.39)$$

where  $\tau_T$  is a second rank symmetric tensor. Based on the Boussinesq eddy viscosity assumption (Schmitt 2007), the Reynolds stress tensor is proportional to the mean strain rate tensor as

$$\tau_T = 2\mu_T \mathbf{S} - \frac{2}{3}k\rho\mathbf{I}, \quad (4.40)$$

where  $\mu_T$  is known as the eddy viscosity;  $\mathbf{S} = \frac{1}{2}(\nabla \bar{\mathbf{U}} + \nabla \bar{\mathbf{U}}^T)$  is the mean strain rate tensor;  $\mathbf{I} = \delta_{ij}$  is an identity matrix;  $k = \frac{1}{2}\overline{U'_i U'_j}$ , is the turbulent kinetic energy.

*Note:* the eddy viscosity  $\mu_T$  in Eq. (4.40) is not the physical property of fluid flow, as its value depends only on the flow conditions. The value of eddy viscosity decreases towards the wall and it becomes zero on the wall.

To calculate  $\mu_T$  and solve the “turbulence closure problem”, the classical  $k - \varepsilon$  model (Launder and Spalding 1972; Wilcox 2006) is used in this study. This model is characterized by two variables: turbulent kinetic energy ( $k$ ) and energy dissipation rate ( $\varepsilon$ ). The transport equation for the turbulent kinetic energy ( $k$ ) is,

$$\frac{\partial(\rho k)}{\partial t} + \nabla \cdot (\rho \bar{\mathbf{U}} k) = \nabla \cdot \left[ \left( \mu + \frac{\mu_T}{\sigma_k} \right) \nabla k \right] + G - \rho \varepsilon \quad (4.41)$$

where  $G = \mu_T \left[ \frac{1}{2}(\nabla \bar{\mathbf{U}} + \nabla \bar{\mathbf{U}}^T) \right]^2$ .

The second variable  $\varepsilon$  determines the scale of turbulence and the corresponding transport equation is

$$\frac{\partial(\rho \varepsilon)}{\partial t} + \nabla \cdot (\rho \bar{\mathbf{U}} \varepsilon) = \nabla \cdot \left[ \left( \mu + \frac{\mu_T}{\sigma_\varepsilon} \right) \nabla \varepsilon \right] - C_1 G \frac{\varepsilon}{k} - C_2 \frac{\varepsilon^2}{k} \quad (4.42)$$

The turbulent viscosity is then defined as

$$\mu_T = \rho C_\mu \frac{k^2}{\varepsilon} \quad (4.43)$$

According to Pope (2000), the constants used in the  $k-\varepsilon$  model are listed as,

$$C_1 = 1.44, \quad C_2 = 1.92, \quad C_\mu = 0.09, \quad \sigma_k = 1.0, \quad \sigma_\varepsilon = 1.3.$$

### 4.3.3 Near-Wall Treatment

The turbulence structure is significantly influenced by the presence of boundary walls (Oosthuizen and Naylor 1999). The boundary layers with very high Reynolds number are very thin, and both velocity and turbulent properties (e.g.  $k$  and  $\varepsilon$ ) have very high gradients (Jasak 2009). In this region, an inverted energy cascade occurs because the small vortices are rolled up and ejected from the wall. Thus, small vortices will accumulate to create bigger ones, which cannot be simulated by the standard  $k-\varepsilon$  model. To overcome this problem, a straightforward approach is to

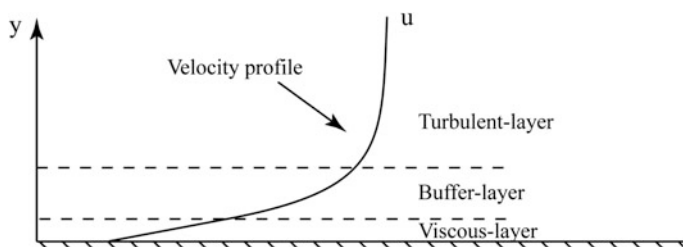
make the fluid mesh grid sufficiently fine near the wall, so that the gradients prevailing there can be accurately solved. However, this approach is very computationally expensive for modelling a complex three-dimensional flow problem. In addition, the extra variables in the  $k-\epsilon$  model also require specifications of their own boundary conditions, which are not *a priori* on purely physical grounds. An alternative approach is to employ a prescribed wall function at the boundary layer of the turbulent flow and assume that the fluid flow near that region behaves in the same way as that of a fully developed turbulent layer (Davidson 2003). The use of wall function can enhance the convergence and stability of numerical simulations.

Figure 4.6 shows the fluid flow velocity profile near the wall, which consists of three distinct flow layers. The very thin layer next to the wall is the viscous layer, in which the velocity profile is linear and the flow can be treated as laminar. The viscous effect of fluid is significant in this layer and the turbulence can be neglected. Next to the viscous layer is the buffer layer in which both viscous and turbulent effects are significant. Above the buffer layer is the turbulent layer where fully turbulent flow is developed. Since the characteristics of fluid flow are different in these flow layers, it is difficult to formulate an analytical relationship for velocity profiles of the entire flow domain. A general approach to handle this problem is first to identify key variables dominating the fluid flow and then formulate proper relationships with some unknown constants by dimensional analysis. The unknown constants can be determined by correlating with experimental or numerical data.

In the viscous layer, the thickness of flow is very small. However, it plays a dominant role in the fluid motion. The velocity gradient inside this layer is very large and the presence of solid boundary walls dampens any eddy motion. Thus, the fluid motion is essentially laminar, so that the shear stress of a Newtonian flow can be calculated as

$$\tau_w = \mu \frac{du}{dy} = \mu \frac{u}{y} = \rho v \frac{u}{y}, \quad (4.44)$$

where  $u$  is the transient fluid velocity parallel to the wall;  $y$  is the distance from the wall;  $v$  is the fluid kinematic viscosity, defined as  $v = \mu/\rho$ .



**Fig. 4.6** The velocity profile near the wall

Since the term  $\sqrt{\frac{\tau_w}{\rho}}$  has the dimension of velocity, it is usually called the friction velocity ( $u_*$ ). Substituting this term into Eq. (4.40), the velocity profile in the viscous layer can be expressed in a dimensionless form as

$$\frac{u}{u_*} = \frac{yu_*}{v} \quad (4.45)$$

Equation (4.45) is called the law of wall. The term  $v/u_*$  has a dimension of length and it can be used to normalize the distance from the wall surface ( $y$ ). Thus, the normalized distance and flow velocity are defined as

$$y^+ = \frac{yu_*}{v} \text{ and } u^+ = \frac{u}{u_*} \quad (4.46)$$

The relationship of Eq. (4.41) then becomes

$$u^+ = y^+ \quad (4.47)$$

Equation (4.47) has been reported to be adequately describe the mean velocity distribution from the wall out to  $y^+ = 5$ . In the turbulent layer ( $y^+ > 30$ ), the velocity profile follows a logarithmic distribution with distance away from the wall (Townsend 1980). The dimensionless form of a log-law wall function is written as

$$\frac{u}{u_*} = \frac{1}{\kappa} \ln E y^+, \quad (4.48)$$

where  $\kappa$  is the von Karman constant with the value of 0.41;  $E = 9.8$  is a constant.

In the buffer layer ( $5 < y^+ \leq 30$ ), both the molecular and turbulent stresses are important. From experiments, the velocity distribution can be approximated as

$$u^+ = 5 \ln y^+ - 3.05 \quad (4.49)$$

When using the wall function, the variables  $k$  and  $\varepsilon$  are not solved at the nodes adjacent to the walls. Instead, they are fixed values (Davidson 2003) defined as

$$k_P = \frac{u_*^2}{\sqrt{C_\mu}} \quad (4.50)$$

$$\varepsilon_P = \frac{u_*^3}{\kappa y} \quad (4.51)$$

where  $C_\mu = \left(\frac{u_*^2}{k}\right)^2$  is a constant (0.09) determined from experiments.

#### 4.3.4 Initial Conditions

In solving the differential equations by the finite difference method, the initial values of related variables, such as,  $k$ ,  $\varepsilon$ ,  $p$ , and  $\mathbf{U}$  should be set appropriately. For a turbulent flow, it is often difficult to do so, because the initial fluid turbulence is rarely known accurately. One common practice is to estimate the initial turbulent properties of the internal fluid flow field and then use the same values as initial estimations for the wall functions. Based on this concept, the following equations are used to estimate  $k$  and  $\varepsilon$  (Wilcox 2006), as

$$k = \frac{3}{2} (|\bar{U}|I)^2 \quad (4.52)$$

$$\varepsilon = C_\mu \frac{k^{\frac{3}{2}}}{l}, \quad (4.53)$$

where  $|\bar{U}|$  is the magnitude of mean fluid flow velocity;  $I$  is the turbulence intensity and  $l$  is the turbulent length scale.

In the current research on grain sedimentation and submerged debris flows, the numerical simulations are assumed to start from an initial static state. The initial values of pressure and velocity are zeros, so that Eqs. (4.52) and (4.53) predict the values of  $k$  and  $\varepsilon$  as zeros. However, as shown in Eq. (4.43),  $\varepsilon$  also appears at the denominator, so that a zero value would cause numerical problems. Therefore, a very small value, for example,  $10^{-6} \text{ m}^2\text{s}^{-3}$  will be used as the initial value of  $\varepsilon$ .

## 4.4 The MPI Implementation and Data Exchange

Simulations of landslides by using the DEM–CFD coupling method present considerable computational challenges. The slope mass is modelled by a collection of polydispersed spheres which might be bonded together to represent an initial integrate soil mass. For example, a typical landslide model in the DEM could consist of approximately 200,000 particles, with the mean diameter of 0.002 m. Based on the DEM stability and accuracy criteria (see Sect. 2.2.2), the numerical time step can be as small as  $10^{-7}$  s. It can be estimated that conducting a 10 min landslide simulation would require approximately  $6 \times 10^9$  iteration steps. For the DEM simulations presented herein, it will take around 23 days using the author's desktop (Intel® Core™ i7 CPU (2.93 GHz)) (for the model with 200,000 particles, it can only perform at most 1000 DEM iteration steps per second). The situation can become even worse if a large portion of fine grains are included in the model.

The DEM and CFD programs used in this research are the open source codes ESyS-Particle (Weatherley et al. 2011) and OpenFOAM (OpenCFD 2004), respectively. Both codes exploit the Message Passing Interface (MPI) parallelization

to speed up the calculation across the parallel computational resources. In the current landslide simulations, the main computational cost comes from the DEM calculation due to a huge number of particles in the model. As for the CFD model, the total number of fluid mesh cells is relatively small, because the sizes of fluid mesh grids are always larger than the size of solid particles. Thus, the available processors and memory of the computer used in this research are not a limiting constraint for the CFD model. As a result, several processors are used in the DEM calculation, while only one processor is assigned to the CFD model. The implementation of MPI in the DEM code has followed a simple master–slave paradigm (Olivier 2001), with a master processor performing the model initialization and domain decomposition (Plimpton 1995). Subsequently, the slave nodes perform computations on the decomposed domains. The temporal synchronizations and output aggregations are carried out by the master processor during the simulation at every iteration step.

For a typical DEM–CFD coupling simulation using the MPI, the computational domain of the DEM model is initially partitioned into several subdomains by the master processor. Each subdomain is assigned a processor to perform local calculations. One processor is assigned to the CFD code to perform the calculation for fluid flow. The particle properties, such as position, diameter and velocity are local to specific processors and are updated within the subdomain. Elements located at the boundaries of subdomains may interact and exchange data with their neighbours at the end of each iteration step, performed by the master processor. The inherent synchronization and nonblocking communication in MPI can increase the computing efficiency, especially for simulations running on the distributed memory clusters (Girolami et al. 2012).

The data exchange programs between the DEM and CFD threads (*N.B.* one thread can be regarded as an independent program.) is based on the DEM–CFD coupling model initially proposed by Chen et al. (2011). In the initial model, the DEM and CFD codes are running on a single processor, such that information of fluid–solid interaction is exchanged sequentially during the simulation. The current research has improved the DEM–CFD coupling code by using a parallel data exchange model as illustrated in Fig. 4.7. The two threads can run in parallel during the simulation, performing numerical calculations and updating solid and fluid properties, respectively. A dynamic linked library (DLL)—the DEM–CFD shared library—has been developed by the author to link these two threads. The calculation and transfer of the fluid–solid coupling information (e.g. buoyant and drag forces) are carried out within the DLL, as illustrated in Fig. 4.8.

At the beginning of the simulation, the DEM thread takes control of the simulation. It receives parameters of granular properties and coupling information from the input file. These parameters will then be transferred into the initiation subroutine of the DEM program. The DEM model is generated accordingly and the simulation time for the DEM and CFD are set as the same value (e.g. 0). As discussed before, the time step used in the DEM is generally much smaller than that used in the CFD, which indicates that the DEM thread can run several iterations per CFD iteration step, so that the total simulation time of the DEM and the CFD threads is the same.

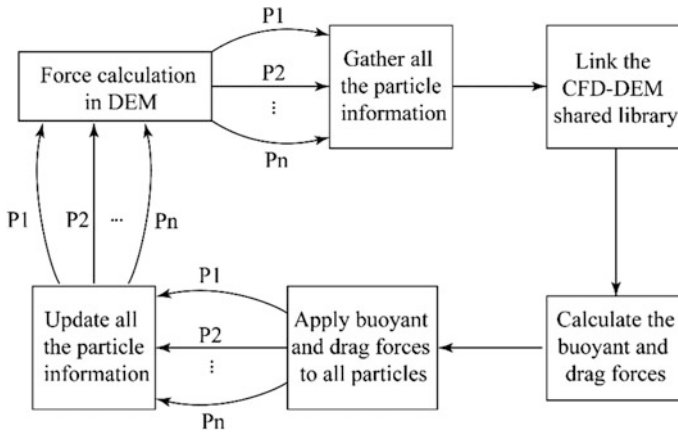


**Fig. 4.7** The diagram of DEM–CFD coupling ( $P_i$  represents the computer processor)

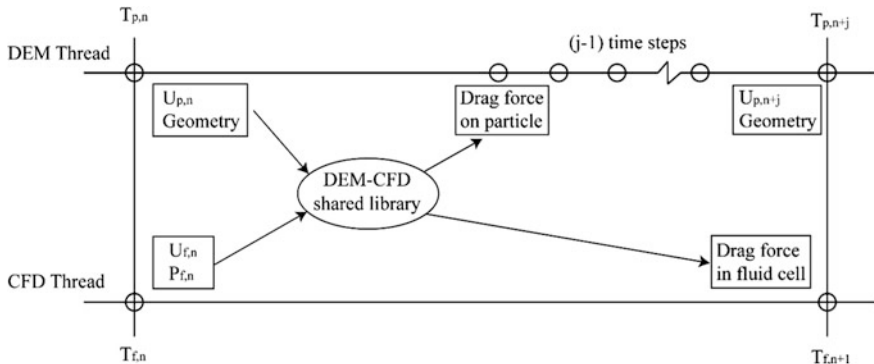


**Fig. 4.8** Data exchange during one DEM–CFD coupling step. The geometric information includes the particle position and radius;  $T_{p,n}$  and  $T_{f,n}$  represent the solid and fluid simulation time at iteration step  $n$ ,  $U_{p,n}$ ,  $U_{f,n}$ ,  $P_{f,n}$  represent the particle velocity, fluid velocity and pressure at step  $n$

The number of iteration steps of the DEM simulation during two successive DEM–CFD coupling steps is called the coupling frequency. The use of a large coupling frequency in the simulations is necessary, based on the following considerations:

- (i) As the CFD calculation uses the PISO (Pressure Implicit Split Operator) method, it will converge at the end of each coupling iteration step (Issa 1986; Jasak 1996);
- (ii) The velocity and displacement of solid particles within one iteration step vary very little and thus there is no need to exchange the granular information between the DEM and CFD threads at every iteration step;
- (iii) By using a relatively large coupling frequency, the efficiency of numerical simulation can be enhanced significantly. However, if the coupling frequency is too large, the motion of solid grains in fluid cannot be well captured by the CFD code within each coupling

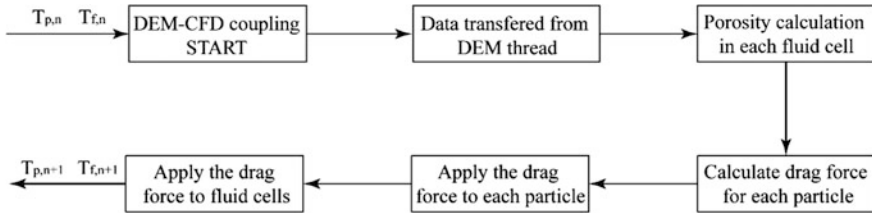


**Fig. 4.9** Data manipulation in the DEM–CFD coupling shared library

step. Therefore, the value of coupling frequency should be chosen based on the stability and accuracy criteria of the DEM and CFD. In this research, it is set within the range of [10, 100] for all simulations.

When the data exchange begins, the DEM thread is activated, while the CFD thread is paused. The DEM thread links the DEM–CFD Shared Library and sends all the particle information, such as the particle velocities, positions and diameters into the shared library. The fluid properties, such as the fluid velocity and pressure, at the previous time step (or initial values) are obtained from the CFD thread. Based on these information, the sample porosity and fluid–solid viscous drag forces are calculated (the detailed algorithm used to calculate the porosity of a fluid mesh cell is presented in Appendix B). Then, the drag forces are transferred to both the DEM and CFD threads, which will be used as the source force terms in the governing momentum equations of the solid and fluid phases. The particle velocity, position and contact forces will then be updated in the DEM thread accordingly. After that, the CFD thread is activated, while the DEM thread is paused. The CFD thread will solve the momentum equation and perform the PISO iteration, so that the fluid velocity and pressure fields are updated. When the CFD calculation finishes, the simulation control returns back to the DEM thread and a new iteration step repeats. This mechanical loop will continue until the prescribed total coupling iteration step is reached. The data manipulation within the shared library is shown in Fig. 4.9.

## 4.5 Fluid Flow Through a Porous Soil Sample

As soil is permeable, water is able to flow through the interconnected pores between solid particles. To quantify this property, it is necessary to study the hydraulic behaviour of soil, when water flows through a soil mass. As discussed in Sect. 1.5.4, based on the value of Reynolds number, four distinct flow regimes exist when fluid flows through a porous medium, namely the laminar, Forchheimer, transition and turbulent flow regimes. In each flow regime, the corresponding hydraulic gradients ( $\Delta h / \Delta L$ ) can be written as functions of superficial fluid flow velocity ( $v$ ).

If the fluid Reynolds number is smaller than 1.0, it is in the laminar flow regime. In this regime, the hydraulic gradient is linearly related to the fluid flow velocity, which is quantified by the Darcy's empirical law (Craig 1997), as

$$\Delta h/\Delta L = i = \frac{1}{k} v, \quad (4.54)$$

where  $k$  is the coefficient of soil permeability.

As a real soil mass normally consists of grains with a wide range of particle size distribution, the coefficient of soil permeability can be evaluated using the *Kozeny–Carman* empirical equation (Ergun 1952; McCabe et al. 2005; Chen et al. 2011),

$$k = \frac{D_{10}^2 n^3 \rho_f g}{150 \mu (1 - n)^2}, \quad (4.55)$$

where  $D_{10}$  is the effective grain size;  $n$  is the porosity of soil sample.

In the laminar flow regime, the fluid head loss is linearly related to the fluid velocity, while the relationship gradually becomes nonlinear for large Reynolds numbers in the Forchheimer, Transient, and Turbulent regimes. As a consequence, the fluid flow properties depend mainly on the soil porosity and fluid hydraulic gradient. Ergun and Orning (1949) stated that the nature of nonlinearity is due to the increasing importance of turbulence in the fluid flow through a porous medium. For a given soil sample with a specific packing porosity, an empirical relationship quantifying the head loss and flow velocity over a wide range of Reynolds number has been proposed by Ergun (1952) as

$$\Delta h/\Delta L = \frac{1 - n}{\rho_f g d n^3} \left\{ 150 \frac{(1 - n) \mu V}{d} + 1.75 \rho_f V^2 \right\}, \quad (4.56)$$

where  $\rho_f$  is the fluid density;  $g$  is the gravitational acceleration;  $d$  is the diameter of a sphere, which can be taken as  $D_{10}$  from the particle size distribution curve.

Trussell and Chang (1999) pointed out that the onset of turbulence in fluid flow tends to occur at different Reynolds numbers, which depends highly on the grain size, shape and packing porosity. A modified equation of Eq. (4.56) is expressed as

$$\Delta h/\Delta L = \frac{1 - n}{\rho_f g d n^3} \left\{ a \frac{(1 - n) \mu V}{d} + b \rho_f V^2 \right\}, \quad (4.57)$$

**Table 4.2** Summary of head loss coefficient for selected medium

Medium	Coefficients		Typical porosities	References
	$a$	$b$		
Crushed anthracite	210–245	3.5–5.3	0.47–0.52	Trussell and Chang (1999)
Crushed sand	110–115	2.0–2.5	0.40–0.43	Chang et al. (1999)
Glass beads	130–150	1.3–1.8	0.38–0.40	Trussell and Chang (1999)

where  $a$  and  $b$  are coefficients related to the linear and nonlinear pressure head loss, which characterize the flow behaviour of a particular type of soil for a range of sizes. The values of  $a$  and  $b$  are listed below in Table 4.2.

As discussed by Trussell and Chang (1999), Eq. (4.57) incorporates linear and nonlinear properties of fluid flow through a porous medium, which is applicable for all flow regimes. Thus, Eq. (4.57) can be used to describe fluid flows through various types of soil. However, one needs to keep in mind that the porosity of soil sample should range from 0.4 to 0.6. For samples with porosity out of this range, Eq. (4.57) may possibly produce erroneous results.

#### 4.5.1 Analytical Solution of Soil Permeability

As discussed before, the momentum equation of a fluid–solid mixture system is

$$\frac{\partial(\rho n \mathbf{U})}{\partial t} + \nabla \cdot (\rho n \mathbf{U} \mathbf{U}) - n \nabla \cdot \boldsymbol{\tau} = -n \nabla p + n \rho_f \mathbf{g} + \bar{\mathbf{f}}_d \quad (4.26')$$

At the steady state, it can be assumed that no acceleration, no inertial effect exists in the fluid–solid mixture system. Thus, the temporal, convection and diffusion terms on the left-hand side (LHS) of Eq. (4.26') are zeroes. The equation can be reduced to Eq. (4.58), as

$$0 = -n \nabla p + n \rho_f \mathbf{g} + \bar{\mathbf{f}}_d \quad (4.58)$$

Thus,

$$\nabla p = \rho_f \mathbf{g} + \frac{\bar{\mathbf{f}}_d}{n}, \quad (4.59)$$

where  $\bar{\mathbf{f}}_d = \frac{\sum_{i=1}^N F_{di}}{V}$ ,  $V$  is the volume of a CFD mesh cell;  $N$  is the total number of grains in that fluid mesh cell. The term  $\rho_f \mathbf{g}$  on the right-hand side (RHS) of Eq. (4.59) can be written as  $\nabla p_s$ , with  $p_s$  being the hydrostatic pressure of fluid. Based on the Di Felice (1994) drag force model, the drag force per fluid volume can be calculated as

$$\bar{\mathbf{f}}_d = \frac{\sum_{i=1}^N f_{di}}{V} = \frac{\sum_{i=1}^N \frac{1}{2} C_d \rho_f \times \frac{1}{4} \pi D_i^2 U_r^2 n^{1-\zeta}}{(\sum_{i=1}^N \pi D_i^3 / 6) / (1-n)} = \frac{3 \rho_f (1-n) n^{1-\zeta} \sum_{i=1}^N C_d U_r^2 D_i^2}{4 \sum_{i=1}^N D_i^3} \quad (4.60)$$

in which,  $U_r$  is the relative velocity between solid particle and fluid.

Thus, Eq. (4.59) becomes

$$\nabla p = \nabla p_s + \frac{3\rho_f(1-n)n^{-\chi}}{4} \frac{\sum_{i=1}^N C_d U_r^2 D_i^2}{\sum_{i=1}^N D_i^3} \quad (4.61)$$

If the fluid flow is in the laminar regime, the Stokes' drag coefficient ( $C_d = 24/\text{Re}$ ) and the porosity correction factor  $\chi = 3.7$  can be used in Eq. (4.61). For simplicity,  $d_i$  is taken as  $D_{10}$ . Thus, the gradient of excess pore water pressure ( $u$ ) is obtained as

$$\nabla u = \nabla p - \nabla p_s = \frac{18\mu(1-n)n^{-4.7}U_r}{D_{10}^2} \quad (4.62)$$

Thus, the hydraulic gradient can be written as

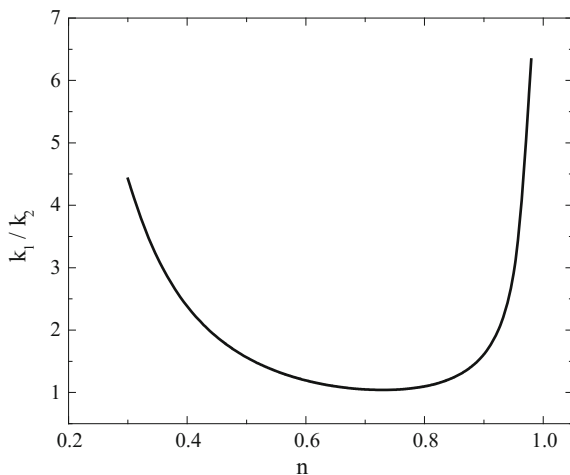
$$i = \frac{\nabla u}{\rho_f g} = \frac{18\mu(1-n)n^{-4.7}U_r}{\rho_f g D_{10}^2} \quad (4.63)$$

Based on Eq. (4.63), the soil permeability can be calculated as

$$k = \frac{nU_r}{i} = \frac{D_{10}^2 n^{5.7} \rho_f g}{18\mu(1-n)} \quad (4.64)$$

From Eqs. (4.55) and (4.64), it can be observed that the soil permeability depends on the parameters of  $D_{10}$ ,  $n$ ,  $\rho_f$ ,  $g$  and  $\mu$ . The only difference between these two definitions is the coefficients used to relate these parameters. In addition, Eq. (4.55) is an empirical correlation of experimental results of fluid pressure drop when it flows through a packed bed of solids, while Eq. (4.64) is an analytical investigation of the governing equation at the microscopic grain-size scale. Due to the simplifications made in deriving Eq. (4.64), it can only produce accurate prediction of permeability of soil consisting of equal-sized grains, while it would give out erroneous results for polydispersed granular sample. Figure 4.10 illustrates a comparison between the soil permeability predicted by the two equations. The porosity of the soil sample is within a reasonable range of [0.3, 1.0]. It can be observed that the predicted value of soil permeability from the empirical and the analytical equations can be very close to each other, when the soil porosity is within the range of 0.6–0.8, while for porosities out of this range, the empirical results are larger than the analytical ones.

**Fig. 4.10** Relationship between the permeability ratio and soil porosity ( $k_1$  is the soil permeability calculated by Eq. (4.55), while  $k_2$  is the soil permeability calculated by Eq. (4.64))



#### 4.5.2 Numerical Model Configuration

In this study, two soil samples with different particle size distributions are used: (1) equal-sized grains and (2) polydispersed grains as listed in Table 4.3. The solid and fluid materials used in these tests are sand and water. As shown in Fig. 4.11, a randomly packed granular assembly is generated within a rectangular prism with dimensions of  $0.05 \text{ m} \times 0.05 \text{ m} \times 0.05 \text{ m}$ . The solid grains are fixed in space, such that the variation of particle motions and interactions can be ignored. The fluid domain has initially been meshed as equal-sized parallelepiped prisms with dimensions of  $0.005 \text{ m}$  in each direction. At the beginning of the simulations, a constant pore water pressure ( $p_0$ ) is applied at the upper boundary of the CFD model, so that water is forced to flow downwards through the porous sand mass. The pore water pressure has been measured near the upper and lower surfaces of the soil sample. The discharge rate of fluid flow is taken as the mean flow velocity at the inlet and outlet boundaries.

**Table 4.3** Properties of soil samples

Sample A			Sample B		
D (mm)	Porosity	Grain number	D (mm)	Porosity	Grain number
2.0	0.64	10,746	[1.80, 3.80]	0.47	8651

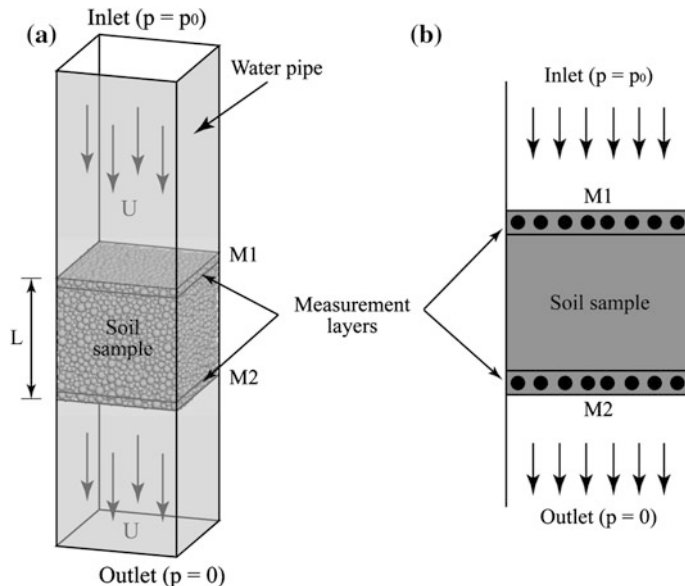


**Fig. 4.11** Model configuration of fluid flow through porous soil sample: **a** left Numerical model configuration; **b** right Detailed view of the measurement layers

#### 4.5.3 Laminar Flow

In the laminar flow regime, the Reynolds number of fluid flow is smaller than 1.0. Thus, the Darcy's law of permeability can be used to describe the relationship between the flow velocity and hydraulic gradient. For simulations using sample A, the flow velocities and hydraulic gradients are linearly related (Fig. 4.12), and the coefficient of soil permeability is 0.48 m/s which can match the analytical and empirical values (i.e. 0.475 and 0.529 m/s) very well.

For soil sample with a polydispersed particle size distribution (sample B), a similar relationship can be found to relate the flow velocities and hydraulic gradients, as shown in Fig. 4.13. The coefficient of soil permeability is obtained as 0.102 m/s which is very close to the empirical value (0.097 m/s) calculated using Eq. (4.55). However, the analytical value (0.056 m/s) cannot match the numerical results. This is due to the fact that Eq. (4.64) is unable to predict the permeability of soil sample consisting of polydispersed particles.

**Fig. 4.12** Relationship between flow velocity and hydraulic gradient for equal-sized sample

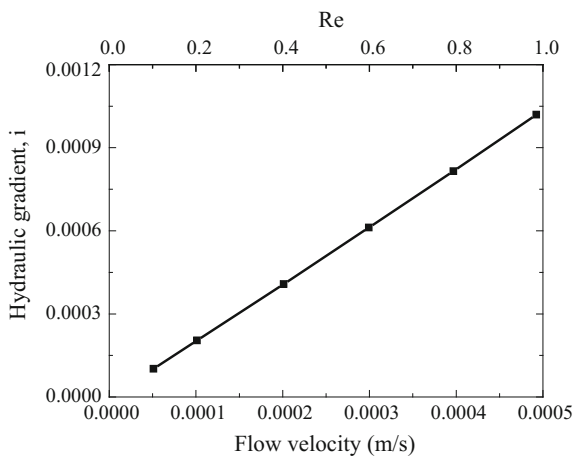
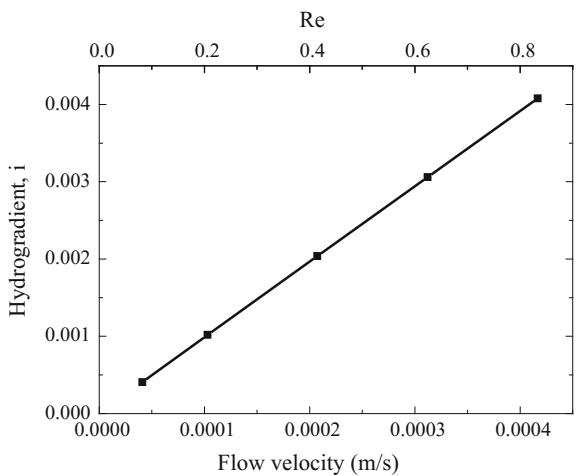


**Fig. 4.13** Relationship between flow velocity and hydraulic gradient for polydispersed sample

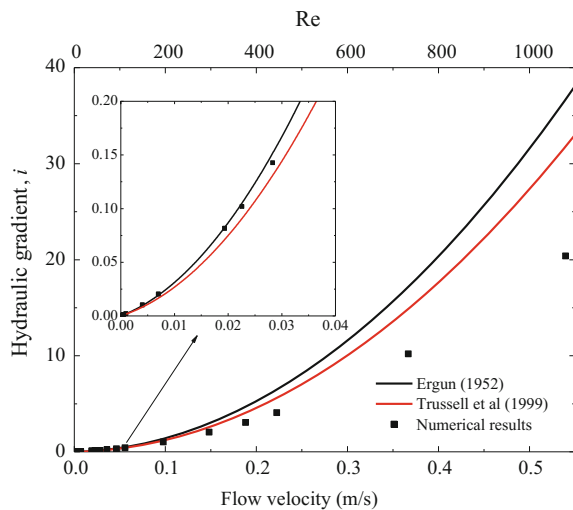


#### 4.5.4 Turbulent Flow

At higher Reynolds numbers, the fluid flow could be in the Forchheimer, Transition or Turbulent regime. At the lower end of these regimes, the laminar flow behaviour is dominant, such that the pressure head loss is approximately linearly related to the flow velocity. At the upper end of these regimes, the fluid flow is fully turbulent, so that the flow velocity is randomly fluctuating about the mean value throughout the fluid domain and the pressure head loss is nonlinearly related to the flow velocity.

For the soil sample composed of equal-sized spheres (sample A), the relationship between the fluid flow velocity and hydraulic gradient is illustrated in Fig. 4.14. According to Fig. 4.14, the numerical results of hydraulic gradient at low fluid

**Fig. 4.14** The relationship between the flow velocity and hydraulic gradient [for the results of Trussell et al. (1999), the coefficients are  $a = 128.5$ ,  $b = 1.5$ ]



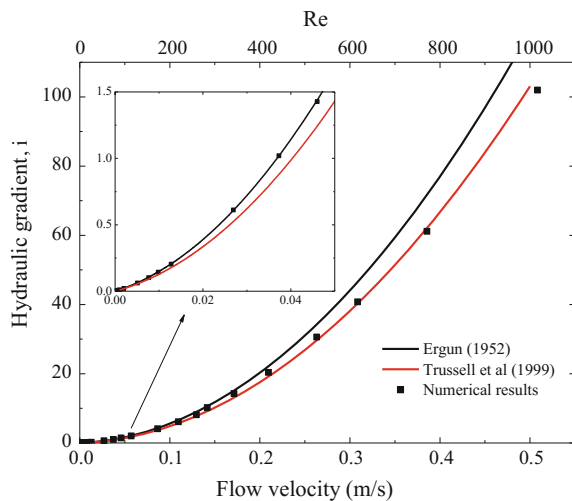
velocity (or low Reynolds number) can match the Ergun and Trussell's empirical results very well, while a large discrepancy is observed when the Reynolds number is larger than 200. As discussed before, Ergun and Trussell's equations cannot give accurate prediction of the fluid head loss for soil samples with porosities outside the suggested range of [0.4, 0.6]. As the soil sample has a porosity of 0.64, the empirical correlations would predict slightly larger values of hydraulic gradient than the numerical ones.

For the soil sample consisting of polydispersed grains (sample B), The numerical results can match the empirical correlating results by Ergun (1952) very well for Reynolds number smaller than 400, while a slight discrepancy occurs at higher Reynolds numbers, as shown in Fig. 4.15. This phenomenon indicates that Ergun's correlation is not accurate to capture the fluid turbulent properties at high Reynolds numbers. On the other hand, the numerical results can match the empirical correlation proposed by Trussell and Chang (1999) very well for Reynolds number up to 1000.

## 4.6 Numerical Investigation of Granular Sedimentation

The sedimentation and consolidation of granular materials are common in nature, either in terrestrial or submarine environments. The granular materials usually settle continuously towards the seabed or the river floor to form a loose sediment layer. As the skeleton of sediment layer is extremely compressible, it would have relatively large strain under additional loads. These processes are very important for solid–liquid separations, as can be found in chemical, mining, wastewater, food, pharmaceutical and some other industries (Di Felice 1999; Bürger and Wendland

**Fig. 4.15** The relationship between fluid velocity and hydraulic gradient [for the results of Trussell et al. (1999), the coefficients are  $a = 128.5$ ,  $b = 1.5$ ]



2001; Chaumeil and Crapper 2014). The related researches can be theoretical, laboratory experimental and numerical investigations on a variety of materials (Kynch 1952; Richardson and Zaki 1954; Been and Sills 1981; Tiller 1981; Shih et al. 1987; Font 1988; Tsuji et al. 1993; Komiwas et al. 2006).

During sedimentation, the average settling velocity of a suspension is the most notable parameter quantifying the dynamic behaviour of the fluid–solid mixture system (Batchelor and Green 1972; Hinch 1977; Batchelor 1982; Batchelor and Wen 1982; Wachmann et al. 1998). As first proposed by Kynch (1952), the analytical settling velocity depends on the concentration of solid materials. This statement has been validated by the experimental measurements of the grain settling rates in granular suspension systems (Been 1980; Been and Sills 1981; Font 1988). Numerical simulations of granular sedimentation mainly focus on the settling and depositional behaviour of solid grains in either monodisperse (Richardson and Zaki 1954; Batchelor and Green 1972; Mills and Snabre 1994) or polydisperse (Shih et al. 1987; Davis and Gecol 1994) systems. These researches reveal three distinct zones from top to bottom in a grain settling system: the hindered settling zone, where the surface settling velocity is approximately constant; the transition zone where the settling rate decreases gradually to zero, and the compression zone where a soil layer is formed at the bottom and consolidation appears due to the self-weight of sediments. However, as reported by Richardson and Zaki (1954), there is no constant settling rate zone for very fine flocculated pulps and their settling rates decrease progressively.

In the literature, research on the mechanical behaviour of suspensions in the hindered and the compression zones has been reported (Stokes 1901; Terzaghi 1943; Kynch 1952). Stokes (1901) first made a theoretical investigation of the forces acting on an isolated spherical particle moving in fluid in the laminar flow

regime. He proposed that the viscous drag force acting on a single particle by fluid is expressed as

$$F = 3\pi\mu U_r D, \quad (4.65)$$

where  $F$  is the viscous drag force;  $\mu$  is the fluid viscosity;  $U_r$  is the relative settling velocity between solid and fluid;  $d$  is the diameter of spherical particle.

The constant relative settling velocity ( $U_0$ ) is reached at an equilibrium state, when the buoyant weight of the particle equals to the viscous drag force.

$$3\pi\mu v_0 D = \frac{\pi D^3}{6} (\rho_s - \rho_f) g \quad (4.66)$$

where  $\rho_s$  is the density of solid particle.

Thus, the expression of the constant relative settling velocity is obtained as

$$v_0 = \frac{gD^2(\rho_s - \rho_f)}{18\mu} \quad (4.67)$$

The corresponding characteristic settling time is defined as

$$t_c = \frac{18\mu H}{gD^2(\rho_s - \rho_f)} \quad (4.68)$$

where  $H$  is the height that the particle settles through.

For many years, the analytical and numerical investigations of sedimentation employing empirical correlations of the mixture properties based on laboratory experiments have been widely reported (Ergun 1952; Richardson and Zaki 1954; Othmer 1956; Wen and Yu 1966; Di Felice 1994; Komiwes et al. 2006). However, a systematic study of sedimentation is still lacking as the fluid–solid mixture presents a highly heterogeneous structure featured by a spatially non-uniform distribution of solid particles (Fitch 1983; Font 1988). The numerical investigation of this research is based on the idea that the motion of solid particles is completely governed by the Newtonian equations of motion and collisions are modelled by the soft particle approach (Komiwes et al. 2006). The fluid flow is calculated by Navier–Stokes equations (Kalthoff et al. 1996; Wachmann et al. 1998; Komiwes et al. 2006). Therefore, the DEM and CFD can be used to study the mechanical and hydraulic behaviour of solid grains and fluid flow, respectively. By coupling these two methods together, a complete analysis of the sedimentation of a fluid–solid mixture system can be achieved (Chen et al. 2011).

This research aims to use the DEM–CFD coupling method to study the settling behaviour of solid grains generated randomly within a parallelepiped prism. Through dimensional analysis, fundamental parameters governing the settling process have been identified as the fluid density ( $\rho_f$ ) and viscosity ( $\mu$ ), the width of the prism ( $W$ ), the diameter of solid grain ( $D$ ) and the porosity of granular sample

(n). Based on the research of Richardson and Zaki (1954), a function relating all these parameters is

$$\frac{U_r}{U_0} = f\left(\frac{\rho_f d U_r}{\mu}, n, \frac{D}{W}\right) \quad (4.69)$$

In the current analyses, the normalized settling time is defined as

$$[T] = \frac{t}{t_c} = \frac{g D^2 (\rho_s - \rho_f) t}{18 \mu H} \quad (4.70)$$

The vertical position of a particle ( $h$ ) is normalized by the initial prism height, as

$$[H] = h/H \quad (4.71)$$

In Eq. (4.69), the first two dimensionless groups on the right-hand side correspond to the Reynolds number and porosity correction of the governing equations used in the DEM–CFD method. The size ratio ( $D/W$ ) represents the influence of model size on the settling velocity. The numerical model used in this research utilizes periodic boundaries for the fluid domain, which can effectively reduce the wall friction effects, as shown in Fig. 4.16. In Fig. 4.16, the parallelepiped prism has equal cross-sectional dimensions of  $0.025 \text{ m} \times 0.025 \text{ m}$  and a height of  $1.0 \text{ m}$ . The solid particles of various sizes are initially randomly generated within the prism and then settle downwards under gravity. The input parameters of the simulations are listed in Table 4.4.

**Fig. 4.16** Configuration of grain sedimentation model [see also Zhao et al. (2014)]

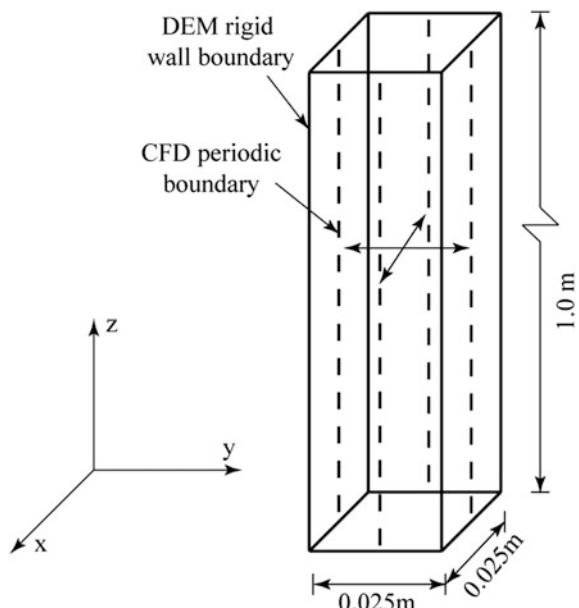


**Table 4.4** Input parameters for the sedimentation simulation

DEM parameters	Value	CFD parameters	Value
Particle diameter, mm	[1.8, 3.8]	Material	Water (at 20 °C)
Density, kg/m <sup>3</sup>	2650	Density, kg/m <sup>3</sup>	1000
Normal stiffness, N/m	$3.0 \times 10^7$	Viscosity, Pa·s	0.001
Shear stiffness, N/m	$2.7 \times 10^7$		
Friction angle, °	30	Simulation parameters	Value
Coefficient of rolling stiffness	1.0	Gravity, m/s <sup>2</sup>	(0.0, -9.81, 0.0)
Coefficient of plastic moment	0.1	DEM time step, s	$10^{-7}$
Damping coefficient	0.0	CFD time step, s	$10^{-5}$
		The coupling frequency <sup>a</sup>	100

<sup>a</sup>The coupling frequency is the iteration steps used in the DEM during each data exchange interval

#### 4.6.1 The Settling of a Single Particle

Simulations of the sedimentation of a single particle have been performed to validate the DEM–CFD coupling code. A solid sphere with radius of 1 mm is placed 9 cm below the upper surface of the fluid domain. The porosity of the CFD mesh cell at which the particle locates is 0.99. The motion of the spherical particle is governed by the equation as below:

$$\frac{4}{3}\pi r^3 \rho_s \frac{\partial U}{\partial t} = \frac{4}{3}\pi r^3 (\rho_s - \rho_f) g - \frac{1}{2}\pi r^2 \rho_f C_d U^2, \quad (4.72)$$

where  $U$  represents the relative velocity between particle and fluid. In Eq. (4.72), the drag force coefficient ( $C_d$ ) can be calculated by Eq. (4.7). Since  $U$  also appears in  $C_d$ , it is not straightforward to obtain an analytical solution for the settling velocity from Eq. (4.72) explicitly. Thus, the numerical technique—forward finite difference—is used to calculate the relative settling velocity. Rearranging Eq. (4.72) as

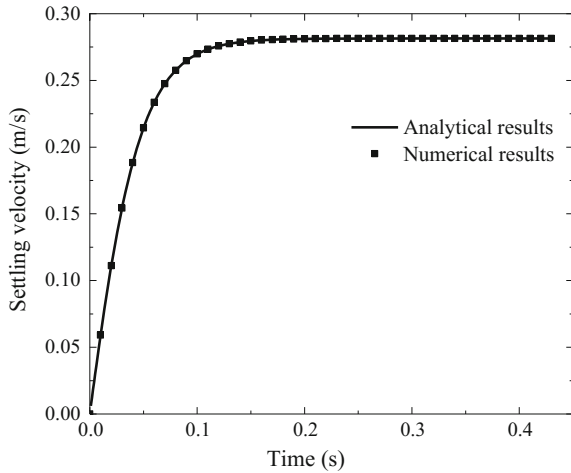
$$\frac{\partial U}{\partial t} = \left(1 - \frac{\rho_f}{\rho_s}\right)g - \frac{3\rho_f}{8r\rho_s} C_d U^2 \quad (4.73)$$

Denoting  $U_i$  and  $U_{i+1}$  as the velocities at the current and next numerical iteration time steps, the difference equation can be written as

$$U_{i+1} = U_i + \left\{ \left(1 - \frac{\rho_f}{\rho_s}\right)g - \frac{3\rho_f}{8r\rho_s} C_d U_i^2 \right\} \Delta t \quad (4.74)$$

Given the initial settling velocity as zero, the iteration continues until a constant settling velocity is reached. The analytical results are compared with the numerical

**Fig. 4.17** The relative settling velocity between solid and fluid during sedimentation

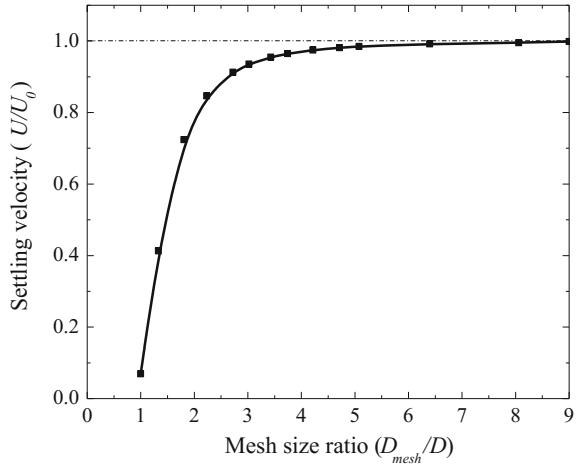


ones, as shown in Fig. 4.17. The numerical results can match well the analytical ones calculated by Eq. (4.74). The constant relative settling velocity is as 0.28 m/s.

As the coupling methodology only describes the average parameters (e.g. drag force, flow velocity and pressure), the fluid flow around a particle is not explicitly represented. In the calculation, the local porosity is assumed to be evenly distributed within one fluid element (Itasca 2008). In order to obtain good numerical results, several DEM particles are required to fit inside one CFD mesh cell, which means the size ratio of fluid mesh size ( $D_{\text{mesh}}$ ) to particle diameter ( $D$ ) should be larger than a critical value. Therefore, a series of numerical simulations with different mesh size ratios have been conducted to study the size effect (i.e. the fluid mesh size varies from 0.0025 to 0.025 m, while the particle diameter remains constant for different simulations). The terminal settling velocity obtained is normalized by the analytical settling velocity ( $U_0$ ), as shown in Fig. 4.18.

It can be observed that the relationship between the normalized constant relative setting velocity and the mesh size ratio ( $D_{\text{mesh}}/D$ ) is nonlinear. As the size ratio increases, the normalized particle settling velocity increases gradually until a steady state settling velocity is reached. The value of size ratio reflects the accuracy of the averaging process used in the DEM–CFD coupling model. If it is too small, intensive fluctuations would occur across the solution domain due to the heterogeneous packing of fluid–solid mixture. According to Fig. 4.18, the particle settling velocity can match well the theoretical value when the size ratio ( $D_{\text{mesh}}/D$ ) is larger than 5. This conclusion also agrees very well with the critical mesh size ratio suggested by Itasca (2008). To consider the resolution of the CFD calculation and possible boundary wall friction effects, one needs to study the influence of the ratio of the CFD model dimension ( $W$ ) to the mesh size ( $D_{\text{mesh}}$ ) on the settling velocities. Itasca (2008) suggests that this ratio should be no less than 5 and the implementation of periodic boundary conditions in the CFD can effectively reduce the boundary wall friction effect.

**Fig. 4.18** Influence of the fluid mesh size ratio ( $D_{\text{mesh}}/D$ ) on the normalized settling velocity



#### 4.6.2 Batch Granular Sedimentation

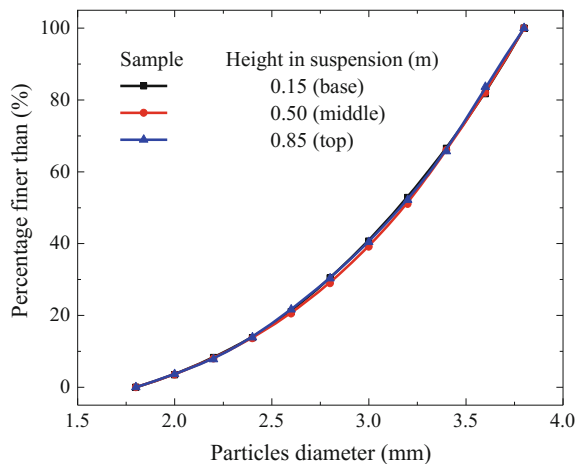
For numerical simulations of batch granular sedimentation, 6000 polydispersed solid spheres are randomly generated within the prism. The particle size distribution (PSD) is checked along the prism.

As shown in Fig. 4.19, the PSD curves of the granular materials at three different locations along the prism (i.e. base, middle and top) overlap each other, indicating that the initial DEM sample is uniformly generated. The average packing porosity of the sample is 0.89. In the following analyses, the fluid domain is meshed in  $x$ ,  $y$  and  $z$  directions with  $5 \times 5 \times 200$  equal-sized fixed-grid parallelepiped cells.

##### 4.6.2.1 Segregation of Grains

According to Stokes's law of sedimentation (Stokes 1901), the coarse grains can settle faster than the finer ones in fluid, leading to a segregation of solid grains. To illustrate this phenomenon, it is helpful to measure the particle size distribution (PSD) at different locations within the sample, as shown in Fig. 4.20. The granular assembly is divided into three distinct layers along the prism (i.e. base, middle and top), with each layer containing the same number of particles. At the beginning of the sedimentation, the segregation phenomenon is not significant, such that the PSD curves for grains locating at the base, middle and top of the prism are almost the same as the initial PSD curve. At  $[T] = 1.8$ , the PSD curve of the base region deviates slightly below the initial PSD due to the accumulation of large grains at the bottom. As the simulation continues, the PSD curves of the grains at the upper and bottom parts deviate gradually from the initial PSD curve. For the PSD curve of the middle region, it remains the same as the initial PSD before  $[T] = 3.6$ , and then deviates gradually towards the base PSD curve. This phenomenon indicates that the

**Fig. 4.19** The particle size distribution curves of the sample



coarse grains can move faster than the finer ones towards the base of the prism, leading to a high concentration of coarse grains at the base and fine grains at the top.

Initially, coarse grains in the top layer settle into the middle region, while the coarse grains in the middle layer settle into the base region. As a result, only the portion of coarse grains at the base has increased, while the PSD of the middle layer remains unchanged. After  $[T] = 5.4$ , a relatively thick deposit is formed at the base, such that the PSD curves of the three layers remain unchanged. Even though some fine grains are still suspended in the fluid, they settle very slowly on top of the deposit. At the end of the simulation, it can be observed that only the PSD curve of the upper region lies above the initial PSD curve, while the PSD curves of the middle and bottom parts overlap each other and lie slightly below the initial PSD curve. This phenomenon indicates that in small-scale sedimentation simulations, the grain segregation is significant near the upper part of the model, while it is not very evident in the middle and bottom parts.

#### 4.6.2.2 Density Profile of the Suspension

An important feature of batch granular sedimentation is the gradual change of bulk density of the suspension due to the segregation of solid grains. The value of bulk density can be calculated by the equation proposed by Di Felice et al. (1989), as

$$\rho_b = n\rho_f + (1 - n)\rho_s \quad (4.75)$$

During the simulation, the value of particle packing porosity in each fluid mesh cell along the prism is recorded, which will then be used to calculate the bulk density of the suspension based on Eq. (4.75). Figure 4.21 illustrates the evolution

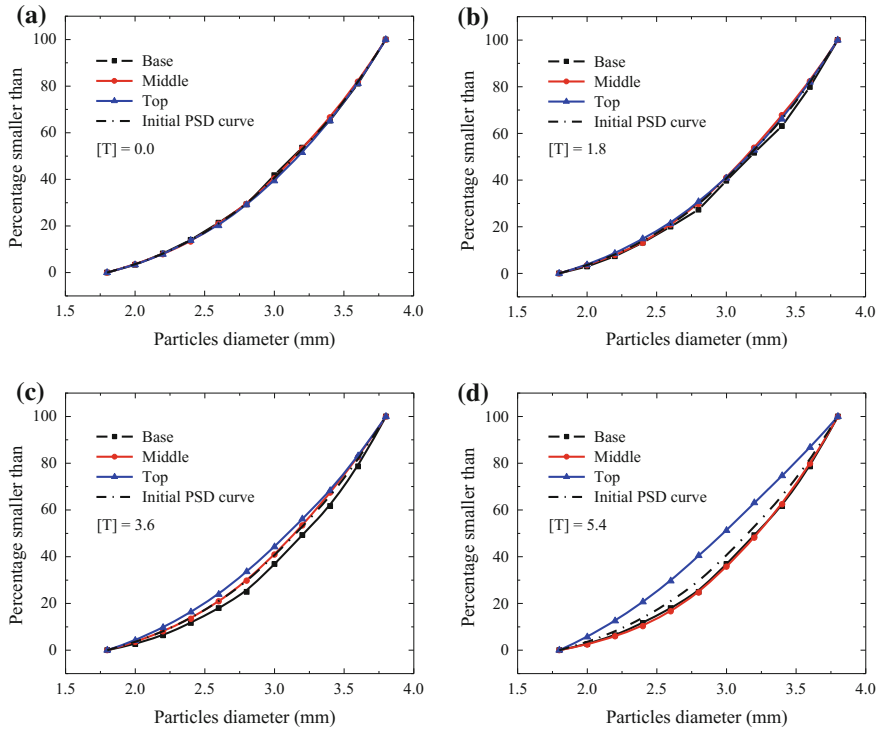
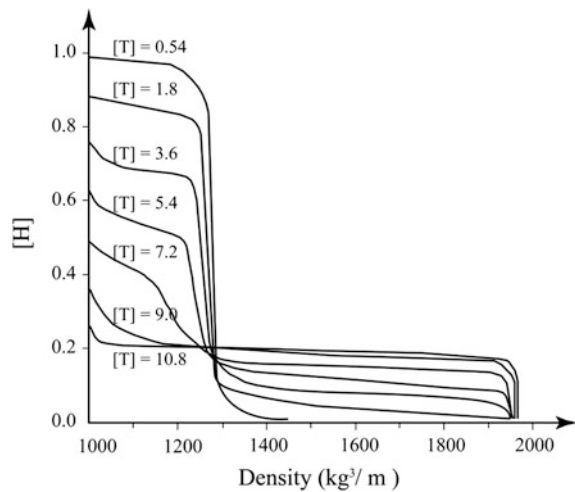


**Fig. 4.20** Particle size distributions in suspensions and sediments at different times

of the bulk density profiles of the fluid–solid mixture. It can be observed that the density gradients along the sample height decreases gradually as a result of intensive segregation of grains. At the bottom region, solid grains accumulate to form a dense sediment layer, which consolidate progressively under self-weight of the overlying grains. After  $[T] = 10.8$ , the bulk density at the bottom reaches a constant value of  $1965 \text{ kg/m}^3$ .

In this study, the positions of solid grains can be extracted during the simulation in the DEM. Figure 4.22 illustrates snapshots of settling column at four distinct settling times, in which a “numerical ruler” consisting of a series of equal-sized ticks is placed beside the sample to show the relative location of these grains. To visualize the grain motion, particles at different heights are coloured red and green. By tracking the positions of the uppermost grains, the position of the fluid–suspension interface can be obtained. However, as many grains would decelerate and consolidate at the bottom, there is no well-defined interface between the suspensions and sediments. Thus, a close investigation of several successive snapshots of the sample has been carried out to find out a stable point of sediment surface for a specific time. The evolution of the suspension–sediment interface is plotted as a dashed curve in Fig. 4.23.

**Fig. 4.21** Density profile of the fluid–solid mixture during the simulation



Based on Fig. 4.21, a series of constant density points along the prism at different settling time can be mapped onto Fig. 4.23. According to Fig. 4.23, the general variation patterns of constant density curves behave similarly to the theoretical results based on Kynch (1952) theory of sedimentation. To be more specific, the upper surface initially accelerates downwards to reach a constant velocity within a very short time, and then settles at a constant velocity towards the bottom. As the initial suspension is uniformly generated, the height against time curve is a straight line in the hindered settling zone on the graph. At the bottom the sediments, the grains decelerate until the velocity becomes zero. The results indicate that the points with water density are located just above the settling curve of the fluid–suspension interface. In the suspension, the bulk density ranges from 1000 to 1500 kg/m<sup>3</sup>. The constant density curves with densities smaller than the initial bulk density rise from

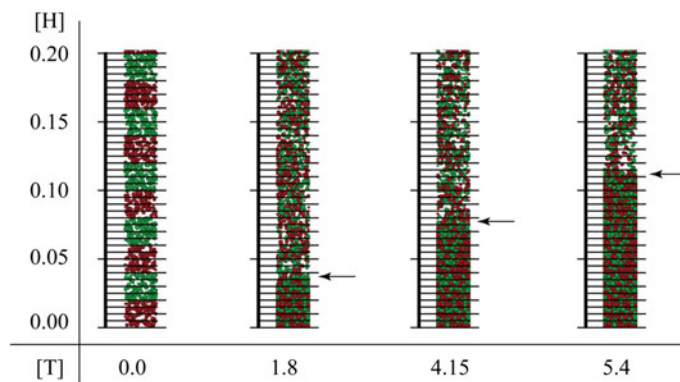


**Fig. 4.22** Measurement of sediment height (the arrow points out the sediment height)

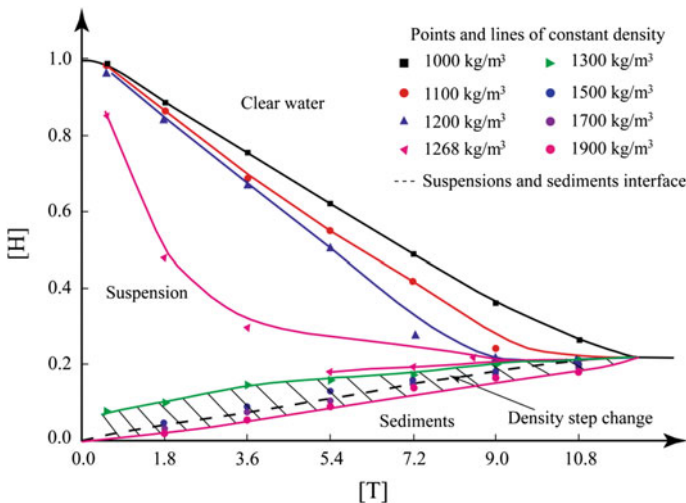


**Fig. 4.23** Height against time plot for constant density lines

the height axis, while other curves representing larger densities rise from the sediment surface. If the bulk density of the suspension is close to the initial bulk density, it would appear in both the suspension, and near the sediment surface due to the gradual segregation of solid grains (e.g. the curve of  $1268 \text{ kg/m}^3$ ). The observations in this research can match the analytical results by Tiller (1981) well.

As grains accumulate at the bottom, the soil bulk density changes gradually from the intermediate to dense state. This is represented by the density step between the suspension, zones of intermediate density and the top of relatively dense grain layer (i.e. the shaded zone on Fig. 4.23). In addition, the stable suspension–sediment interface curve passes through this region and is very close to the  $1700 \text{ kg/m}^3$  density curve, which suggests that a stable soil structure can be formed with density being equal to or slightly larger than  $1700 \text{ kg/m}^3$ .

#### 4.6.2.3 Excess Pore Water Pressure and Effective Stress

During the simulation, the excess pore water pressure ( $u$ ) along the prism is recorded in the CFD code, based on which, the evolution of the excess pore water pressures (normalized by the hydrostatic water pressure at the bottom:  $p_0 = \rho_f g H$ ) at the bottom is obtained (see Fig. 4.24). As the grains accelerate immediately after releasing, the excess pore water pressure increases quickly to reach the peak value of 0.17 at  $[T] = 0.54$ . After that time, a loose soil structure builds up at the bottom, and the excess pore water pressure dissipates gradually. A linear pressure dissipation period is observed between  $[T] = 0.54$  and  $[T] = 7.2$ . After  $[T] = 7.2$ , a

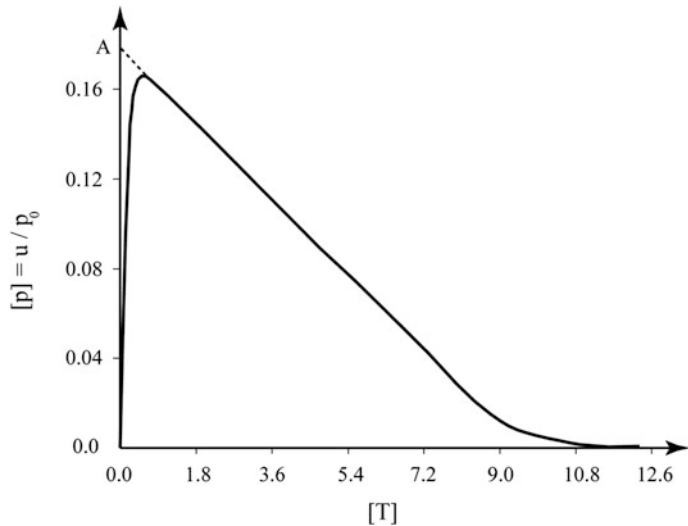


**Fig. 4.24** Evolution of pore pressure at the bottom of prism ( $p_0$  is the hydrostatic pore pressure)

sediment layer is formed at the base, and the excess pore water pressure dissipates slowly due to soil consolidation.

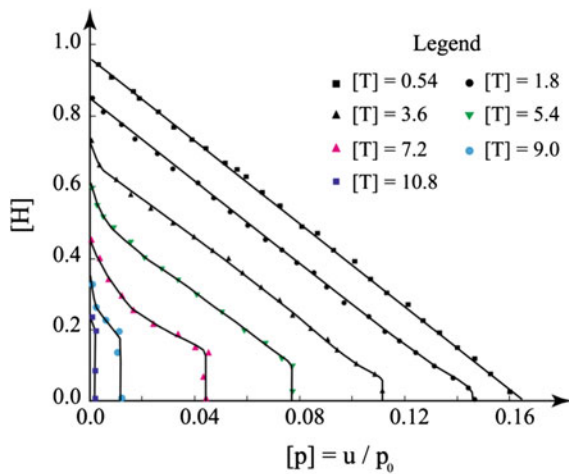
Considering the fact that part of the grains accumulated at the bottom before  $[T] = 0.54$ , the theoretical maximum excess pore water pressure is higher than the measured value. A rational estimation of the peak excess pore water pressure from Fig. 4.24 can be the intercept of the linear pressure line on the vertical axis at point A, with a normalized excess pore water pressure of 0.178. On the other hand, the analytical maximum excess pore water pressure can be calculated as the difference between the total stress and the hydrostatic water pressure of the system (see Eq. (4.76)) at the beginning of the simulation.

$$u_{e\_max}/p_0 = \frac{[n\rho_f + (1-n)\rho_s]gH - \rho_f gH}{\rho_f gH} = (1-n) \left( \frac{\rho_s}{\rho_f} - 1 \right) \quad (4.76)$$

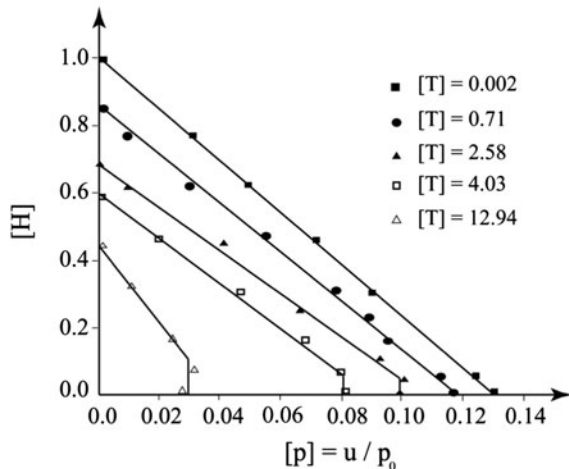
Based on the input parameters, the analytical maximum pore water pressure is calculated as 0.18 which can match the estimated peak value from Fig. 4.24 ( $\approx 0.178$ ).

The isochrones of excess pore water pressures are given in Fig. 4.25a. As only water exists in the region above the solid–water interface, the excess pore water pressure is zero. From  $[T] = 0.54$ , the excess pore water pressure builds up and varies linearly along the prism. As time passes by, the linear distribution pattern remains in the upper region of the prism, while at the bottom, there exists a region of constant excess pore pressure. This can be explained by the fact that once the grains stop moving, there is no relative flow between solid grains and fluid, and

**Fig. 4.25** Isochrones of excess pore water pressure along the prism at different time



(a) numerical results of the DEM-CFD coupling simulation



(b) results from Been [Been and Sills, 1981]  
(the time has been normalized by the characteristic settling time of a grain with diameter of 5  $\mu\text{m}$ )

therefore no excess pore water pressure gradient exists in the sediment. However, in the suspension, the solid grains can settle downwards continuously, and thus, the linear distribution pattern can be maintained there. A qualitative comparison is made between the numerical results (Fig. 4.25a) and the experimental results from Been and Sills (1981) (Fig. 4.25b). Even though the materials used in the numerical and experimental models are very different, the general features of the isochrones of excess pore water pressure presented in a dimensionless form are qualitatively the same.

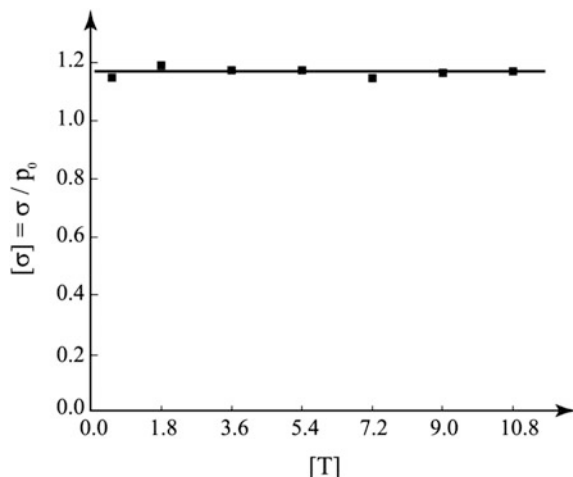
During the simulation, the total stress acting on the bottom of the prism is calculated by the pore pressure and contact forces, as

$$\sigma = p_s + u + \frac{F}{S}, \quad (4.77)$$

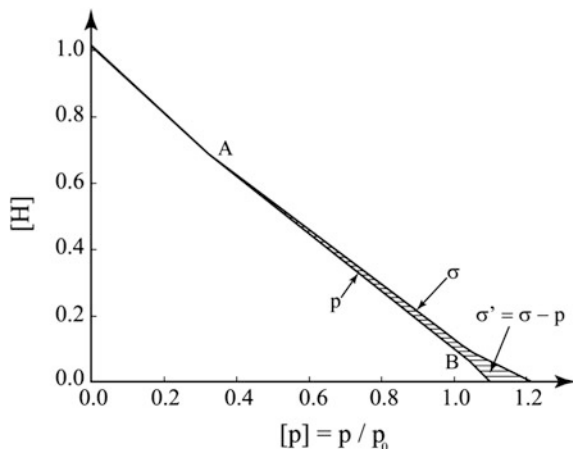
where  $p_s$  is the hydrostatic pressure;  $u$  is the excess pore water pressure;  $F$  is the contact force exerted by sediments on the bottom of prism;  $S$  is the cross section area of the prism.

Figure 4.26 shows that the total stress measured at the base of the prism is almost constant throughout the simulation. This phenomenon indicates that the periodic boundary condition used in the simulation can effectively reduce the wall friction effects on the overall settling behaviour of solid grains. According to Been (1980), the total stress of the suspension along the height of the prism can be evaluated by integrating the bulk density of suspensions, while the effective stress is calculated by subtracting the measured pore water pressure from the total stress. Figure 4.27 illustrates that the distribution of pore water pressure and total stress along the prism height at  $[T] = 3.6$ . At this time instant, the solid grains initially located at the upper part of the prism (above point A) have already settled downwards, such that only water exists there. Thus, the pore water pressure is equal to the total stress. In the suspension (between points A and B), grains can either settle at a constant velocity (near Point A) or collide with each other forming a loose structure (near Point B). The weight of solid grains is partly or wholly supported by the fluid viscous drag and hydrostatic forces. Thus, the curve of pore water pressure deviates gradually from the total stress curve, indicating that the effective stresses occur within the sample. In the sediments (below point B), the soil structure can sustain the overlying loads and a relatively large effective stress exists there.

**Fig. 4.26** Total stress at the base of the bottom

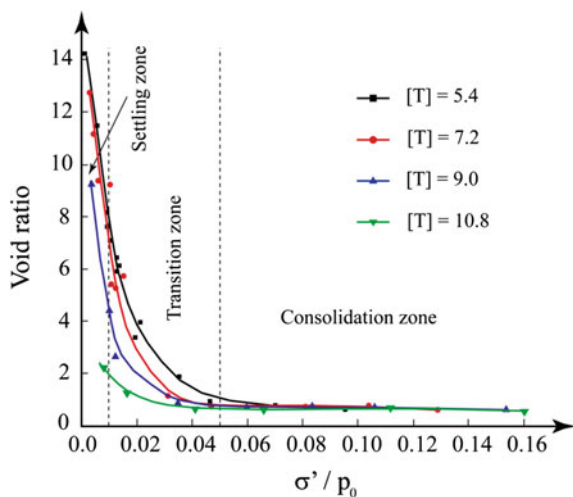


**Fig. 4.27** Stress distribution along the prism at  $[T] = 3.6$



The relationship between the soil void ratio and normalized effective stress ( $\sigma'$ ) within the sample at different settling times is shown in Fig. 4.28. According to Fig. 4.28, three distinct zones of the relationship between effective stress and void ratio can be identified: settling, transition and consolidation zones. The settling zone appears when the normalized effective stress is smaller than 0.01. In this zone, the void ratio varies widely from 4.0 to 14, indicating that the soil is extremely compressible. In the transition zone, a loose soil structure begins to build up and the effective stress increases from 0.01 to 0.05, while the void ratio decreases from 5.0 to 0.5 gradually. However, no unique relationship between void ratio and effective stress is observed. In the consolidation zone, the compressibility of soil is low and the void ratio varies very little.

**Fig. 4.28** Relationship between the void ratio and normalized effective stress at various simulation times (the data points represent results from locations equally spaced along the column)



#### 4.6.2.4 Energy of Solid Grains in the System

The grain settling process is accompanied by energy conservation and transformation. Initially, a static suspension is generated within the prism. The total energy is defined as the summation of potential energy of each individual particle before sedimentation.

$$E_0 = \sum_{i=1}^{N_p} m_i g H_i, \quad (4.78)$$

where  $m_i$  and  $H_i$  are the mass and height of a single particle  $i$ , respectively;  $N_p$  is the total number of grains. In this model, the initial total potential energy ( $E_0$ ) is 0.896 J.

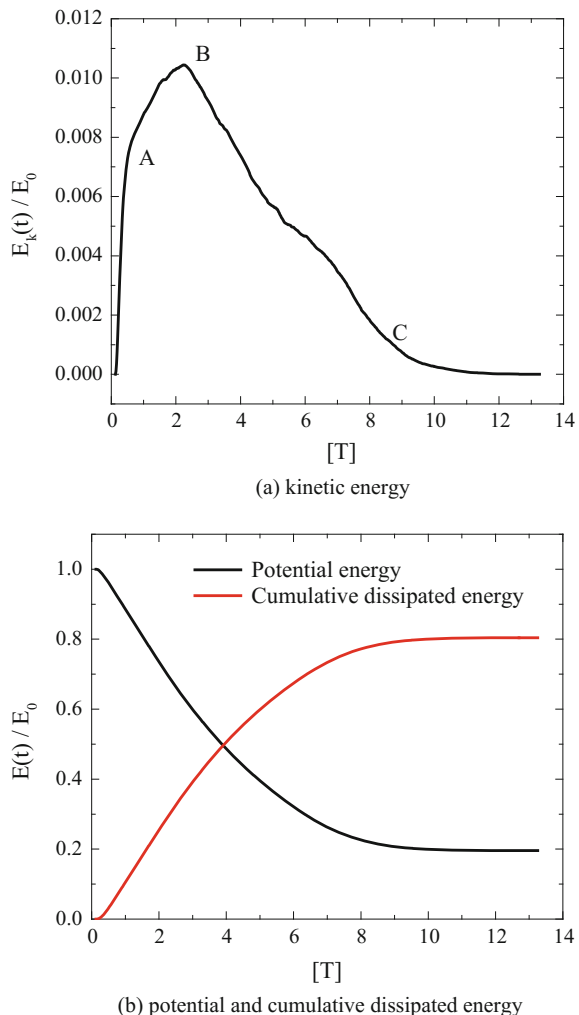
As the simulation continues, the settling velocity increases as part of the initial potential energy transforms into the kinetic energy. The kinetic energy of solid grains at a specific time is defined as the summation of translational and rotational kinetic energy,

$$E_k = \frac{1}{2} \sum_{i=1}^{N_p} \left( m_i |V_i|^2 + I_i |\omega_i|^2 \right), \quad (4.79)$$

where  $|V_i|$  and  $|\omega_i|$  are the magnitudes of the translational and rotational velocity of particle  $i$ ;  $I$  is the moment of inertia, defined as  $I = 2mR^2/5$  for a spherical particle.

As the motion of solid grains is hindered by fluid, the major portion of potential energy is dissipated via the fluid viscous drag forces. The dissipated energy transforms into heat and fluid potential and kinetic energy. When particles collide or slide over each other, part of the kinetic energy can be dissipated via plastic contact and inter-particle friction. Therefore, the cumulative energy dissipation is simply calculated as the difference between the initial total energy and the sum of potential and kinetic energy at a specific time. Figure 4.29 illustrates the evolution of kinetic, potential and cumulative dissipated energy throughout the simulation. According to Fig. 4.29a, it can be observed that the kinetic energy only amounts to a small fraction of the total energy, which indicates that the settling velocities of grains in the fluid are very small. Initially, as the solid grains accelerate to settle downwards from rest, the kinetic energy increases linearly until it reaches point A. After point A, an increasing number of grains would settle at constant velocities and some grains would also deposit onto the bottom floor. Thus, the increasing rate of kinetic energy decreases gradually. At point B, the kinetic energy of the granular system reaches the maximum value, which amounts to only 1% of the total energy. After point B, solid grains would continuously deposit on the bottom floor, which is represented by a gradual decrease of kinetic energy. After point C, a loose granular layer is built up at the bottom and the corresponding energy would gradually

**Fig. 4.29** Evolution of energy [the value of energy is normalized by the initial total energy ( $E_0$ )]



approach a constant value due to soil consolidation. Figure 4.29b indicates that throughout the simulation, around 80% of the initial total energy has been dissipated.

#### 4.6.2.5 Force Chain of the Sediments

During the grain sedimentation, the sediments accumulate gradually at the bottom of the prism to form a structured soil layer, which can be visualized by plotting the contact force chains of the whole granular packing, as shown in Fig. 4.30. In these graphs, straight lines are used to connect the centres of each pair of particles in

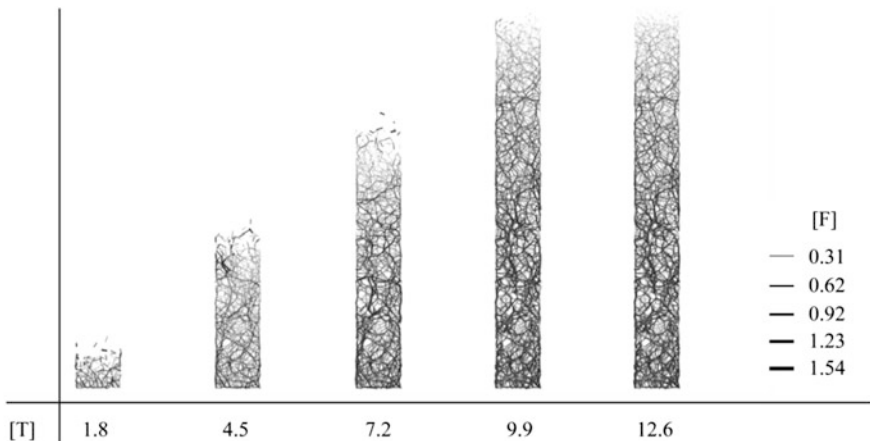


**Fig. 4.30** Force chains of the sediments at different time

contact. The width of these lines is proportional to the magnitude of contact forces, while the orientation aligns to the direction of contact force vector. The contact force is normalized by the characteristic hydrostatic force acting on the cross section of a solid particle (e.g. the diameter is  $D$ ) at the bottom of the prism, as shown in Eq. (4.80).

$$[F] = \frac{F}{(\rho_s - \rho_f)gH_i D^2} \quad (4.80)$$

By plotting the contact forces of all the grain contacts as straight lines in the model, a graph of force chain can be obtained. At the beginning of the simulation, the sediment layer is very thin, such that the contact forces between grains are very small. As the soil structure builds up gradually, the magnitude of contact force is mainly controlled by the self-weight of solid grains. Due to soil consolidation, the contact forces at the bottom increase gradually. The final stable soil structure has strong force chains preferable orient vertically, indicating that the self-weight of soil has a significant influence on the distribution of contact forces.

## 4.7 Conclusions

This chapter sets out to investigate the granular sedimentation via the DEM–CFD coupling algorithm. The simulations of fluid flow through a porous soil sample and granular batch sedimentation were used to validate the DEM–CFD coupling code. For the first test, the model of water flowing through a granular sample is used to

study the behaviour of soil seepage. Based on this study, conclusions can be drawn as

- (i) The numerical results have confirmed the statement by Trussell and Chang (1999) that the fluid flow through a porous media can be in either laminar or turbulent regime based on the Reynolds number. In the laminar regime, the permeability of soil is calibrated via the relationship between hydraulic gradient and flow velocity. The numerical results can match the analytical and empirical ones well.
- (ii) In the turbulent flow regime, the relationship between the hydraulic gradient and flow velocity has been studied and compared with the empirical correlations by Ergun (1952) and Trussell and Chang (1999). The analyses indicate that the DEM–CFD coupling model can capture realistic hydraulic behaviour of fluid flow in a wide range of Reynolds number (i.e. up to 1000). The numerical results can match the empirical ones by Trussell and Chang (1999) well.

In modelling the granular sedimentation in water, the numerical results obtained for the settling of a single particle can match the available analytical solutions very well. This research also provides criterion of numerical accuracy in the DEM–CFD coupling calculations: the size ratio between the fluid mesh cell and particle diameter should be larger than 5. It also shows that the use of periodic boundary in the lateral directions of the fluid domain can effectively reduce the fluid boundary wall friction effects. The findings of granular batch sedimentation can be concluded as

- (i) During the batch sedimentation, progressive segregation of solid grains along the prism can be visualized by the particle size distribution curves at different locations within the sample. The segregation is significant near the upper region of the model, while it is not very evident in the middle and bottom regions. This is partly because only a narrow particle size is used in the simulations. Due to the grain segregation, coarse grains can accumulate at the bottom, leaving the finer ones settle onto the upper surface of the deposit. As a result, the gradients of bulk density profile curves increase gradually.
- (ii) In the suspension zone, any constant density curve with a density smaller than the initial bulk density originates from the height axis, while others start from the sediment surface. At the end of the simulation, the bulk density of the sediments reaches a constant value. The curves describing the vertical downward trajectory of the fluid—suspension interface and the increase of suspension—sediment interface can match the theoretical results proposed by Kynch (1952) very well.
- (iii) As solid grains continuously settle downwards, forming a loose sediments layer at the bottom of the prism, the sediments consolidate slowly under the self-weight of overlaying grains. During this process, the excess pore water pressure builds up and dissipates slowly. The normalized maximum excess pore water pressure of the suspension is 0.178, which is very close to the

analytical value (i.e. 0.18). When presented as dimensionless quantities, the isochrones of excess pore water pressure can qualitatively match the experimental results by Been and Sills (1981). Throughout the simulation, around 80% of the initial potential energy of grains has been dissipated via water viscous force and inter-particle collision/friction.

In this chapter, a DEM–CFD coupling formulation is presented for the investigation of grain sedimentation in fluids. Many other applications of the formulation are possible, e.g. submarine landslides, mudflows, river scouring, etc. The computational efficiency of the numerical model depends highly on the numbers of particles present and the size of the mesh cells in the CFD model.

# Chapter 5

## Investigation of Submerged Debris Flows

This chapter presents a numerical investigation of submerged debris flows using the DEM–CFD coupling model. The same DEM model configuration for granular column collapse as that discussed in Chap. 3 has been used in this research to simulate the mechanical behaviour of solid particles, while an incompressible, viscous fluid flow model has been introduced to capture the hydraulic behaviour of fluid flow in the submerged environment. This research aims to shed light on the fluid–solid interaction and the hydraulic properties of submerged debris flows. Conclusions are drawn with regard to the ability of the DEM–CFD coupling algorithm to model the sediment transportation and deposition processes.

### 5.1 Model Configuration

The initial static fluid–solid mixture system is shown in Fig. 5.1. The configuration of the granular column model and the notations are the same as those discussed in Chap. 3. The DEM model is bounded by the CFD fluid domain as represented by a dashed prism. The boundary conditions of the CFD model are set as below:

- (i) As the plane strain conditions are desired in the simulation, the fluid model has a periodic boundary in the lateral direction, labelled as E.
- (ii) An open air boundary condition is used in the upper boundary (G). The back (F) and frontal (H) walls have slip boundary conditions. The bottom boundary (I) has a non-slip boundary condition.

The generation of the DEM sample has been detailed in Chap. 3 and the same procedure is employed in the current simulations.

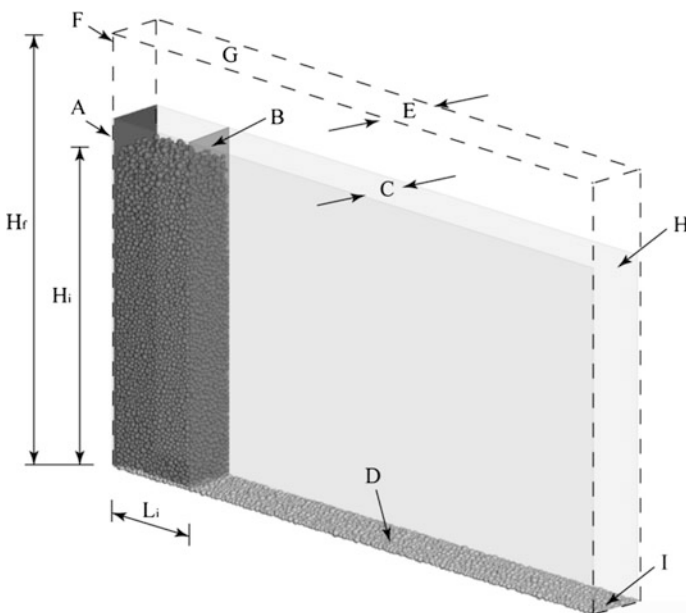


**Fig. 5.1** Model configuration of the submerged debris flow

## 5.2 Physical Properties of Sediments

Typical submerged landslides can involve solid materials of various sizes. Several site investigations provide evidence that sediments transported to a long distance away from their original locations are generally very fine materials, such as clay, mud and fine silt (Prior et al. 1984; Lipman et al. 1988; Hubble et al. 2012). The deposits consist of sand overlain by mud (Talling et al. 2007). An example of a submarine landslide is the Kitimat landslide, British Columbia ( $53^{\circ} 59'N$ ,  $128^{\circ} 41'W$ ) occurred in 1975, as shown in Fig. 5.2. It can be observed that the major coarse debris materials (e.g. breccia and gravel) are deposited near the toe of the original slope, while the fine materials (e.g. clay, mud and silt) are transported to a long distance away from the source region. Observations have shown that the debris flow has extended to more than 5 km away from the delta slope over the almost flat floor of the fjord (Prior et al. 1984). The sediment samples have been obtained from seven piston cores, as labelled in Fig. 5.2. The particle-size distributions of four samples are summarized in Fig. 5.3 and the main conclusion can be drawn as:

- (i) The size of sediments are normally finer than 1 mm for different samples obtained with piston cores;

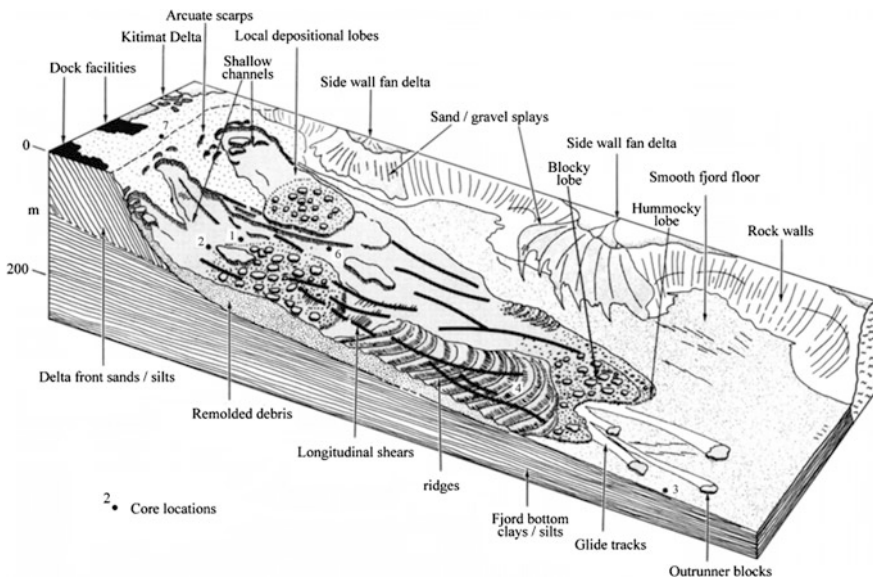
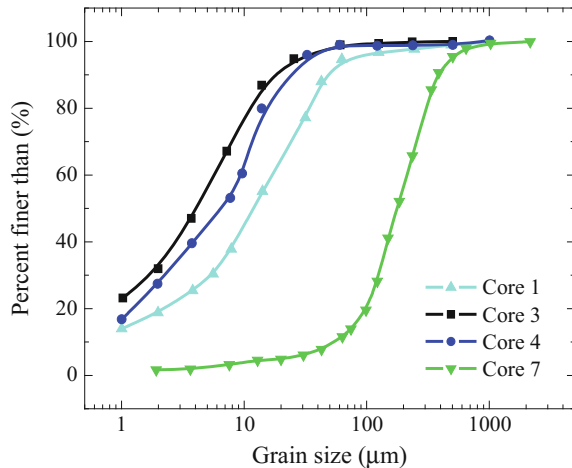


**Fig. 5.2** Schematic view of the sea floor near the Kitimat delta (after Prior et al. 1984)

**Fig. 5.3** Cumulative grain-size distribution curves of bulk samples from cores 1, 3, 4, and 7



- (ii) A large portion of coarse grains are found near the crown of the slide (e.g. core 7), while finer particles are found near the deposit front (e.g. core 3 and 4), which suggests that the fine grains can travel a longer distance than the coarser ones.

Similar results are obtained from dredged samples in the southeastern Australian continental margin landslides (Hubble et al. 2012), in which a large amount of

grains have particle sizes ranging from 2.0 to 200  $\mu\text{m}$ . Due to the limitation of the DEM model, the simulations cannot include all particles with a wide range of sizes. As the main purpose of the current study is to demonstrate the capability of the DEM–CFD model in analysing the mechanical behaviour of submerged debris flows, the numerical model uses a relatively coarse sand grains with a narrow particle-size distribution (see Sect. 2.2.1). In order to reproduce realistic mechanical and hydraulic behaviour of fine grains using the current DEM configuration, proper scaling laws based on the dimensional analyses will be used. By doing so, the computational cost can be acceptable for simulations consisting of a reasonable number of grains. A detailed analysis will be provided in the following sections.

### 5.3 Dimensional Analysis

A dimensional analysis has been performed for numerical investigations of submerged debris flows, based on a simple granular column collapse model. As the DEM model configuration for dry and submerged debris flows are the same, the same set of parameters will be used. The parameters involved in the simulations are listed in Table 5.1, where the units are expressed using the fundamental dimensions of  $M$ ,  $L$  and  $T$  (i.e. mass, length and time). Performing the dimensional analysis, and assuming all the microscopic contact parameters in the DEM model are the same as

**Table 5.1** Input parameters of the DEM–CFD model

	Parameter	Symbol	Unit of measure
Independent parameters	Initial model length and height	$L_i, H_i$	[L]
	Particle diameter	$D$	[L]
	Particle density	$\rho_s$	[ML <sup>-3</sup> ]
	Gravitational acceleration	$g$	[LT <sup>-2</sup> ]
	Sample porosity	$n$	[–]
	Normal stiffness	$K_n$	[MT <sup>-2</sup> ]
	Shear stiffness	$K_s$	[MT <sup>-2</sup> ]
	Particle friction angle	$\theta$	[–]
	Coefficient of rolling stiffness	$\beta$	[–]
	Coefficient of plastic moment	$\eta$	[–]
Dependent parameters	Fluid density	$\rho_f$	[ML <sup>-3</sup> ]
	Fluid viscosity	$\mu$	[ML <sup>-1</sup> T <sup>-1</sup> ]
	Deposit length and height	$L_f, H_f$	[L]
	Particle velocity	$V$	[LT <sup>-1</sup> ]
	Flow duration time	$t$	[T]

The symbol “[–]” denotes that the parameter is inherently dimensionless

those used in modelling dry granular flows, the relationship between the independent and dependent dimensionless groups is written as:

$$([L], [H], [V], [T]) = f(a, [\varepsilon], [\rho], [S], Re, n, \theta, v, \beta, \eta) \quad (5.1)$$

In the current analysis, the major dimensionless groups for the DEM model will be kept the same as those obtained in Chap. 3. However, due to the presence of water, some previously used dimensionless groups in the DEM model should be modified and new groups in the DEM–CFD coupling model will be formulated accordingly. These groups include the physical properties of sediments, microscopic particle contact parameters and fluid flow properties. The two new dimensionless groups  $[\rho]$  and  $Re$ , known as density ratio and Reynolds number, are expressed as:

$$[\rho] = \frac{\rho_s}{\rho_f} \quad (5.2)$$

$$Re = \frac{\rho_f D v_0}{\mu} = \frac{\rho_f g D^3 (\rho_s - \rho_f)}{18 \mu^2} \quad (5.3)$$

The Reynolds number is defined at the microscopic grain-size scale by using the characteristic settling velocity of a single sphere in the laminar flow regime (see Chap. 4). However, as the fluid flow may not be laminar, Eq. (5.3) only defines the characteristic Reynolds number of a submerged landslide and may not be the exact value for a real fluid flow. Alternatively, the Reynolds number can be expressed in a general form as:

$$Re_{\text{micro}} = \sqrt{\frac{\rho_f g (\rho_s - \rho_f)}{18}} \frac{D^{3/2}}{\mu} \quad (5.4)$$

Some previously defined parameters, such as  $[V]$ ,  $[T]$  and  $[\varepsilon]$ , should be modified based on the hydrodynamic processes (e.g. settling and consolidation) under analysis. The characteristic strain of the model is defined as:

$$[\varepsilon] = \frac{(\rho_s - \rho_f) g H_i (1 - n)}{K_n / D} \quad (5.5)$$

The dimensionless debris flow velocity and duration time are obtained by studying the grain settling and soil consolidation processes, as detailed in the following section.

### 5.3.1 Discussion of the Dimensionless Groups

As discussed in Chap. 4, the constant relative settling velocity ( $v_0$ ) of a single particle is reached when the viscous drag force is balanced by the buoyant gravity force.

$$v_0 = \frac{gD^2(\rho_s - \rho_f)}{18\mu} \quad (5.6)$$

The dimensionless particle settling velocity is defined as the ratio of the particle settling velocity ( $v$ ) to the constant settling velocity.

$$[V] = \frac{v}{v_0} = \frac{18\mu v}{gD^2(\rho_s - \rho_f)} \quad (5.7)$$

The characteristic settling time is defined as:

$$t_s = \frac{H_i}{v_0} = \frac{18\mu H_i}{gD^2(\rho_s - \rho_f)} \quad (5.8)$$

The dimensionless time used in the simulation is defined as the ratio of the duration time of the submerged debris flow to the characteristic settling time, as:

$$[T_s] = \frac{t}{t_s} = \frac{gD^2(\rho_s - \rho_f)t}{18\mu H_i} \quad (5.9)$$

As Eq. (5.6) represents the constant relative settling velocity of a single particle in the laminar fluid flow regime, it is not applicable for flows in the Forchheimer, Transition and Turbulent regimes. Thus, an appropriate evaluation of the particle settling velocity should be made numerically by using Eq. (4.74). However, in the definition of dimensionless groups, Eq. (5.6) will be used as the characteristic settling velocity of a granular system.

In the consolidation process, the granular assembly undergoes compression due to self-weight. Excess pore water pressure can build up within the sample if soil permeability is low. As time passes by, the pore pressure would dissipate gradually to zero and the effective stress within the granular assembly increases to its maximum value. Thus, the consolidation process is time-dependent and a dimensionless group to quantify this process should be based on the consolidation time. One obvious group is obtained from Terzaghi's consolidation theory (Terzaghi 1943) which defines the dimensionless time factor as:

$$T_v = \frac{c_v t}{H^2}, \quad (5.10)$$

where  $t$  is the consolidation time;  $c_v$  is the coefficient of consolidation, defined as:

$$c_v = \frac{k}{m_v \rho_f g}, \quad (5.11)$$

where  $m_v$  and  $k$  are coefficients of volume compressibility and permeability, which can be assumed to be constants, and depend on particle-size distribution, shape and soil structure.

As discussed in Chap. 3, the coefficient of soil permeability can be approximated as:

$$k = \frac{\rho_f g D^2 n^{5.7}}{18\mu(1-n)} \quad (5.12)$$

The coefficient of volume compressibility is defined as (Chen et al. 2011):

$$m_v = \frac{D}{K_n} \quad (5.13)$$

By substituting Eqs. (5.13) and (5.12) into Eq. (5.11), one can get

$$c_v = \frac{k}{m_v \rho_f g} = \frac{D n^{5.7} K_n}{18\mu(1-n)} \quad (5.14)$$

Substituting Eq. (5.14) into (5.10), the dimensionless consolidation time becomes,

$$T_v = \frac{c_v t}{H^2} = \frac{t D n^{5.7} K_n}{18\mu(1-n) H^2} \quad (5.15)$$

Equation (5.15) indicates that the consolidation time of a granular assembly depends on both the macroscopic sample properties (i.e.  $H$ ,  $n$  and  $\mu$ ) and the microscopic particle properties (i.e.  $D$  and  $K_n$ ). The consolidation time can be long in view of the following conditions:

- (i) If the soil sample is very thick, the seepage path of fluid flow can be very long;
- (ii) If the fluid is very viscous, the fluid velocity can be very small;
- (iii) If the grain is very fine or the soil is dense, the sample permeability is very low.

The submerged debris flow is a very complicated geotechnical phenomenon, involving both grain settling and soil consolidation. Depending on the research areas of interest, either Eqs. (5.9) or (5.15) can be used as the dimensionless time in the analyses. The derivation of governing dimensionless groups in the above investigates the physics of submerged debris flows, instead of analysing the units of

each parameter, to get the dimensionless groups. Although there is some freedom in the choice of the dimensionless parameters (Palmer 2008), such a choice can closely match the problem under analysis.

### 5.3.2 Summary of the Dimensionless Groups

Any numerical simulation attempting to reproduce the general behaviour of real in situ landslides should have the same values of governing dimensionless groups as those in real cases. Therefore, the input parameters should be scaled so that proper values of dimensionless groups can be obtained. The corresponding output parameters can be obtained by using scaling laws derived from dimensional analyses. The ranges of some input dimensionless groups are shown in Table 5.2 (*N.B.* the value of aspect ratio is not listed here, because it is not applicable to real and experimental observations.).

According to Table 5.2, it can be concluded that the current numerical model can reproduce realistic values of model characteristic strain, density ratio and Reynolds number, while it is unable to reproduce correct model size ratio. This conclusion indicates that it is possible to simulate grain settling behaviour by small-scale numerical models, while it is very difficult to model the correct consolidation time. This is due to the fact that the consolidation of soil is influenced by many factors, especially by the model size, as characterized by the group [S]. The dimensionless consolidation time can be rewritten as:

$$T_v = \frac{tDn^{5.7}k_n}{18\mu(1-n)H^2} = \frac{tn^{5.7}k_n}{18\mu(1-n)H[S]} \quad (5.16)$$

The range of model size ratio in real debris flows is far larger than that used in the current numerical simulations. As the small-scale numerical model cannot reproduce correct values of [S], it is impossible to capture the full picture of consolidation. Therefore, the current study mainly focuses on the propagation and

**Table 5.2** Typical ranges of dimensionless groups (reference data can be found in Appendix A)

	[ $\varepsilon$ ]	[ $\rho$ ]	[S]	[ $Re$ ]
Real landslides	[8.8e-5, 0.029]	[1.95, 2.9]	[ $1.1 \times 10^5$ , $9.33 \times 10^8$ ]	[0.0004, 882.2]
Laboratory tests	N/A	[2.0, 2.7]	N/A	[0.0005, 126.1]
Numerical simulations	[8.9e-5, 0.09]	2.65	[25, 250]	[8.5, 85]

deposition of submerged debris flows, in which the flow duration time is quantified by the dimensionless settling time.

In a typical submerged landslide, the fluid material is generally sea water with a density of  $1025 \text{ kg/m}^3$  and viscosity of  $0.001 \text{ Pa s}$ . The solid materials involved can range from very fine clay to coarse gravel and boulder. According to Hubble et al. (2012), the bulk density of sediments from several landslide sites in the southeastern Australia ranges from  $8.9$  to  $11.8 \text{ kN/m}^3$ . Considering the loosely packed state of sediments at seabed, it is assumed that the density of a single solid grain is  $2650 \text{ kg/m}^3$ , which can roughly match the density of coarse quartz grains. Thus, the density ratio  $[\rho]$  of 2.6 is used in this research.

Analyses of the dimensionless groups listed in Eq. (5.1) show that some variables can either change systematically in association with other variables or are constrained by the presence or absence of certain conditions. These relationships may reveal the fundamental mechanisms that control the submerged debris flows and provide insights into how they can be mobilized to run a very long distance (Lee et al. 1991). Although a complete analysis of all these relationships is beyond the scope of this research, the author believes that two particular dimensionless groups are worth investigating: the characteristic strain,  $[\varepsilon] = (\rho_s - \rho_f)gH_iD/K_n$  and the Reynolds number,  $Re = \sqrt{\frac{\rho_f g(\rho_s - \rho_f)}{18\mu}} D^{3/2}$ . These two groups are thought to be the most significant ones, governing the motion of debris flows. As real submerged debris flows can have a wide range of sizes and the solid materials involved are of various sizes, these two dimensionless groups would have a coupled influence on the motion of debris flows. A detailed parametrical analysis of these groups will be provided in the following sections.

The current research using small-scale numerical models is unable to reproduce the correct model size ratio due to the constraint of computational power. However, this analysis aims to reveal the general features of submerged debris flows based on simple and well controlled conditions. Even though the numerical results cannot reflect the complete mechanical and hydraulic behaviour of real submerged debris flows, some meaningful conclusions can still be drawn regarding the capability of the DEM–CFD coupling model.

## 5.4 Modelling of Small-Scale Submerged Debris Flows

In this section, the numerical results of small-scale submerged debris flows are presented, with special focus on the mechanical and hydraulic behaviour of granular particles and fluid. The input parameters for the related DEM–CFD coupling simulations are listed in “SS1” of Appendix C.

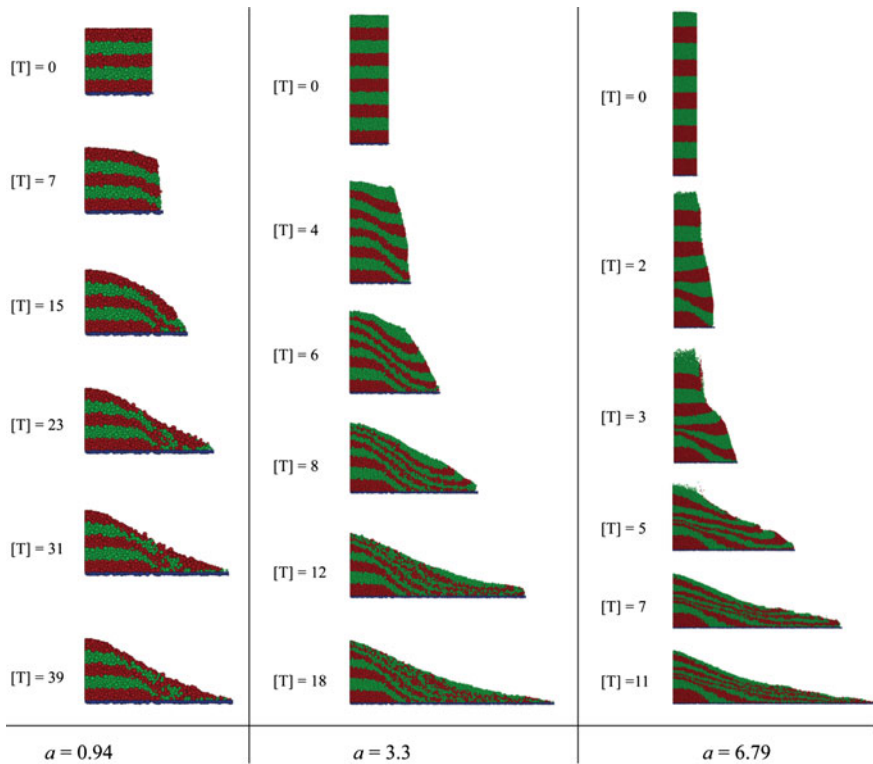
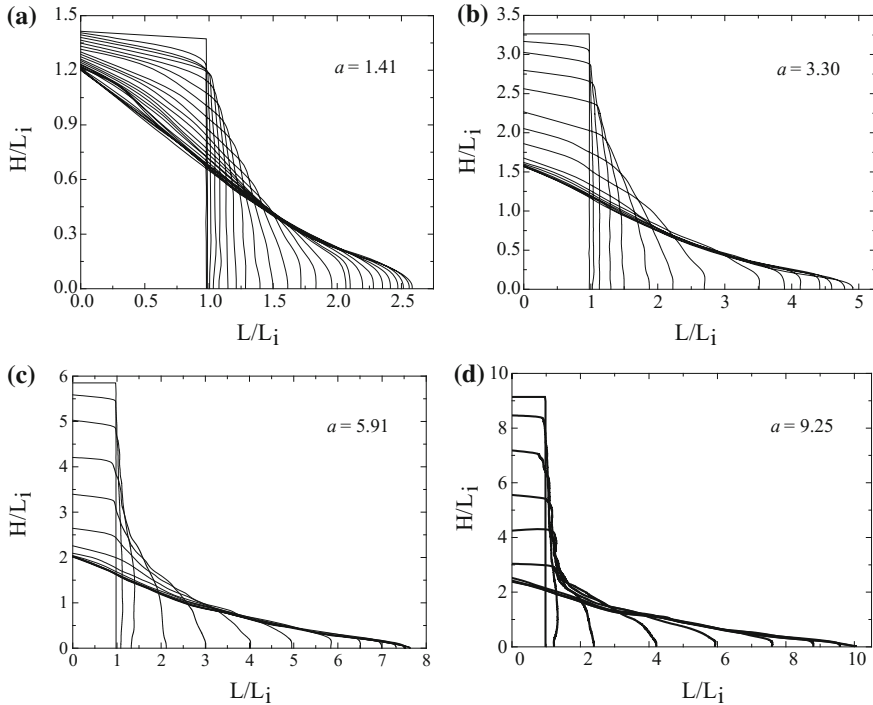


Fig. 5.4 Three sequences of snapshots for the collapse of granular columns ( $Re = 85$ )

#### 5.4.1 Deformation of the Granular Assembly

The dynamic motion and depositional morphology of granular assemblies are illustrated by a sequence of snapshots in Fig. 5.4. From these images, three distinct patterns of debris motion can be identified. For granular columns with small aspect ratio (i.e.  $a = 0.94$ ), only the upper front region of the granular mass crumbles downwards, tilting and thinning into a grain layer on the horizontal floor. The final deposit has a roughly “truncated cone” shape with the same height as the initial column height. Throughout the simulation, a static pile region exists at the bottom left of the granular assembly, above which, intensive shearing occurs between particles with high velocity gradients.

For columns with larger aspect ratios, the major granular mass is involved in motion. Depending on the value of aspect ratio, the solid grains would go through a process of either sliding or sliding plus free settling. For intermediate aspect ratio (i.e.  $a = 3.3$ ), the slope failure is mainly by sliding, in which the granular materials in the upper region would descent and spread outwards along the floor. Intensive shearing occurs at the surface between the static pile and the upper moving mass.



**Fig. 5.5** Evolution of granular profiles (Profiles normalized by the initial column width and are traced at successive simulation time ( $\Delta[T] = 1.0$ ),  $Re = 85$ )

The final deposit has a conical shape, and the height of which is smaller than the initial column height. For large granular columns (i.e.  $a = 5.91$ ), a short period of free settling exists for grains locating at the upper part of the model, in which the solid particles suspend in water and move slowly.

According to Fig. 5.4, it can be observed that granular columns would go through very large deformations during the propagation of debris flows. The evolution of debris profiles can vary dramatically for different granular columns, as shown in Fig. 5.5.

For columns with small aspect ratios (i.e.  $a = 1.41$ ), only a small fraction of granular materials is involved in motion. As the solid materials collapse onto the ground floor, the upper surface of the sample inclines gradually until the angle of repose is reached. The final deposit has a shape of curved trigonal prism, with its height close to the initial column height. As the value of aspect ratio increases gradually, the majority of debris materials are involved in motion. The granular materials would stretch along the horizontal floor, forming an elongated and thin granular layer. The general patterns of debris flow discussed above are similar to

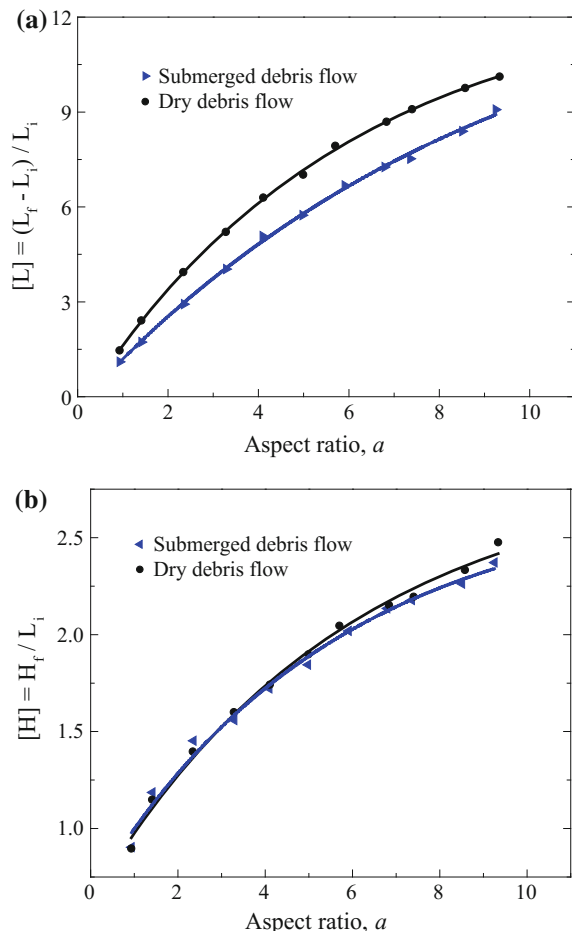
those analysed in Chap. 3 for dry debris flows. The only difference is that the profiles of submerged granular deposits are relatively flat and very few dispersed grains are observed in the outermost region.

### 5.4.2 Influence of Initial Column Aspect Ratio

As a preliminary study, the simulations of submerged debris flows have been performed using the same DEM model configurations as those used in Chap. 3. This numerical model has effectively revealed the important influence of granular column aspect ratio on the dynamic motion and depositional morphology of debris materials.

Figure 5.6 compares the relationship between normalized run-out distance, deposit height and the column aspect ratio for the submerged and terrestrial dry granular flows. It can be concluded that the submerged debris flows have a lower

**Fig. 5.6** Comparison between numerical results of submerged and dry granular flows ( $Re = 85$ ).  
**a** Relationship between the normalized run-out distance and column aspect ratio;  
**b** relationship between the normalized height and column aspect ratio

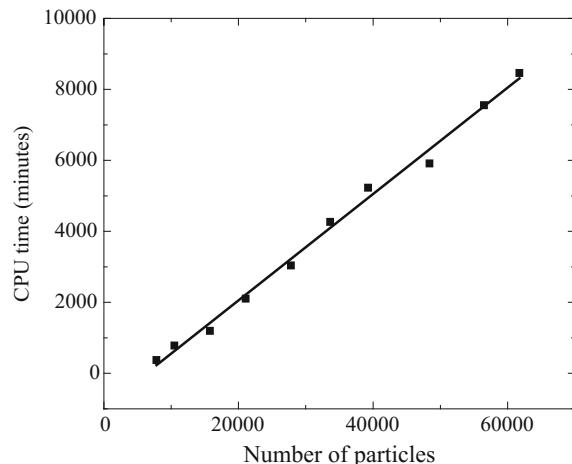


mobility than the dry granular flows, while they have almost the same final deposit heights. This phenomenon can be explained by the fact that the kinetic energy of submerged grains would dissipate quickly via the fluid viscous drag forces. Even though the positive excess pore pressure generated within the sediments can decrease the inter-particle friction, its magnitude is still too small to mobilize the debris materials to travel a long distance. In addition, if the initial granular assembly is dense, the negative excess pore water pressure generated during the sample dilation would inhibit the motion of solid grains (Iverson et al. 2000).

In the current analyses, the calculations were carried out on a desktop PC using three of the four cores of an Intel® Core™ i7 CPU (2.93 GHz). The computational time is linearly related to the number of particles in the granular model, as shown in Fig. 5.7.

The use of computer cluster for the simulations might help decrease the computational time. However, as the current MPI parallelization is based on a domain decomposition strategy, the parallel efficiency depends highly on the choice of subdomains. For the DEM model with a plane strain condition, the domain decomposition is normally done along the zero-strain direction, so that the number of grains in each subdomain is approximately the same. Decomposition of domains in other directions should be carried out carefully, because the computational time is mainly controlled by the processor running the slowest. In addition, the data exchange between subdomains can also take a long time. For instance, the computation can be very costly for one subdomain containing a huge number of grains, while the other subdomains contain only few grains. Thus, the current DEM–CFD model is not appropriate for simulations with a huge number of grains on a computer cluster.

**Fig. 5.7** Computational time used in simulations (the DEM time step is  $1.0 \times 10^{-7}$  s,  $Re = 85$ )

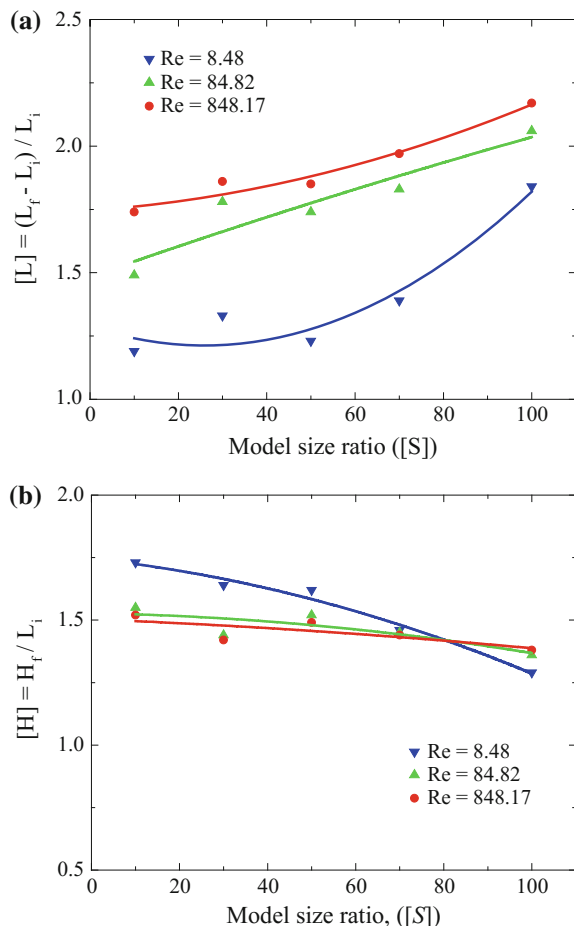


### 5.4.3 Influence of Model Size Ratio

As discussed in Chap. 3, the model size ratio, defined as the ratio of the model height to the mean particle diameter, has significant influence on the motion of dry granular materials. For the dry granular flows, a value of 40 has been identified as the threshold of the model size ratio. If  $[S]$  is larger than 40, the numerical results are independent of the choice of  $[S]$ . However, in the submerged environment, this dimensionless group should be calibrated for different flow conditions.

Figure 5.8 compares the normalized run-out distance and deposit height for samples of various model size ratios. Results are also examined at increasing Reynolds number to investigate the combined effect of flow property and model size ratio. According to Fig. 5.8, it can be observed that the mobility of debris flow increases with the model size ratio. This phenomenon is particularly evident for

**Fig. 5.8** Influence of  $[S]$  on  
**a** the run-out distance, and  
**b** deposit height



flows with very small Reynolds number, in which, the fluid viscous effect plays a significant role in governing the debris motion.

Ideally, the value of  $[S]$  should be chosen as large as possible, so that the numerical model can be comparable with the real submerged debris flows. However, the current DEM model has the difficulty in simulating the behaviour of granular assemblies composed of a huge number of grains due to the unacceptable long computational time.

Figure 5.9 illustrates the computational time required in simulating debris flows with various model size ratios. It can be observed that the computational time increases slowly with the model size ratio, when  $[S]$  is smaller than 50, while it increases quickly as  $[S]$  becomes larger than 50. In addition, for the same value of model size ratio, the computational time decreases with the Reynolds number. This effect is particularly evident for large values of  $[S]$ . For a granular column with aspect ratio of 2.0,  $L_i$  of 0.1 m (i.e.  $[S] = 100$ ), it could consist of more than 50,000 particles, which would place a heavy burden on the current computational resources (e.g. simulation time can be more than 7 days). The situation becomes even worse for simulations using large granular columns. As this study aims to study the general mechanical and hydraulic behaviour of submerged debris flows, the model dimensions are limited to small values, such that the initial column length (i.e.  $L_i$ ) is fixed as 0.05 m, while the height is scaled up/down according to different column aspect ratios.

Since the field investigations always focus on the coefficient of flow mobility (i.e.  $L_{\max}/H_{\max}$ , with  $L_{\max}$  and  $H_{\max}$  being the maximum run-out distance and deposit height), the following analyses will mainly discuss the relationship between the coefficient of mobility and model size ratio, as shown in Fig. 5.10. It can be observed that the real landslides normally have size ratios larger than  $10^5$ , while the numerical models can have model size ratios up to 200 and the experiments can use model size ratios as large as 2000. According to Fig. 5.10, it can be concluded that on average, the coefficient of landslide mobility increases with the model size ratio, which suggests that the current small-scale numerical model using the DEM–CFD

**Fig. 5.9** Computational time versus model size ratio (the DEM time step is  $5.0 \times 10^{-7}$  s)

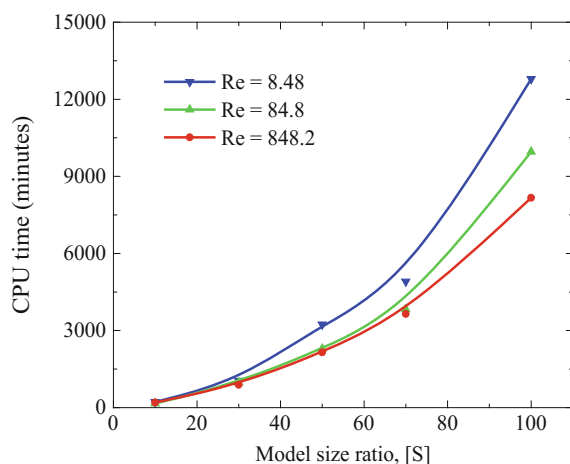
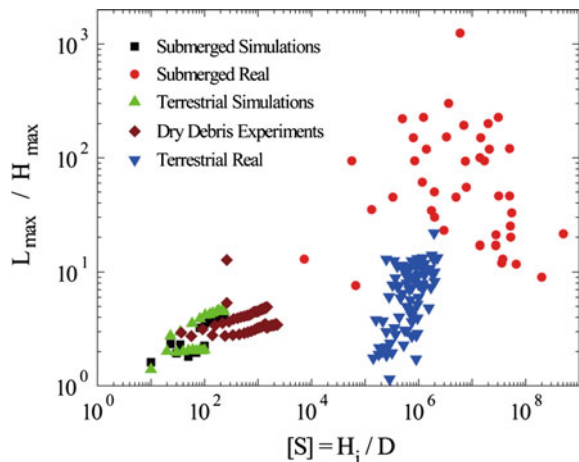


**Fig. 5.10** Relationship between model size ratio and coefficient of mobility. The legend “Simulations” denotes the numerical simulations; “Real” denotes the site investigations (the source data can be found in Appendix B); “Experiments” denotes the laboratory experiments (Source Lajeunesse et al. 2005; Lube et al. 2005)



coupling method can potentially reproduce the correct behaviour of submerged debris flows, if the model size ratio employed in the DEM model can increase to a value very close to that of real landslides. However, this cannot be achieved until extremely efficient computing resources are available.

#### 5.4.4 Influence of Characteristic Strain and Reynolds Number

The dimensions of real submerged landslides are far larger than the numerical models. For instance, the heights of real landslides can exceed 1000 m, while the size of current numerical models only ranges from 0.05 to 0.5 m. In addition, the solid materials involved in real landslides are diverse, ranging from fine silts to gravel. However, the current research only focuses on the medium and coarse sands. Because of these differences, some parameters of numerical models should be scaled up/down, so that the values of dimensionless groups can match those of real submerged landslides. By investigating the characteristic strain and Reynolds number in Eqs. (5.5) and (5.4), the values of normal contact stiffness ( $K_n$ ) and fluid viscosity ( $\mu$ ) can be scaled up/down. As they only appear in these two dimensionless groups, the scaling will not influence the value of other dimensionless groups. The parameters estimated from real submerged landslides are listed in Table 5.3.

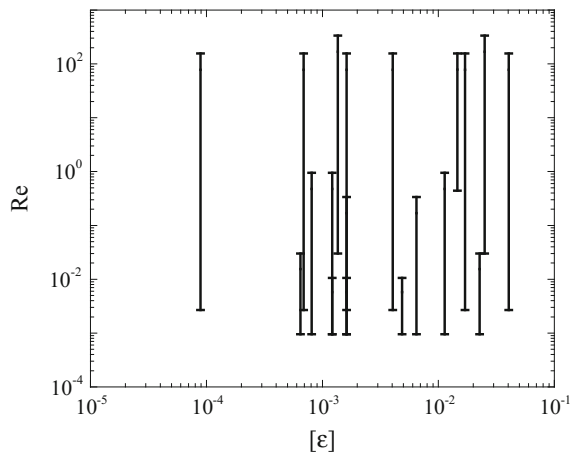
The combination of the characteristic strain and Reynolds number encountered in real submerged landslides is illustrated in Fig. 5.11. The numerical model has employed a granular column with an initial aspect ratio of 3.3. The height of the column is 0.165 m and the effective particle size ( $D_{10}$ ) is 2.0 mm. A reasonable range of  $Re$  and  $[\varepsilon]$  was reproduced, as shown by the red lines in Fig. 5.12.

Several discrete points on these lines have been selected as the input parameters of numerical simulations. If  $Re$  and  $[\varepsilon]$  are very small, very large value of fluid

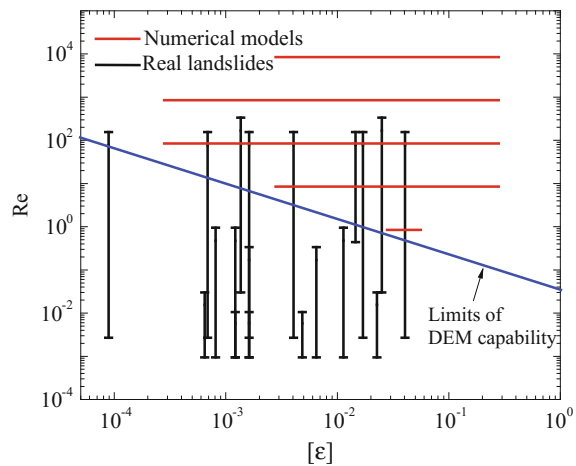
**Table 5.3** Parameters estimated from real submerged landslides

Parameters	Unit	Values
$\rho_f$	kg/m <sup>3</sup>	1000
$\rho_s$	kg/m <sup>3</sup>	2650
$g$	m/s <sup>2</sup>	9.81
$K_n$	N/m	$3.0 \times 10^7$
$H$	m	[10, 3000]
$D$	mm	[0.001, 10]
$\mu$	Pa s	0.001
$[\varepsilon]$	—	$[8.1 \times 10^{-5}, 0.024]$
$Re$	—	$[9.5 \times 10^{-4}, 950]$

**Fig. 5.11**  $[\varepsilon]$  and  $Re$  for real submerged landslides (data cited from Edgers and Karlsrud 1982)



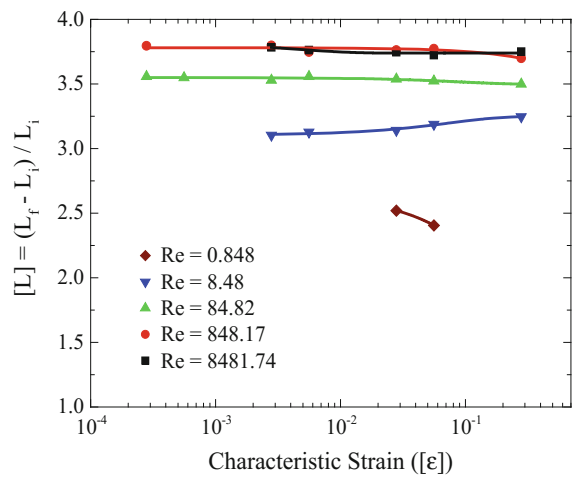
**Fig. 5.12** The range of  $Re$  and  $[\varepsilon]$  in numerical simulations



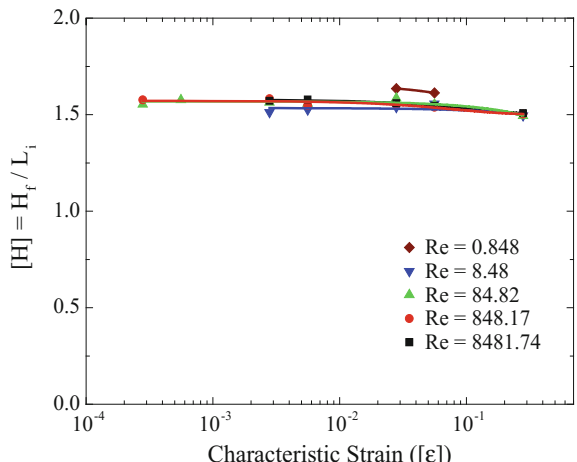
viscosity and particle contact stiffness will be used. The corresponding numerical simulations require the use of very small time steps (e.g.  $\Delta \leq 10^{-8}$  s), so that the numerical stability and accuracy can be maintained. However, this requirement would increase the total simulation time significantly, which to some extent is unacceptable in numerical simulations (see Figs. 5.7 and 5.9). According to Fig. 5.12, the blue line shows the limit of the current DEM capability in simulating submerged landslides. The DEM–CFD model can only reproduce the values of  $Re$  and  $[\varepsilon]$  above the blue line, while it is very difficult to simulate the submerged landslides in regions below the limiting line.

Figure 5.13 compares the depositional morphologies of sediments for samples with various Reynolds numbers and characteristic strains. On average, the length

**Fig. 5.13** Comparison between results for different Reynolds numbers



(a) relationship between the normalized runout distance and characteristic strain



(b) relationship between the normalized deposit height and characteristic strain

and height of the final deposits are unaffected by the characteristic strains for a specific Reynolds number, which indicates that granular columns with different dimensions would result in similar depositional profiles. This phenomenon effectively reflects the behaviour of slowly slumped debris materials, in which the fluid viscous drag forces and inter-particle frictions are significant in controlling the deposition of debris materials. Figure 5.13a also indicates that the normalized run-out distance is very sensitive to the Reynolds number. At a specific value of characteristic strain,  $[L]$  increases gradually with  $Re$ , while it remains constant if  $Re$  is larger than 800. Due to the limitation of computational power, the Reynolds number in the current study is larger than 8.48, which effectively reveals the sedimentary behaviour of relatively coarse grains.

#### **5.4.5 Influence of Material Internal Friction Angle**

According to the discussion in Sect. 2.2.3, any combination of the microscopic inter-particle friction angle and rolling resistant parameters can produce a unique value of material internal friction angle, which influence the depositional behaviour of granular materials significantly. The relationship between the run-out distance, deposit height and material internal friction angle is shown in Fig. 5.14.

As shown in Fig. 5.14, the normalized run-out distance decreases, while the final deposit height increases gradually with the material internal friction angle. When compared with the dry granular flows, the submerged debris flows have smaller values of  $[L]$  and larger values of  $[H]$ , under the same initial model configurations. The presence of water would damp the dynamics of debris flows significantly, so that the solid mass would deposit near the toe of the slope, leading to a short run-out distance and large deposit height.

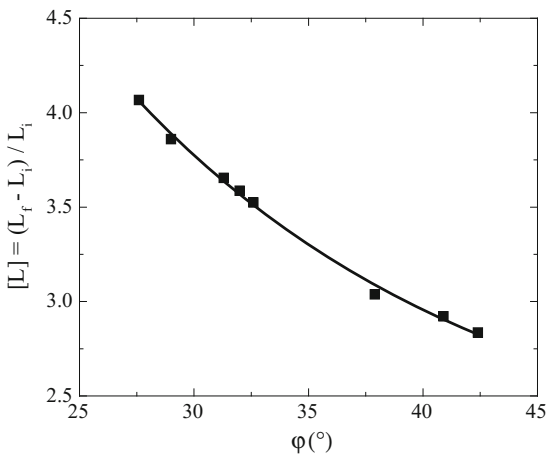
### **5.5 Mechanical and Hydrodynamic Analyses**

To investigate the mechanical and hydraulic behaviour of submerged debris flows, the solid and fluid properties, such as grain velocity, force chain and stress distribution and fluid excess pore water pressure, will be analysed. The input parameters for the DEM–CFD coupling simulations are listed in “SS2” of Appendix C.

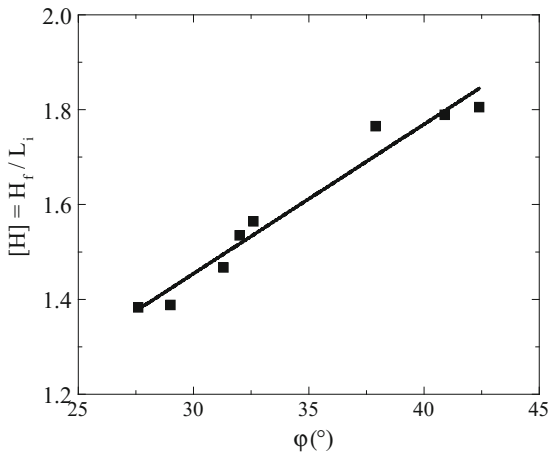
#### **5.5.1 Evolution of Particle Velocity Field**

In the dimensional analyses, the particle velocity is normalized by the relative settling velocity of a single particle with a diameter of  $D_{10}$  by Eq. (4.74) (i.e.  $v_0 =$

**Fig. 5.14** Influence of material internal friction angle on granular depositional morphology



(a) normalized runout distance of the granular assembly



(b) normalized deposit height of the granular assembly

0.28 m/s). To visualize the evolution of particle velocity field, the velocity vectors have been scaled by the magnitudes of velocities, as shown in Fig. 5.15.

At the beginning of the submerged debris flow, the upper grains fall downwards and spread horizontally. The maximum granular velocity occurs in a triangular wedge zone in the upper front region. In the bottom region, the particle velocity remains as zero. During the simulation, the normalized particle velocity can be as large as 2.0, indicating that the grains can move faster than the constant relative settling velocity of a single particle with diameter  $D_{10}$ . When compared with the particle velocity field of dry granular flows, the solid grains move much slower in the submerged environment. This phenomenon can be explained by the fact that during the submerged debris flow, the grain velocity is mainly controlled by the

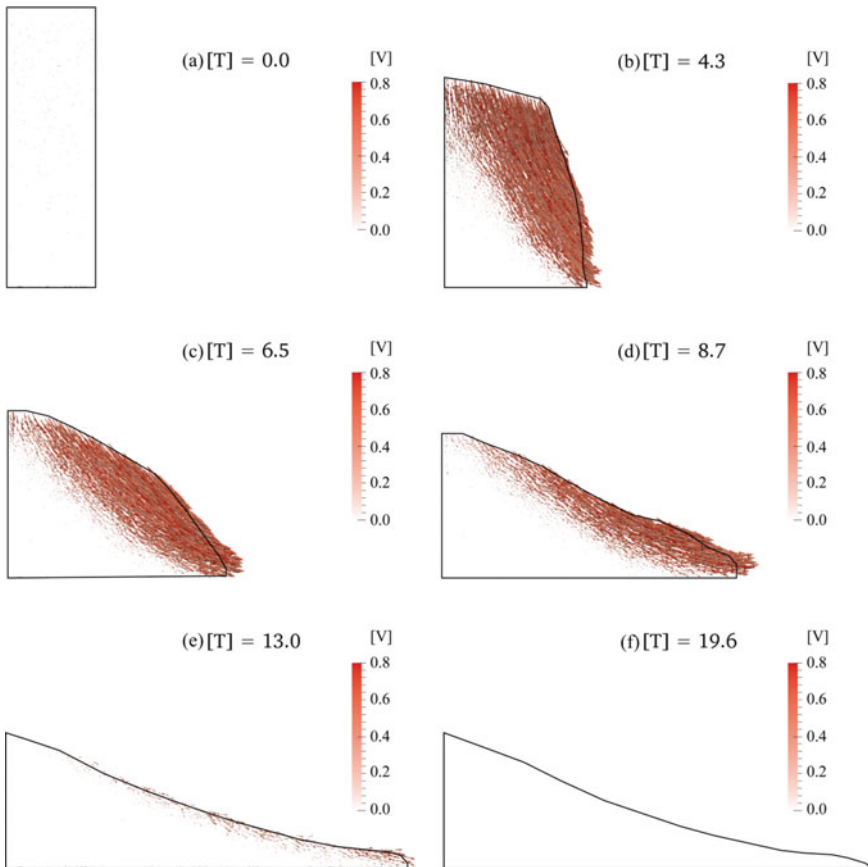


**Fig. 5.15** Evolution of grain velocities (the *black curves* represent granular profiles)

viscous drag force exerted by fluid on debris materials. As the fluid viscous drag force is proportional to the square of the velocity, any high velocity initially acquired from the collapse of granular column will be rapidly lost (Norem et al. 1990).

### 5.5.2 Fluid Velocity Field

During the simulation, the fluid velocity is generated by the viscous drag forces of the fluid–solid interactions. The evolution of fluid velocity field (plotted as vectors) is shown in Fig. 5.16. As the granular materials fall downwards and spread horizontally, the fluid motion occurs exactly in the same region as the moving grains. The magnitudes of fluid velocities are almost the same as the particle velocity fields

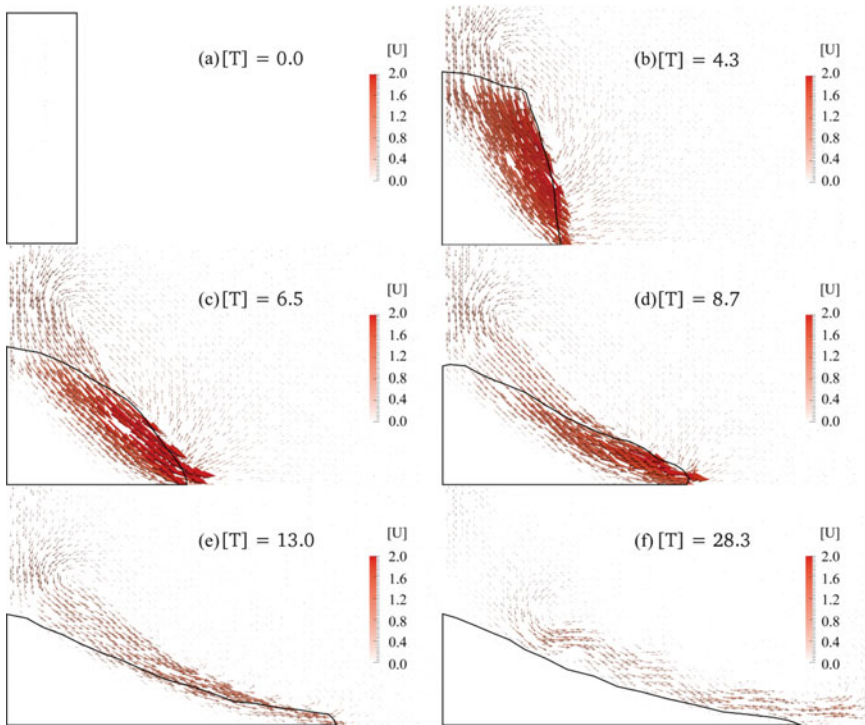


**Fig. 5.16** Evolution of fluid velocity (the *black curves* represent granular profiles)

shown in Fig. 5.15. During the debris propagation process, the fluid circulation phenomenon occurs near the slope surface in the rear region, as represented by the flow vector at the normalized time of 4.3, 6.5, 8.7 and 13.0. At the end of the granular deposition process, the solid materials stop moving, while very small fluid velocity still exists near the slope surface. This phenomenon can be used to explain the sediment transport process near the seabed, that very fine solid grains can be entrained in the ocean currents and transported to travel very long distances.

### 5.5.3 Relative Velocity Between Particle and Water

As discussed in Chap. 4, the generation of excess pore pressure depends mainly on the relative velocity between fluid and solid particles. The evolution of the relative velocities during the submerged debris flow is illustrated in Fig. 5.17. On this graph, the solid grains are set with different colours according to the magnitudes of relative velocities, so that the distribution of relative velocity fields can be clearly identified. It can be observed that the relative motion between solid and fluid phases

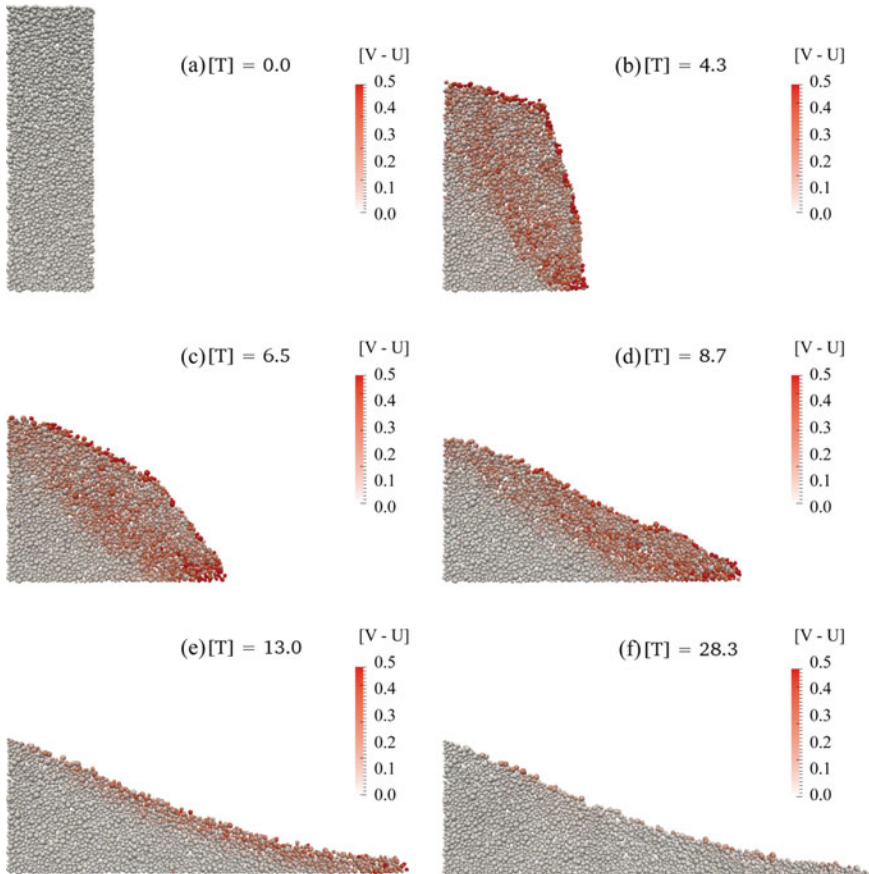


**Fig. 5.17** Evolution of the relative velocity field between particle and water

mainly occur near the slope surface, while the materials remain static in the bottom region.

As the driving force of the submerged debris flow is mainly the gravity of solid particles, these grains would settle in water for a certain distance until the constant relative settling velocities can be reached (see Sect. 4.6.1). For the small-scale model, the height of the column is very short, such that the grains cannot settle freely for this distance, because they would collide with the floor or the deposited grains. According to Fig. 5.17, the magnitude of the relative velocities is smaller than 50% of the constant relative settling velocity of a single particle, indicating that none of these grains can reach the steady settling state. Therefore, the small-scale numerical models used in the current study cannot produce high excess pore pressure during the submerged debris flows.

### 5.5.4 Distribution of Excess Pore Water Pressure

The use of small-scale DEM samples in modelling submerged debris flows makes it very difficult to distinguish the dilative and contractive deformation of soil mass accurately. However, it is possible to investigate these zones by studying the distribution of excess pore water pressure because the excess pore water pressure is very sensitive to sample deformations. As discussed in Sect. 1.3, the positive excess pore water pressure occurs in the shear contraction zones, while the negative pore water pressure exists in the shear dilation zones. Thus, by investigating the distribution of excess pore water pressure within the granular assembly, it is possible to get the correct patterns of soil deformation. This technique is only valid inside the soil mass, while near the slope surface, it only reflects the relative motion between solid grain and fluid.

Figure 5.18 illustrates the evolution of granular profiles and the corresponding excess pore water pressures. Initially, a static granular pile is generated underwater

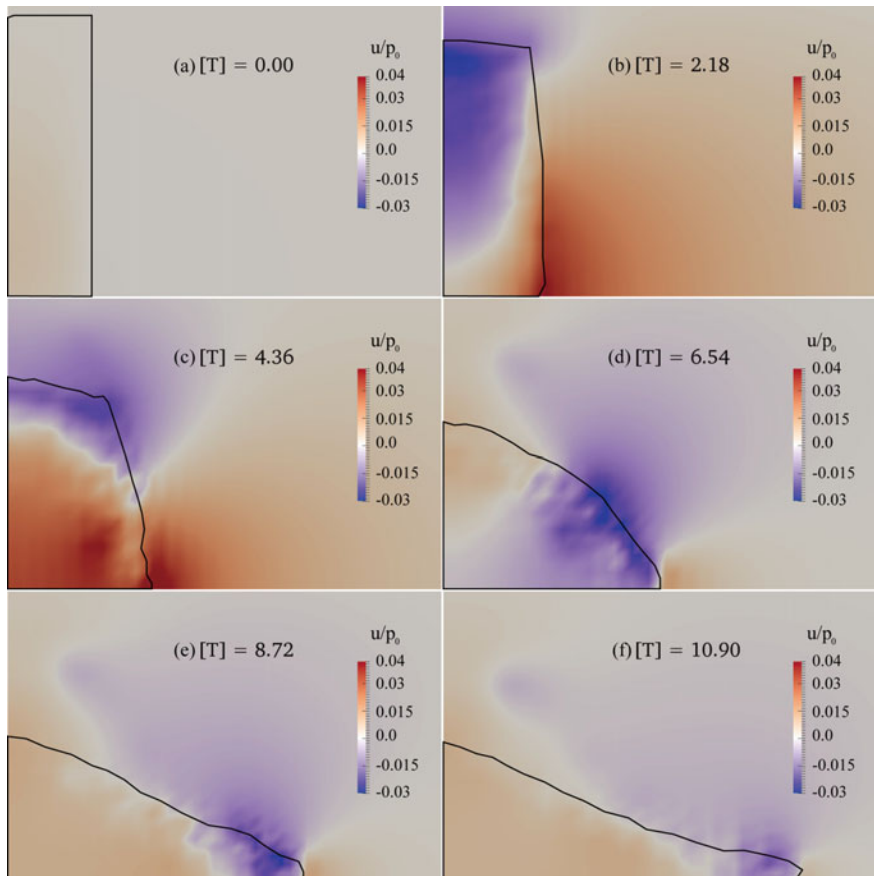


**Fig. 5.18** Evolution of excess pore water pressure (the *black curves* represent granular profiles; “ $u$ ” represents the excess pore water pressure, “ $p_0$ ” is the effective soil stress defined as:  $p_0 = (1 - n)(\rho_s - \rho_f)gH_i$ )

and the excess pore water pressure is zero within the sample. Once released, the upper grains fall downwards and the bottom grains move horizontally. Thus, the bottom front part of the sample is in compression, while the upper region is in dilation. The excess pore water pressures are positive and negative in those two regions, respectively. As the upper grains continuously collide with grains in the bottom, the bottom region of the granular mass contracts gradually, maintaining positive excess pore water pressures. After  $[T] = 6.54$ , the horizontal spreading of grains is dominant, such that the dilative zone of the sample mainly occurs at the moving front, in which the excess pore water pressures are mainly negative. Meanwhile, the slowly moving or static region of the granular sample consolidates very little, leading to very small variation of excess pore water pressures within the granular assembly. Throughout the simulation, the maximum normalized excess pore water pressure is 0.04, which is far smaller than the characteristic effective stress of the granular sample. Thus, the small-scale submerged debris flows cannot be mobilized to run a long distance.

### 5.5.5 Evolution of Force Chains

As discussed in Chap. 3, the contact forces between particles can be visualized by using graphs of force chains. In Fig. 5.19, the magnitudes of particle contact forces are normalized by the characteristic contact force ( $[F] = F_c / ((1 - n)(\rho_s - \rho_f)gH_iD^2)$ ).

Before the initiation of debris flows, the granular assembly remains static and large contact forces are found near the bottom of the granular column, where the overlaying solid weight is large. Near the upper surface of slope, the packing is very loose, so that the force chains are very thin. Once released, the solid grains near the initial confining wall collapse downwards immediately onto the ground floor and spread horizontally. The contact forces at the moving front decrease quickly to very small values. The large contact forces mainly concentrate within the static granular pile region, with their orientations direct parallel to the sliding surface. At the end of the simulation, the contact forces between grains at the deposit surface are negligibly small, while the large contact forces occur mainly near the ground floor with their orientations direct approximately parallel to the sliding surface.

### 5.5.6 Distribution of Effective Stress

As discussed in Sect. 1.3, the failure and mobility of debris materials depends highly on the effective stress within the granular sample. To analyse the evolution and distribution of effective stresses in the current DEM model, the stress tensor has been defined by invoking the micro–macro averaging technique (Thornton and Antony 2000), as discussed in Chap. 2. In the current section, the contour of major

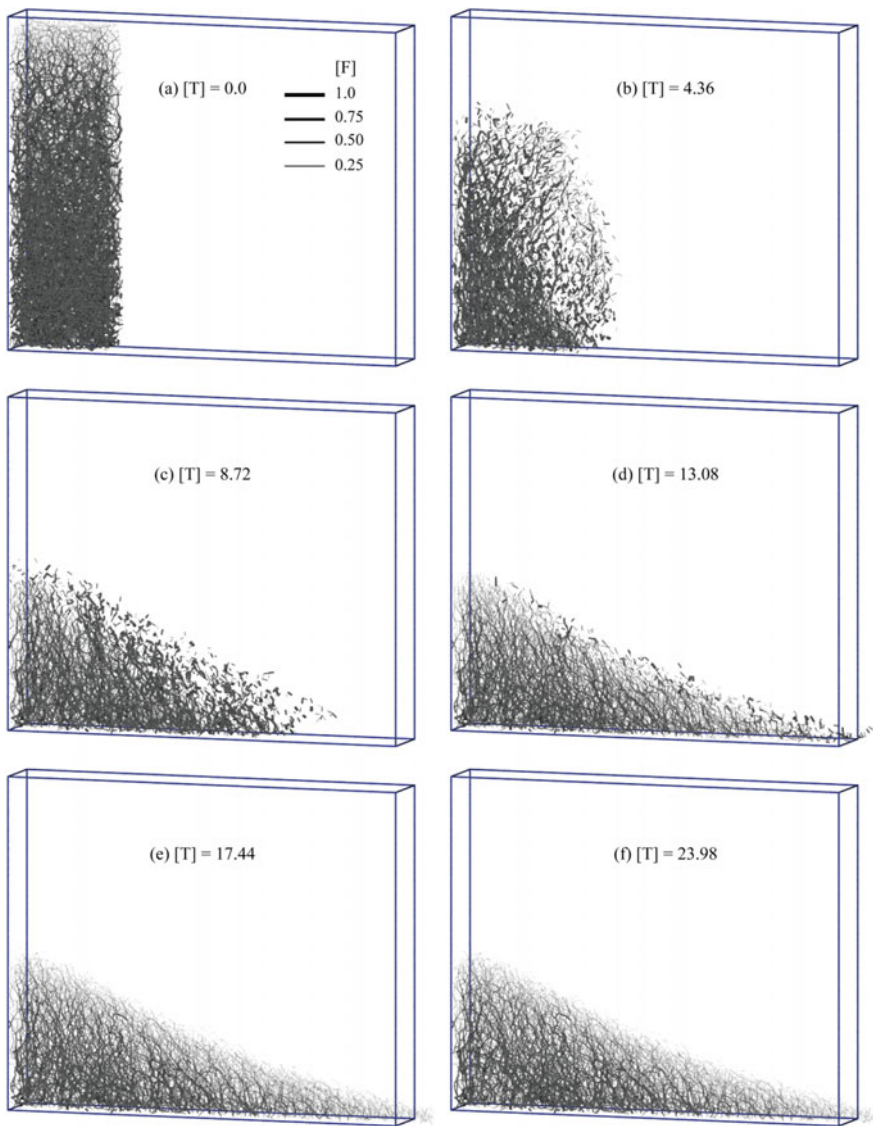


**Fig. 5.19** Evolution of force chains during the simulation

principal stress (normalized by the characteristic effective stress of the initial granular column ( $p_0 = (1 - n)(\rho_s - \rho_f)gH_i$ )) is illustrated in Fig. 5.20.

At the beginning of the simulation, the effective stress increases linearly with the column depth. Once the confining wall is removed, the effective stresses near the front surface of the column are released simultaneously (e.g. at  $[T] = 2.18$ ) and the high effective stresses concentrate mainly in the static pile region of the granular

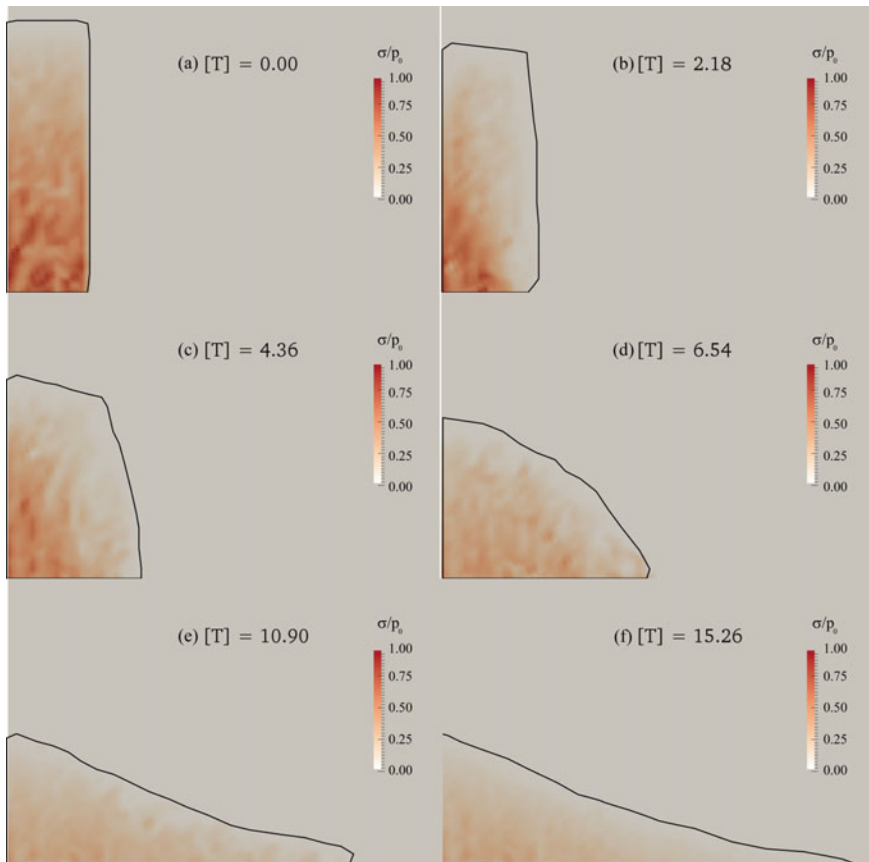
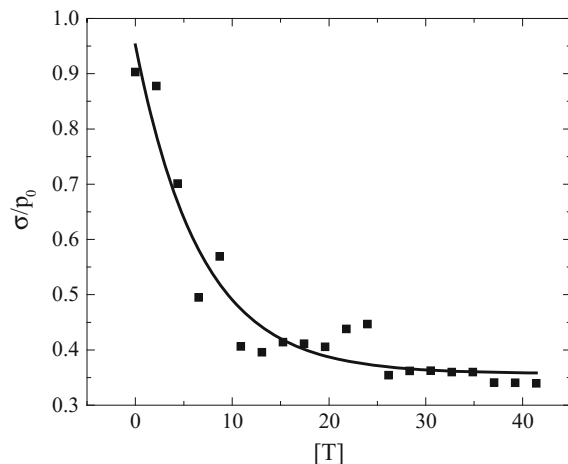


**Fig. 5.20** Distribution of effective stresses with the granular assembly (the *black curves* represent granular profiles)

assembly. At the end of the simulation, a thin and loose grain layer is formed on the ground floor with effective stresses being smaller than 0.25. Throughout the simulation, the peak value of effective stress is observed in the static pile region, while the minimum value occurs near the slope surface. The variation of effective stress within the granular assembly against time is illustrated in Fig. 5.21. According to Fig. 5.21, the maximum normalized value of effective stress is 0.92, which can match the theoretical value (=1.0) well. When compared with the excess pore water pressure generated during the submerged debris flows (see Fig. 5.18), it is clear to observe that the normalized excess pore water pressure can only amount to approximately 4% of the effective stress, which is too small to mobilize the granular materials to run a long distance.

**Fig. 5.21** The maximum effective stress measured during the simulation



### 5.5.7 Distribution of Bulk Coordination Number

The packing state of granular assembly can be visualized by the distribution of bulk coordination numbers, as illustrated in Fig. 5.22. At  $[T] = 0.0$ , the whole granular sample is static, such that all the particles are in contact with each other. The average bulk coordination number within the sample is around 6.5. The maximum bulk coordination number (i.e. 7.0) is found at the bottom of the column, while the minimum coordination numbers occur near the boundary in which solid grains are partly in contact with the rigid walls. After the initiation of debris flow, the bulk coordination number of grains near the sliding interface is relatively small, as shown by the enclosed dashed curves at  $[T] = 4.36$  and  $[T] = 8.72$ . In these regions, intensive dilative deformations occur, leading to a quick decrease of particle contacts. Additionally, the low coordination region is also observed at the slope surface where the solid grains are in dynamic motion. As the debris flow propagates horizontally, the granular materials can finally form a static deposit on the floor, in which the value of coordination number increases with the depth of the granular deposits.

### 5.5.8 Evolution of the Run-out Distance and Deposit Height

The evolution of debris run-out distance and deposit height for different granular columns are displayed in Fig. 5.23. In these graphs, the duration time of the simulation is defined as  $[T] = gD^2(\rho_s - \rho_f)t/(18\mu L_i)$ , such that it is clear to compare the absolute duration time for different granular columns. According to Fig. 5.23, it can be observed that different granular columns present similar depositional behaviour. The final normalized run-out distance and deposit height increase with

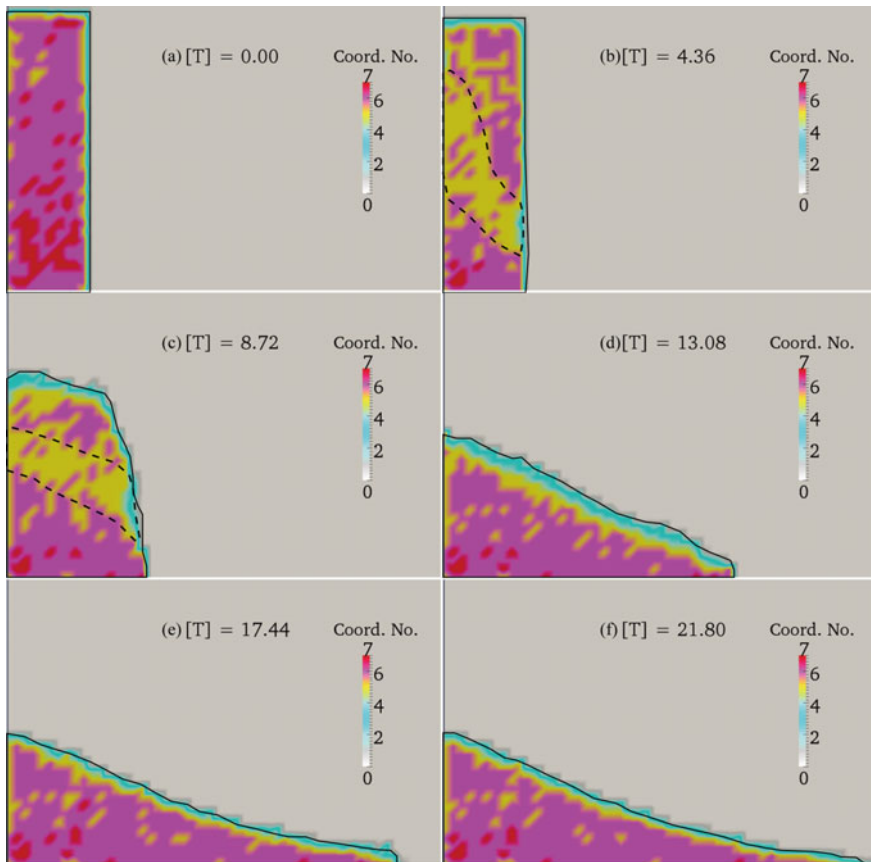


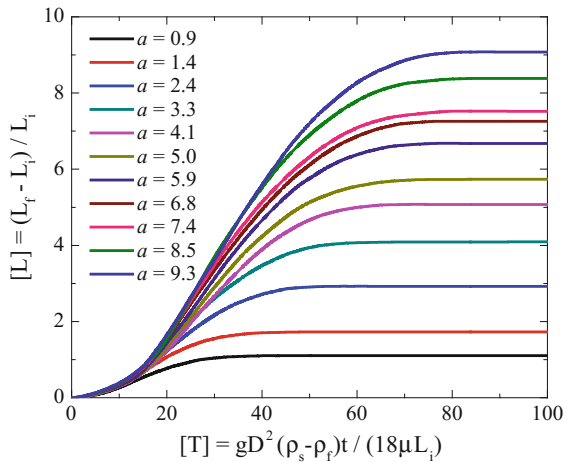
**Fig. 5.22** Evolution of the bulk coordination number of the granular assembly (the *black curves* represent granular profiles)

the initial column aspect ratios. During the submerged debris flows, the dynamic motion of grains would go through four transient stages: initial acceleration, a phase of approximately constant velocity followed by deceleration and the final stage of static granular deposition. The small granular columns can reach each stage earlier and take less time for each stage than the large columns.

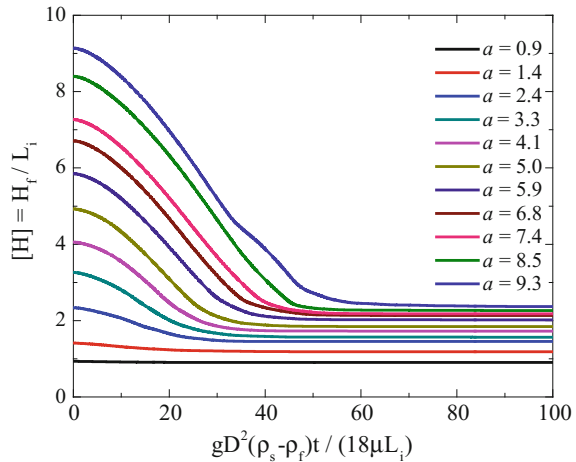
## 5.6 Modelling of Large-Scale Landslides

As discussed in the previous sections, the simulation of submerged debris flows using small-scale numerical models can reproduce the same grain settling time as that in real submerged landslides. However, it is impossible to get the consolidation

**Fig. 5.23** Evolution of debris run-out distance and height during simulations



(a) evolution of the normalized debris runout distance



(b) evolution of the normalized debris height

time correct due to the limited number of grains used in the simulation. Consequently, the induced excess pore water pressure is very small and unable to mobilize the debris materials to travel a long distance. The difference between the numerical and field observations is believed to result from the use of small-scale numerical models, such that the model size ratio is far smaller than those of real submerged landslides. To overcome this difficulty, a modified scaling relationship of drag force is provided in this section, which is expected to reveal the correct grain sedimentation and consolidation mechanisms in modelling submerged debris flows. In the DEM model, the width of the initial granular column is chosen as 50 m, while the height can range from 50 to 300 m. The diameters of solid grains

are set within the range of [1.8, 3.8] m, such that the total number of particles (i.e. 20,000) in the model is acceptable for the current computational power and memory capacity.

According to Chap. 4, the particle size is closely related to the hydraulic properties of soil. To make sure the large grains used in the current analyses can reproduce the correct hydraulic behaviour of soil, it is assumed that one large particle represents a clump of real sized sand grains. A schematic view of the real submerged slope is shown in Fig. 5.24.

The diameters of the scaled and real sand grains are denoted as  $D$  and  $d$ . Thus, the total number of particles ( $N$ ) in the clump can be approximated as:

$$N = \frac{D^3}{d^3} \quad (5.17)$$

The fluid viscous drag force acting on a clump of fine grains is written as the summation of the drag forces acting on individual grains in Eq. (5.18).

$$F_d = \frac{1}{2} C_d \rho_f \frac{\pi d^2}{4} |\mathbf{U} - \mathbf{V}| (\mathbf{U} - \mathbf{V}) n^{-\zeta+1} \times \frac{D^3}{d^3} \quad (5.18)$$

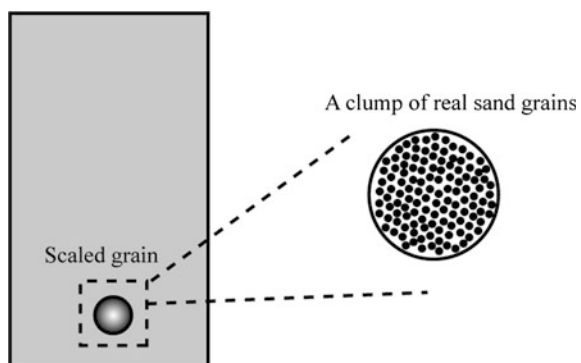
The drag force acting on a scaled particle is calculated in the DEM–CFD coupling code as:

$$F'_d = \frac{1}{2} C'_d \rho_f \frac{\pi D^2}{4} |\mathbf{U} - \mathbf{V}| (\mathbf{U} - \mathbf{V}) n^{-\zeta+1} \quad (5.19)$$

Thus, the drag force calculated by Eq. (5.19) should be scaled up by a factor ( $\alpha$ ), such that it equals that calculated by Eq. (5.18).

$$\alpha = \frac{F_d}{F'_d} = \frac{C_d n^{-\zeta+\zeta'}}{C'_d} \cdot \frac{D}{d} \quad (5.20)$$

**Fig. 5.24** Schematic view of real submerged slope and a clump of fine sediments



Since  $C_d$  and  $\chi$  are functions of fluid Reynolds number, Eq. (5.20) can be reduced to  $\alpha = D/d$  if  $Re$  is chosen the same for these two terms (see the input parameters in Appendix C). The hydrostatic forces acting on a scaled particle and a clump of sand grains are the same, because it is determined only by the volume of solid materials. It is also worth noting that the other parameters for the real and scaled particles are shown in Appendix C, so that realistic soil properties can be modelled in the numerical simulations. This method of scaling up the particle diameter is referred to in the literature as particle “coarse graining” or “parcel-based” approach, and is increasingly used in DEM simulations (Radl et al. 2011; Hilton and Cleary 2012; Sakai et al. 2012; Baran et al. 2013).

The loose and dense samples are prepared according to the following procedures:

- (i) Loose sample: DEM spheres of diameters in the range of [1.8, 3.8] m are generated randomly by ESyS-Particle, using the model configuration in Fig. 5.1. The width of the prism is set as 50 m, while the length of the periodic cell is 30 m. The column height can range from 50 to 300 m for different aspect ratios. The total number of grains ranges from 5000 to 25,000 and the porosity is 0.49.
- (ii) Dense sample: After the generation of a loose sample, gravity is applied to all particles. After the gravitational deposition, a dense sample is obtained. The porosity of the dense sample is 0.34.

For the following analyses, the input parameters of the simulations using the DEM–CFD coupling algorithm are listed in “LS1” and “LS2” of Appendix C.

### 5.6.1 Determination of Numerical Time Step

After obtaining the loose and dense samples, the simulations of granular column collapse are conducted to investigate the mechanical and hydraulic behaviour of debris flows. Based on Eq. (2.9), the critical time step for the granular system consisting of scaled large grains using linear-spring contact model is calculated as 0.02 s. However, since the drag forces have been artificially scaled up, a smaller numerical time step should be used in the simulation, in view of the following two considerations:

- (i) During the gravity-driven debris flows, the viscous drag force acting on a single solid particle should be smaller than the gravity force, such that the simulation is stable. If a large time step is used, the change of particle velocity within one iteration step might result in a rapid increase of viscous drag force. An artificial scaling up of this drag force can possibly make it exceed the gravity force. The resultant unbalanced force acting on an individual particle may cause it to move unrealistically. Consequently, the simulation would go unstable.

- (ii) A large time step can also cause numerical inaccuracy during the simulation. As discussed in Sect. 2.2.2, the numerical integration errors generated in the DEM would inevitably violate the energy conservation of a granular system.

To explore these two considerations, simulations of un-damped granular collision by the DEM and the submerged debris deposition by the DEM–CFD coupling method have been performed. For the first simulation, the model configurations are similar to those presented in Sect. 2.2.2, while the scaled particle diameters are used. The numerical results are presented in terms of the kinetic energy of the whole granular system for simulations using different time steps, as shown in Fig. 5.25. It can be observed that only the simulations using a time step smaller than  $10^{-4}$  s can satisfy the energy conservation criterion. Thus, the critical time step of the DEM collision model is chosen as  $10^{-4}$  s.

For the second simulation, the deposition of granular materials in the submerged environment (i.e. Fig. 5.1) is simulated using the DEM–CFD coupling method. The kinetic energy of the granular assembly is recorded for simulations with various time steps. According to Fig. 5.26, it can be observed that the kinetic energy of the granular system increases gradually as the grains deposit continuously onto the floor. In this process, the relationship between the kinetic energy and simulation time is the same for simulations using different time steps. As the grains can collide with each other, the simulation becomes unstable if the time step is larger than a critical value, as represented by a sudden increase of the total kinetic energy of the granular system. For simulations using time steps smaller than the critical value, the total kinetic energy would initially increase and then decrease gradually, due to the deposition of granular materials. The critical time step for simulations with  $\alpha = 100$  is  $10^{-5}$  s, while for  $\alpha = 1000$ , it is  $10^{-6}$  s, as illustrated in Fig. 5.26a, b. This

**Fig. 5.25** The kinetic energy of the granular system

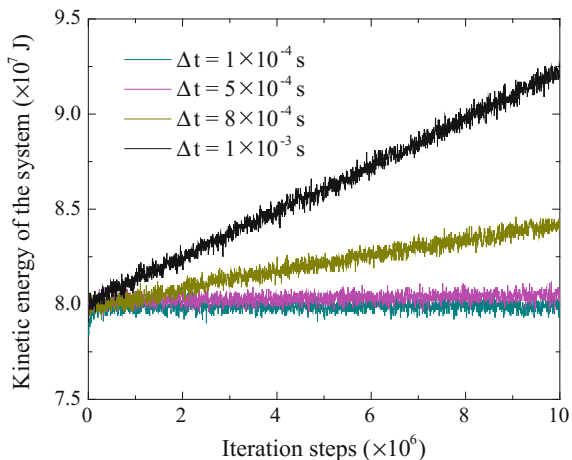
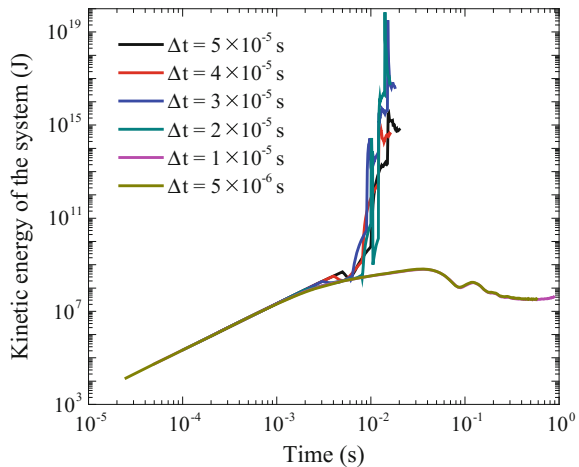
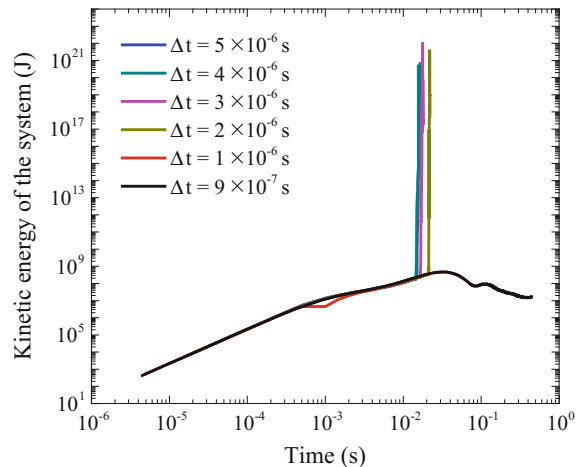


**Fig. 5.26** Determination of the time step for the DEM–CFD modelling



(a) Kinetic energy of grains in the DEM-CFD model, with  $\alpha = 100$



(b) Kinetic energy of grains in the DEM-CFD model, with  $\alpha = 1000$

suggests that the critical time step may be inversely proportional to the scaling factor, which is consistent with the hypothesis that the instability of the DEM–CFD simulation is due to the viscous force becoming excessively large within an iteration step.

Based on the discussions above, the scaling factor ( $\alpha$ ) of 100 and the numerical time step of  $1 \times 10^{-5}$  s are used in the current analyses. By doing so, the scaled particles can effectively represent clumps of fine grains of diameters in the range of [0.018, 0.038] m. Using a standard desktop PC, for the loose and dense samples with initial column aspect ratio of 3.0, the computational times are 107 and 150 h,

respectively. Although the use of larger scaling factor (e.g.  $\alpha = 1000$ ) can allow the modelling of very fine sediments, the computational time would become inconveniently large. Therefore, as a preliminary study, the current analysis will only focus on simulations using a scaling factor of 100.

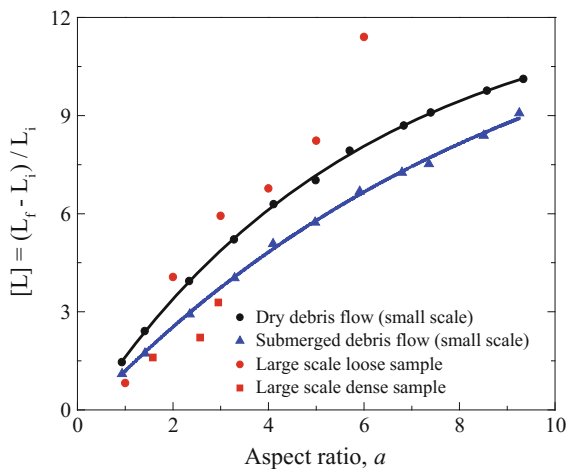
By scaling the drag force with a factor 100, the current numerical model can simulate the submerged debris flow consisting of  $2.5 \times 10^{10}$  solid particles. According to Fig. 5.7 and assuming the computational time and the number of grains are linearly related, the time used in modelling the submerged debris flows with real grain sizes via the DEM–CFD coupling model can be as large as  $4.7 \times 10^7$  h, which is completely unrealistic for scientific research. Thus, the scaling method used in the current research is a useful tool that can be used to investigate large-scale submerged landslides within a realistic timescale.

### 5.6.2 *The Mobility of Large-Scale Submerged Landslides*

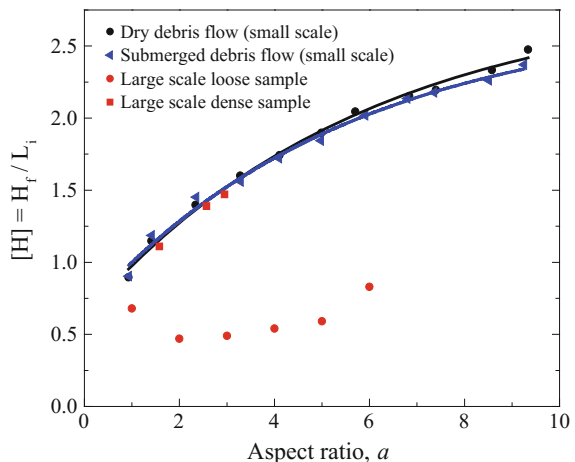
To evaluate the mobility of large-scale submerged landslides, granular columns of different aspect ratios have been used in the DEM–CFD coupling simulations. The numerical results obtained are compared with those discussed in the dry granular flows and small-scale submerged debris flows, as illustrated in Fig. 5.27. It can be observed that the large-scale submerged granular flows present different depositional mechanisms. For dense samples, the normalized run-out distance and deposit height are close to those of small-scale submerged debris flows, with the run-out distance rather shorter, presumably because of increased effective stress due to negative pore pressures. For loose samples, the granular materials have very high mobility, such that they can travel very long distances, forming very thin and gentle deposit layers. As a result, for granular samples with the same initial column aspect ratio (e.g.  $a > 1.0$ ), the loose samples normally have relatively large normalized run-out distance and small deposit height than other samples. For loose samples with aspect ratios larger than 6, the mobility of granular materials increases faster than those of smaller granular columns.

This phenomenon can be used to explain the sediment transport process, in which the fine grains in the suspensions are entrained by the fluid turbulent currents to travel a long distance. In addition, it is also due to the positive excess pore water pressures within the granular assembly, which reduce the effective stresses and hence increase the flow mobility. However, at small aspect ratios (e.g.  $a = 1.0$ ), the granular materials can travel a relatively short distance, because only a small amount of grains exist in the model, so that the excess pore water cannot be maintained within the granular assembly. As a result, the granular materials would quickly deposit on the ground floor, with relatively short run-out distance and large deposit height.

**Fig. 5.27** Comparison between small- and large-scaled simulations



(a) relationship between the normalized runout distance and aspect ratio



(b) relationship between the normalized deposit height and aspect ratio

### 5.6.3 Mechanical and Hydraulic Behaviour of Loose Sample

Field investigations have shown that the geological morphology of slopes can be very flat in the submerged environment. Under transient natural events, such as earthquakes and volcano eruptions, these slopes could fail within a short period of time due to the external impact forces. The failed solid mass can disintegrate and move along the slope into the deep ocean. This process of slope failure would

produce a very loose granular assembly near the slope source region. The reported huge submerged landslides mainly occur on slopes with declivity ranges from  $0.01^\circ$  to  $0.5^\circ$  (Field et al. 1982) and the mobilized solid mass can slide downwards into the very deep ocean basin, travelling up to 5 km away from the slope source region (Hühnerbach and Masson 2004). In this section, the loose granular sample is used to investigate the behaviour of submerged debris flows, with special focus on slope deformation, debris velocity, evolution of excess pore water pressure and effective stress. The input parameters for the related simulations can be found in “LS1” of Appendix C.

### 5.6.3.1 Evolution of Particle Velocity Field

During the simulation, the particle velocity is normalized by the constant relative settling velocity of a sand grain (i.e. after using the viscous scaling) according to Eq. (4.74) ( $=1.0$  m/s). The deformation of granular assembly and the evolution of particle velocity field (plotted as vectors) is shown in Fig. 5.28. It can be observed that the maximum normalized grain velocity is 10 times the constant relative settling velocity. As the debris flow propagates horizontally, the upper grains suspend in water and move at high velocities with the fluid currents. For grains in the bottom region, they decelerate gradually due to the basal friction.

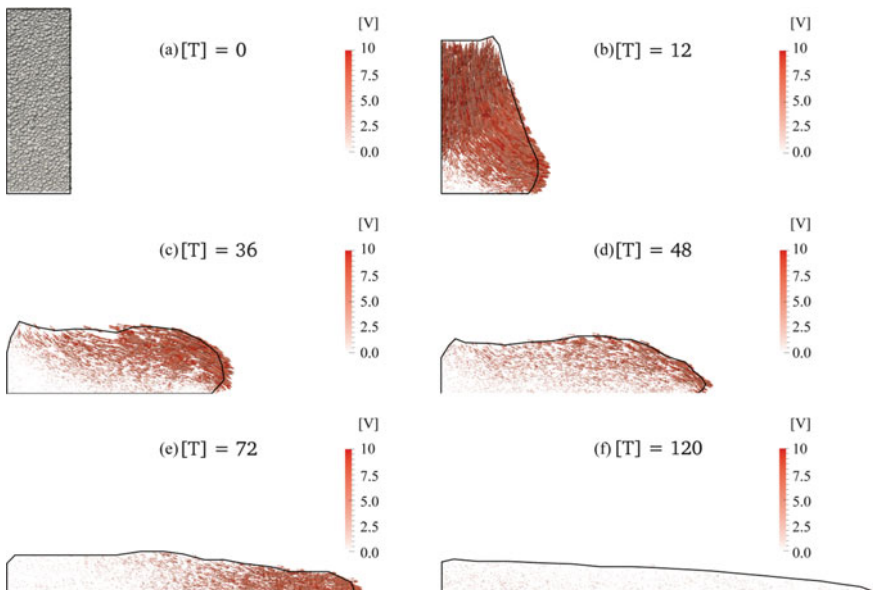


**Fig. 5.28** Evolution of particle velocity field (the *black curves* represent granular profiles)

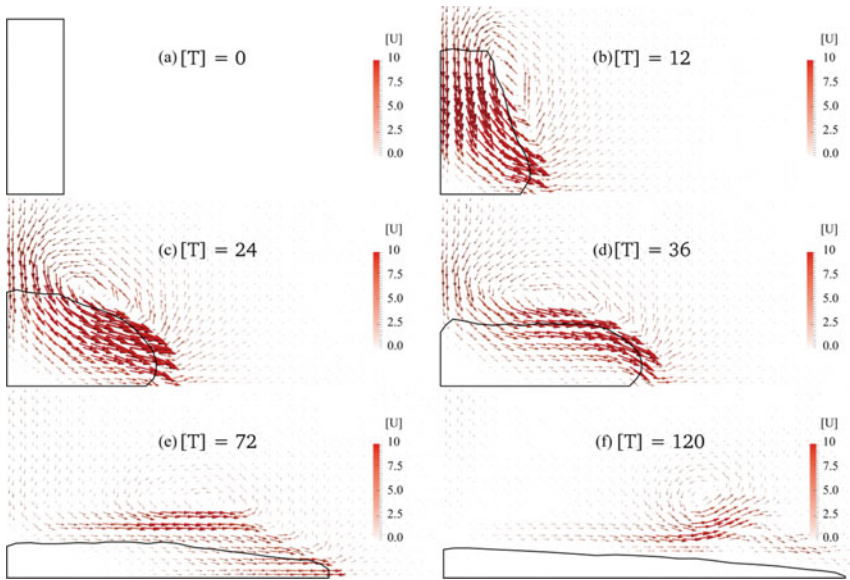


**Fig. 5.29** Evolution of the fluid velocity field (the black curves represent granular profiles)

### 5.6.3.2 Evolution of Fluid Velocity Field

The evolution and distribution of fluid velocity field (plotted as vectors) are shown in Fig. 5.29. It can be observed that at the beginning of the simulation, the fluid velocity increases gradually due to the drag forces occurring when solid grains settle downwards and spread horizontally. During this process, the fluid velocity field has the same distribution pattern as the particle velocity field (see Fig. 5.28). Meanwhile, a fluid flow vortex occurs near the slope surface, as represented by the circulation of fluid flow. After  $[T] = 72$ , the solid grains continuously deposit on the floor forming a static granular pile. As a result, the fluid velocity decreases slowly to zero within the granular deposit, while small fluid velocities still exist near the slope surface.

### 5.6.3.3 Relative Velocity Between Particle and Water

The evolution of relative velocities between particle and water is shown in Fig. 5.30. It can be observed that the maximum relative settling velocity can be three times the constant relative settling velocity of a single particle, which occurs near the flow surface. As the relative motion between solid and fluid is mainly controlled by the gradient of pore water pressure, the region with high velocity has large pressure gradients (see Fig. 5.31). According to the discussion in Sect. 5.5.3,

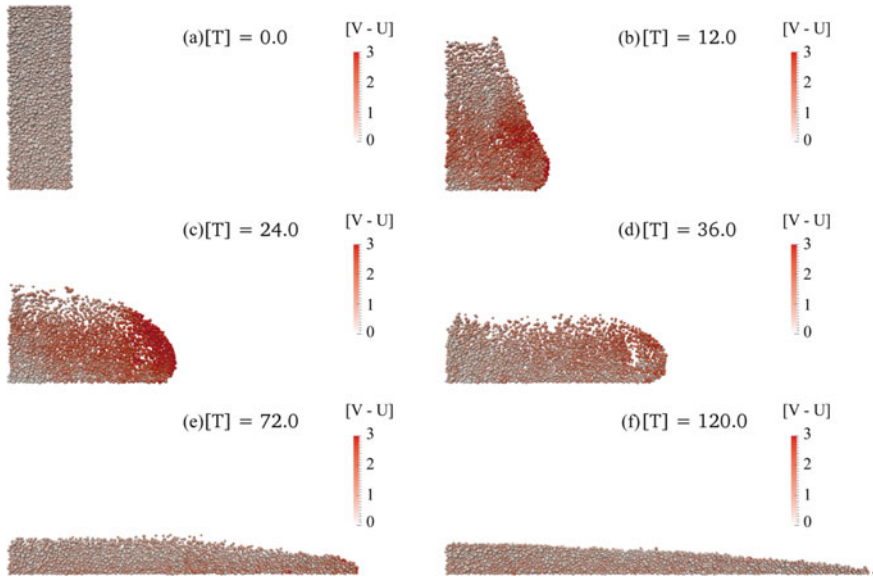


**Fig. 5.30** Evolution of the relative velocity field between particle and water

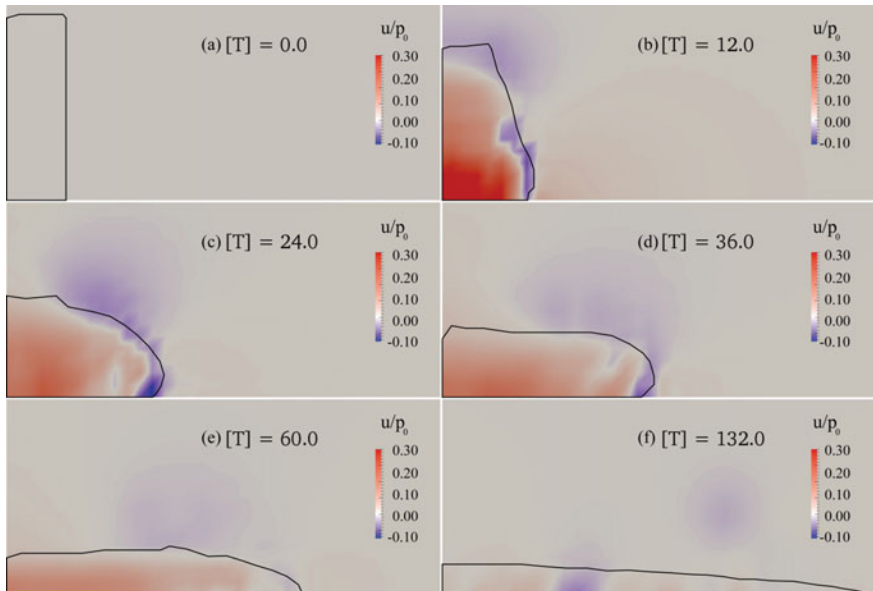


**Fig. 5.31** Evolution of excess pore water pressure (the black curves represent granular profiles)

the distribution of large relative velocity within the loose granular sample can lead to the generation of high positive excess pore water pressures, which could increase the mobility of the submerged debris flows.

#### 5.6.3.4 Evolution of Excess Pore Water Pressure

The evolution of excess pore water pressure during the submerged debris flow is illustrated in Fig. 5.31. It can be observed that the positive excess pore water pressure can amount to 35% of the characteristic effective stress of the initial granular column ( $p_0 = (1 - n)(\rho_s - \rho_f)gH_i$ ), which can effectively increase the mobility of granular materials in the submerged environment. The induced excess pore water pressure within the granular assembly is mainly positive, while only a small region of negative excess pore pressure exists at the front part of sliding solid mass. When compared with the results obtained from small-scale submerged granular flows in Sect. 5.5.4, the large-scale DEM–CFD coupling model of a loose granular assembly can effectively reproduce high mobilization features of real submerged landslides (Hampton et al. 1996).

According to Fig. 5.31, negative excess pore water pressure is observed in the flowing front of the granular assembly. This phenomenon can be explained by the fact that particles in the front region move faster than any other grains behind, leading to a gradual expansion of the granular sample in the horizontal direction. In addition, the grains near the upper surface of the flow would settle downwards, causing a compression of the granular sample. Therefore, the combined effect of horizontal expansion and vertical compression of the sample could produce the distribution of excess pore water pressure shown in Fig. 5.31. However, it is still not clear about the thickness of the negative pressure region and how its distribution would be for real submerged landslides consisting of millions of grains. According to the current analyses, two assumptions are proposed as: (1) This region only exists near the front surface, with a thickness of several grains; (2) The thickness of this region is proportional to the size of the debris mass. As it is computationally very expensive to simulate large-scale submerged landslides (e.g. a scaling factor of 10,000), these two competing assumptions have not been explored in this research. However, it is recommended to carry out related work in future researches.

#### 5.6.3.5 Evolution of Effective Stress

The evolution of effective stresses within the loose granular assembly is shown in Fig. 5.32. At  $[T] = 0$ , a loose granular sample is generated within a rectangular prism. As only a few particle contacts exist in the model, the effective stress within the granular assembly is close to zero. Once released, grains in the upper region fall downwards, colliding with grains in the lower region. Thus, the effective stresses

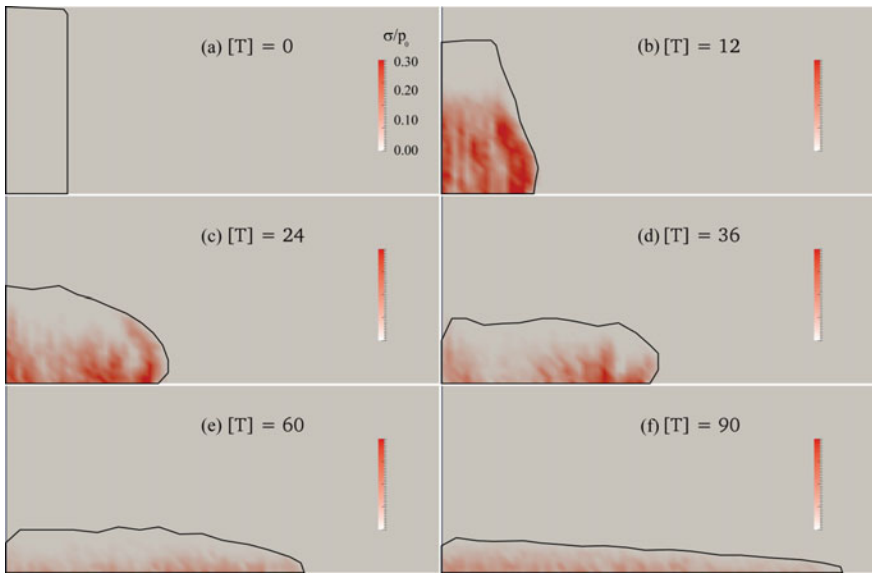


**Fig. 5.32** Evolution of effective stresses within the granular assembly (the *black curves* represent granular profiles)

would increase gradually at the bottom. Grains in the upper region would settle slowly in water and the effective stresses remain as zero. At the end of the simulation, a static and thin granular deposit can form along the horizontal floor, with the normalized effective stresses smaller than 0.10.

#### 5.6.3.6 Evolution of Bulk Coordination Number

The distribution of bulk coordination number reflects the packing state of the granular assembly, as shown in Fig. 5.33. At  $[T] = 0$ , the loose sample is generated within the rectangular prism. As no particle contacts exist in the model, the bulk coordination number is zero. Once released, the grains fall downwards and collide with each other. As a result, the bulk coordination number increases with the depth. In the upper region, many grains remain suspended in water, such that the bulk coordination numbers remain as zero. After  $[T] = 90$ , the granular materials gradually deposit on the floor, forming a static granular assembly. The corresponding coordination number of the deposit has a maximum value of 7 in the bottom region near the floor, while it is smaller than 2 near the slope surface.

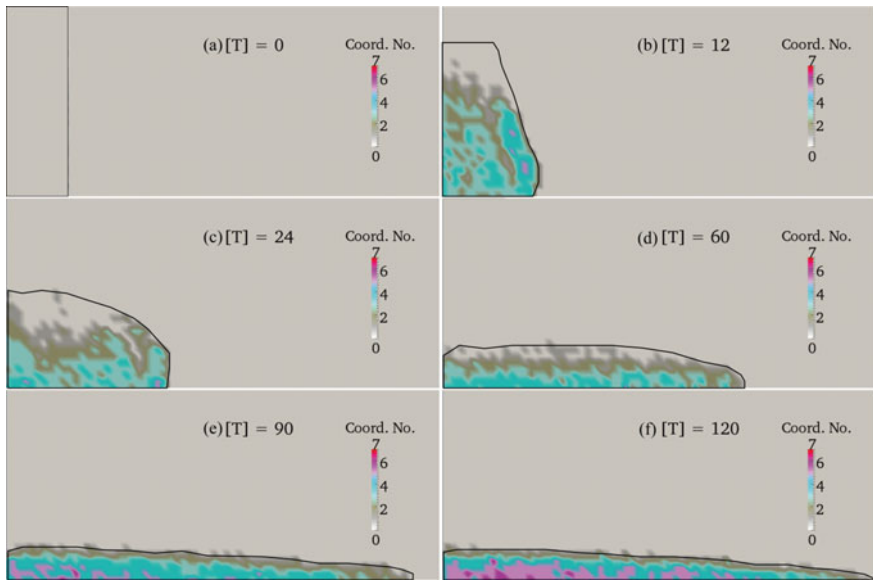


**Fig. 5.33** Evolution of coordination number of the granular assembly (the *black curves* represent granular profiles)

### 5.6.4 Mechanical and Hydraulic Behaviour of Dense Sample

On relatively gentle slopes, the solid mass can fail under slow geological processes, such as sea-level change and gas hydrate dissociation. These processes are widely observed on seabed as submarine slumps (Moore 1961), in which relatively dense sediment blocks can fail and slide along the submarine slopes. To investigate this process, the dense granular sample has been employed in the DEM–CFD coupling simulations in this section, with regard to the mechanical and hydraulic behaviour of submerged granular flows. The input parameters for the related simulations can be found in “LS2” of Appendix C.

#### 5.6.4.1 Evolution of Particle Velocity Field

During the submerged dense granular flow, the evolution of particle velocity field (plotted as vectors) is shown in Fig. 5.34, in which the normalized particle velocity is defined the same as that used in Sect. 5.6.3.1. It can be observed that the upper part of the granular column would expand when the solid grains fall downwards and spread horizontally, while the bottom region remains static. When compared

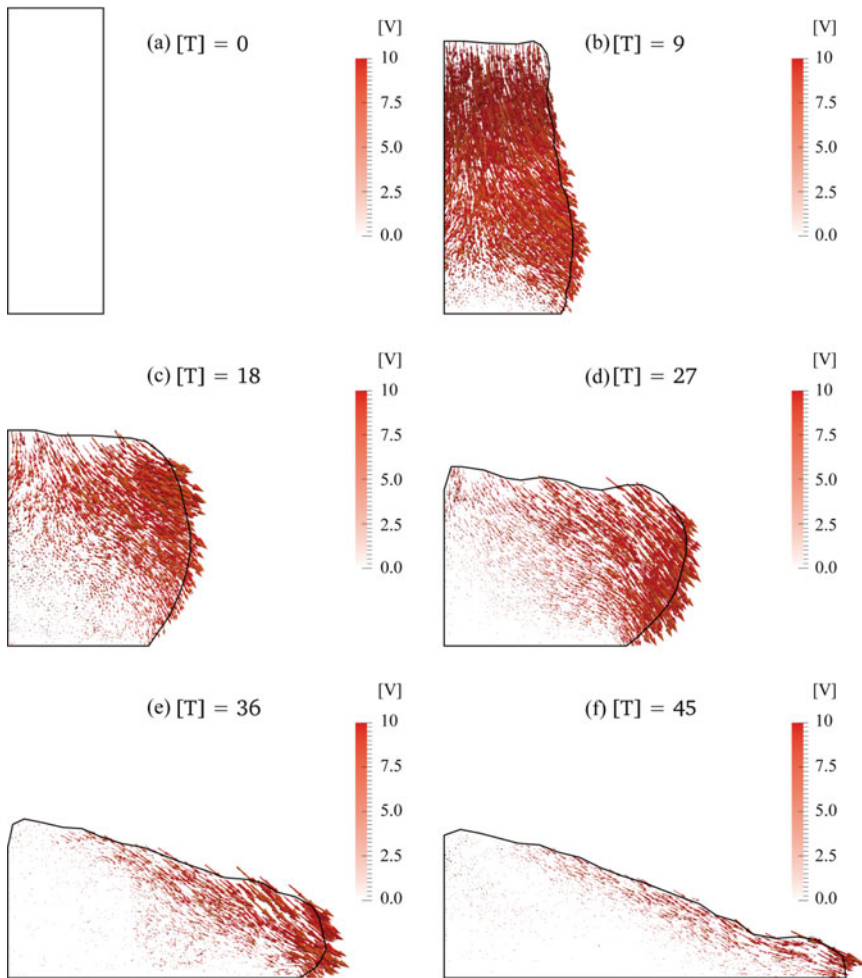


**Fig. 5.34** Evolution of particle velocity field (the *black curves* represent granular profiles)

with the distribution of particle velocity field of loose granular sample, the particles in the dense sample move relatively slow. This can be explained by the fact that the particle velocities acquired from the initial fall of granular assembly would decrease quickly due to high friction forces between solid grains and fluid viscous drag forces. In addition, the negative excess pore water pressures generated during the submerged granular flow can inhibit the motion of solid grains. As a consequence, the grains would slump slowly on the floor. At the end of the simulation, a static granular deposit forms near the slope source region with a relatively short run-out distance.

### 5.6.4.2 Evolution of Fluid Velocity Field

During the submerged dense granular flow, the evolution of fluid velocity field (plotted as vectors) behaves similarly to the particle velocity field, as shown in Fig. 5.35. It can be observed that the high fluid velocity occurs near the upper part of the granular column, which corresponds to the same region where the solid grains fall downwards and move horizontally, while it is close to zero near the bottom of the initial granular column. The magnitude of the normalized fluid velocity can be as large as 10 which is very close to the particle velocity. After  $[T] = 36$ , the major granular materials deposit on the horizontal floor. The fluid motion only occurs near the slope surface, while it remains static within the

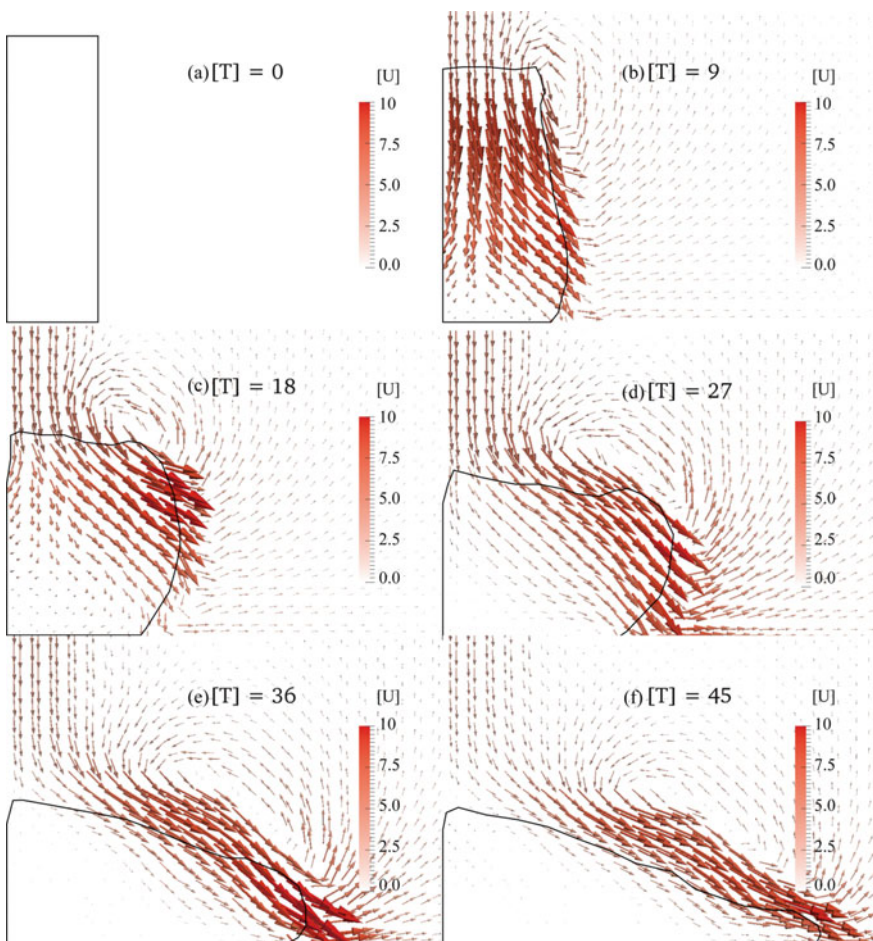


**Fig. 5.35** Evolution of the fluid velocity filed (the *black curves* represent granular profiles)

granular deposit. When compared with the distribution of fluid velocities in the submerged loose granular flow in Sect. 5.6.3.2, the fluid flow in the current analysis has relatively small velocity and no vortex has been observed throughout the simulation.

#### 5.6.4.3 Relative Velocity Between Particle and Water

During the simulation, the relative velocity between particle and water is shown in Fig. 5.36. It can be observed that the normalized relative velocity can be as large as

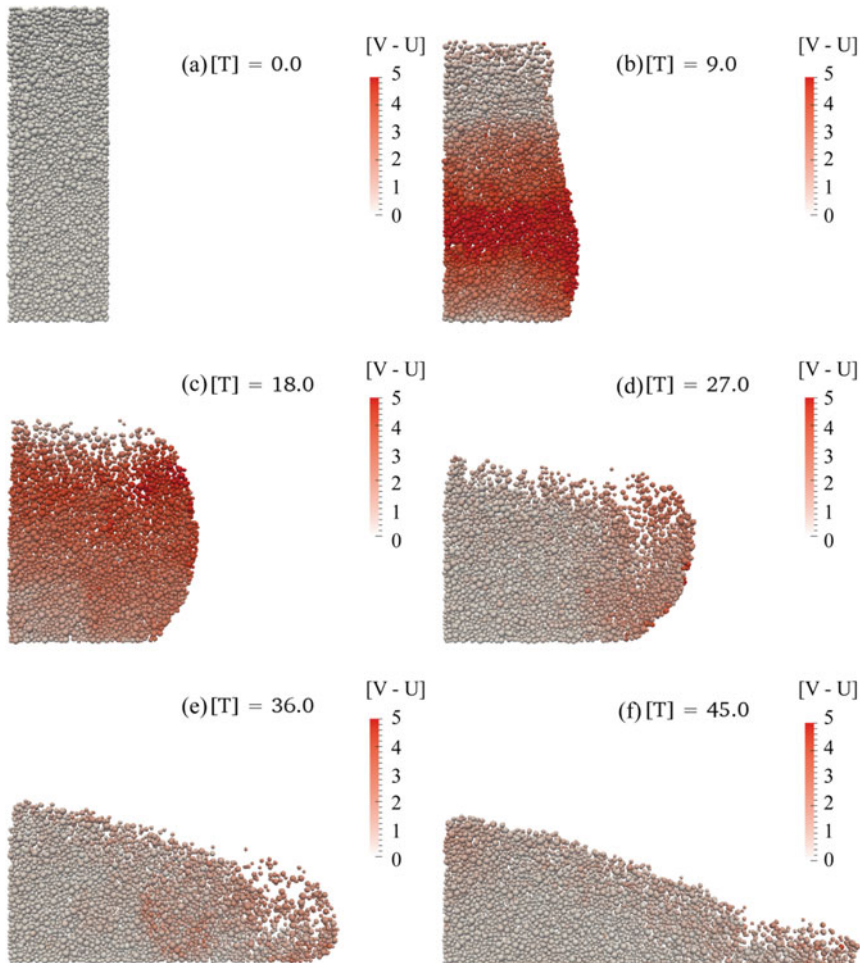


**Fig. 5.36** Evolution of the relative velocity field between particle and water

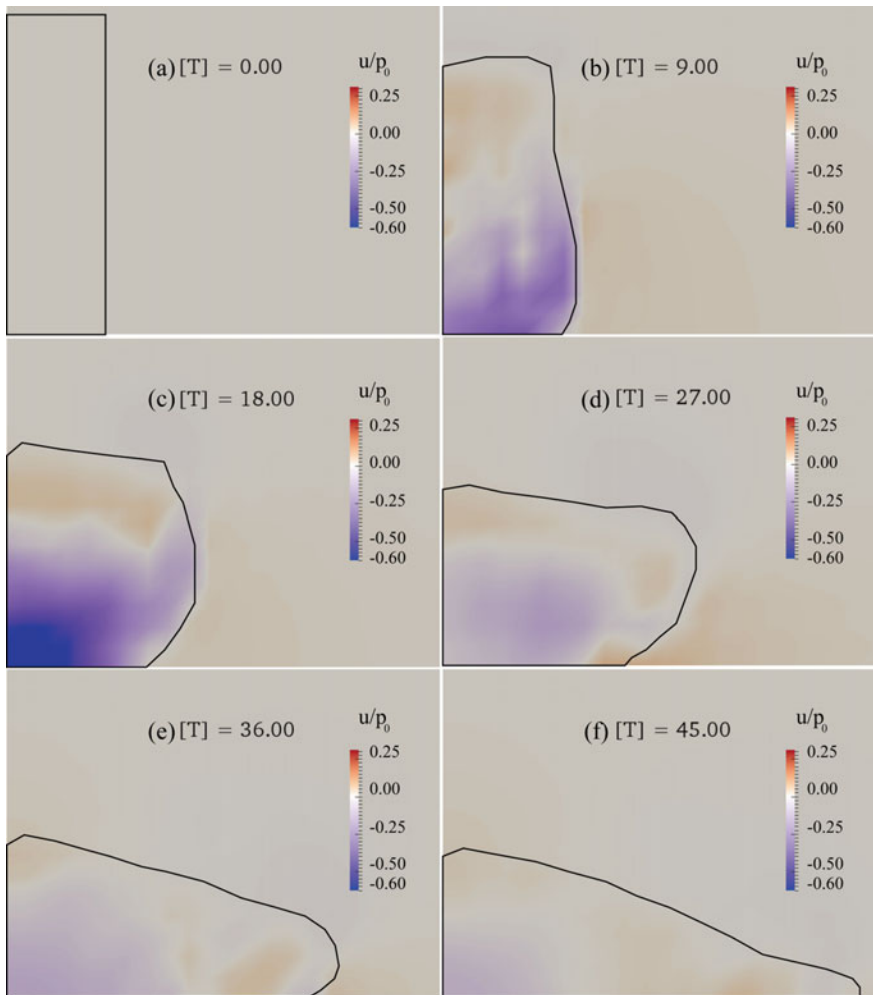


**Fig. 5.37** Evolution of excess pore water pressure (the *black curves* represent granular profiles)

5 at the propagation stage of the submerged dense granular flow. After  $[T] = 27$ , the relative velocity decreases quickly to be smaller than 2, which occurs mainly near the flow front.

#### 5.6.4.4 Evolution of Excess Pore Water Pressure

In the submerged environment, the failure of dense granular assembly would cause the sample to dilate. As a consequence, negative excess pore water pressures would occur within the sample and thus inhibit the granular motion, as illustrated in Fig. 5.37.

It can be observed that the negative excess pore water pressures mainly occur at the bottom of the sample, which amount up to 60% of the characteristic effective stress of the initial granular column. The negative excess pore water pressure occurs in the same region as the high relative velocity field, as shown in Fig. 5.36. Positive excess pore water pressures occur at the top region due to the gradual sedimentation of upper grains. However, their magnitudes are relatively small when compared with the negative excess pore water pressures. Therefore, the upper grains can slide over the bottom static granular pile, forming a thick deposit on the ground floor.

#### 5.6.4.5 Evolution of Effective Stress

The evolution of effective stress within the dense granular assembly is shown in Fig. 5.38. At  $[T] = 0.0$ , the granular column is densely packed and the effective stress increases linearly with the column depth. The maximum effective stress occurs at the bottom of the column, which matches the characteristic effective stress of the initial granular column well. Once released, the granular materials in the upper region fall downwards, while grains in the bottom region are pushed to move horizontally. The inertial forces exerted by the upper grains would place an additional force on particles in the lower region. As a result, the effective stress increases gradually in the bottom region, while it decreases in the upper region. As some grains in the upper region can suspend in the fluid without any contact with other grains, the effective stress there can remain as zero. At the end of the simulation, a static granular deposit is formed on the ground floor and the magnitudes of effective stresses within the granular assembly is smaller than 0.25.

#### 5.6.4.6 Evolution of Bulk Coordination Number

The evolution of bulk coordination number for submerged dense debris flow is shown in Fig. 5.39. As the solid grains are initially in contact, the bulk coordination number increases with the depth and the average coordination number is around 6. Once released, the granular assembly would expand to fall downwards and move horizontally, so that the bulk coordination number of the granular sample decrease gradually. As many grains in the upper region of the sample become suspended in water, the bulk coordination number there remains as zero. At the end of the simulation, a static granular deposit is formed on the floor, which has a similar distribution pattern of coordination number as that of the loose sample (Fig. 5.33). The bulk coordination number is smaller than 2 near the slope surface, while it is around 6 in the slope source region.

This section has analysed the different mechanical and hydraulic behaviour of submerged debris flows and slumps using a modified scaling relationship of drag

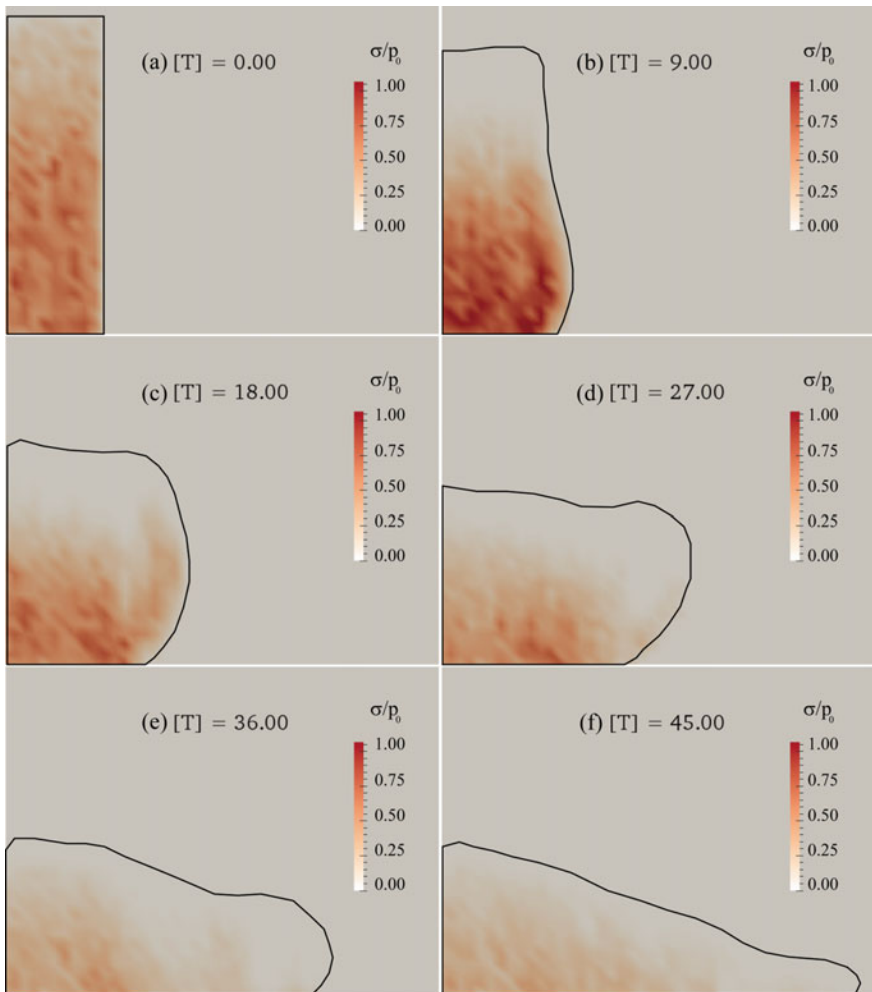


**Fig. 5.38** Distribution of effective stress within the granular assembly (the *black curves* represent granular profiles)

force in the DEM–CFD coupling model. The numerical results have been obtained, regarding the mechanisms controlling the motion of submerged landslides. It can be concluded that the induced high positive excess pore water pressure can mobilize debris flows, while negative excess pore water pressure would inhibit the granular motion. Therefore, the submerged landslides with very long run-out distances should be initially loose or become loose during the disintegrative motion after the slope failure.

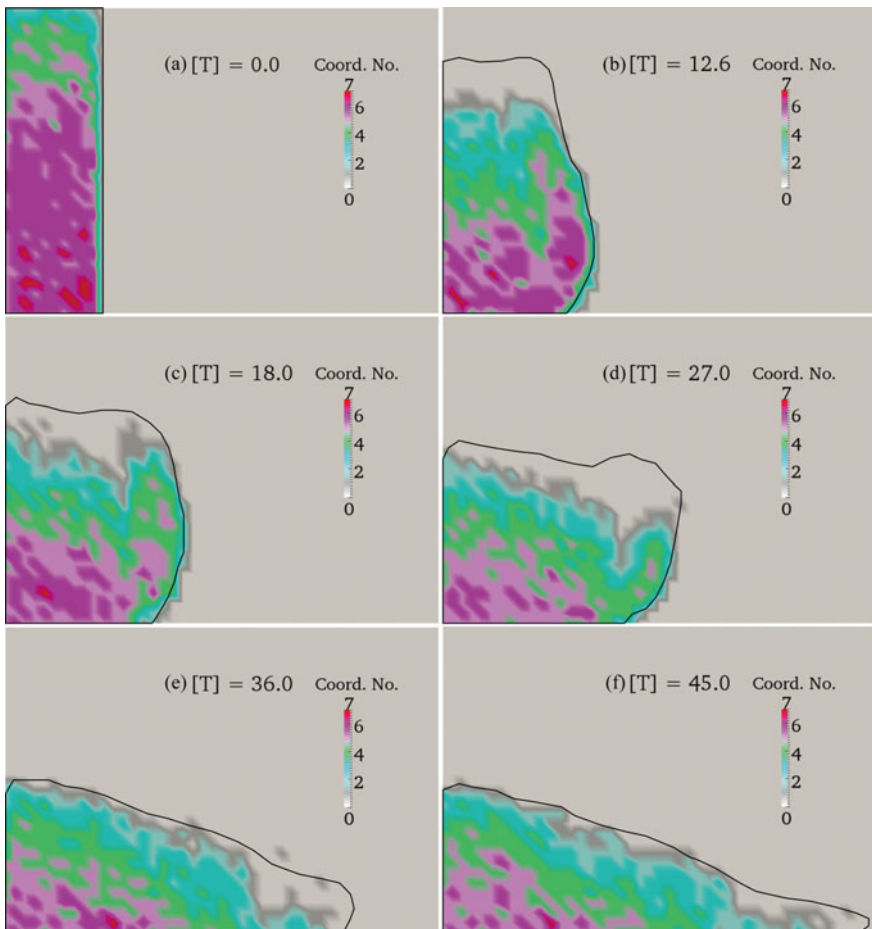


**Fig. 5.39** Evolution of coordination number of the granular assembly (the *black curves* represent granular profiles)

## 5.7 Conclusions

In this chapter, the DEM–CFD coupling method has been employed to investigate the mechanical and hydraulic behaviour of submerged granular flows. A set of governing dimensionless groups have been identified via dimensional analyses. The influence of these dimensionless groups on the depositional behaviour of granular materials was analysed, with two main objectives: (i) to provide detailed information of the influence of micro- and macroscopic dimensionless groups on the submerged debris flows; (ii) to give insights into the mobilization process of submerged landslides.

In the submerged environment, the small-scale submerged granular flows have shorter run-out distances and higher deposit heights than their terrestrial counterparts with the same model configurations. During the simulation, the excess pore water pressure generated within the granular assembly of small-scale models amount to only a small fraction (i.e. less than 4%) of the characteristic effective stress of the initial granular column, which is insufficient to mobilize a large amount of granular materials to run a long distance. The numerical results also reveal the limitation of the DEM–CFD coupling method that only a small number of particles can be used in the simulation, due to the extremely high computational cost. Thus, some fundamental features of real large-scale submerged debris flows cannot be reproduced. For instance, the very fine materials, such as silt, clay and mud, have been reported to be responsible for many huge onshore/offshore landslides on very gentle slopes (Mitchell and Soga 2005; Dean 2009), while the current small-scale numerical model cannot reproduce this feature.

To overcome the limitations of small-scale numerical simulations, a modified scaling relationship of drag force has been employed in modelling large-scale landslides. By choosing relatively large grain diameters and proper scaling factors, the large solid grains can effectively represent a clump of very fine particles. In this research, the positive excess pore water pressure within the sample can amount up to 35% of the effective stress of the submerged slope. As a result, the loose samples can run a very long distance, representing the features of real submerged debris flows, while dense samples can only run a very short distance, revealing the general features of submerged slumps.

This research has successfully identified the general features of submerged debris flows using the DEM–CFD coupling model. Future work on this subject will be mainly the improvement of the DEM capability in modelling a wide variety of solid materials, especially very fine grains, so that a complete study of the mechanical and hydraulic behaviour of submerged landslides can be made.

# **Chapter 6**

## **Conclusions and Recommendations for Future Work**

This chapter presents a summary of the main conclusions reached in this book. The chief contributions and findings are outlined and suggestions are advanced for future researches.

### **6.1 Summary and Conclusions**

In this book, the results of a series of numerical experiments using the DEM and CFD have been presented, with the attempt to clarify the intricate behaviour of large-scale landslide-induced debris flows in the terrestrial and submerged environments. The main challenge has been identified as the modelling of a variety of solid materials and the use of correct model size ratio (i.e. the ratio of model size to the mean grain diameter) in simulating large-scale debris flows. In particular, it is still uncertain whether the DEM and DEM–CFD coupling models are capable of revealing the mechanical and hydraulic behaviour of debris flows. These problems have been addressed in this book through an investigation of a simple granular column collapse model, regarding the deformation and dynamic motion of debris flows. Based on this work, the general mechanisms of the initiation, propagation and deposition of terrestrial and submerged debris flows have been clarified. In addition, this research has also demonstrated the capability of the DEM and DEM–CFD coupling methods in analysing the complicated behaviour of granular materials in the processes of settling and consolidation.

Overall, the main contributions of this research have involved the following studies: (i) a review of the literature on terrestrial and submerged landslides; (ii) the validation of the DEM as a suitable numerical tool to study the realistic soil properties; (iii) the study of the initiation, propagation and deposition of dry granular flows; (iv) the validation of the DEM–CFD coupling algorithm as a suitable tool to study the fluid–solid interactions and finally (v) the investigation of

submerged debris flows using the DEM–CFD coupling. The key findings from each of these studies are summarized as below.

(i) Review of the literature on terrestrial and submerged landslides

- The classification of terrestrial and submerged landslides has been made based on the dynamic motion of slope mass. Among various types of landslides, the debris flow is identified as the most hazardous event due to its high mobility and huge amount of energy released within a short period of time. To provide some insights into this field, theoretical, experimental and numerical research have been reported in the literature. Particular focus has been put on the significant influence of water on the mobilization of debris flows. It has been observed that the generation and dissipation of excess pore water pressures during debris flows can directly influence the dynamic motion of solid materials.
- Although the experimental research has shed some light on the mechanisms of debris flows, it is still unable to explain the apparent long run-out distance of submerged landslides, where a large amount of water is present. Thus, the numerical investigation using the DEM–CFD coupling approach has been proposed as a possible tool for understanding and predicting the mechanical and hydraulic behaviour of submerged landslides.

(ii) DEM as a suitable numerical tool to study soil behaviour

- In the DEM mode, a very simple and effective un-damped particle collision model has been employed to determine the numerical time step. By using the critical time step, the energy of the whole system can remain constant throughout the simulation. As a damped granular system requires the use of smaller time step than that predicted by an un-damped model, the time step selected is believed to be applicable in landslide simulations.
- The motion of real solid grains in debris flows is inhibited by high friction due to particle friction and interlocking, such that the granular assembly can only travel a short distance. To consider the particle shape effect, the rolling resistance contact model has been implemented in the DEM code. Additionally, the soil strength properties, such as the internal friction angle and angle of repose have been calibrated via numerical triaxial tests and granular column collapse model.

(iii) Study of the initiation, propagation and deposition of dry granular flows

- A dimensional analysis of a simple granular column collapse model has been performed, based on which, a set of fundamental dimensionless groups was formulated. A parametric study was conducted to clarify the influence of these governing dimensionless groups on the depositional behaviour of debris materials. In particular, the relationships between the column aspect ratio, characteristic strain, model size ratio, material

internal friction angle and normalized run-out distance, deposit height have been investigated.

- Detailed analyses of the mechanical behaviour of granular flows were conducted on a specific granular column with aspect ratio of 3.3, regarding the particle velocity profile, energy evolution, packing state, stress distribution and the particle mobility.

(iv) Study of the fluid–solid interactions using the DEM–CFD coupling algorithm

- A new parallel data exchange program using the Message Passing Interface (MPI) has been developed in the original DEM–CFD coupling code (Chen et al. 2011).
- The DEM–CFD coupling algorithm has been validated using two benchmark numerical simulations: (a) fluid flow through a porous soil sample, and (b) modelling of grain batch sedimentation. In the first example, the numerical results have been compared with the empirical correlations proposed by Ergun (1952) and Trussell and Chang (1999). It has been observed that the relationship between flow velocity and hydraulic gradient can be linear or parabolic, based on the Reynolds number of fluid flow. The second example investigates the settling behaviour of grains in water. The periodic boundary condition used in the CFD model can effectively reduce the wall friction effects. Due to the segregation of grains along the prism depth, coarse grains accumulate at the bottom, while fine grains deposit on the top surface of sediments. This phenomenon leads to a gradual change of density gradients and particle-size distributions. The evolution of the fluid–suspension interface and the suspension–sediment interface can match the theoretical results proposed by Kynch (1952) very well.

(v) Investigation of submerged debris flows

- The granular column collapse model has been used to investigate the mechanical and hydraulic behaviour of submerged debris flows, based on which, a detailed dimensional analysis has been performed. The influence of the fundamental dimensionless groups on the propagation and deposition of debris materials has been analysed using the DEM–CFD model. Conclusions are drawn with regard to the ability of the DEM–CFD coupling model to simulate the dynamic motion of granular materials and hydraulic response of fluid.
- Using the small-scale DEM models, the magnitude of excess pore water pressure generated during debris flows amounts to less than 4% of the effective stress of the granular assembly, which is not large enough to mobilize debris materials to run long distances. The limitation is due to the fact that the model size ratio in the simulation is smaller than the real value, such that the consolidation of sediments and the induced excess pore water pressure cannot be accurately simulated.

- A modified scaling relationship of drag force has been employed in studying large-scale landslides. By scaling up the particle diameters and drag forces, a large DEM particle can represent a clump of fine particles. As a result, the positive excess pore water pressure within the sample can amount up to 35% of the effective slope stress. Loose granular samples can travel a long distance, representing the features of real submerged debris flows, while dense samples can only travel a short distance, revealing the general features of slumps.
- Based on the current computational resources, the DEM is still unable to simulate large-scale landslides consisting of millions of grains. However, the scaling method employed in this research can significantly reduce the simulation time.

## 6.2 Recommendations for Future Work

Based on the summary of the current research, recommendations for future work include:

- (i) The numerical model should be able to simulate a wider range of solid materials, so that the correct mechanical and hydraulic behaviour of debris flows can be obtained. This requirement would increase the number of grains in the model and thus increase the computational cost significantly. The simulations in the current research are mainly run on a desktop PC, in which the maximum number of DEM particles is 100,000. For simulation with more particles, it is suggested to use computer clusters to carry out the DEM and DEM–CFD coupling simulations.
- (ii) Verification of the capability of the modified DEM–CFD coupling model in investigating large-scale submerged debris flows (see Chap. 5) using more powerful computational resources is recommended. In particular, the combined effects of horizontal expansion and vertical compression of the debris mass on the distribution of excess pore water pressures remain to be explored.
- (iii) The modelling of free water surface and unsaturated soil sample will be challenging tasks for investigating debris flows. To accomplish these tasks, the volume of fluid (VOF) and capillary force model could be implemented in the current DEM–CFD coupling program.
- (iv) Simulations considering the typography of slopes are needed in evaluating the potential risks of real landslides. In particular, case studies of debris flows should be performed using the DEM and DEM–CFD coupling methods.

# Appendix A

## Summary of the Selected Landslides

### *Terrestrial volcanic landslides*

Name	$L_{\max}$ (km)	$H_{\max}$ (km)	$V$ ( $\text{km}^3$ )	References
Akagi	19	2.4	4	Hayashi and Self (1992)
Asakusa	6.5	1	0.04	Hayashi and Self (1992)
Asama	20	1.8	2	Hayashi and Self (1992)
Bandai-san 1888	11	1.2	1.5	Hayashi and Self (1992)
Bezymianni 1956	18	2.4	0.8	Hayashi and Self (1992)
Callaqui	15	3.1	0.15	Hayashi and Self (1992)
Chaos Crags	5	0.65	0.15	Hayashi and Self (1992)
Chimborazo	35	3.6	8.1	Hayashi and Self (1992)
Chokai	25	2.2	3.5	Hayashi and Self (1992)
Colima	40	4	12.5	Hayashi and Self (1992)
Egmont (Opua)	27	2.5	0.35	Hayashi and Self (1992)
Egmont (Pungarehu)	31	2.6	7.5	Hayashi and Self (1992)
Fuji	24	2.5	1.8	Hayashi and Self (1992)
Galunggung	25	1.9	2.9	Hayashi and Self (1992)
Iriga	11	1.05	1.5	Hayashi and Self (1992)
Iwaki	14	1.6	1.3	Hayashi and Self (1992)
Jocotitlan	12	1.15	2.8	Siebe et al. (1992)
Komagatake	11.5	1	0.25	Hayashi and Self (1992)
Kurohime	6	0.8	0.12	Hayashi and Self (1992)
Mageik	9	0.8	0.09	Hayashi and Self (1992)
Mawenzi	60	4.5	7.1	Hayashi and Self (1992)
Meru	50	3.9	15	Hayashi and Self (1992)
Monbacho	12	1.3	1	Hayashi and Self (1992)
Mt. S. Helen 1980	24	2.55	2.5	Hayashi and Self (1992)

(continued)

(continued)

<i>Terrestrial volcanic landslides</i>				
Name	$L_{\max}$ (km)	$H_{\max}$ (km)	$V$ ( $\text{km}^3$ )	References
Myoko (Sekikawa)	19	2	0.8	Hayashi and Self (1992)
Myoko (Taguchi)	8	1.4	0.23	Hayashi and Self (1992)
Ovalnaya Zimina	17	2.4	0.4	Hayashi and Self (1992)
Papandayan	11	1.5	0.14	Hayashi and Self (1992)
Peteroa	85	3.9	16	Hayashi and Self (1992)
Popa	11	1.2	0.8	Hayashi and Self (1992)
Popocatepetl	33	4	28	Hayashi and Self (1992)
Shasta	50	3.55	26	Hayashi and Self (1992)
Shiveluch	12	2	1.5	Hayashi and Self (1992)
Sierra Velluda	25	3.4	0.5	Hayashi and Self (1992)
Socompa	35	3.25	17	Hayashi and Self (1992)
Soufriere Guadeloupe	9.5	1.35	0.5	Siebert (1984)
St. Helens	16	1.75	1	Siebert (1984)
Tashiro	8.8	0.7	0.55	Hayashi and Self (1992)
Tateshina	12.5	1.4	0.35	Hayashi and Self (1992)
Unzen	6.5	0.85	0.34	Hayashi and Self (1992)
Usu	6.5	0.5	0.3	Hayashi and Self (1992)
Vesuvius 1944	0.64	0.575	0.000179	Hazlett et al. (1991)
Vesuvius 1945	0.94	0.505	0.0009	Hazlett et al. (1991)
Vesuvius 1946	0.5	0.285	0.00055	Hazlett et al. (1991)
Vesuvius 1947	0.96	0.47	0.000793	Hazlett et al. (1991)
Vesuvius 1948	1.24	0.636	0.001	Hazlett et al. (1991)
Vesuvius 1949	0.68	0.36	0.0011	Hazlett et al. (1991)
Vesuvius 1950	0.82	0.41	0.00116	Hazlett et al. (1991)
Yatsugatake (Nirasaki)	32	2.4	9	Hayashi and Self (1992)
Yatsugatake (Otsukigawa)	12.5	1.4	0.27	Hayashi and Self (1992)
<i>Terrestrial non-volcanic landslides</i>				
Blackhawk	9.6	1.2	0.28	Hayashi and Self (1992)
Corno di desde	3.7	1.2	0.02	Hayashi and Self (1992)
Deyen, Glans	6.6	0.74	0.6	Hayashi and Self (1992)
Diaberets	5.5	1.9	0.05	Hayashi and Self (1992)
Disentis	2.1	0.74	0.015	Hayashi and Self (1992)
Elm	2.3	0.71	0.01	Hayashi and Self (1992)
Engelberg	7.4	1.6	2.75	Hayashi and Self (1992)
Fernpass	15.6	1.4	1	Hayashi and Self (1992)
Flims	15.6	2	12	Hayashi and Self (1992)
Frank	3.5	0.87	0.03	Hayashi and Self (1992)
Garnish	7.5	1.9	0.8	Hayashi and Self (1992)
Goldau	6	1.2	0.035	Hayashi and Self (1992)

(continued)

(continued)

<i>Terrestrial volcanic landslides</i>						
Name	$L_{\max}$ (km)	$H_{\max}$ (km)	$V$ ( $\text{km}^3$ )	References		
Gros Ventre	3.4	0.56	0.038	Hayashi and Self (1992)		
Kandertal	9.9	1.9	0.14	Hayashi and Self (1992)		
Maligne Lake	5.47	0.92	0.5	Hayashi and Self (1992)		
Medicine Lake	1.22	0.32	0.086	Hayashi and Self (1992)		
Madison	1.6	0.43	0.029	Hayashi and Self (1992)		
Mombiel	0.8	0.37	0.0008	Hayashi and Self (1992)		
Obersee GL	5	1.8	0.12	Hayashi and Self (1992)		
Pamir	6.2	1.5	2	Hayashi and Self (1992)		
Poshivo	4.1	1.5	0.15	Hayashi and Self (1992)		
Saidmarreh	18.9	1.5	20	Hayashi and Self (1992)		
Schachental	3.1	1.8	0.0005	Hayashi and Self (1992)		
Scimada Saoseo	5.5	1.5	0.08	Hayashi and Self (1992)		
Sherman	6.2	1.3	0.03	Hayashi and Self (1992)		
Siders	17.4	2.4	1.5	Hayashi and Self (1992)		
Tamins	13.5	1.3	1.3	Hayashi and Self (1992)		
Voint	1.5	0.5	0.25	Hayashi and Self (1992)		
Val Lagone	2.4	1.05	0.00065	Hayashi and Self (1992)		
Voralpsee	3.4	1.1	0.03	Hayashi and Self (1992)		
Wengen 1	1.1	0.5	0.0025	Hayashi and Self (1992)		
Wengen 2	1.4	0.59	0.0055	Hayashi and Self (1992)		
<i>Submarine landslides</i>						
Name	$L_{\max}$ (km)	$H_{\max}$ (km)	$V$ ( $\text{km}^3$ )	Slope ( $^\circ$ )	Material	References
Alika-1	105	5.3	1800	15–20	Sandy silt, gravel	Hürlimann et al. (2001)
Alika-2	95	4.8	300			Normark et al. (1993)
A1	370	1.7	250			Lipman et al. (1988)
A2	160	1.5	22			Lipman et al. (1988)
A3	140	1.4	8.5			Lipman et al. (1988)
A4A	130	1.3	320			Lipman et al. (1988)
A4B	400	2	320			Lipman et al. (1988)
Afen slide	12		0.14	0.7–2.5		Wilson et al. (2004)
Agulhas	106	0.38				Hampton et al. (1996)
Albatross Bank	5.3	0.3		7		Prior and Coleman (1979)
Alsek	2	0.02		1.3		Schwab and Lee (1993)
Atlantic Coast	3.4	0.03		3.8		Prior and Coleman (1979)
Bassein	215	2.2	800	6		Moore et al. (1976)
Bay of Biscay	21	0.25				Prior and Coleman (1979)

(continued)

(continued)

Name	$L_{\max}$ (km)	$H_{\max}$ (km)	$V$ (km <sup>3</sup> )	Slope (°)	Material	References
Blake Escarpment	42	3.6	600	8.6		Dillon et al. (1993)
California	3.5	0.15	0.25	1–10	Sandy silt	Edgers and Karlsrud (1982)
Canary debris flow	600	3	400	0–1	Volcanic sediment	Masson et al. (1998)
Cape Fear	30	0.7		4.2		Popenoe et al. (1991)
Copper river delta	18	0.115	24	1	Muddy sand	Edgers and Karlsrud (1982)
East Break East	70	1.15	13	1.5		McGregor et al. (1993)
East Break West	110	1.1	160	1.5		McGregor et al. (1993)
El Golfo avalanche	65		165	1–10	Volcanic sediment	Masson (1996)
Grand Banks	110	5	200	3.5	Glacigenic sediment	Fine et al. (2005)
Helsinki Harbour	0.4	0.011	6E –06		Sand / Silt	Prior and Coleman (1979)
Icy Bay	12	80	32	0.4	Clayey silt	Lee and Edwards (1986)
Kae Lae slide	60	5	40			Lipman et al. (1988)
Kayak Trough	15	0.15	5.9	1	Clayey silt	Carlson and Molnia (1977)
Kidnappers Slump	11	0.2	8	1–4	Sandy silt and clay	Lewis (1971)
Kitimat slide	6	0.2	0.2		Fine sand	Prior et al. (1984)
La Orotava valley	15	2.2			Volcanic sediment	Hürlimann et al. (2001)
Magdalena Delta	24	1.4	0.3	2	Clayey silt	Shepard (1973)
Messina	220	3.2	0.001	1.5–2.5	Sand/Silt	Billi et al. (2008)
Mid. Alb. Bank	5.3	0.6	19		Silty clay	Hampton et al. (1996)
Mid. Atl. Cont.	3.5	0.3	0.4		Sand, Silty clay	Lewis (1971)
Mississippi River delta		0.02	0.04	0.5		Edgers and Karlsrud (1982)
Molokai slide	130	5.2	1100			Lipman et al. (1988)
Navarin Canyon	6	0.175	5	3		Carlson et al. (1993)
Nuuanu slide, Hawaii	230	5	5000	0–5	Volcanic rock	Moore et al. (1989)
Oahu slide	180	5.5	1800			Lipman et al. (1988)

(continued)

(continued)

Name	$L_{\max}$ (km)	$H_{\max}$ (km)	$V$ (km <sup>3</sup> )	Slope (°)	Material	References
Orkdalsfjord	22.5	0.5	0.025	3.5	Sand / Silt	Prior and Coleman (1979)
Paoanui	70	200	1	1–6	Volcanic ash	Lewis (1971)
Portlock Bank	6.5	0.2		4		Prior and Coleman (1979)
Ranger	37	0.8	20	3	Clayey silt	Normark (1974)
Rockall	160	0.33	300	2		Prior and Coleman (1979)
Sagami Wan			70	11		Edgers and Karlsrud (1982)
Sandnesjoen	1.2	0.18	0.005			Edgers and Karlsrud (1982)
Santa Barbara	2.3	0.12	0.02	4.8	Silty clay	Edwards et al. (1993)
Scripps Canyon		0.006	5E–5	7		Edgers and Karlsrud (1982)
Seward	3	0.2	0.003	25		Hampton et al. (1993)
Sokkelvik	5	0.1	0.005		Quick clay, sand	Edgers and Karlsrud (1982)
Spanish Sahara	700	3.1	600	0.05–1.6	Pelagic sediment	Gee et al. (1999)
Storegga slide	810	1.7	2400	1.4–0.05		Haflidason et al. (2004)
Sur	70	0.75	0.5	10		Gutmacher and Normark (1993)
Suva, Fiji	110	1.8	0.15	3	Sand	Rahiman et al. (2007)
Tenerife Island	100	3.7	1000	5–10	Sandy silt, gravel	Watts and Masson (1995)
Tristan de Cunha	50	3.75	150			Holcomb and Searle (1991)
Valdez	1.28	0.17	0.075	6	Gravelly sand	Edgers and Karlsrud (1982)
Wil. Canyon	60	2.8	11	8.6	Silty clay	Edgers and Karlsrud (1982)

## Appendix B

### Calculation of Porosity

As each fluid mesh cell is a fixed and enclosed space, the solid particles may move across the fluid mesh boundaries frequently during the simulation. The approach to calculate the porosity of a fluid mesh cell only accounts for the solid volume of a particle when its centre lies within that mesh cell. However, this method is not accurate, as the solid spheres can be intersected by the mesh boundaries. One assumption is that the bounding surface of fluid mesh cells can deform so that they never cut through the dispersed particles (Brennen 2005). However, it is very difficult to do so in a fixed grid Eulerian fluid domain. In Fig. B.1a, b, two different granular packing patterns can be identified, while Fig. B.1c illustrates the intersection between one solid particle and a plane. In Fig. B.1a, all particles are packed within the fluid mesh cells and the porosity can be calculated as

$$n = (V_f - V_s)/V_f = 1 - \sum_{i=1}^{N_p} V_{si} / V_f, \quad (\text{B.1})$$

where  $n$  is the porosity;  $V_f$  is the volume of the mesh cell;  $V_s$  is the total volume of the solid grains;  $V_{si}$  is the volume of a single particle  $i$ ;  $N_p$  is the number of particles.

In Fig. B.1b, the fluid cell boundary plane intersects some solid particles. For particles at the boundary, the exact solid volume locating inside the fluid mesh cell should be calculated. Assuming the fluid mesh boundary intersects  $M_p$  particles and denoting the solid volume outside the mesh cell of a single particle  $j$  as  $V_{oj}$ , the porosity is calculated as:

$$n = (V_f - V_s)/V_f = 1 - \left( \sum_{i=1}^{N_p} V_{si} - \sum_{j=1}^{M_p} V_{oj} \right) / V_f. \quad (\text{B.2})$$

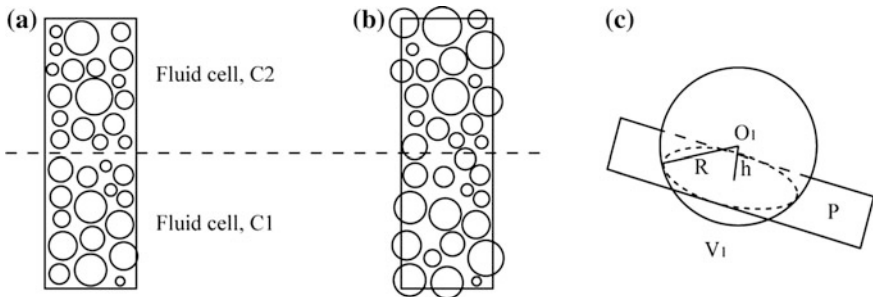


**Fig. B.1** The particle packing state in fluid mesh cells

In Fig. B.1c, the volume  $V_1$  is calculated as

$$V_1 = \pi R(R - h)^2 - \frac{1}{3}\pi(R - h)^3. \quad (\text{B.3})$$

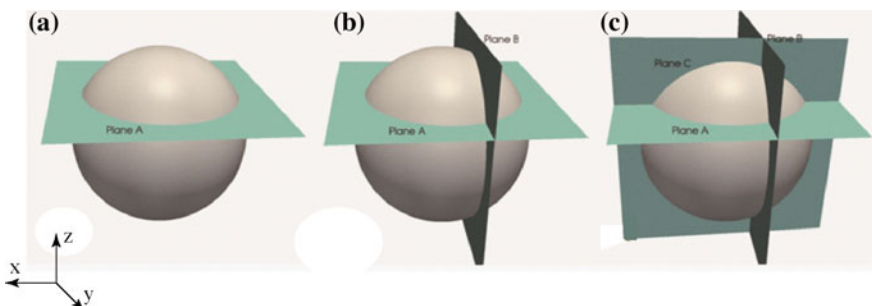
In a 3D model, the intersection patterns can be categorized into three fundamental cases, as shown in Fig. B.2.

In the following illustrations from Figs. B.3, B.4, and B.5, the projected relative locations of sphere and fluid mesh cell boundaries are represented by circles and straight lines. The shaded areas are used to show the solid volumes intersected by the boundaries.

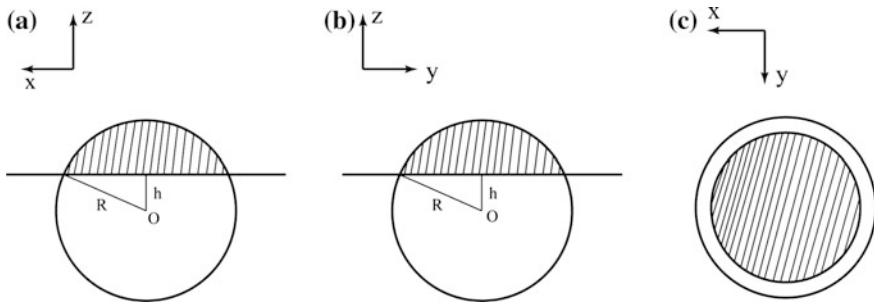
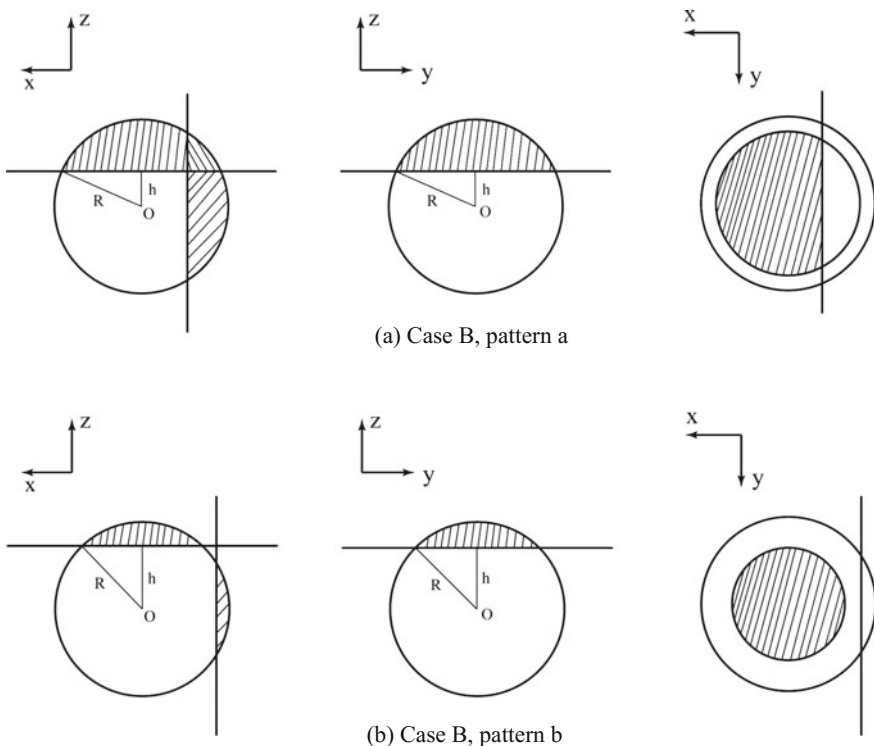
In case A, the projection of the sphere and plane in three different directions are shown in Fig. B.3.

For case B and C, according to the relative positions of the planes in space, several sub-intersection patterns can be identified, as shown in Figs. B.4, and B.5.

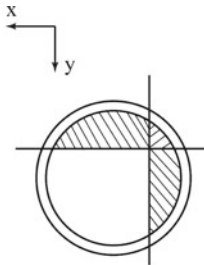
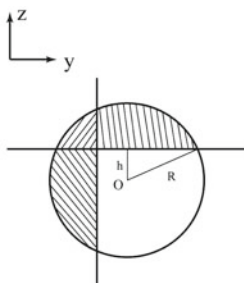
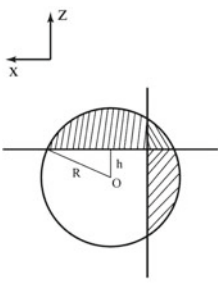
From the discussions above, it can be observed that the intersection between the fluid mesh cell boundaries and solid particles can be different according to the relative location of the solid particle and fluid mesh cell boundaries. To get the



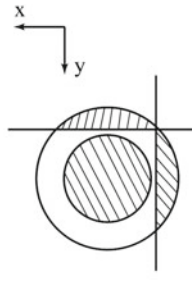
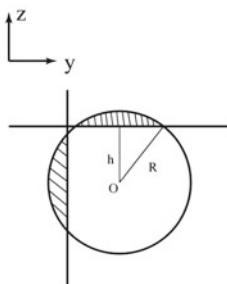
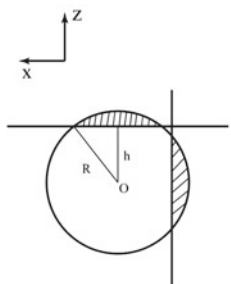
**Fig. B.2** The solid–fluid intersection patterns

**Fig. B.3** The projections of intersection pattern A**Fig. B.4** The projections of intersection pattern B

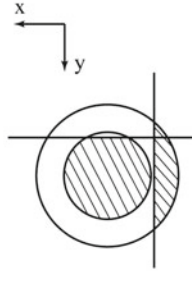
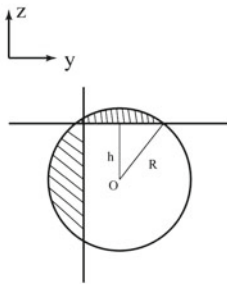
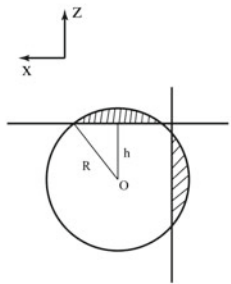
accurate values of porosity for each fluid mesh cell, it is highly necessary to calculate the accurate solid volume for each part of intersected solid volumes. In the following sections, the analytical equations used to calculate the solid volume in case B(a) is derived.



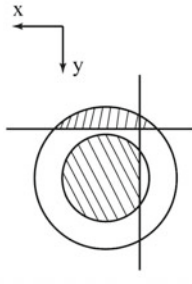
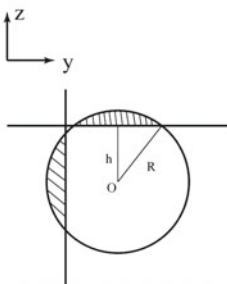
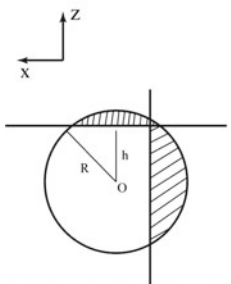
(a) Case C, pattern a



(b) Case C, pattern b



(c) Case C, pattern c



(d) Case C, pattern d

**Fig. B.5** The projections of intersection pattern C

The volume of the coloured region in Fig. B.6 is represented by the diagram shown in Fig. B.7. The parameters  $a$  and  $b$  are the distance from the sphere centre to the  $y-z$  and  $x-z$  coordinate planes. The solid volume is expressed in an integral form, as

$$V1 = \int_{-\sqrt{R^2-a^2-b^2}}^{\sqrt{R^2-a^2-b^2}} \left[ \int_b^{\sqrt{r^2-a^2}} (\sqrt{r^2-y^2} - a) dy \right] dz \quad (B.4)$$

where  $r = \sqrt{R^2 - z^2}$  is the radius of the intersection circle at the height of  $z$ . The inner integration of Eq. (B.4) is expressed as

$$\begin{aligned} & \int_b^{\sqrt{R^2-a^2-z^2}} (\sqrt{R^2 - z^2 - y^2} - a) dy \\ &= \left[ \frac{y}{2} \sqrt{R^2 - z^2 - y^2} + \frac{R^2 - z^2}{2} \arcsin \frac{y}{\sqrt{R^2 - z^2}} - ay \right]_b^{\sqrt{R^2-a^2-z^2}} \\ &= \frac{a}{2} \sqrt{R^2 - a^2 - z^2} + \frac{R^2 - z^2}{2} \arcsin \sqrt{\frac{R^2 - a^2 - z^2}{R^2 - z^2}} - a \sqrt{R^2 - a^2 - z^2} \\ &\quad - \frac{b}{2} \sqrt{R^2 - b^2 - z^2} - \frac{R^2 - z^2}{2} \arcsin \frac{b}{\sqrt{R^2 - z^2}} + ab \end{aligned} \quad (B.5)$$

Since  $\arcsin \sqrt{\frac{R^2-a^2-z^2}{R^2-z^2}} = \arcsin \sqrt{1 - \frac{a^2}{R^2-z^2}} = \arccos \frac{a}{\sqrt{R^2-z^2}}$ , let  $r = \sqrt{R^2 - z^2}$ , then

$$\begin{aligned} r \times \sin \left( \arccos \left( \frac{a}{\sqrt{R^2 - z^2}} \right) \right) &= \sqrt{R^2 - a^2 - z^2} \\ r \times \cos \left( \arcsin \left( \frac{b}{\sqrt{R^2 - z^2}} \right) \right) &= \sqrt{R^2 - b^2 - z^2} \end{aligned} \quad (B.6)$$

Thus, the integration Eq. (B.5) becomes,

$$\begin{aligned} & \int_b^{\sqrt{R^2-a^2-z^2}} (\sqrt{R^2 - z^2 - y^2} - a) dy = \frac{r^2}{2} \left( \arccos \left( \frac{a}{r} \right) - \arcsin \left( \frac{b}{r} \right) \right) \\ & - \frac{a}{2} \left( r \times \sin \left( \arccos \left( \frac{a}{r} \right) \right) - b \right) - \frac{b}{2} \left( r \times \cos \left( \arcsin \left( \frac{b}{r} \right) \right) - a \right) \end{aligned} \quad (B.7)$$

Thus, Eq. (B.4) becomes

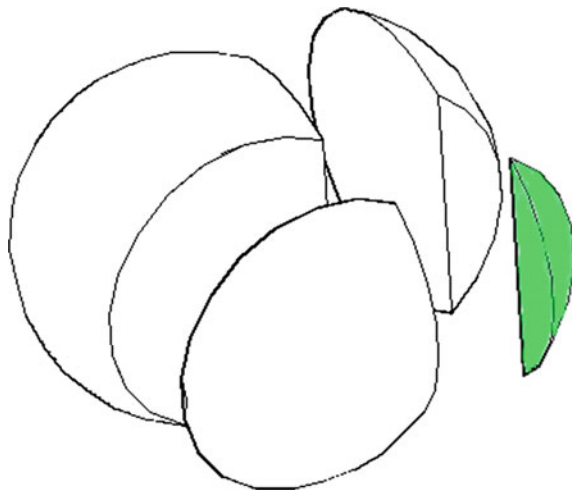


**Fig. B.6** The three-dimensional view of intersection pattern B(a)

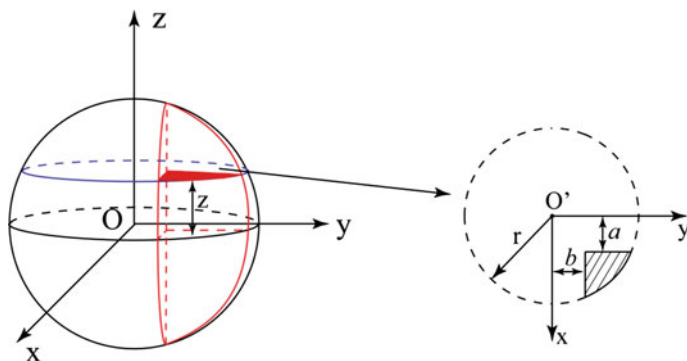


**Fig. B.7** The projections of intersections

$$V1 = \int_{-\sqrt{R^2-a^2-b^2}}^{\sqrt{R^2-a^2-b^2}} \left[ \frac{r^2}{2} \left( \arccos\left(\frac{a}{r}\right) - \arcsin\left(\frac{b}{r}\right) \right) - \frac{a}{2} \left( r \times \sin\left(\arccos\left(\frac{a}{r}\right)\right) - b \right) - \frac{b}{2} \left( r \times \cos\left(\arcsin\left(\frac{b}{r}\right)\right) - a \right) \right] dz \quad (\text{B.8})$$

The integration in Eq. (B.8) cannot be done analytically. Thus, the numerical Gauss-Legendre integration method will be used, as shown below.

First, let

$$\begin{aligned} F(z) = & \frac{r^2}{2} \left( \arccos\left(\frac{a}{r}\right) - \arcsin\left(\frac{b}{r}\right) \right) \\ & - \frac{a}{2} \left( r \times \sin\left(\arccos\left(\frac{a}{r}\right)\right) - b \right) - \frac{b}{2} \left( r \times \cos\left(\arcsin\left(\frac{b}{r}\right)\right) - a \right) \end{aligned} \quad (\text{B.9})$$

Then, let

$$\begin{aligned} A &= -\sqrt{R^2 - a^2 - b^2} \\ B &= \sqrt{R^2 - a^2 - b^2} \end{aligned} \quad (\text{B.10})$$

Thus, Eq. (B.8) becomes

$$V_1 = \int_A^B F(z) \, dz \quad (\text{B.11})$$

The method of Gauss–Legendre integration is expressed as:

$$\begin{aligned} V_1 &= \int_A^B F(z) \, dz = \frac{B-A}{2} \int_{-1}^1 F\left(\frac{A+B}{2} + \frac{B-A}{2}t\right) dt \\ &\approx \frac{B-A}{2} \sum_{i=0}^m C_i F\left(\frac{A+B}{2} + \frac{B-A}{2} t_i\right) \end{aligned} \quad (\text{B.12})$$

where  $m$  is the number of integration points;  $t_i$  is the value of integration point;  $C_i$  is the corresponding coefficient. Table B.1 shows the integration points and their coefficients.

**Table B.1** The Gauss–Legendre integration coefficients

$M$	$t_i$		$C_i$	
2	$\pm 0.5774$		1	
3	$\pm 0.7746$	0	0.5556	0.8889
4	$\pm 0.8611$	$\pm 0.34$	0.3478	0.6521
5	$\pm 0.9062$	$\pm 0.5385$	0.2369	0.4786
	0		0.5689	
6	$\pm 0.9325$	$\pm 0.6612$	0.1713	0.3608
	$\pm 0.2386$		0.4679	
7	$\pm 0.9491$	$\pm 0.7415$	0.1295	0.2797
	$\pm 0.4058$	0	0.3818	0.4180
8	$\pm 0.9603$	$\pm 0.7967$	0.1012	0.2224
	$\pm 0.5255$	$\pm 0.1834$	0.3137	0.3627

For other intersection patterns, the same procedure as that discussed above can be used to calculate the solid intersection volume. One only needs to change the lower and upper limits of the integral equation to the correct intersection height in the  $z$  direction.

# Appendix C

## Input Parameters for Simulations

Simulations <sup>a</sup>	SD1	SD2	SS1	SS2	LS1	LS2
<i>DEM parameters</i>						
$L_i$ (m)	0.05	0.05	0.05	0.05	50	50
$H_i$ (m)	0.05–0.5	0.165	0.05–0.5	0.165	150	150
$D_{10}$ (m)	0.002	0.002	0.002	0.002	2	2
$\rho_s$ (kg/m <sup>3</sup> )	2650	2650	2650	2650	2650	2650
$K_n$ (N/m)	$3.0 \times 10^7$	$3.0 \times 10^7$	$3.0 \times 10^7$	$3.0 \times 10^7$	$3.0 \times 10^7$	$3.0 \times 10^7$
$K_s$ (N/m)	$2.7 \times 10^7$	$2.7 \times 10^7$	$2.7 \times 10^7$	$2.7 \times 10^7$	$2.7 \times 10^7$	$2.7 \times 10^7$
$\theta$	30	30	30	30	30	30
$\beta$	1	1	1	1	1	1
$\eta$	0.1	0.1	0.1	0.1	0.1	0.1
Damping	0	0	0	0	0	0
<i>CFD parameters</i>						
$\rho_f$ (kg/m <sup>3</sup> )	N/A	N/A	1000	1000	1000	1000
$\mu$ (Pa s)	N/A	N/A	0.01	0.01	0.1	0.1
<i>Simulation parameters</i>						
Gravity (m/s <sup>2</sup> )	981	981	981	981	9.81	9.81
DEM time step (s)	$10^{-7}$	$10^{-7}$	$10^{-7}$	$10^{-7}$	$10^{-5}$	$10^{-5}$
CFD time step (s)	N/A	N/A	$10^{-5}$	$10^{-5}$	$10^{-3}$	$10^{-3}$
Coupling frequency <sup>b</sup>	N/A	N/A	100	100	100	100
Scaling factor	N/A	N/A	1	1	100	100
<i>Dimensionless groups</i>						
$a$	1–10	3.3	1–10	3.3	3	3
$[\varepsilon]$	$[5, 50] \times 10^{-6}$	$1.65 \times 10^{-5}$	$[3, 30] \times 10^{-6}$	$10^{-5}$	0.082	0.112
$[\rho]$	2.65	2.65	2.65	2.65	2.65	2.65
$[S]$	25–250	82	25–250	82	80	80

(continued)

(continued)

Simulations <sup>a</sup>	SD1	SD2	SS1	SS2	LS1	LS2
$Re$	N/A	N/A	85	85	2682	2682
$n$	0.43	0.43	0.43	0.43	0.49	0.34
$\theta$	30	30	30	30	30	30
$\beta$	1	1	1	1	1	1
$\eta$	0.1	0.1	0.1	0.1	0.1	0.1

<sup>a</sup>The label “SD” denotes “small scale dry granular flow model”; “SS” denotes “small scale submerged granular flow model”; “LS” denotes “Large scale submerged granular flow model”

<sup>b</sup>The coupling frequency is the iteration steps in the DEM during one data exchange interval

# References

- Adams, M. J., & Briscoe, B. J. (1994). Deterministic micromechanical modelling of failure or flow in discrete planes of densely packed particle assemblies: Introductory principles, In A. Mehta (Ed.), *Granular matter* (pp. 259–291). New York: Springer. doi:[10.1007/978-1-4612-4290-1\\_8](https://doi.org/10.1007/978-1-4612-4290-1_8)
- Allen, M. P., & Tildesley, D. J. (1989). *Computer simulation of liquids* (408 p.). Clarendon Press.
- Ancey, C. (2007). Plasticity and geophysical flows: A review. *Journal of Non-Newtonian Fluid Mechanics*, 142(1–3), 4–35. doi:[10.1016/j.jnnfm.2006.05.005](https://doi.org/10.1016/j.jnnfm.2006.05.005)
- Ancey, C., Iverson, R. M., Rentschler, M., & Denlinger, R. P. (2008). An exact solution for ideal dam-break floods on steep slopes. *Water Resources Research*, 44(1), 1–10. doi:[10.1029/2007wr006353](https://doi.org/10.1029/2007wr006353) (doi:[Artn W01430](#))
- Anderson, J. D. (1995). *Computational fluid dynamics: The basics with applications* (547 p.). McGraw-Hill.
- Anderson, T. B., & Jackson, R. (1967). A fluid mechanical description of fluidized beds: Equations of motion. *Industrial and Engineering Chemistry Fundamentals*, 6(4), 527–539. doi:[citeulike-article-id:3002000](#)
- Andrade, J. E., Chen, Q., Le, P. H., Avila, C. F., & Matthew Evans, T. (2012). On the rheology of dilative granular media: Bridging solid- and fluid-like behavior. *Journal of the Mechanics and Physics of Solids*, 60(6), 1122–1136. doi:[10.1016/j.jmps.2012.02.011](https://doi.org/10.1016/j.jmps.2012.02.011)
- Andresen, A., & Bjerrum, L. (1967). Slides in subaqueous slopes in loose sand and silt. In A. F. Richards (Ed.), *Marine geotechnique* (pp. 211–239). University of Illinois Press.
- Assier-Rzadkiaeic, S., Heinrich, P., Sabatier, P. C., Savoye, B., & Bourillet, J. F. (2000). Numerical modelling of a landslide-generated Tsunami: The 1979 nice event. *Pure and Applied Geophysics*, 157(10), 1707–1727. doi:[10.1007/p100001057](https://doi.org/10.1007/p100001057)
- Bürger, R., & Wendland, W. L. (2001). Sedimentation and suspension flows: Historical perspective and some recent developments. *Journal of Engineering Mathematics*, 41(2), 101–116. doi:[10.1023/a:1011934726111](https://doi.org/10.1023/a:1011934726111)
- Bagnold, R. A. (1954). Experiments on a gravity-free dispersion of large solid spheres in a Newtonian fluid under shear. *Proceedings of the Royal Society of London. Series A. Mathematical and Physical Sciences*, 225(1160), 49–63.
- Balmforth, N. J., & Kerswell, R. R. (2005). Granular collapse in two dimensions. *Journal of Fluid Mechanics*, 538, 399–428.
- Baran, O., Kodl, P., & Aglave, R. H. (2013). DEM simulations of fluidized bed using a scaled particle approach *rep* (pp. 1–9).
- Bardet, J. P., & Proubet, J. (1991). A numerical investigation of the structure of persistent shear bands in granular media. *Geotechnique*, 41(4), 599–613.
- Barrett, P. J. (1980). The shape of rock particles, a critical review. *Sedimentology*, 27(3), 291–303. doi:[10.1111/j.1365-3091.1980.tb01179.x](https://doi.org/10.1111/j.1365-3091.1980.tb01179.x)
- Batchelor, G. K. (1982). Sedimentation in a dilute polydisperse system of interacting spheres. Part 1. General theory. *Journal of Fluid Mechanics*, 119, 379–408. doi:[10.1017/S0022112082001402](https://doi.org/10.1017/S0022112082001402)

- Batchelor, G. K., & Green, J. T. (1972). The hydrodynamic interaction of two small freely-moving spheres in a linear flow field. *Journal of Fluid Mechanics*, 56, 375–400. doi:[10.1017/S0022112072002927](https://doi.org/10.1017/S0022112072002927)
- Batchelor, G. K., & Wen, C. S. (1982). Sedimentation in a dilute polydisperse system of interacting spheres. Part 2. Numerical results. *Journal of Fluid Mechanics*, 124, 495–528.
- Bathe, K. J., & Wilson, E. L. (1976). *Numerical methods in finite element analysis* (528 p.). Prentice-Hall.
- Been, K. (1980). *Stress strain behaviour of a cohesive soil deposited under water* (257 p.). University of Oxford.
- Been, K., & Sills, G. C. (1981). Self-weight consolidation of soft soils: An experimental and theoretical study. *Geotechnique*, 31(4), 519–535.
- Beetstra, R., van der Hoef, M. A., & Kuipers, J. A. M. (2007). Drag force of intermediate Reynolds number flow past mono- and bidisperse arrays of spheres. *AIChE Journal*, 53(2), 489–501. doi:[10.1002/aic.11065](https://doi.org/10.1002/aic.11065)
- Belheine, N., Plassiard, J. P., Donzé, F. V., Darve, F., & Seridi, A. (2009). Numerical simulation of drained triaxial test using 3D discrete element modeling. *Computers and Geotechnics*, 36(1–2), 320–331.
- Billi, A., Funiciello, R., Minelli, L., Faccenna, C., Neri, G., Orecchio, B., et al. (2008). On the cause of the 1908 Messina tsunami, southern Italy. *Geophysical Research Letters*, 35(6), 1–5. doi:[10.1029/2008gl033251](https://doi.org/10.1029/2008gl033251)
- Boon, C. W., Housby, G. T., & Utili, S. (2012). A new algorithm for contact detection between convex polygonal and polyhedral particles in the discrete element method. *Computers and Geotechnics*, 44, 73–82. doi:[10.1016/j.compgeo.2012.03.012](https://doi.org/10.1016/j.compgeo.2012.03.012)
- Boon, C. W., Housby, G. T., & Utili, S. (2013). A new contact detection algorithm for three-dimensional non-spherical particles. *Powder Technology*, 248, 94–102. doi:[10.1016/j.powtec.2012.12.040](https://doi.org/10.1016/j.powtec.2012.12.040)
- Booth, J. S., O’Leary, D. W., Popenoe, P., & Danforth, W. W. (1991). U.S. Atlantic Continental slope landslides: Their distribution, general attributes, and implications. In *Submarine landslides: Selected studies in the U.S. exclusive economic zone* (pp. 14–22). U.S. Geological Survey Bulletin 2002.
- Booth, J. S., O’Leary, D. W., Popenoe, P., Robb, J. M., & McGregor, B. A. (1988). Map and tabulation of quaternary mass movements along the United States-Canadian Atlantic continental slope from 32°00' to 47°00'N. latitude. In *U.S. geological survey miscellaneous field studies map MF-2027*.
- Bovis, M. J., & Dagg, B. R. (1992). Debris flow triggering by impulsive loading: Mechanical modelling and case studies. *Canadian Geotechnical Journal*, 29(3), 345–352. doi:[10.1139/t92-040](https://doi.org/10.1139/t92-040)
- Bowman, E. T., Take, W. A., Rait, K. L., & Hann, C. (2012). Physical models of rock avalanche spreading behaviour with dynamic fragmentation. *Canadian Geotechnical Journal*, 49(4), 460–476. doi:[10.1139/t2012-007](https://doi.org/10.1139/t2012-007)
- Boylan, N., & Gaudin, C. (2010). *Modelling of submarine slides in the geotechnical centrifuge*. Paper presented at 7th International Conference on Physical Modelling in Geotechnics (ICPMG 2010). Zurich, Switzerland.
- Brand, E. W. (1981). *Some thoughts on rain-induced slope failures*. Paper presented at Proceedings of the 10th International Conference on Soil Mechanics and Foundation Engineering.
- Brennen, C. E. (2005). *Fundamentals of multiphase flow* (368 p.). Cambridge University Press.
- Brilliantov, N. V., Albers, N., Spahn, F., & Pöschel, T. (2007). Collision dynamics of granular particles with adhesion. *Physical Review E*, 76(5), 1–12.
- Brown, P., & Lawler, D. (2003). Sphere drag and settling velocity revisited. *Journal of Environmental Engineering*, 129(3), 222–231. doi:[10.1061/\(asce\)0733-9372\(2003\)129:3\(222\)](https://doi.org/10.1061/(asce)0733-9372(2003)129:3(222)
- Bryn, P., Berg, K., Forsberg, C. F., Solheim, A., & Kvalstad, T. J. (2005). Explaining the Storegga slide. *Marine and Petroleum Geology*, 22(1–2), 11–19. doi:[10.1016/j.marpetgeo.2004.12.003](https://doi.org/10.1016/j.marpetgeo.2004.12.003)

- Bui, H. H., Fukagawa, R., Sako, K., & Ohno, S. (2008). Lagrangian meshfree particles method (SPH) for large deformation and failure flows of geomaterial using elastic-plastic soil constitutive model. *International Journal for Numerical and Analytical Methods in Geomechanics*, 32(12), 1537–1570. doi:[10.1002/Nag.088](https://doi.org/10.1002/Nag.088)
- Burk, C. A., Drake, C. L. (1974). *The geology of continental margins* (1009 p.). New York: Springer-Verlag.
- Cannon, S. H., & Michael, J. A. (2011). Emergency assessment of postwildfire debris-flow hazards for the 2011 Motor Fire, Sierra and Stanislaus National Forests (10 p.). California: U.S. Rep.
- Carlson, P. R., Karl, H. A., Edwards, B. D., Gardner, J. V., & Hall, R. (1993). Mass movement related to large submarine canyons along the Beringian margin, Alaska. In *Submarine landslides: Selected studies in the U.S. exclusive economic zone* (pp. 104–116). U.S. Geological Survey Bulletin 2002.
- Carlson, P. R., & Molnia, B. F. (1977). Submarine faults and slides on the continental shelf, northern Gulf of Alaska. *Marine Geotechnology*, 2(1–4), 275–290. doi:[10.1080/10641197709379784](https://doi.org/10.1080/10641197709379784)
- Carrara, A., Crosta, G., & Frattini, P. (2008). Comparing models of debris-flow susceptibility in the alpine environment. *Geomorphology*, 94(3–4), 353–378. doi:[10.1016/j.geomorph.2006.10.033](https://doi.org/10.1016/j.geomorph.2006.10.033)
- Carrigy, M. A. (1970). Experiments on the angles of repose of granular materials. *Sedimentology*, 14(3–4), 147–158. doi:[10.1111/j.1365-3091.1970.tb00189.x](https://doi.org/10.1111/j.1365-3091.1970.tb00189.x)
- Casagli, N., Ermini, L., & Rosati, G. (2003). Determining grain size distribution of the material composing landslide dams in the Northern Apennines: Sampling and processing methods. *Engineering Geology*, 69(1–2), 83–97. doi:[10.1016/s0013-7952\(02\)00249-1](https://doi.org/10.1016/s0013-7952(02)00249-1)
- Casagrande, A. (1936). Characteristics of Cohesionless soils affecting the stability of slopes and earth fills. *Journal of the Boston Society of Civil Engineers*, 23(1), 13–32.
- Chang, M., Trussell, R. R., Guzman, V., Martinez, J., & Delaney C. K. (1999). Laboratory studies on the clean bed headloss of filter media, *Aqua*, 48(4), 137–145. doi:[10.1046/j.1365-2087.1999.00139.x](https://doi.org/10.1046/j.1365-2087.1999.00139.x)
- Chaumeil, F., & Crapper, M. (2014). Using the DEM-CFD method to predict Brownian particle deposition in a constricted tube. *Particuology*, (0), 1–13. doi:[10.1016/j.partic.2013.05.005](https://doi.org/10.1016/j.partic.2013.05.005)
- Chen, F. (2009). *Coupled flow discrete element method application in granular porous media using open source codes* (117 p.). Ph.D Thesis, University of Tennessee—Knoxville.
- Chen, F., Drumm, E. C., & Guiochon, G. (2011). Coupled discrete element and finite volume solution of two classical soil mechanics problems. *Computers and Geotechnics*, 38(5), 638–647. doi:[10.1016/j.compgeo.2011.03.009](https://doi.org/10.1016/j.compgeo.2011.03.009)
- Chen, H., Crosta, G. B., & Lee, C. F. (2006). Erosional effects on runout of fast landslides, debris flows and avalanches: A numerical investigation. *Geotchnique*, 56(5), 305–322.
- Chen, J., Ke, P., & Zhang, G. (2007). Slope stability analysis by strength reduction elasto-plastic FEM. *Mechanical Behavior of Materials X, Pts 1 and 2*, 345–346, 625–628.
- Choi, H. G., & Joseph, D. D. (2001). Fluidization by lift of 300 circular particles in plane Poiseuille flow by direct numerical simulation. *Journal of Fluid Mechanics*, 438, 101–128.
- Cleary, P. W., & Campbell, C. S. (1993). Self-lubrication for long runout landslides: Examination by computer simulation. *Journal of Geophysical Research: Solid Earth*, 98(B12), 21911–21924.
- Cleary, P. W., & Frank, M. (2006). *Three-dimensional discrete element simulation of axi-SYMMETRIC collapses of granular columns* (pp. 89–111).
- Cleary, P. W., & Prakash, M. (2004). Discrete-element modelling and smoothed particle hydrodynamics: Potential in the environmental sciences. *Philosophical Transactions of the Royal Society of London. Series A: Mathematical, Physical and Engineering Sciences*, 362 (1822), 2003–2030.
- Cleary, P. W., & Sawley, M. L. (2002). DEM modelling of industrial granular flows: 3D case studies and the effect of particle shape on hopper discharge. *Applied Mathematical Modelling*, 26(2), 89–111. doi:[10.1016/s0307-904x\(01\)00050-6](https://doi.org/10.1016/s0307-904x(01)00050-6)

- Coleman, J. M., & Garrison, L. E. (1977). Geological aspects of marine slope stability, northwestern Gulf of Mexico. *Marine Geotechnology*, 2(1–4), 9–44. doi:[10.1080/10641197709379769](https://doi.org/10.1080/10641197709379769)
- Coulter, S. E. (2005). *Seismic initiation of submarine slope failures using physical modeling in a geotechnical centrifuge* (MEng thesis). Memorial University of Newfoundland.
- Courant, R., Friedrichs, K., & Lewy, H. (1928). On the partial difference equations of mathematical physics. *IBM Journal of Research and Development*, 11(2), 215–234.
- Coussot, P., & Piau, J. M. (1994). On the behavior of fine mud suspensions. *Rheologica Acta*, 33 (3), 175–184. doi:[10.1007/bf00437302](https://doi.org/10.1007/bf00437302)
- Craig, R. F. (1997). *Soil mechanics* (458 p.). London and New York: E & FN SPON.
- Crosta, G. B., Chen, H., & Lee, C. F. (2004). Replay of the 1987 Val Pola landslide, Italian Alps. *Geomorphology*, 60(1–2), 127–146. doi:[10.1016/j.geomorph.2003.07.015](https://doi.org/10.1016/j.geomorph.2003.07.015)
- Crosta, G. B., Frattini, P., & Fusi, N. (2007). Fragmentation in the Val Pola rock avalanche, Italian Alps. *Journal of Geophysical Research: Earth Surface*, 112(F1), F01006. doi:[10.1029/2005jf000455](https://doi.org/10.1029/2005jf000455)
- Crosta, G. B., Imposimato, S., & Roddeman, D. (2009). Numerical modeling of 2-D granular step collapse on erodible and nonerodible surface. *Journal of Geophysical Research: Earth Surface*, 114(F3), 1–19. doi:[10.1029/2008jf001186](https://doi.org/10.1029/2008jf001186)
- Crosta, G. B., Imposimato, S., Roddeman, D., Chiesa, S., & Moia, F. (2005). Small fast-moving flow-like landslides in volcanic deposits: The 2001 Las Colinas Landslide (El Salvador). *Engineering Geology*, 79(3–4), 185–214. doi:[10.1016/j.enggeo.2005.01.014](https://doi.org/10.1016/j.enggeo.2005.01.014)
- Crosta, G. B., Imposimato, S., & Roddeman, D. G. (2003). Numerical modelling of large landslides stability and runout. *Natural Hazards and Earth System Science*, 3(6), 523–538.
- Cruden, D. M., & Varnes, D. J. (1996). Landslide types and processes. In Turner A. K. and Shuster R. L. (Eds.), *Landslides: Investigation and mitigation (National Research Council (U.S.) transportation research board special report)* (pp. 36–75). National Academy Press.
- Cui, L., & O'Sullivan, C. (2006). Exploring the macro- and micro-scale response of an idealised granular material in the direct shear apparatus. *Geotechnique*, 66(7), 455–468.
- Cundall, P. A. (1987). *Computer simulations of dense sphere Assemblies*. Paper presented at in Proceedings of the U.S./Japan Seminar on the Micromechanics of granular Materials, Sendai-Zao, Japan.
- Cundall, P. A. (1988). Formulation of a three-dimensional distinct element model-Part I. A scheme to detect and represent contacts in a system composed of many polyhedral blocks. *International Journal of Rock Mechanics and Mining Sciences*, 25(3), 107–116.
- Cundall, P. A., & Strack, O. D. L. (1979). A discrete numerical model for granular assemblies. *Geotechnique*, 29(1), 47–65.
- Dade, W., & Huppert, H. (1998). Long-runout rockfalls. *Geology*, 26(9), 803–806.
- DallaValle, J. M. (1948). *Micromeritics: The technology of fine particles* (2nd ed., 555 p.). Pitman Pub. Corp.
- Davidson, L. (2003). *An introduction to turbulence models* (48 p.). Gotebor, Sweden: Chalmers University of Technology.
- Davis, R. H., & Gecol, H. (1994). Hindered settling function with no empirical parameters for polydisperse suspensions. *AICHe Journal*, 40(3), 570–575. doi:[10.1002/aic.690400317](https://doi.org/10.1002/aic.690400317)
- De, A. K. (2007). *A textbook of inorganic chemistry* (914 p.). New Age International.
- De Blasio, F. V., & Elverhøi, A. (2008). A model for frictional melt production beneath large rock avalanches. *Journal of Geophysical Research: Earth Surface*, 113(F2), F02014.
- Dean, E. T. R. (2009). *Offshore geotechnical engineering* (552 p.). Thomas Telford Ltd.
- DEM Solutions. (2010). *EDEM-CFD Coupling for FLUENT: User Guide* (25 p.).
- Denlinger, R. P., & Iverson, R. M. (2001). Flow of variably fluidized granular masses across three-dimensional terrain: 2. Numerical predictions and experimental tests. *Journal of Geophysical Research: Solid Earth*, 106(B1), 553–566. doi:[10.1029/2000jb900330](https://doi.org/10.1029/2000jb900330)
- Di Felice, R. (1994). The voidage function for fluid-particle interaction systems. *International Journal of Multiphase Flow*, 20(1), 153–159.

- Di Felice, R. (1999). The sedimentation velocity of dilute suspensions of nearly monosized spheres. *International Journal of Multiphase Flow*, 25(4), 559–574. doi:[10.1016/S0301-9322\(98\)00084-6](https://doi.org/10.1016/S0301-9322(98)00084-6)
- Di Felice, R., Foscolo, P. U., & Gibilaro, L. G. (1989). The experimental determination of the interaction force on spheres submerged in liquid fluidized beds. *Chemical Engineering and Processing: Process Intensification*, 25(1), 27–34. doi:[10.1016/0255-2701\(89\)85003-2](https://doi.org/10.1016/0255-2701(89)85003-2)
- Dillon, W. P., Scanlon, K. M., Valentine, P. C., & Huggett, Q. J. (1993). Acient crustal fractures control the location and size of collapsed blocks at the Blake Escarpment, east of Florida. In *Submarine landslides: Selected studies in the U.S. exclusive economic zone* (pp. 54–59). U.S. Geological Survey Bulletin 2002.
- Ding, J., & Gidaspow, D. (1990). A bubbling fluidization model using kinetic theory of granular flow. *AIChE Journal*, 36(4), 523–538.
- Doraiswamy, D., Mujumdar, A. N., Tsao, I., Beris, A. N., Danforth, S. C., & Metzner, A. B. (1991). The Cox-Merz rule extended: A rheological model for concentrated suspensions and other materials with a yield stress. *Journal of Rheology*, 35(4), 647–685.
- Drew, D. A., & Lahey, R. T. (1990). Some supplemental analysis concerning the virtual mass and lift force on a sphere in a rotating and straining flow. *International Journal of Multiphase Flow*, 16(6), 1127–1130.
- Duursma, G., Crapper, M., Whitelaw, S., Wong, W. S., & McMullan, K. (2009). DEM-CFD modelling of voidage and heat transfer in fluidized beds. In *8th World Congress of Chemical Engineering*.
- Dyka, C. T., & Ingel, R. P. (1995). An approach for tension instability in smoothed particle hydrodynamics (SPH). *Computers & Structures*, 57(4), 573–580. doi:[10.1016/0045-7949\(95\)00059-P](https://doi.org/10.1016/0045-7949(95)00059-P)
- Eckersley, D. (1990). Instrumented laboratory flowslides. *Geotechnique*, 40(3), 489–502.
- Edgers, L., & Karlslrud, K. (1982). *Soil flows generated by submarine slides—Case studies and consequences*. Paper presented at Proceedings of the Third International Conference on the Behaviour of Offshore Structures.
- Edwards, B. D., Lee, H. J., & Field, M. F. (1993). Seismically induced mudflow in Santa Barbara Basin, California. In *Submarine landslides: Selected studies in the U.S. exclusive economic zone* (pp. 167–175). U.S. Geological Survey Bulletin 2002.
- Ergun, S. (1952). Fluid flow through packed columns. *Chemical Engineering Progress*, 48(2), 89–94.
- Ergun, S., & Orning, A. A. (1949). Fluid flow through randomly packed columns and fluidized beds. *Industrial & Engineering Chemistry*, 41(6), 1179–1184. doi:[10.1021/ie50474a011](https://doi.org/10.1021/ie50474a011)
- Fairchild, L. H. (1987). The importance of lahar initiation processes. *Reviews in Engineering Geology*, 7, 51–62.
- Fang, H.-Y. (1991). *Foundation engineering handbook*. CBS Publishers & Distributors.
- Field, M. E., Gardner, J. V., Jennings, A. E., & Edwards, B. D. (1982). Earthquake-induced sediment failures on a 0.25° slope, Klamath River delta, California. *Geology*, 10(10), 542–546.
- Fine, I. V., Rabinovich, A. B., Bornhold, B. D., Thomson, R. E., & Kulikov, E. A. (2005). The grand banks landslide-generated tsunami of November 18, 1929: Preliminary analysis and numerical modeling. *Marine Geology*, 215(1–2), 45–57. doi:[10.1016/j.margeo.2004.11.007](https://doi.org/10.1016/j.margeo.2004.11.007)
- Fitch, B. (1983). Kynch theory and compression zones. *AIChE Journal*, 29(6), 940–947. doi:[10.1002/aic.690290611](https://doi.org/10.1002/aic.690290611)
- Font, R. (1988). Compression zone effect in batch sedimentation. *AIChE Journal*, 34(2), 229–238. doi:[10.1002/aic.690340207](https://doi.org/10.1002/aic.690340207)
- Gabet, E. J., & Mudd, S. M. (2006). The mobilization of debris flows from shallow landslides. *Geomorphology*, 74(1–4), 207–218. doi:[10.1016/j.geomorph.2005.08.013](https://doi.org/10.1016/j.geomorph.2005.08.013)
- Gee, M. J. R., Masson, D. G., Watts, A. B., & Allen, P. A. (1999). The Saharan debris flow: An insight into the mechanics of long runout submarine debris flows. *Sedimentology*, 46(2), 317–335. doi:[10.1046/j.1365-3091.1999.00215.x](https://doi.org/10.1046/j.1365-3091.1999.00215.x)

- Girolami, L., Hergault, V., Vinay, G., & Wachs, A. (2012). A three-dimensional discrete-grain model for the simulation of dam-break rectangular collapses: Comparison between numerical results and experiments. *Granular Matter*, 14(3), 381–392. doi:[10.1007/s10035-012-0342-3](https://doi.org/10.1007/s10035-012-0342-3)
- Gray, J. P., Monaghan, J. J., & Swift, R. P. (2001). SPH elastic dynamics. *Computer Methods in Applied Mechanics and Engineering*, 190(49–50), 6641–6662. doi:[10.1016/S0045-7825\(01\)00254-7](https://doi.org/10.1016/S0045-7825(01)00254-7)
- Greene, H. G., Gardner-Taggart, J., Ledbetter, M. T., Barminski, R., Chase, T. E., Hicks, K. R., et al. (1991). Offshore and onshore liquefaction at Moss Landing spit, central California—Result of the October 17 1989, Loma Prieta earthquake. *Geology*, 19(9), 945–949.
- Gue, C. S. (2012). Submarine landslide flows simulation through centrifuge modelling (PhD Thesis). University of Cambridge.
- Gui, M. W. B., Garnier, M. D., Corté, J., Bagge, J. F., Gunnar, Laue, J.; Renzi, R. (1999). Centrifuge cone penetration tests in sand. *Geotechnique*, 49(4), 543–552.
- Guo, Y. (2010). A coupled DEM/CFD analysis of die filling process (PhD Thesis, 309 p.). The University of Birmingham.
- Gutfraind, R., & Savage, S. B. (1998). Flow of fractured ice through wedge-shaped channels: Smoothed particle hydrodynamics and discrete-element simulations. *Mechanics of Materials*, 29(1), 1–17. doi:[10.1016/S0167-6636\(97\)00072-0](https://doi.org/10.1016/S0167-6636(97)00072-0)
- Gutmacher, C. E., & Normark, W. R. (1993). Sur submarine slide, a deep-water sediment slope failure. In *Submarine landslides: Selected studies in the U.S. exclusive economic zone* (pp. 158–166). U.S. Geological Survey Bulletin 2002.
- Guzzetti, F., Carrara, A., Cardinali, M., & Reichenbach, P. (1999). Landslide hazard evaluation: A review of current techniques and their application in a multi-scale study, Central Italy. *Geomorphology*, 31(1–4), 181–216. doi:[10.1016/S0169-555X\(99\)00078-1](https://doi.org/10.1016/S0169-555X(99)00078-1)
- Hühnerbach, V., & Masson, D. G. (2004). Landslides in the North Atlantic and its adjacent seas: An analysis of their morphology, setting and behaviour. *Marine Geology*, 213(1–4), 343–362. doi:[10.1016/j.margeo.2004.10.013](https://doi.org/10.1016/j.margeo.2004.10.013)
- Hürlimann, M., Ledesma, A., & Martí, J. (2001). Characterisation of a volcanic residual soil and its implications for large landslide phenomena: Application to Tenerife, Canary Islands. *Engineering Geology*, 59(1–2), 115–132. doi:[10.1016/S0013-7952\(00\)00069-7](https://doi.org/10.1016/S0013-7952(00)00069-7)
- Haflidason, H., Sejrup, H. P., Berstad, I. M., Nygård, A., Richter, T., Bryn, P., et al. (2003). A weak layer feature on the Northern Storegga slide escarpment. In J. Mienert and P. Weaver (Eds.), *European margin sediment dynamics* (pp. 55–62). Springer Berlin Heidelberg. doi:[10.1007/978-3-642-55846-7\\_7](https://doi.org/10.1007/978-3-642-55846-7_7)
- Haflidason, H., Sejrup, H. P., Nygård, A., Mienert, J., Bryn, P., Lien, R., et al. (2004). The Storegga Slide: Architecture, geometry and slide development. *Marine Geology*, 213(1–4), 201–234. doi:[10.1016/j.margeo.2004.10.007](https://doi.org/10.1016/j.margeo.2004.10.007)
- Hampton, M. A., Lee, H. J., & Locat, J. (1996). Submarine landslides. *Reviews of Geophysics*, 34 (1), 33–59. doi:[10.1029/95rg03287](https://doi.org/10.1029/95rg03287)
- Hampton, M. A., Lemke, R. W., & Coulter, H. W. (1993). Submarine landslides that had a significant impact on man and his activities: Seward and Valdez, Alaska. In *Submarine landslides: Selected studies in the U.S. exclusive economic zone* (pp. 123–134). U.S. Geological Survey Bulletin 2002.
- Harp, E. L., Wells, W. G., & Sarmiento, J. G. (1990). Pore pressure response during failure in soils. *Geological Society of America Bulletin*, 102(4), 428–438.
- Hayashi, J. N., & Self, S. (1992). A comparison of pyroclastic flow and debris avalanche mobility. *Journal of Geophysical Research: Solid Earth*, 97(B6), 9063–9071. doi:[10.1029/92jb00173](https://doi.org/10.1029/92jb00173)
- Hazlett, R. W., Buesch, D., Anderson, J. L., Elan, R., & Scandone, R. (1991). Geology, failure conditions, and implications of seismogenic avalanches of the 1944 eruption at Vesuvius, Italy. *Journal of Volcanology and Geothermal Research*, 47(3–4), 249–264. doi:[10.1016/0377-0273\(91\)90004-J](https://doi.org/10.1016/0377-0273(91)90004-J)

- Hermann, A., Lein, M., & Schwerdtfeger, P. (2007). The search for the species with the highest coordination number. *Angewandte Chemie International Edition*, 46(14), 2444–2447. doi:[10.1002/anie.200604148](https://doi.org/10.1002/anie.200604148)
- Hertz, H. (1882). Über die berührung fester elastischer Körper. *Journal für die Reine und Angewandte Mathematik*, 29, 156–171.
- Highland, L. M. (2010). Worldwide overview of large landslides of the 20th and 21st centuries. <http://landslides.usgs.gov/learning/majorls.php>
- Highland, L. M., & Bobrowsky, P. (2008). *The landslide handbook—A guide to understanding landslides*: Reston, Virginia, U.S., Geological Survey Circular 1325.
- Hilton, J., & Cleary, P. W. (2012). Comparison of resolved and coarse grain dem models for gas flow through particle beds. In *Ninth International Conference on CFD in the Minerals and Process Industries* (pp. 1–6). Melbourne.
- Hinch, E. J. (1977). An averaged-equation approach to particle interactions in a fluid suspension. *Journal of Fluid Mechanics*, 83, 695–720. doi:[10.1017/S0022112077001414](https://doi.org/10.1017/S0022112077001414)
- Hogg, A. J. (2007). Two-dimensional granular slumps down slopes. *Physics of Fluids*, 19(9). doi:[10.1063/1.2762254](https://doi.org/10.1063/1.2762254) (doi:[Artn 093301](#))
- Holcomb, R. T., & Searle, R. C. (1991). Large landslides from oceanic volcanoes. *Marine Geotechnology*, 10(1–2), 19–32.
- Houlsby, G. T. (2009). Potential particles: A method for modelling non-circular particles in DEM. *Computers and Geotechnics*, 36(6), 953–959. doi:[10.1016/j.compgeo.2009.03.001](https://doi.org/10.1016/j.compgeo.2009.03.001)
- Hubble, T., Yu, P., Airey, D., & Clarke, S. (2012). *Physical properties and age of continental slope sediments dredged from the Eastern Australian continental margin—Implications for timing of Slope failure*. Paper Presented at 5th International Symposium—Submarine Mass Movements and Their Consequences, Dordrecht: Springer.
- Hungr, O. (1995). A model for the runout analysis of rapid flow slides, debris flows, and avalanches. *Canadian Geotechnical Journal*, 32(4), 610–623. doi:[10.1139/t95-063](https://doi.org/10.1139/t95-063)
- Hungr, O., & Evans, S. G. (2004). Entrainment of debris in rock avalanches: An analysis of a long run-out mechanism. *Geological Society of America Bulletin*, 116(9), 1240–1252.
- Hutchinson, J. N. (1988). General report: Morphological and geotechnical parameters of landslides in relation to geology and hydrogeology. Proceedings, Fifth International Symposium on Landslides (Ed: Bonnard, C.), pp. 3–35 Rotterdam.
- Ilstad, T., Marr, J. G., Elverhoi, A., & Harbitz, C. B. (2004). Laboratory studies of subaqueous debris flows by measurements of pore-fluid pressure and total stress. *Marine Geology*, 213(1–4), 403–414. doi:[10.1016/j.margeo.2004.10.016](https://doi.org/10.1016/j.margeo.2004.10.016)
- Issa, R. I. (1986). Solution of the implicitly discretised fluid flow equations by operator-splitting. *Journal of Computational Physics*, 62(1), 40–65. doi:[10.1016/0021-9991\(86\)90099-9](https://doi.org/10.1016/0021-9991(86)90099-9)
- Itasca. (2003). *PFC3D: Theory and background* (97 p.). Itasca Consulting Group.
- Itasca. (2008). *CCFD-PFC documentaton.pdf* (104 p.). USA: Itasca Consulting Group Inc Minnesota.
- Iverson, R. M. (1985). A constitutive equation for mass-movement behavior. *Journal of Geology*, 93(2), 143–160.
- Iverson, R. M. (1997). The physics of debris flows. *Reviews of Geophysics*, 35, 245–296.
- Iverson, R. M., & Major, J. J. (1986). Groundwater seepage vectors and the potential for hillslope failure and debris flow mobilization. *Water Resources Research*, 22(11), 1543–1548. doi:[10.1029/WR022i011p01543](https://doi.org/10.1029/WR022i011p01543)
- Iverson, R. M., Reid, M. E., Iverson, N. R., LaHusen, R. G., Logan, M., Mann, J. E., et al. (2000). Acute sensitivity of landslide rates to initial soil porosity. *Science*, 290(5491), 513–516.
- Iverson, R. M., Reid, M. E., & LaHusen, R. G. (1997). Debris-flow mobilization from landslides. *Annual Review of Earth and Planetary Sciences*, 25(1), 85–138.

- Iverson, R. M., Reid, M. E., Logan, M., LaHusen, R. G., Godt, J. W., & Griswold, J. P. (2011). Positive feedback and momentum growth during debris-flow entrainment of wet bed sediment. *Nature Geoscience*, 4(2), 116–121.
- Iwashita, K. (1998). Rolling resistance at contacts in simulation of shear band development by DEM. *Journal of Engineering Mechanics*, 124(285), 285–292.
- Jackson, R. (2000). *The dynamics of fluidized particles* (352 p.). Cambridge University Press.
- Jasak, H. (1996). *Error analysis and estimation for the finite volume method with applications to fluid flows* (PhD Thesis). London Imperial College.
- Jasak, H. (2009). Turbulence Modelling for CFD. *Report for the NUMAP-FOAM Summer school* (51 p.). Croatia: University of Zagreb.
- Jiang, M., Zhu, H., & Li, X. (2010). Strain localization analyses of idealized sands in biaxial tests by distinct element method. *Frontiers of Architecture and Civil Engineering in China*, 4(2), 208–222. doi:[10.1007/s11709-010-0025-2](https://doi.org/10.1007/s11709-010-0025-2)
- Jiang, M. J., Yu, H. S., & Harris, D. (2005). A novel discrete model for granular material incorporating rolling resistance. *Computers and Geotechnics*, 32(5), 340–357. doi:[10.1016/j.comgeo.2005.05.001](https://doi.org/10.1016/j.comgeo.2005.05.001)
- Jing, L., & Stephansson, O. (2007). *Fundamentals of discrete element methods for rock engineering: Theory and applications* (543 p.). Elsevier Science & Technology Books.
- Johnson, A. M. (1965). *A model for debris flow* (Ph.D Thesis, 474 p.). Pennsylvania State University.
- Johnson, A. M. (1984). Debris flow. In Brunsden D, Prior DB (Eds.), *Slope instability* (p. 104). New York: John Wiley.
- Johnson, G. R., & Beissel, S. R. (1996). Normalized smoothing functions for SPH impact computations. *International Journal for Numerical Methods in Engineering*, 39(16), 2725–2741. doi:[10.1002/\(sici\)1097-0207\(19960830\)39:16<2725::aid-nme973>3.0.co;2-9](https://doi.org/10.1002/(sici)1097-0207(19960830)39:16<2725::aid-nme973>3.0.co;2-9)
- Kafui, D. K., Johnson, S., Thornton, C., & Seville, J. P. K. (2011). Parallelization of a Lagrangian-Eulerian DEM/CFD code for application to fluidized beds. *Powder Technology*, 207(1–3), 270–278.
- Kafui, K. D., Thornton, C., & Adams, M. J. (2002). Discrete particle-continuum fluid modelling of gas-solid fluidised beds. *Chemical Engineering Science*, 57(13), 2395–2410.
- Kalthoff, W., Schwarzer, S., Ristow, G., & Herrmann, H. J. (1996). On the application of a novel algorithm to hydrodynamic diffusion and velocity fluctuations in sedimenting systems. *International Journal of Modern Physics C*, 07(04), 543–561. doi:[10.1142/s0129183196000466](https://doi.org/10.1142/s0129183196000466)
- Kerswell, R. R. (2005). Dam break with Coulomb friction: A model for granular slumping? *Physics of Fluids*, 17(5), 1–16.
- Komiwas, V., Mege, P., Meimon, Y., & Herrmann, H. (2006). Simulation of granular flow in a fluid applied to sedimentation. *Granular Matter*, 8(1), 41–54. doi:[10.1007/s10035-005-0220-3](https://doi.org/10.1007/s10035-005-0220-3)
- Kunitz, M. (1926). An empirical formula for the relation between viscosity of solution and volume of solute. *The Journal of General Physiology*, 9(6), 715–725.
- Kynch, G. J. (1952). A theory of sedimentation. *Transactions of the Faraday Society*, 48, 166–176.
- Lacaze, L., Phillips, J. C., & Kerswell, R. R. (2008). Planar collapse of a granular column: Experiments and discrete element simulations. *Physics of Fluids*, 20(6), 1–12.
- Lajeunesse, E., Mangeney-Castelnau, A., & Vilotte, J. P. (2004). Spreading of a granular mass on a horizontal plane. *Physics of Fluids*, 16(7), 2371–2381.
- Lajeunesse, E., Monnier, J. B., & Homsy, G. M. (2005). Granular slumping on a horizontal surface. *Physics of Fluids*, 17(10), 1–15.
- Lajeunesse, E., Quantin, C., Allemand, P., & Delacourt, C. (2006). New insights on the runout of large landslides in the Valles-Marineris canyons, Mars. *Geophysical Research Letters*, 33(4), L04403. doi:[10.1029/2005gl025168](https://doi.org/10.1029/2005gl025168)
- Launder, B. E., & Spalding, D. B. (1972). *Mathematical models of turbulence* (424 p.). Academic Press.

- Lee, H., & Edwards, B. (1986). Regional method to assess offshore slope stability. *Journal of Geotechnical Engineering*, 112(5), 489–509. doi:[10.1061/\(ASCE\)0733-9410\(1986\)112:5\(489\)](https://doi.org/10.1061/(ASCE)0733-9410(1986)112:5(489))
- Lee, H. J., Schwab, W. C., & Booth, J. S. (1991). Submarine landslides: An introduction. In *Submarine landslides: Selected studies in the U.S. exclusive economic zone*. U.S. Geological Survey Bulletin 2002.
- Legros, F. (2002). The mobility of long-runout landslides. *Engineering Geology*, 63(3–4), 301–331. doi:[10.1016/S0013-7952\(01\)00090-4](https://doi.org/10.1016/S0013-7952(01)00090-4)
- Lewis, K. B. (1971). Slumping on a Continental Slope Inclined at 1°–4°. *Sedimentology*, 16(1–2), 97–110.
- Li, X. S. (1997). Modeling of dilative shear failure. *Journal of Geotechnical and Geoenvironmental Engineering*, 123(7), 609–616.
- Lipman, P. W., Normark, W. R., Moore, J. G., Wilson, J. B., & Guttmacher, C. E. (1988). The giant submarine Alikai Debris Slide, Mauna Loa, Hawaii. *Journal of Geophysical Research: Solid Earth*, 93(B5), 4279–4299. doi:[10.1029/JB093iB05p04279](https://doi.org/10.1029/JB093iB05p04279)
- Locat, J., & Lee, H. J. (2002). Submarine landslides: Advances and challenges. *Canadian Geotechnical Journal*, 39(1), 193–212. doi:[10.1139/t01-089](https://doi.org/10.1139/t01-089)
- Locat, P., Couture, R., Leroueil, S., Locat, J., & Jaboyedoff, M. (2006). Fragmentation energy in rock avalanches. *Canadian Geotechnical Journal*, 43(8), 830–851. doi:[10.1139/t06-045](https://doi.org/10.1139/t06-045)
- Longva, O., Janbu, N., Blikra, L. H., & Bøe, R. (2003). *The 1996 Finneidfjord slide; seafloor failure and slide dynamics*. Paper presented at Submarine Mass Movements and Their Consequences. Springer Netherlands. January 1, 2003.
- Lowe, D. R. (1976). Grain flow and grain flow deposits. *Journal of Sedimentary Research*, 46(1), 188–199.
- Lu, M., & McDowell, G. R. (2007). The importance of modelling ballast particle shape in the discrete element method. *Granular Matter*, 9(1–2), 69–80. doi:[10.1007/s10035-006-0021-3](https://doi.org/10.1007/s10035-006-0021-3)
- Lube, G., Huppert, H. E., Sparks, R. J., & Hallworth, M. A. (2004). Axisymmetric collapses of granular columns. *Journal of Fluid Mechanics*, 508, 175–199.
- Lube, G., Huppert, H. E., Sparks, R. S., & Freundt, A. (2005). Collapses of two-dimensional granular columns. *Physical Review E*, 72.
- Lucas, A., & Mangeney, A. (2007). Mobility and topographic effects for large Valles Marineris landslides on Mars. *Geophysical Research Letters*, 34(10), 1–5. doi:[10.1029/2007gl029835](https://doi.org/10.1029/2007gl029835) (doi:[Artn L10201](#))
- Major, J. J., & Pierson, T. C. (1992). Debris flow rheology: Experimental analysis of fine-grained slurries. *Water Resources Research*, 28(3), 841–857. doi:[10.1029/91wr02834](https://doi.org/10.1029/91wr02834)
- Mangeney, A., Bouchut, F., Villette, J. P., Lajeunesse, E., Aubertin, A., & Pirulli, M. (2005). On the use of Saint Venant equations to simulate the spreading of a granular mass. *Journal of Geophysical Research-Solid Earth*, 110(B9).
- Mangeney, A., Roche, O., Hungr, O., Mangold, N., Faccanoni, G., & Lucas, A. (2010). Erosion and mobility in granular collapse over sloping beds. *Journal of Geophysical Research: Earth Surface*, 115(F3), F03040. doi:[10.1029/2009jf001462](https://doi.org/10.1029/2009jf001462)
- Masson, D., Canals, M., Alonso, B., Urgeles, R., & Huhnerbach, V. (1998). The Canary Debris flow: Source area morphology and failure mechanisms. *Sedimentology*, 45(2), 411–432. doi:[10.1046/j.1365-3091.1998.0165f.x](https://doi.org/10.1046/j.1365-3091.1998.0165f.x)
- Masson, D. G. (1996). Catastrophic collapse of the volcanic island of Hierro 15 ka ago and the history of landslides in the Canary Islands. *Geology*, 24(3), 231–234.
- Masson, D. G., Harbitz, C. B., Wynn, R. B., Pedersen, G., & Løvholt, F. (2006). Submarine landslides: Processes, triggers and hazard prediction. *Philosophical Transactions of the Royal Society A: Mathematical, Physical and Engineering Sciences*, 364(1845), 2009–2039.
- Masson, D. G., Watts, A. B., Gee, M. J. R., Urgeles, R., Mitchell, N. C., Le Bas, T. P., et al. (2002). Slope failures on the flanks of the western Canary Islands. *Earth-Science Reviews*, 57(1–2), 1–35. doi:[10.1016/S0012-8252\(01\)00069-1](https://doi.org/10.1016/S0012-8252(01)00069-1)

- Matsumoto, M., & Nishimura, T. (1998). Mersenne twister: A 623-dimensionally equidistributed uniform pseudo-random number generator. *ACM Transactions on Modeling and Computer Simulation (TOMACS)*, 8(1), 3–30.
- McCabe, W., Smith, J., & Harriott, P. (2005). *Unit operations of chemical engineering* (1140 p.). New York: McGraw-Hill.
- McDonnell, J. J. (1990). The influence of macropores on debris flow initiation. *Quarterly Journal of Engineering Geology*, 23(4), 325–331. doi:[10.1144/Gsl.Qjeg.1990.023.04.06](https://doi.org/10.1144/Gsl.Qjeg.1990.023.04.06)
- McDougall, S., & Hungr, O. (2004). A model for the analysis of rapid landslide motion across three-dimensional terrain. *Canadian Geotechnical Journal*, 41(6), 1084–1097. doi:[10.1139/t04-052](https://doi.org/10.1139/t04-052)
- McGregor, B. A., Rothwell, R. G., Kenyon, N. H., & Twichell, D. C. (1993). Salt tectonics and slope failure in an area of salt domes in the northwestern Gulf of Mexico. In *Submarine landslides: Selected studies in the U.S. exclusive economic zone* (pp. 92–96). U.S. Geological Survey Bulletin 2002.
- Mills, P., & Snabre, P. (1994). Settling of a suspension of hard spheres. *EPL (Europhysics Letters)*, 25(9), 651.
- Mindlin, R. D., & Deresiewicz, H. (1953). Elastic spheres in contact under varying oblique force. *Journal of Applied Mechanics*, 20, 327–344.
- Mitchell, J. K. (1988). Confronting natural disasters: An international decade for natural hazard reduction U.S. National Research Council. *Environment: Science and Policy for Sustainable Development*, 30(2), 25–29.
- Mitchell, J. K., & Soga, K. (2005). *Fundamentals of soil behavior* (592 p.). John Wiley and Sons.
- Modenese, C. (2013). Numerical study of the mechanical properties of lunar soil by the discrete element method (D. Phil Thesis, 199 p.). University of Oxford.
- Modenese, C., Utili, S., & Houslsby, G. T. (2012). A numerical investigation of quasi-static conditions for granular media. *International Symposium on Discrete Element Modelling of Particulate Media*, edited (pp. 187–195). Birmingham: RSC Publishing.
- Mohrig, D., Ellis, C., Parker, G., Whipple, K. X., & Hondzo, M. (1998). Hydroplaning of subaqueous debris flows. *Geological Society of America Bulletin*, 110(3), 387–394.
- Mohrig, D., Elverhøi, A., & Parker, G. (1999). Experiments on the relative mobility of muddy subaqueous and subaerial debris flows, and their capacity to remobilize antecedent deposits. *Marine Geology*, 154(1–4), 117–129. doi:[10.1016/S0025-3227\(98\)00107-8](https://doi.org/10.1016/S0025-3227(98)00107-8)
- Monaghan, J. J. (2000). SPH without a tensile instability. *Journal of Computational Physics*, 159 (2), 290–311. doi:[10.1006/jcph.2000.6439](https://doi.org/10.1006/jcph.2000.6439)
- Moore, D. G. (1961). Submarine slumps. *Journal of Sedimentary Research*, 31(3), 343–357.
- Moore, D. G., Curray, J. R., & Emmel, F. J. (1976). Large submarine slide (olistostrome) associated with Sunda Arc subduction zone, northeast Indian Ocean. *Marine Geology*, 21(3), 211–226. doi:[10.1016/0025-3227\(76\)90060-8](https://doi.org/10.1016/0025-3227(76)90060-8)
- Moore, J. G., Clague, D. A., Holcomb, R. T., Lipman, P. W., Normark, W. R., & Torresan, M. E. (1989). Prodigious submarine landslides on the Hawaiian Ridge. *Journal of Geophysical Research: Solid Earth*, 94(B12), 17465–17484. doi:[10.1029/JB094iB12p17465](https://doi.org/10.1029/JB094iB12p17465)
- Moore, J. G., van Andel, T. H., Blow, W. H., & Heath, G. R. (1970). Large submarine slide off the northeastern continental margin of Brazil. *American Association of Petroleum Geologists*, 54, 125–128.
- Morris, J. P., Fox, P. J., & Zhu, Y. (1997). Modeling low reynolds number incompressible flows using SPH. *Journal of Computational Physics*, 136(1), 214–226. doi:[10.1006/jcph.1997.5776](https://doi.org/10.1006/jcph.1997.5776)
- Mothes, P. A., Hall, M. L., & Janda, R. J. (1998). The enormous Chillos Valley Lahar: An ash-flow-generated debris flow from Cotopaxi Volcano, Ecuador. *Bulletin of Volcanology*, 59 (4), 233–244. doi:[10.1007/s00450050188](https://doi.org/10.1007/s00450050188)
- Muhlhaus, H. B., & Vardoulakis, I. (1987). The thickness of shear bands in granular materials. *Geotechnique*, 37(3), 271–283.

- Ng, T. (2009). Discrete element method simulations of the critical state of a granular material. *International Journal of Geomechanics*, 9(5), 209–216. doi:[10.1061/\(asce\)1532-3641\(2009\)9:5\(209\)](https://doi.org/10.1061/(asce)1532-3641(2009)9:5(209))
- Norem, H., Locat, J., & Schieldrop, B. (1990). An approach to the physics and the modeling of submarine flowslides. *Marine Georesources & Geotechnology*, 9(2), 93–111. doi:[10.1080/10641199009388233](https://doi.org/10.1080/10641199009388233)
- Normark, W. R. (1974). Ranger submarine slide, Northern Sebastian Vizcaino Bay, Baja California, Mexico. *Geological Society of America Bulletin*, 85(5), 781–784.
- Normark, W. R., Moore, J. G., & M. E. Torresan (1993). Giant volcano-related landslides and the development of the Hawaiian Islands. In *Submarine landslides: Selected studies in the U.S. exclusive economic zone* (pp. 14–22). U.S. Geological Survey Bulletin 2002.
- O'Leary, D. W. (1991). Submarine mass movement, a formative process of passive continental margins: The Munson-Nygren landslide complex and the Southeast New England landslide complex. In *U.S. Geological Survey Bulletin 2002*.
- Oda, M., & Kazama, H. (1998). Micro-structure of shear band and its relation to the mechanism of dilatancy and failure of granular soils. *Geotechnique*, 48(4), 465–481.
- Oda, M., Konishi, J., & Nemat-Nasser, S. (1982). Experimental micromechanical evaluation of strength of granular materials: Effects of particle rolling. *Mechanics of Materials*, 1(4), 269–283. doi:[10.1016/0167-6636\(82\)90027-8](https://doi.org/10.1016/0167-6636(82)90027-8)
- Olivier, B. (2001). The Master-Slave paradigm with heterogeneous processors.
- Oosthuizen, P. H., & Naylor, D. (1999). *Introduction to convective heat Transfer analysis* (620 p.). WCB/McGraw Hill.
- OpenCFD. (2004). OpenFOAM—The open source CFD toolbox. <http://www.openfoam.com/>
- Othmer, D. F. (1956). *Fluidization* (231 p.). New York: Reinhold Publishing Corporation.
- Pöschel, T., & Buchholtz, V. V. (1993). Static friction phenomena in granular materials: Coulomb law versus particle geometry. *Physical Review Letters*, 71(24), 3963–3966.
- Palmer, A. C. (2008). *Dimensional analysis and intelligent experimentation* (154 p.). World Scientific.
- Parrinello, M., & Rahman, A. (1980). Crystal structure and pair potentials: A molecular-dynamics study. *Physical Review Letters*, 45(14), 1196–1199.
- Phillips, C. J., & Davies, T. R. H. (1991). Determining rheological parameters of debris flow material. *Geomorphology*, 4(2), 101–110. doi:[10.1016/0169-555X\(91\)90022-3](https://doi.org/10.1016/0169-555X(91)90022-3)
- Phillips, J. C., Hogg, A. J., Kerswell, R. R., & Thomas, N. H. (2006). Enhanced mobility of granular mixtures of fine and coarse particles. *Earth and Planetary Science Letters*, 246(3–4), 466–480.
- Phillips, R., & Byrne, P. M. (1994). Modelling slope liquefaction due to static loading. *47th Canadian Geotechnical Conference*, edited (pp. 317–326). Canada: Halifax.
- Pierson, T. C. (1983). Soil pipes and slope stability. *Quarterly Journal of Engineering Geology*, 16 (1), 1–11. doi:[10.1144/Gsl.Qjeg.1983.016.01.01](https://doi.org/10.1144/Gsl.Qjeg.1983.016.01.01)
- Plafker, G., & Erickson, G. E. (1978). *Nevados Huascaran avalanches, Peru*. Paper Presented at Rockslides and Avalanches. 1: Natural Phenomena. Amsterdam: Elsevier.
- Plassiard, J.-P., Belheine, N., & Donzé, F.-V. (2009). A spherical discrete element model: Calibration procedure and incremental response. *Granular Matter*, 11(5), 293–306. doi:[10.1007/s10035-009-0130-x](https://doi.org/10.1007/s10035-009-0130-x)
- Plimpton, S. (1995). Fast parallel algorithms for short-range molecular dynamics. *Journal of Computational Physics*, 117(1), 1–19. doi:[10.1006/jcph.1995.1039](https://doi.org/10.1006/jcph.1995.1039)
- Pohlman, N. A., Severson, B. L., Ottino, J. M., & Lueptow, R. M. (2006). Surface roughness effects in granular matter: Influence on angle of repose and the absence of segregation. *Physical Review E*, 73(3), 031304.
- Pope, S. B. (2000). *Turbulent flows*. Cambridge University Press.
- Popenoe, P., Schmuck, E. A., & Dillon, W. P. (1991). The cape fear landslide: Slope failure associated with salt diapirism and gas hydrate decomposition. In *Submarine landslides: Selected studies in the U.S. exclusive economic zone*. U.S. Geological Survey Bulletin 2002.

- Potts, D. M., & Zdravkovic, L. (2001). *Finite element analysis in geotechnical engineering* (427 p.). London: Thomas Telford Publishing.
- Potyondy, D. O., & Cundall, P. A. (2004). A bonded-particle model for rock. *International Journal of Rock Mechanics and Mining Sciences*, 41(8), 1329–1364. doi:[10.1016/j.ijrmms.2004.09.011](https://doi.org/10.1016/j.ijrmms.2004.09.011)
- Prior, D. B., Bornhold, B. D., & Johns, M. W. (1984). Depositional characteristics of a submarine debris flow. *The Journal of Geology*, 92(6), 707–727.
- Prior, D. B., & Coleman, J. M. (1979). Submarine landslides—Geometry and nomenclature. *Zeitschrift für Geomorphologie*, 23, 415–426.
- Prior, D. B., Coleman, J. M. (1982). Active slides and flows in underconsolidated marine sediments on the slopes of the Mississippi delta. In S. Saxov & J. K. Nieuwenhuis (Eds.), *Marine slides and other mass movements* (pp. 21–49). Springer US. doi:[10.1007/978-1-4613-3362-3\\_3](https://doi.org/10.1007/978-1-4613-3362-3_3)
- Radjaï, F., & Dubois, F. (2011). *Discrete-element modeling of granular materials* (448 p.). Iste/Wiley Publishing.
- Radl, S., Radeke, C., Khinast, J. G., & Sundaresan, S. (2011). Parcel-based approach for the simulation of gas-particle flows. In *8th International Conference on CFD in Oil & Gas, Metallurgical and Process Industries* (pp. 1–10). SINTEF/NTNU, Trondheim Norway.
- Rahiman, T. I. H., Pettinga, J. R., & Watts, P. (2007). The source mechanism and numerical modelling of the 1953 Suva tsunami, Fiji. *Marine Geology*, 237(1–2), 55–70. doi:[10.1016/j.margeo.2006.10.036](https://doi.org/10.1016/j.margeo.2006.10.036)
- Rahman, M. H. (1997). Slope stability analysis of the heterogeneous coastal cliff by the finite element method (FEM). *Deformation and Progressive Failure in Geomechanics—Is-Nagoya'97* (707–712).
- Rankine, W. J. M. (1857). On the stability of loose earth. *Philosophical Transactions of the Royal Society of London*, 147(ArticleType: research-article/Full publication date: 1857/), 9–27. doi:[10.2307/108608](https://doi.org/10.2307/108608)
- Reid, M. E., Nielsen, H. P., & Dreiss, S. J. (1988). Hydrologic factors triggering a shallow hillslope failure. *Bulletin Association of Engineering Geologists*, 25, 349–361.
- Richardson, J. F., & Zaki, W. N. (1954). Sedimentation and fluidisation: Part I. *Chemical Engineering Research and Design*, 75, Supplement(0), S82–S100. doi:[10.1016/s0263-8762\(97\)80006-8](https://doi.org/10.1016/s0263-8762(97)80006-8)
- Roche, O., Attali, M., Mangeney, A., & Lucas, A. (2011). On the run-out distance of geophysical gravitational flows: Insight from fluidized granular collapse experiments. *Earth and Planetary Science Letters*, 311(3–4), 375–385. doi:[10.1016/j.epsl.2011.09.023](https://doi.org/10.1016/j.epsl.2011.09.023)
- Rodine, J. D. (1974). Analysis of the mobilization of debris flows (PhD Thesis, 226 p.). Stanford, CA: Stanford University.
- Rothenburg, L., & Bathurst, R. J. (1992). Micromechanical features of granular assemblies with planar elliptical particles. *Geotechnique*, 42(1), 79–95.
- Rowe, P. W. (1962). The stress-dilatancy relation for static equilibrium of an assembly of particles in contact. *Proceedings of the Royal Society of London. Series A. Mathematical and Physical Sciences*, 269(1339), 500–527.
- Sakai, M., Takahashi, H., Pain, C. C., Latham, J.-P., & Xiang, J. (2012). Study on a large-scale discrete element model for fine particles in a fluidized bed. *Advanced Powder Technology*, 23 (5), 673–681. doi:[10.1016/j.apt.2011.08.006](https://doi.org/10.1016/j.apt.2011.08.006)
- Saucedo, R., Macias, J. L., Sheridan, M. F., Bursik, M. I., & Komorowski, J. C. (2005). Modeling of pyroclastic flows of Colima Volcano, Mexico: Implications for hazard assessment. *Journal of Volcanology and Geothermal Research*, 139(1–2), 103–115.
- Savage, S. B., & Hutter, K. (1989). The motion of a finite mass of granular material down a rough incline. *Journal of Fluid Mechanics*, 199, 177–215.
- Schlichting, H., & K. Gersten (2000). *Boundary-layer theory*. 8th Revised and Enlarged Edition (799 p.). Springer.

- Schmitt, F. G. (2007). About Boussinesq's turbulent viscosity hypothesis: Historical remarks and a direct evaluation of its validity. *Comptes Rendus Mécanique*, 335(9–10), 617–627. doi:[10.1016/j.crme.2007.08.004](https://doi.org/10.1016/j.crme.2007.08.004)
- Schofield, A. N., & Wroth, C. P. (1968). *Critical state soil mechanics* (310 p.). London: McGraw-Hill.
- Schupp, J. (2009). Upheaval buckling and flotation of buried offshore pipelines (DPhil Thesis). University of Oxford.
- Schuster, R. L., & Fleming, R. M. (1986). Economic losses and fatalities due to landslides. *Bulletin American Association Engineering Geologists*, 23(1), 11–28.
- Schwab, W. C., & Lee, H. J. (1993). Processes controlling the style of mass movement in glaciomarine sediment: Northeastern Gulf of Alaska. In *Submarine landslides: Selected studies in the U.S. exclusive economic zone* (pp. 1–10). U.S. Geological Survey Bulletin 2002.
- Shafipour, R., & Soroush, A. (2008). Fluid coupled-DEM modelling of undrained behavior of granular media. *Computers and Geotechnics*, 35(5), 673–685. doi:[10.1016/j.compgeo.2007.12.003](https://doi.org/10.1016/j.compgeo.2007.12.003)
- Sharma, J. S., & Bolton, M. D. (1996). Centrifuge modelling of an embankment on soft clay reinforced with a geogrid. *Geotextiles and Geomembranes*, 14(1), 1–17. doi:[10.1016/0266-1144\(96\)00003-9](https://doi.org/10.1016/0266-1144(96)00003-9)
- Shepard, F. P. (1973). Sea floor off Magdalena delta and Santa Marta Area, Colombia. *Geological Society of America Bulletin*, 84(6), 1955–1972.
- Shih, Y. T., Gidaspow, D., & Wasan, D. T. (1987). Hydrodynamics of sedimentation of multisized particles. *Powder Technology*, 50(3), 201–215. doi:[10.1016/0032-5910\(87\)80065-7](https://doi.org/10.1016/0032-5910(87)80065-7)
- Shimizu, Y. (2011). Microscopic numerical model of fluid flow in granular material. *Geotechnique*, 61(10), 887–896.
- Shreve, R. L. (1968). Leakage and fluidization in air-layer lubricated avalanches. *Geological Society of America Bulletin*, 79(5), 653–658.
- Siavoshi, S., & Kudrolli, A. (2005). Failure of a granular step. *Physical Review E (Statistical, Nonlinear, and Soft Matter Physics)*, 71(5). doi:[citeulike-article-id:11391495](https://doi.org/10.1103/PhysRevE.71.051302)
- Siebe, C., Komorowski, J.-C., & Sheridan, M. (1992). Morphology and emplacement of an unusual debris-avalanche deposit at Jocotitlán volcano, Central Mexico. *Bulletin of Volcanology*, 54(7), 573–589. doi:[10.1007/bf00569941](https://doi.org/10.1007/bf00569941)
- Siebert, L. (1984). Large volcanic debris avalanches: Characteristics of source areas, deposits, and associated eruptions. *Journal of Volcanology and Geothermal Research*, 22(3–4), 163–197. doi:[10.1016/0377-0273\(84\)90002-7](https://doi.org/10.1016/0377-0273(84)90002-7)
- Soeters, R., & van Westen, C. J. (1996). Slope instability recognition, analysis and zonation. In A. K. Turner & R. L. Schuster (Eds.), *Landslides: Investigation and mitigation* (pp. 129–177). Washington, D. C.: National Academy Press.
- Spence, K. J., & Guymer, I. (1997). Small-scale laboratory flowslides. *Geotechnique*, 47(5), 915–932.
- Staron, L., & Hinch, E. (2007). The spreading of a granular mass: Role of grain properties and initial conditions. *Granular Matter*, 9(3–4), 205–217. doi:[10.1007/s10035-006-0033-z](https://doi.org/10.1007/s10035-006-0033-z)
- Staron, L., & Hinch, E. J. (2005). Study of the collapse of granular columns using DEM numerical simulation. *Journal of Fluid Mechanics*, 545, 1–27.
- Staron, L., & Lajeunesse, E. (2009). Understanding how volume affects the mobility of dry debris flows. *Geophysical Research Letters*, 36(12), L12402. doi:[10.1029/2009gl038229](https://doi.org/10.1029/2009gl038229)
- Stokes, G. G. (1901). *Mathematical and physical papers* (416 p.). Cambridge University Press.
- Sultan, N., Cochonat, P., Foucher, J. P., Mienert, J., Hafstadson, H., & Sejrup, H. P. (2003). Effect of gas hydrates dissociation on seafloor slope stability. In J. Locat, J. Mienert, & L. Boisvert, *Submarine mass movements and their consequences* (pp. 103–111). Netherlands: Springer. doi:[10.1007/978-94-010-0093-2\\_12](https://doi.org/10.1007/978-94-010-0093-2_12)
- Swegle, J. W., Hicks, D. L., & Attaway, S. W. (1995). Smoothed particle hydrodynamics stability analysis. *Journal of Computational Physics*, 116(1), 123–134. doi:[10.1006/jcph.1995.1010](https://doi.org/10.1006/jcph.1995.1010)

- Syamlal, M. (1987). The derivation of a drag Coefficient formula from velocity-voidage correlations. *Unpublished report*, 1–20.
- Takeda, H., Miyama, S. M., & Sekiya, M. (1994). Numerical simulation of viscous flow by smoothed particle hydrodynamics. *Progress of Theoretical Physics*, 92(5), 939–960.
- Talling, P. J., et al. (2007). Onset of submarine debris flow deposition far from original giant landslide. *Nature*, 450(7169), 541–544. doi:[10.1038/Nature06313](https://doi.org/10.1038/Nature06313)
- Tang, C. L., Hu, J. C., Lin, M. L., Angelier, J., Lu, C. Y., Chan, Y. C., et al. (2009). The Tsaojing landslide triggered by the Chi-Chi earthquake, Taiwan: Insights from a discrete element simulation. *Engineering Geology*, 106(1–2), 1–19. doi:[10.1016/j.enggeo.2009.02.011](https://doi.org/10.1016/j.enggeo.2009.02.011)
- Taylor, R. N. (1995). *Geotechnical centrifuge technology* (296 p.). Taylor & Francis.
- Tennekes, H., & Lumley, J. L. (1972). *A first course in turbulence* (1st ed., 300 p.). Cambridge: The MIT Press.
- Terzaghi, K. (1943). *Theoretical soil mechanics* (510 p.). New York: John Wiley and Sons.
- Terzaghi, K., Peck, R. B., & Mesri, G. (1996). *Soil mechanics in engineering practice* (549 p.). London: John Wiley & Sons.
- Thompson, E. L., & Huppert, H. E. (2007). Granular column collapses: Further experimental results. *Journal of Fluid Mechanics*, 575, 177–186.
- Thornton, C. (2000). Numerical simulations of deviatoric shear deformation of granular media. *Geotechnique*, 50(1), 43–53.
- Thornton, C., & Antony, S. J. (1998). Quasi-static deformation of particulate media. *Philosophical Transactions of the Royal Society of London. Series A: Mathematical, Physical and Engineering Sciences*, 356(1747), 2763–2782.
- Thornton, C., & Antony, S. J. (2000). Quasi-static shear deformation of a soft particle system. *Powder Technology*, 109(1–3), 179–191. doi:[10.1016/S0032-5910\(99\)00235-1](https://doi.org/10.1016/S0032-5910(99)00235-1)
- Tiller, F. M. (1981). Revision of kynch sedimentation theory. *AIChE Journal*, 27(5), 823–829. doi:[10.1002/aic.690270517](https://doi.org/10.1002/aic.690270517)
- Ting, J. M., Corkum, B. T., Kauffman, C. R., & Greco, C. (1989). Discrete numerical-model for soil mechanics. *Journal of Geotechnical Engineering-ASCE*, 115(3), 379–398.
- Toda, K., & Furuse, H. (2006). Extension of Einstein's viscosity equation to that for concentrated dispersions of solutes and particles. *Journal of Bioscience and Bioengineering*, 102(6), 524–528.
- Townsend, A. A. R. (1980). *The structure of turbulent shear flow* (2nd ed., 429 p.). Cambridge University Press.
- Trussell, R., & Chang, M. (1999). Review of flow through porous media as applied to head loss in water filters. *Journal of Environmental Engineering*, 125(11), 998–1006.
- Tsuji, Y., Kawaguchi, T., & Tanaka, T. (1993). Discrete particle simulation of two-dimensional fluidized bed. *Powder Technology*, 77(1), 79–87. doi:[10.1016/0032-5910\(93\)85010-7](https://doi.org/10.1016/0032-5910(93)85010-7)
- Tsuji, Y., Tanaka, T., & Ishida, T. (1992). Lagrangian numerical-simulation of plug flow of cohesionless particles in a horizontal pipe. *Powder Technology*, 71(3), 239–250.
- USGS. (1982). Goals and tasks of the landslide part of a ground-failure hazards reduction program. *Rep.*, 44 p.
- USGS. (2004). Landslide types and processes. *Rep.* (4 p.). U.S. Geological Survey.
- Utili, S., Zhao, T., & Housby, G. T. (2015). 3D DEM investigation of granular column collapse: Evaluation of debris motion and its destructive power. *Engineering Geology*, 186, 3–16. doi:[10.1016/j.enggeo.2014.08.018](https://doi.org/10.1016/j.enggeo.2014.08.018)
- Vacondio, R., Mignosa, P., & Pagani, S. (2013). 3D SPH numerical simulation of the wave generated by the Vajont rockslide. *Advances in Water Resources*, 59, 146–156. doi:[10.1016/j.advwatres.2013.06.009](https://doi.org/10.1016/j.advwatres.2013.06.009)
- Vallance, J. W., & Scott, K. M. (1997). The Osceola Mudflow from Mount Rainier: Sedimentology and hazard implications of a huge clay-rich debris flow. *Geological Society of America Bulletin*, 109(2), 143–163.

- Vendeville, B. C., & Gaullier, V. (2003). Role of pore-fluid pressure and slope angle in triggering submarine mass movements: Natural examples and pilot experimental models. In J. Locat, J. Mienert, & L. Boisvert (Eds.), *Submarine mass movements and their consequences* (pp. 137–144). Springer Netherlands, doi:[10.1007/978-94-010-0093-2\\_16](https://doi.org/10.1007/978-94-010-0093-2_16)
- Voight, B., Janda, R. J., Glicken, H., & Douglass, P. M. (1983). Nature and mechanics of the Mount St Helens rockslide-avalanche of 18 May 1980. *Geotechnique*, 33, 243–273.
- Voight, B., & Sousa, J. (1994). Lessons from Ontake-san: A comparative analysis of debris avalanche dynamics. *Engineering Geology*, 38(3–4), 261–297. doi:[10.1016/0013-7952\(94\)90042-6](https://doi.org/10.1016/0013-7952(94)90042-6)
- Wachmann, B., Kalthoff, W., Schwarzer, S., & Herrmann, H. J. (1998). Collective drag and sedimentation: Comparison of simulation and experiment in two and three dimensions. *Granular Matter*, 1(2), 75–82. doi:[10.1007/s100350050012](https://doi.org/10.1007/s100350050012)
- Walton, O., Moor, C. P., & Gill, K. (2007). Effects of gravity on cohesive behavior of fine powders: Implications for processing Lunar regolith. *Granular Matter*, 9(5), 353–363. doi:[10.1007/s10035-006-0029-8](https://doi.org/10.1007/s10035-006-0029-8)
- Wang, G., & Sassa, K. (2001). Factors affecting rainfall-induced flowslides in laboratory flume tests. *Geotechnique*, 51(7), 587–599.
- Watts, A. B., & Masson, D. G. (1995). A giant landslide on the north flank of Tenerife, Canary Islands. *Journal of Geophysical Research: Solid Earth*, 100(B12), 24487–24498. doi:[10.1029/95jb02630](https://doi.org/10.1029/95jb02630)
- Weatherley, D., Boros, V., & Hancock, W. (2011). *ESyS-particle tutorial and user's guide version 2.1* (153 p.). Earth Systems Science Computational Centre, The University of Queensland.
- Weaver, P. P. E., & Kuijpers, A. (1983). Climatic control of turbidite deposition on the Madeira Abyssal Plain. *Nature*, 306, 360–363.
- Wen, C. Y., & Yu, Y. H. (1966). Mechanics of fluidization. *Chemical Engineering Progress Symposium Series*, 62(62), 100–111.
- Wieczorek, G. F. (1987). Effect of rainfall intensity and duration on debris flows in the central Santa Cruz Mountains, California. In J. e. Costa & G. F. Wieczorek (Eds.), *Debris flows/avalanches: Process, recognition, and mitigation* (pp. 93–104). Boulder, Colorado: Geological Society of America.
- Wilcox, D. C. (2006). *Turbulence modeling for CFD* (522 p.). DCW Industries, Incorporated.
- Williams, K. C., Chen, W., Weeger, S., & Donohue, T. J. (2014). Particle shape characterisation and its application to discrete element modelling. *Particuology*, 12, 80–89. doi:[10.1016/j.partic.2013.02.014](https://doi.org/10.1016/j.partic.2013.02.014)
- Wilson, C. K., Long, D., & Bulat, J. (2004). The morphology, setting and processes of the Afen Slide. *Marine Geology*, 213(1–4), 149–167. doi:[10.1016/j.margeo.2004.10.005](https://doi.org/10.1016/j.margeo.2004.10.005)
- Wood, D. M. (1990). *Soil behaviour and critical state soil mechanics* (426 p.). Cambridge University Press.
- Wu, C.-Y., & Cocks, A. C. F. (2006). Numerical and experimental investigations of the flow of powder into a confined space. *Mechanics of Materials*, 38(4), 304–324. doi:[10.1016/j.mechmat.2005.08.001](https://doi.org/10.1016/j.mechmat.2005.08.001)
- Xu, G. L., Huang, H., Bai, Y. S., & Zhang, W. S. (2011). On the application of finite element method (FEM) to the slope stability analyses. *Mechanical, Materials and Manufacturing Engineering, Pts 1-3*, 66-68, 1913–1916. doi:[10.4028/www.scientific.net/AMM.66-68.1913](https://doi.org/10.4028/www.scientific.net/AMM.66-68.1913)
- Yang, C.-Y., Ding, Y., York, D., & Broeckx, W. (2008). Numerical simulation of sedimentation of microparticles using the discrete particle method. *Particuology*, 6(1), 38–49. doi:[10.1016/j.partc.2007.10.006](https://doi.org/10.1016/j.partc.2007.10.006)
- Yano, K., & Daido, A. (1965). Fundamental study on mud-flow. *Bulletin of the Disaster Prevention Research Institute*, 14(2), 69–83.
- Yu, S., Adams, M., Gururajan, B., Reynolds, G., Roberts, R., & Wu, C.-Y. (2013). The effects of lubrication on roll compaction, ribbon milling and tabletting. *Chemical Engineering Science*, 86, 9–18. doi:[10.1016/j.ces.2012.02.026](https://doi.org/10.1016/j.ces.2012.02.026)

- Zeghal, M., & El Shamy, U. (2004). A continuum-discrete hydromechanical analysis of granular deposit liquefaction. *International Journal for Numerical and Analytical Methods in Geomechanics*, 28(14), 1361–1383. doi:[10.1002/nag.390](https://doi.org/10.1002/nag.390)
- Zenit, R. (2005). Computer simulations of the collapse of a granular column. *Physics of Fluids*, 17(3).
- Zhang, D., & Whiten, W. J. (1996). The calculation of contact forces between particles using spring and damping models. *Powder Technology*, 88(1), 59–64. doi:[10.1016/0032-5910\(96\)03104-X](https://doi.org/10.1016/0032-5910(96)03104-X)
- Zhang, J., Fan, L.-S., Zhu, C., Pfeffer, R., & Qi, D. (1999). Dynamic behavior of collision of elastic spheres in viscous fluids. *Powder Technology*, 106(1–2), 98–109. doi:[10.1016/S0032-5910\(99\)00053-4](https://doi.org/10.1016/S0032-5910(99)00053-4)
- Zhao, T., Houldsby, G. T., & Utili, S. (2014). Investigation of granular batch sedimentation via DEM–CFD coupling. *Granular Matter*, 16(6), 921–932. doi:[10.1007/s10035-014-0534-0](https://doi.org/10.1007/s10035-014-0534-0)
- Zhou, G. G. D., & Ng, C. W. W. (2010). Numerical investigation of reverse segregation in debris flows by DEM. *Granular Matter*, 12(5), 507–516. doi:[10.1007/s10035-010-0209-4](https://doi.org/10.1007/s10035-010-0209-4).
- Zhou, S. H., Liu, J. G., Wang, B. L., Yang, L. C., & Gong, Q. M. (2002). *Centrifugal model test on the stability of underwater slope*. Paper presented at Physical modelling in Geotechnics: ICPMG' 02, Swets & Zeitlinger Lisse, A.A. Balkema, Canada.